2009, VOLUME 4

PROGRESS IN PHYSICS

"All scientists shall have the right to present their scientific research results, in whole or in part, at relevant scientific conferences, and to publish the same in printed scientific journals, electronic archives, and any other media." — Declaration of Academic Freedom, Article 8

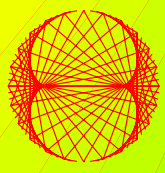

ISSN 1555-5534

The Journal on Advanced Studies in Theoretical and Experimental Physics, including Related Themes from Mathematics

PROGRESS IN PHYSICS

A quarterly issue scientific journal, registered with the Library of Congress (DC, USA). This journal is peer reviewed and included in the abstracting and indexing coverage of: Mathematical Reviews and MathSciNet (AMS, USA), DOAJ of Lund University (Sweden), Zentralblatt MATH (Germany), Scientific Commons of the University of St. Gallen (Switzerland), Open-J-Gate (India), Referativnyi Zhurnal VINITI (Russia), etc.

To order printed issues of this journal, contact the Editors. Electronic version of this journal can be downloaded free of charge:
http://www.ptep-online.com

Postal address

Department of Mathematics and Science,
University of New Mexico,
200 College Road,
Gallup, NM 87301, USA

This journal is powered by LaTeX

A variety of books can be downloaded free from the Digital Library of Science:
http://www.gallup.unm.edu/∼smarandache

ISSN: 1555-5534 (print)
ISSN: 1555-5615 (online)

Standard Address Number: 297-5092
Printed in the United States of America

OCTOBER 2009 **VOLUME 4**

CONTENTS

Information for Authors and Subscribers

Progress in Physics has been created for publications on advanced studies in theoretical and experimental physics, including related themes from mathematics and astronomy. All submitted papers should be professional, in good English, containing a brief review of a problem and obtained results.

All submissions should be designed in LaTeX format using *Progress in Physics* template. This template can be downloaded from *Progress in Physics* home page http://www.ptep-online.com. Abstract and the necessary information about author(s) should be included into the papers. To submit a paper, mail the file(s) to the Editor-in-Chief.

All submitted papers should be as brief as possible. We accept brief papers, no larger than 8 typeset journal pages. Short articles are preferable. Large papers can be considered in exceptional cases to the section *Special Reports* intended for such publications in the journal. Letters related to the publications in the journal or to the events among the science community can be applied to the section *Letters to Progress in Physics*.

All that has been accepted for the online issue of *Progress in Physics* is printed in the paper version of the journal. To order printed issues, contact the Editors.

This journal is non-commercial, academic edition. It is printed from private donations. (Look for the current author fee in the online version of the journal.)

Kirchhoff's Law of Thermal Emission: 150 Years

Pierre-Marie Robitaille

Department of Radiology, The Ohio State University, 395 W. 12th Ave, Suite 302, Columbus, Ohio 43210, USA

E-mail: robitaille.1@osu.edu

In this work, Kirchhoff's law (Kirchhoff G. *Monatsberichte der Akademie der Wissenschaften zu Berlin*, sessions of Dec. 1859, 1860, 783–787) is being revisited not only to mark its 150th anniversary but, most importantly, to highlight serious overreaching in its formulation. At the onset, Kirchhoff's law correctly outlines the equivalence between emission and absorption for an opaque object under thermal equilibrium. This same conclusion had been established earlier by Balfour Stewart (Stewart B. *Trans. Royal Soc. Edinburgh*, 1858, v. 22(1), 1–20). However, Kirchhoff extends the treatment beyond his counterpart, stating that cavity radiation must always be black, or normal: depending only on the temperature and the frequency of observation. This universal aspect of Kirchhoff's law is without proper basis and constitutes a grave distortion of experimental reality. It is readily apparent that cavities made from arbitrary materials ($\varepsilon < 1$) are never black. Their approach to such behavior is being driven either by the blackness of the detector, or by black materials placed near the cavity. Ample evidence exists that radiation in arbitrary cavities is sensitive to the relative position of the detectors. In order to fully address these issues, cavity radiation and the generalization of Kirchhoff's law are discussed. An example is then taken from electromagnetics, at microwave frequencies, to link results in the resonant cavity with those inferred from the consequences of generalization.

1 Introduction

Kirchhoff's law is one of the simplest and most misunderstood in thermodynamics [1, 2]. It is widely considered to be the first of the laws of thermal emission [3–7]. In simple mathematical terms, Kirchhoff's law can take on several formulations, which stem from the equivalence between the coefficients of emission, ε, and absorption, α, at thermal equilibrium. The most general expression of Kirchhoff's law for opaque objects is, in fact, a statement of Stewart's law [6], namely, $\varepsilon = 1 - \rho$, where ρ corresponds to the coefficient of reflection. However, Kirchhoff's law [1, 2] is much farther reaching than Stewart's [6], in requiring that radiation within an enclosure, or cavity, must always be black, or normal [5]. Kirchhoff conceives that the ratio of emissive power, e, to absorptive power, a, of all bodies can be described by a universal function, f, common to all radiation within enclosures: $e/a = f(T, \lambda)$. Furthermore, this must be the case in a manner which is independent of the nature and shape of the enclosure, and which depends only on the temperature, T, of the system and the wavelength, λ, of observation [1, 2, 5, 7].

Kirchhoff's law constitutes an attempt to summarize the state of knowledge in radiative heat transfer during the mid-1800's. At the time, physicists created blackbodies from graphite plates, by lining the interior of cavities with soot, or by coating objects with black paint containing soot [8]. Contrary to Gustav Kirchhoff [1, 2], Balfour Stewart, in 1858 [6], stated that radiation in thermal equilibrium depends on the constituents involved and his treatment did not lead to a universal function. If Kirchhoff's law can be expressed as $e/a = f(T, \lambda)$, then Stewart's would be $e/a = f'(T, \lambda, N)$, where N represents all factors linked to the nature of the emitter itself and f' is not universal. Like Kirchhoff, Stewart based his ideas on Prévost's theory of exchanges [9, 10], which was ultimately linked to the study of radiation within enclosures. The distinctions between Stewart's formulation and Kirchhoff's are profound [11, 12]. Kirchhoff's ideas advocate a universal function [5]. Stewart's do not [6, 11, 12].

Today, 150 years after its formulation [1, 2], the foundation of Kirchhoff's law still rests on condensed matter physics. Blackbodies continue to be highly specialized objects [13–25] constructed from absorbers which are nearly perfect over the frequency range of interest. Yet, if Kirchhoff was correct about the nature of radiation within cavities, it should be possible to assemble a blackbody from any material. Surely, the presence of the universal function, f, dictates that cavity radiation must always be black, or normal [5]. All that should be theoretically required is thermal equilibrium with the walls of an enclosure. The attributes of the walls, or its contents, should be inconsequential. However, the body of experimental knowledge, relative to the assembly of blackbodies in the laboratory, stands firmly opposed to this concept [13–25]. True blackbodies [13–25] are extremely difficult to produce and testify against Kirchhoff's universal formulation [1, 2, 5]. Stewart's law [6] alone, not Kirchhoff's [1, 2], is supported by a careful consideration of experimental reality [8, 12–41]. Still, a cursory review of the literature, relative to cavity emission, would suggest that arbitrary cavities can appear black. Furthermore, the trend towards blackness appears to increase as "truer" cavities are produced. This seems to

be the case, irrespective of the emissivity of the cavity walls. The subject is a fascinating problem in physics.

2 Cavity radiation

While ideal blackbodies do not exist in nature, laboratory examples approach theoretical performances, especially when narrow frequency and temperature ranges are considered [8, 13–25]. Typically, the best laboratory blackbodies are constructed from highly absorbing walls ($\alpha \approx 1$) usually containing soot, carbon black, or graphite [8, 13–25]. Cavities which operate in the far infrared may also be lined with metals, metal blacks, or metal oxides [35–41]. Blackbody enclosures are often made isothermal using water, oil, or molten metal baths. Alternatively, metal freezing point techniques or electrical heating elements may ensure isothermal operation. The vast body of the laboratory evidence supports the idea that standard blackbodies are always made from highly absorbing materials set to function in an isothermal state.

Nonetheless, in treating cavity radiation from a theoretical standpoint, Planck invokes the perfectly reflecting enclosure [7, 8]. This is an interesting approach, since perfectly reflecting enclosures are adiabatic by definition and cannot therefore participate in the exchange of heat, either through emission or absorption. Planck, though, requires that the interior of such cavities contains black radiation [7; §51–52], in conformity with Kirchhoff's law [1, 2]. In so insisting, Planck makes constant recourse [8] to a minute particle of carbon [7; §51–52]. He inserts the particle into the cavity, in order to ensure that the latter appropriately holds black radiation. Planck invokes carbon, despite the fact that Kirchhoff's law should have ensured the presence of the radiation sought. In the end, and though carbon particles are perfect absorbers, Planck treats them simply as catalysts, and ignores their importance to the blackbody problem [7, 8].

It remains commonly acknowledged that all cavity radiation must be black. This is the case even though cavities with arbitrary walls of low emissivity are never used as laboratory blackbody standards [13–25]. Clearly, there is more to the understanding of arbitrary cavities than the belief that they are black [1, 2, 5]. In any case, when arbitrary cavities are analyzed with radiometric detectors, they do appear to become black, as seen in classic texts [i.e. 28] and the references they contain [29–34, 42–48]. Ample theoretical work reinforces this position [i.e. 42–48]. Monte Carlo calculations on lambertian spherical arbitrary cavities constructed from walls of low emissivity provide a good example [28]. Such calculations lead to apparent cavity emissivities approaching 1 [28]. These amazing results hint at proof, at least on the surface, that Kirchhoff's law is fully valid. Unfortunately, it can be shown that such conclusions are erroneous.

Let us return for a moment to Planck's treatment [7] and the perfectly reflecting cavity containing a carbon particle [8]. A schematic representation of this situation is presented in Figure 1A. Since the cavity wall is perfectly reflecting, one can treat it as an adiabatic boundary producing no radiation of its own. All of the radiation which comes to fill the cavity is being produced by the carbon particle [12]. As a result, if one examines the contents of the cavity through a small hole, the radiation it contains will obviously be black. Now, let us displace the carbon particle, such that it is located just outside the aperture leading to the cavity (see Fig. 1B). From this position, the particle will once again be able to fill the cavity with photons, and the observer will find that its interior contains black radiation. Finally, let us place the carbon particle well outside the cavity itself, such that its radiation can still penetrate the cavity (see Fig. 1C). In this instance, the observer will record that the cavity is black, but not because it was able to become black on its own. It is black simply because the carbon particle has filled the cavity with radiation.

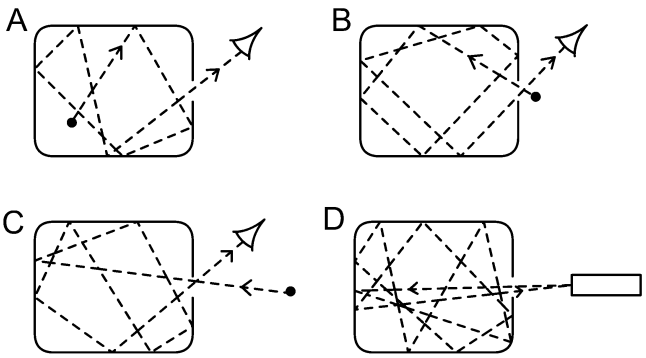

Fig. 1: Schematic representation of a perfectly reflecting cavity A) containing a carbon particle, B) with a carbon particle near the aperture, C) with a carbon particle farther from the aperture, and D) with the carbon particle replaced by a physical detector. The eye represents a point of detection. Note that if perfectly reflecting cavities contain any radiation whatsoever, it is solely because they have been filled with photons either from the carbon particle or the detector.

Returning to the days of Kirchhoff, it is evident that limited experimental means existed. As a result, cavity radiation was monitored through a combination of prisms, for frequency differentiation, and thermometers, for energy detection. These thermometers were always blackened with soot, as Langley reminds us in 1888: "*I may reply that we have lately found an admirable check on the efficiency of our optical devices in the behavior of that familiar substance lampblack, which all physicists use either on the thermometers, thermopiles, or bolometers*" [49]. Consequently, by sampling the cavity with a thermometer coated with lampblack, every experimentalist brought about for himself the result which he sought. All cavities appeared black, because all cavities were being filled unintentionally with black radiation. Adding the carbon particle directly to the interior of the cavity simply helped to bring about the desired experimental scenario.

In Fig. 1D, a cavity is represented along with a radiometric detector. In order to maintain a logical progression, let us assume that the cavity is perfectly reflecting in its interior.

In this case, the cavity itself cannot emit any photons [12]. A small hole is made into the cavity, and the radiation contained within it can be sampled with the radiometer. The cavity will be found to contain black radiation [12]. Yet, if the cavity was a perfect reflector, then how could its interior be black? The answer, of course, is similar to what Planck had done with the small carbon particle. A carbon particle, no matter how tiny [8, 12], will instantly fill an experimental cavity with black radiation. Planck, in fact, relies on this reality [7; §51–52]. Now, consider our radiometric detector. This instrument must have high photon capture rates. That is to say, it must possess an elevated absorptivity. As a result, by Stewart's law [6], it must also possess a high emissivity. Thus, if the cavity appears black, it is only because it has been filled with black radiation by the detector. Again, the experimentalist inadvertently produced the expected result.

In order to more fully appreciate the role of the detector in generating black radiation within cavities, let us consider the classic works by De Vos [32, 33] and Ono [28, 34]. Even though he is addressing arbitrary cavities, De Vos emphasizes that: "*The radiation emerging from the hole of observation in the blackbody should be an approximation, as well as possible, to the theoretical blackbody radiation*" [32]. A cursory examination of these studies would lead one to believe that all arbitrary cavities are indeed black. However, upon closer analysis, these investigators have not distinguished themselves from their predecessors. De Vos elegantly links mathematical and experimental results obtained from cavities [32]. If the cavities appear black under certain viewing conditions, it is simply because black radiation has been injected into them using detectors. De Vos notes that in order to sample black radiation in a spherical cavity of arbitrary construction: "*It is necessary to take care that the surface element observed is not perpendicular to the direction of observation*" [32]. The reason for this statement is evident. If the surface element was perpendicular, most of the radiation introduced by the detector into the cavity would undergo normal specular reflection back out of the cavity and the latter would not appear black. In subsequently describing the tubular blackbody (see Figure 2A), De Vos states that: "*The actual value of the quality will be better than calculated in this way but only slightly better since the radiant intensity decreases rapidly towards the ends of the tube*" [32]. Of course, the detector is pumping radiation into the hole at the center of the tube. It is, therefore, simple to understand why radiation must fall rapidly towards the ends of the tube. Clearly, the tubular cavity is manifesting the performance of the detector. In fact, De Vos himself unintentionally makes the point: "*Owing to the small hole in the tungsten tube a small quantity of energy was available only. Hence it was necessary to use radiation receivers of high sensitivity*" [33]. De Vos might have more appropriately written that it was important for the detector to provide an ample supply of photons. For his part, Ono has demonstrated that the apparent emission of the tubular cavity depends on the position of the detector itself. Ono writes: "*The apparent emissivity has deep minima around $\theta = 0^\circ$ at which specularly reflected radiation escapes through the lateral hole. The shallow minima around 30° are also due to specular reflection effects where incident radiation escapes after two successive specular reflections*" [28, p. 605]. This situation is reproduced schematically in Fig. 2B. Of course, the incident radiation arises from the detector. It alone is filling the cavity with black radiation. The cavity itself is not producing this radiation for, if it did, the position of the detector would be immaterial. This is certain proof that Kirchhoff's law does not hold. Much depends on the detector, not on the cavity.

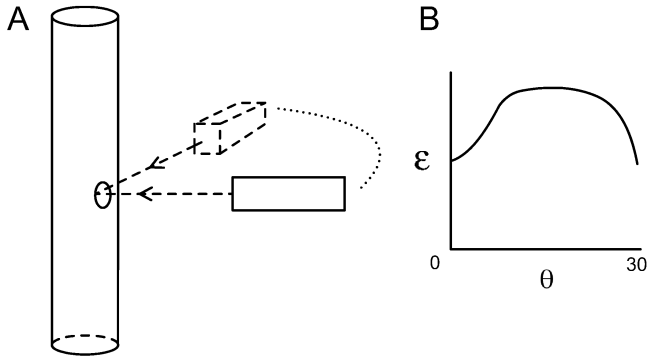

Fig. 2: A) Schematic representation of a tubular cavity and a detector. B) Illustration of the type of result seen with the detector as a function of angle from the normal. Note how there is less emission measured at 0° and 30°.

The point is further amplified by considering the work of Sparrow and Heinisch [30]. The authors demonstrate that the normal emission from a cylindrical cavity is absolutely dependent on the distance of the detector from the cavity. They fail to examine the cavity as a function of detector angle. Still, it is obvious that distance variations should not be occurring. Again, the detector is critically important in flooding the cavity with radiation.

Vollmer's studies [29] help us to understand that arbitrary cavities are not black, despite the fact that, at least on the surface, they point to the contrary. His work is particularly interesting, as it aims to reconcile theoretical foundations, stemming from Buckley's classic paper [42], with experimental data. Surprising agreement is obtained between theory and experiment. In the limit, these results appear to re-emphasize that cylindrical cavities of sufficient size, made from arbitrary materials, will indeed behave as blackbodies. Everything seems to rest on solid footing, until the experimental setup is carefully examined. In order to reach agreement with theory, the apparatus used not only supplied the typical detector radiation, but also a black bellows, a black water cooled shutter, and a black water cooled cylinder [42]. Given these many possible sources of black radiation in front of the cavity opening, there can be little wonder that the cavity begins to appear black. In reality, the contrary position should have

been adopted. How surprising that, bombarded with black radiation, some cavities still fail to be able to appear fully black.

R. E. Bedford, though he believes in the validity of Kirchhoff's law, re-emphasizes the point that arbitrary cavities are simply not black [28; p. 678]: "*A blackbody is a lambertian emitter; with the exception of a spherical cavity, none of the blackbody simulators we will discuss will radiate directionally as does a blackbody*". Yet, as seen above for the spherical cavity, "*It is necessary to take care that the surface element observed is not perpendicular to the direction of observation*" [32]. Consequently, when these two excerpts are taken together, Bedford's statement constitutes a direct refutation of Kirchhoff's law. The situation deteriorates further: "*At some angle of view away from the normal to the cavity aperture (the angle depending on the particular cavity shape), the cavity radiance will begin to drop sharply from its axial value as that part of the wall becomes visible where $\varepsilon_a(y)$ near the aperture is much lower than $\varepsilon_a(x)$ deep within the cavity. In most cases this deficiency in emitted energy will be significant only at angles of view larger than are subtended by most pyrometers*" [28; p. 678]. In any event, the point is made. None of the cavities modeled can ever truly be considered blackbodies. Arbitrary materials are not lambertian and their emissivity can never be black [5]. Spherical cavities must be monitored with careful attention to the angle of observation. This should not occur if they were truly blackbodies.

If Monte Carlo simulations and other calculations reveal that arbitrary cavities move to blackness independent of wall emissivities, it is strictly because such methods fill the cavities with black radiation [42–48]. Once again, blackbodies are unique in possessing lambertian surfaces. Thus, models which utilize lambertian surfaces of low emissivity represent situations which have no counterparts in nature. In addition, there can be no difference between placing a carbon particle in a cavity, in order to ensure the presence of black radiation, and simply filling the cavity with black radiation without physically making recourse to carbon. Monte Carlo simulations introduce black photons into cavities. Hence, they become black. The process is identical to placing a highly emitting carbon particle, or radiometer, at the opening of a cavity. No proof is provided by computational methods that arbitrary cavities contain black radiation.

It can be stated that Monte Carlo simulations obtain similar answers by modeling the repeated emission of photons directly from the cavity walls. In this case, computational analysis relies on internal reflection to arrive at a cavity filled with black radiation. The problem is that this scenario violates the first law of thermodynamics and the conservation of energy. It is not mathematically possible to maintain an isothermal cavity while, at the same time, enabling its walls to lose a continual stream of photons. Such approaches build up the photon density in the cavity at the expense of wall cooling. These methods must therefore be forbidden on grounds that they violate the 1st law of thermodynamics.

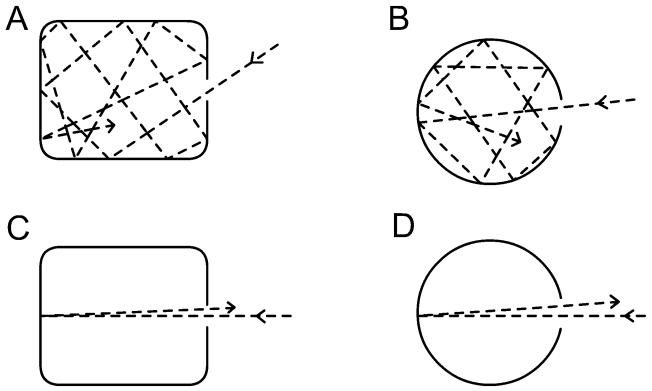

Fig. 3: Schematic representations typically used to argue that cavity radiation is always black. Figure A is similar to Figure 6.1 in [50]. Figure B is similar to 5.6 in [51]. Note that figures illustrating immediate reflection back out of the cavity (C and D) are never invoked. This is precisely because they represent direct physical proof that arbitrary cavities are not black.

It is commonly argued [50, 51] that a cavity with a sufficiently small hole contains black radiation. For example, in his classic text on the photosphere D. F. Gray writes: "*Let us begin with a container that is completely closed except for a small hole in one wall. Any light entering the hole has a very small probability of finding its way out again, and eventually will be absorbed by the walls of the container or the gas inside the container... We have constructed a perfect absorber*" [50; p. 100]. In reality, the maintenance of thermal equilibrium requires that if a photon enters the cavity, another photon must exit. The experimentalist will never be able to discern whether the exiting photon was 1) the same, 2) a photon that was newly emitted without reflection, 3) a photon that had previously undergone several reflections before exiting the cavity, or 4) a photon that had undergone a nearly infinite number of internal reflections before exiting the cavity. Each of these cases corresponds to different types of cavities, made either from arbitrary walls, perfectly absorbing walls, or perfectly reflecting walls. In any case, a photon must exit to maintain thermal equilibrium and nothing has been learned about the internal nature of the cavity. Clearly, given thermal equilibrium and the first law of thermodynamics, we cannot be sure that the radiation inside the cavity was black. Such arguments [50; p. 100–101] are unsound *a priori*. Notice, for instance, the types of figures typically associated with such rhetoric: the photon is usually drawn such that normal and immediate specular reflection back out of the cavity is discounted (see Figure 3A–B). This is precisely because immediate specular reflection of the photon back out of the cavity provides a sound logical defeat of such arguments (see Figure 3C–D).

In summary, the radiation contained inside arbitrary cavities is not black and depends exclusively on 1) the nature of the cavity, and 2) the nature of the radiation which is permitted to enter. If excellent radiometers are used, they will be

good emitters, and will act to fill the cavities with black radiation. As such, it seems logical, although counterintuitive, that the sampling of cavity radiation should be performed with suboptimal radiometers. Radiometers for these studies should not have high photon capture rates. Such devices would provide lower photon emission towards the cavity. In so doing, they would minimally alter the true nature of the radiation they seek to measure. Perhaps, by using cryogenic devices, it might be possible to build detectors which retain adequate sensitivity. By maintaining lower detector emissions, the true nature of radiation within cavities might be ascertained. The proper result should echo Stewart, as previously demonstrated mathematically [12].

3 The generalization of Kirchhoff's law

The proofs of Kirchhoff's law are usually limited to the realm of geometrical optics. In his classic paper [2], Kirchhoff states in a footnote: "*The effect of the diffraction of the rays by the edges of opening 1 is here neglected. This is allowable if openings 1 and 2, though infinitely small in comparison with their distance apart, be considered as very great in comparison with the length of a wave*." Since Planck's treatment of Kirchhoff's law is also based on geometric optics, Planck writes: "*Only the phenomena of diffraction, so far at least as they take place in space of considerable dimensions, we shall exclude on account of their rather complicated nature. We are therefore obliged to introduce right at the start a certain restriction with respect to the size of the parts of space to be considered. Throughout the following discussion it will be assumed that the linear dimensions of all parts of space considered, as well as the radii of curvature of all surfaces under consideration, are large compared to the wave lengths of the rays considered. With this assumption we may, without appreciable error, entirely neglect the influence of diffraction caused by the bounding surfaces, and everywhere apply the ordinary laws of reflection and refraction of light. To sum up: We distinguish once for all between two kinds of lengths of entirely different orders of magnitudes — dimensions of bodies and wave lengths. Moreover, even the differentials of the former, i.e., elements of length, area and volume, will be regarded as large compared with the corresponding powers of wave lengths. The greater, therefore, the wave length of the rays we wish to consider, the larger must be the parts of space considered. But, inasmuch as there is no other restriction on our choice of size of the parts of space to be considered, this assumption will not give rise to any particular difficulty*" [7; §2]. Kirchhoff and Planck specifically excluded diffraction. They do so as a matter of mathematical practicality. The problem of diffraction greatly increases the mathematical challenges involved. As a result, Kirchhoff and Planck adapt a physical setting where its effects could be ignored. This is not a question of fundamental physical limitation.

Nonetheless, the first section of Kirchhoff's law, namely the equivalence between the absorption and emission of energy by an opaque material at thermal equilibrium, has been generalized to include diffraction. Correctly speaking, this constitutes an extension of Stewart's law, as will be discussed below.

Much of the effort in generalizing Kirchhoff's (Stewart's) law can be attributed to Sergi M. Rytov, the Russian physicist. Indeed, it appears that efforts to generalize Kirchhoff's law were largely centered in Russia [52–55], but did receive attention in the West [56, 57]. Though Rytov's classic work appears initially in Russian [52], later works have been translated into English [53]. In describing their theoretical results relative to the generalization of Kirchhoff's law, Rytov and his associates [53; §3.5] write: "*Equations (3.37-39) can be termed Kirchhoff's form of the FDT (fluctuation-dissipation theorem), as they are a direct generalization of Kirchhoff's law in the classical theory of thermal radiation. This law is known to relate the intensity of the thermal radiation of a body in any direction to the absorption in that body when exposed to a plane wave propagating in the opposite direction...*" The authors continue: "*and most important, (3.37–39) contain no constraints on the relationships between the wavelength λ and characteristic scale l of the problem (the size of the bodies, the curvature radii of their surfaces, the distances from the body to an observation point, etc.). In other words, unlike the classical theory of thermal radiation, which is bound by the constraints of geometrical optics, we can now calculate the second moments of the fluctuational field, that is to say both the wave part (taking into account all the diffraction phenomena), and the nonwave (quasistationary) part for any λ vs l ratio*" [53; §3.5].

A discussion of the fluctuation-dissipation theorem (FTD), as it applies to thermal radiation, can also be found in the book by Klyshko [54]. This text provides a detailed presentation of the generalization of Kirchhoff's law [54; §4.4 and 4.5]. Apresyan and Kravtsov also address generalization in their work on radiative heat transfer [55]. They summarize the point as follows: "*In this formulation, the Kirchhoff statement — that the radiating and absorbing powers of a body are proportional to each other — as was initially derived in the limit of geometrical optics, is valid also for bodies with dimension below or about the wavelength*" [55; p. 406].

It appears that the generalized form of Kirchhoff's law has been adapted by the astrophysical community [57]. Like the Russians before them, Linsky and Mount [56] assume that the equality between emissivity and absorptivity at thermal equilibrium is a sufficient statement of Kirchhoff's law [1, 2]. They refer to a Generalized Kirchhoff's Law (GKL) as $E(\mu_0) = 1 - \rho(\mu_0)$, where $E(\mu_0)$ is the directional spectral emissivity and $\rho(\mu_0)$ corresponds to the directional hemispherical reflectivity [56]. This statement should properly be referred to as Stewart's law [6], since Stewart was the first to argue for the equality between the emissivity and absorptiv-

ity of an opaque material under conditions of thermal equilibrium. Furthermore, Stewart's law makes no claim that the radiation within opaque cavities must be black, or normal [5]. Seigel [11] speaks for physics when he outlines the important distinction between Stewart's law [6] and Kirchhoff's [1, 2]. He writes: "*Stewart's conclusion was correspondingly restricted and did not embrace the sort of connection between the emissive and absorptive powers of different materials, through a universal function of wavelength and temperature which Kirchhoff established*" [11; p. 584]. Herein, we find the central difference between Stewart and Kirchhoff. It is also the reason why Kirchhoff's law must be abandoned. In fact, since universality is not valid, there can be no more room for Kirchhoff's law in physics.

Returning to Rytov and his colleagues, following their presentation of the generalization of Kirchhoff's law [53; §3.5], they move rapidly to present a few examples of its use [53; §3.6] and even apply the treatment to the waveguide [53; §3.7]. Interestingly, though the authors fail to discuss the microwave cavity, from their treatment of the waveguide, it is certain that the radiation within the cavity cannot be black. It must depend on the dimensions of the cavity itself. Such a result is a direct confirmation of Stewart's findings [6], not Kirchhoff's [1, 2]. As a consequence, the generalization of Kirchhoff's law brings us to the conclusion that the radiation within cavities is not black, and the second portion of Kirchhoff's law is not valid.

These questions now extend to ultra high field magnetic resonance imaging [58, 59], and hence the problem of radiation within cavities should be reexamined in the context of the generalization of Kirchhoff's law [52–55]. Since generalization extends to situations where cavity size is on the order of wavelength, it is appropriate to turn to this setting in magnetic resonance imaging. In fact, this constitutes a fitting end to nearly 10 years of searching to understand why microwave cavities are not black, as required by Kirchhoff's law.

4 Cavity radiation in magnetic resonance imaging

Prior to treating the resonant microwave cavity, it is important to revisit Kirchhoff's claims. In his derivation, Kirchhoff initially insists that his treatment is restricted to the study of heat radiation. He reminds the reader that: "*All bodies emit rays, the quality and intensity of which depend on the nature and temperature of the body themselves*" [2]. Then, he immediately eliminates all other types of radiation from consideration: "*In addition to these, however, there may, under certain circumstances, be rays of other kinds, — as, for example, when a body is sufficiently charged with electricity, or when it is phosphorescent or fluorescent. Such cases are, however, here excluded*" [2]. Kirchhoff then proceeds to provide a mathematical proof for his law. Surprisingly, he then reintroduces fluorescence. This is precisely to make the point that, within cavities, all radiation must be of a universal nature. Moreover, this occurs in a manner which is completely independent of the objects they contain, even if fluorescent, or any other processes. Kirchhoff writes: "*The equation $E/A = e$ cannot generally be true of such a body, but it is true if the body is enclosed in a black covering of the same temperature as itself, since the same considerations that led to the equation in question on the hypothesis that the body C was not fluorescent, avail in this case even if the body C be supposed to be fluorescent*" [2]. Kirchhoff deliberately invokes the all encompassing power of universality and its independence from all processes, provided enclosure is maintained.

Consequently, two important extensions exist. First, given the generalization of Kirchhoff's law [52–55], it is appropriate to extend these arguments to the microwave cavity. In this experimental setting, the wavelengths and the size of the object are on the same order. Furthermore, assuming thermal equilibrium, it is proper to consider steady state processes beyond thermal radiation. This is provided that a cavity be maintained. In any event, it is established that thermal loses exist within microwave devices. Thus, we can examine the electromagnetic resonant cavity in light of Kirchhoff's law.

When the use of the blackbody resonator in UHFMRI was advanced [60], it was not possible to reconcile the behavior of such a coil, given the conflict between Kirchhoff's law [1, 2] and the known performance of cavities in electromagnetics [61, 62]. A photograph of a sealed blackbody resonator for UHFMRI [60] is presented in Figure 4. In the simplest sense, this resonant cavity is an enclosure in which radiation can solely enter, or exit through, at a single drive point. The radiation within such cavities should be black, according to Kirchhoff [1, 2]. Nonetheless, measurements of the real cavity show that it does not contain black radiation, as demonstrated experimentally in Figure 5. Resonant cavities are well known devices in electromagnetics [61, 62]. Their radiation is determined purely by the constituent properties of the cavity and its dimensions [61, 62]. This point is affirmed in Figure 5. In its current form, Kirchhoff's law [1, 2] stands at odds against practical microwave techniques [61, 62]. Since this knowledge should not be discounted, something must be incorrect within Kirchhoff's law. Everything about the blackbody resonator presented in Figure 4 echoes Planck, yet the radiation it contains is not black [5]. The type of radiation within this cavity is being determined by electromagnetics [61, 62], not by Kirchhoff's law. Only the attributes of any substance present and that of the enclosed resonant elements, along with the size and shape of the enclosure itself, govern the type of radiation. For example, as seen in Figs. 4 and 5, the simple addition of echosorb acts to significantly alter the resonances within such cavities. The associated loses are thermal. Of course, at these frequencies, echosorb is not a perfect absorber and the radiation inside the cavity cannot easily be made black. Still, in partial deference to Kirchhoff, if a perfect absorber could be found, the radiation within cav-

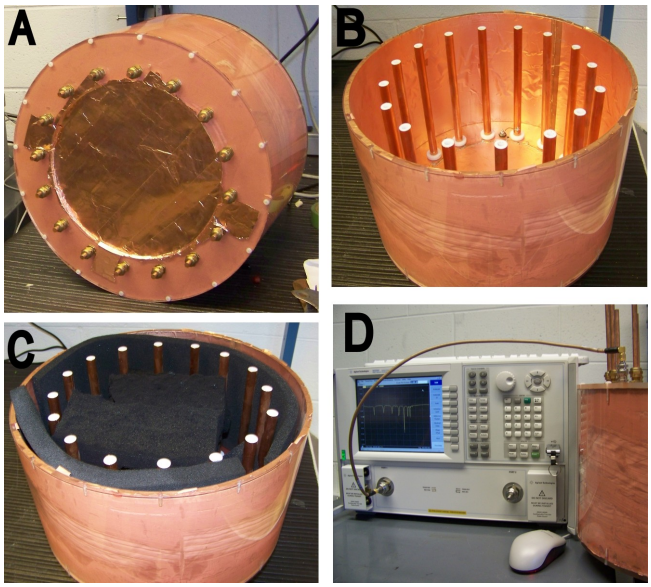

Fig. 4: A) End-view photograph of a sealed blackbody resonator [60] for use in UHFMRI studies. This device behaves as a resonant cavity [61, 62] and is constructed by sealing both ends of the well-known TEM resonator [63, 64]. In this particular case, one of the ends of the resonator was made by sealing an acrylic ring with a thin copper sheet which was then re-enforced with copper tape on the inner and outer surfaces. All other assembly details are as previously reported [60]. When a resonator is sealed at both ends to make a cavity [61, 62], radiation can solely enter or leave the device through a single drive port. As such, the blackbody resonator can be regarded as the electromagnetic equivalent of Kirchhoff's blackbody [1, 2, 5, 7], with the important difference, of course, that the radiation inside such a device is never black. This constitutes a direct refutation of Kirchhoff's law of thermal emission as demonstrated experimentally in Fig. 5. B) Photograph of the interior of the blackbody coil illustrating the TEM rods, the interior lined with copper, and the drive point. Note that for these studies, a matching capacitor [60] was not utilized, as the measurement of interest does not depend on matching a given resonance to 50 ohms. It is the resonant nature of the coil itself which is of interest, not the impedance matching of an individual resonant frequency. C) Photograph of the blackbody coil filled with pieces of Echosorb. D) Photograph of the blackbody coil connected to an Agilent Technologies N5230C 300kHz – 6 GHz PNA-L Network Analyzer using an RG400 cable and SMA connectors. Since the RF coil was assembled with a BNC connector, an SMA/BNC adaptor was utilized to close the RF chain. The calibration of the analyzer was verified from 200–400 MHz using a matched load of 50 ohms placed directly on the network analyzer port. In this case, the return loss (S11) was less than -40 dB over the frequency range of interest. The matched load was also placed on the end of the test cable used for these studies and in this case the return loss (S11) was less than -25 dB from 200–400 MHz. The network analyzer provides a continuous steady state coherent source of radiation into the cavity. The coherence of this radiation is critical to the proper analysis of the returned radiation by the network analyzer. This does not alter the conclusions reached. Only the ability to properly monitor cavity behavior is affected by the use of incoherent radiation. The cavity, of course, is indifferent to whether or not the radiation incident upon it is coherent.

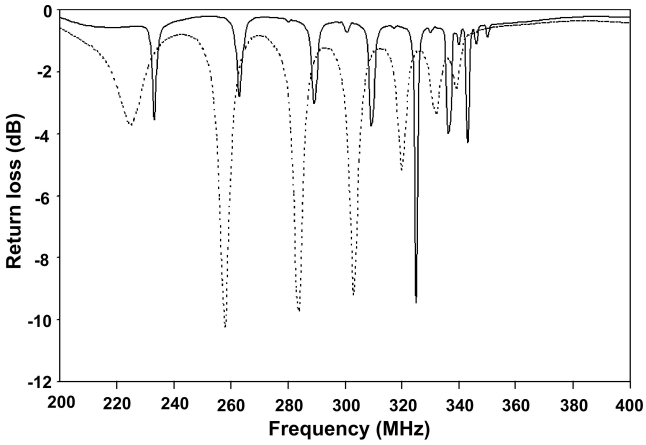

Fig. 5: Plot of the return loss (S11) for the blackbody coil (solid line) as measured from 200–400 MHz. Note that even though this cavity is completely closed, the radiation within this device is not black. Several sharp resonances are observed whose resonant position depend on the nature of the resonant cavity itself (dimension of the cavity, quality of the inner copper lining, dimensions of the TEM resonant elements, degree of insertion of the struts into the TEM elements, etc.). It is the presence of such resonances within cavities that forms the basis of practical electromagnetics and enables the use of resonant cavities in both EPR and MRI [61, 62]. If Kirchhoff's law of thermal emission had been correct, such a resonant device would not exist. The problem is easily rectified if one adopts Stewart's formulation for the treatment of thermal emission [6]. The dashed line displays the return loss (S11) for the blackbody coil filled with the carbon-foam Echosorb as measured from 200–400 MHz. Note that Echosorb is not a perfect absorber of radiation at these frequencies. But since this foam is somewhat absorbing, the resonance lines are broadened substantially. The return losses at several frequencies are lower, as is to be expected from the introduction of an absorbing object within a resonant cavity. If a perfect absorber could be found at these frequencies, the return loses would become extremely low across the entire frequency range of interest. Given these measurements and access to resonant devices, network analyzers and microwave technology, it is likely that Kirchhoff would have reconsidered the formulation of his law of thermal emission.

ities containing such objects would be black. Nonetheless, only Stewart's law [6] is formulated in such a way as to conform with results from electromagnetics [61, 62].

5 Conclusions

Tragically, if Kirchhoff believed in universality, it was because he did not properly treat both reflection and absorption, as previously highlighted [12]. The correct treatment of radiation at thermal equilibrium was first performed by Stewart, in 1858 [6]. Stewart properly addresses reflection [6, 8, 12], and does not arrive at universality. Unfortunately, Stewart's formulation lacked mathematical rigor [6, 12] and this did not help in drafting a central law of thermal emission. At the same time, in deriving Kirchhoff's law in his treatise, Planck fails to fully treat reflection [7; §6]. Like Kirchhoff

his teacher, Planck is thereby lead erroneously to the concept that all enclosures contain black radiation. Planck begins his derivation of Kirchhoff's law by considering elements $d\tau$ within an extended substance. He then analyzes the radiation emitted by these elements, but ignores the coefficient of reflection, ρ_ν. He writes: "*total energy in a range of frequency from ν to $\nu + d\nu$ emitted in the time dt in the direction of the conical element $d\Omega$ by a volume element $d\tau$*" [7; §6] is equal to $dt\, d\tau\, d\Omega\, d\nu\, 2\varepsilon_\nu$. As a result, he is brought to a universal function, which is independent of the nature of the object, and affirms the validity of Kirchhoff's law: $\varepsilon_\nu / a_\nu = f(T, \nu)$. In this equation, the coefficient of emission, ε_ν, the coefficient of absorbance, a_ν, the temperature, T, and the frequency, ν, alone are considered. Had Planck properly addressed the coefficient of reflection, ρ_ν, and recognized that the total radiation which leaves an element is the sum produced by the coefficients of emission, ε_ν, and reflection, ρ_ν, he would have obtained $(\varepsilon_\nu + \rho_\nu)/(a_\nu + \rho_\nu) = f'(T, \nu, N)$, where the nature of the object, N, determined the relative magnitudes of ε_ν, a_ν, and ρ_ν. By moving to the interior of an object and neglecting reflection, Planck arrives at Kirchhoff's law, but the consequence is that his derivation ignores the known truth that opaque objects possess reflection.

Given thermal equilibrium, the equivalence between the absorptivity, a_ν, and emissivity, ε_ν, of an object was first recognized by Stewart [6]. Stewart's formulation preserves this central equivalence. Only, it does not advance the universality invoked by Kirchhoff [1, 2]. At the same time, it remains fortunate for human medicine that Kirchhoff's law of thermal emission does not hold. If it did, MRI within cavities [60] would not be possible. Devices containing solely black radiation would be of no use, either as microwave components, or as antenna for human imaging. Physics and medicine should return thereby, by necessity, to Stewart's formulation [6] and the realization that radiation within cavities depends not uniquely on frequency and temperature, as stated by Kirchhoff [1, 2], but also on the attributes of the cavity itself and the materials it contains. This contribution was first brought to physics by Balfour Stewart [6]. Stewart's law, not Kirchhoff's, properly describes physical reality as observed in the laboratory across all subdisciplines of physics and over the entire span of the electromagnetic spectrum.

Practical blackbodies are always made from specialized substances which are nearly perfect absorbers over the frequency range of interest [13–25]. Accordingly, the nature of the enclosure is important, in opposition to Kirchhoff's law which claims independence from the properties of the walls and its contents. Through the formulation of his law of thermal emission, Balfour Stewart [6], unlike Kirchhoff, recognized the individualized behavior of materials in thermal equilibrium. In addition, it is well-established that the radiation within microwave cavities is not necessarily black. Rather, it depends on the nature, shape, contents, and dimensions of the enclosure itself. This is in accordance with Stewart's law. Alternatively, if Kirchhoff's law was correct, cavities should strictly contain blackbody radiation and their use in radio and microwave circuitry would be pointless. Network analyzer measurements of return losses for a sealed enclosure, or blackbody resonator [60], from 200–400 MHz, confirm that Kirchhoff's law of thermal emission does not hold within arbitrary resonant cavities.

At the same time, the physics community is justified in taking a cautious approach in these matters. After all, it was Planck [5] who provided the functional form contained in Kirchhoff's law [1, 2]. As a result, there is an understandable concern, that revisiting Kirchhoff's law will affect the results of Planck himself and the foundation of quantum physics [5]. There is cause for concern. The loss of the universal function brings about substantial changes not only in astrophysics, but also in statistical thermodynamics.

Relative to Planck's equation itself, the solution remains valid. It does however, become strictly limited to the problem of radiation within cavities which are known to be black (i.e. made of graphite, lined with soot, etc). Universality is lost. As for the mathematical value of Planck's formulation for the perfectly absorbing cavity, it is preserved. In describing blackbody radiation, Planck consistently invokes the presence of a perfect absorber. In his treatise [7], he repeatedly calls for a minute particle of carbon [8]. Planck views this particle as a simple catalyst, although it can be readily demonstrated that this is not the case: the carbon particle acted as a perfect absorber [12]. As a result, I have stated that Kirchhoff's law is not universal [8, 12, 26, 27] and is restricted to the study of cavities which are either made from, or contain, perfect absorbers. Arbitrary cavity radiation is not black [12]. There can be no universal function. Planck's equation presents a functional form which, far from being universal, is highly restricted to the emission of bodies, best represented on Earth by materials such as graphite, soot, and carbon black [8].

In closing, though 150 years have now elapsed since Kirchhoff and Stewart dueled over the proper form of the law of thermal emission [11, 12], little progress has been made in bringing closure to this issue. Experimentalists continue to unknowingly pump black radiation into arbitrary cavities using their detectors. Theorists replicate the approach with Monte Carlo simulations. At the same time, astrophysicists apply with impunity the laws of thermal emission [1–7] to the stars and the universe. Little pause is given relative to the formulation of these laws [1–7] using condensed matter. The fact that all of electromagnetics stands in firm opposition to the universality, instilled in Kirchhoff's law, is easily dismissed as science unrelated to thermal emission [61, 62]. Losses in electromagnetics are usually thermal in origin. Nonetheless, electromagnetics is treated almost as an unrelated discipline. This occurs despite the reality that Kirchhoff himself specifically included other processes, such as fluorescence, provided enclosures were maintained. Though the generalization of Kirchhoff's law is widely recognized

as valid [52–55], its application to the microwave cavity has been strangely omitted [52], even though it is used in treating the waveguide. This is the case, even though waveguides and cavities are often treated in the same chapters in texts on electromagnetics. All too frequently, the simple equivalence between apparent spectral absorbance and emission is viewed as a full statement of Kirchhoff's law [57, 65], adding further confusion to the problem. Kirchhoff's law must always be regarded as extending much beyond this equivalence. It states that the radiation within all true cavities made from arbitrary walls is black [1, 2]. The law of equivalence [57, 65] is Stewart's [6].

Most troubling is the realization that the physical cause of blackbody radiation remains as elusive today as in the days of Kirchhoff. Physicists speak of mathematics, of Planck's equation, but nowhere is the physical mechanism mentioned. Planck's frustration remains: "*Therefore to attempt to draw conclusions concerning the special properties of the particles emitting rays from the elementary vibrations in the rays of the normal spectrum would be a hopeless undertaking*" [7; §111]. In 1911, Einstein echoes Planck's inability to link thermal radiation to a physical cause: "*Anyway, the h-disease looks ever more hopeless*" [66; p. 228]. Though he would be able to bring a ready derivation of Planck's theorem using his coefficients [67], Einstein would never be able to extract a proper physical link [68]. In reality, we are no closer to understanding the complexities of blackbody radiation than scientists were 150 years ago.

Acknowledgements

William F. Moulder from the Electrosciences Laboratory is recognized for measuring return losses specific to this experiment. Brief access to the Agilent Technologies network analyzer was provided by the Electrosciences Laboratory. Luc Robitaille is acknowledged for figure preparation.

Dedication

This work is dedicated to my eldest sister, Christine.

Submitted on May 27, 2009 / Accepted on May 29, 2008
First published online on June 19, 2009

References

1. Kirchhoff G. Über den Zusammenhang zwischen Emission und Absorption von Licht und. Wärme. *Monatsberichte der Akademie der Wissenschaften zu Berlin*, sessions of Dec. 1859, 1860, 783–787.
2. Kirchhoff G. Über das Verhältnis zwischen dem Emissionsvermögen und dem Absorptionsvermögen. der Körper für Wärme und Licht. *Poggendorfs Annalen der Physik und Chemie*, 1860, v. 109, 275–301. (English translation by F. Guthrie: Kirchhoff G. On the relation between the radiating and the absorbing powers of different bodies for light and heat. *Phil. Mag.*, 1860, ser. 4, v. 20, 1–21).
3. Wien W. Über die Energieverteilung in Emissionspektrum eines schwarzen Körpers. *Ann. Phys.*, 1896, v. 58, 662–669.
4. Stefan J. Über die Beziehung zwischen der Warmestrahlung und der Temperature. *Sitzungsberichte der mathematischnaturwissenschaftlichen Classe der kaiserlichen Akademie der Wissenschaften*, Wien 1879, v. 79, 391–428.
5. Planck M. Über das Gesetz der Energieverteilung im Normalspektrum. *Annalen der Physik*, 1901, v. 4, 553–563 (English translation by ter Haar D.: Planck M. On the theory of the energy distribution law in the normal spectrum. The old quantum theory. Pergamon Press, 1967, 82–90; also Planck's December 14, 1900 lecture Zur Theorie des Gesetzes der Energieverteilung in Normalspectrum, which stems from this paper, can be found in either German, or English, in: Kangro H. Classic papers in physics: Planck's original papers in quantum physics. Taylor & Francis, London, 1972, 6–14 or 38–45).
6. Stewart B. An account of some experiments on radiant heat, involving an extension of Prévost's theory of exchanges. *Trans. Royal Soc. Edinburgh*, 1858, v. 22(1), 1–20 (also found in Harper's Scientific Memoirs, edited by J. S. Ames: The Laws of Radiation and Absorption: Memoirs of Prévost, Stewart, Kirchhoff, and Kirchhoff and Bunsen, translated and edited by D. B. Brace, American Book Company, New York, 1901, 21–50).
7. Planck M. The theory of heat radiation. P. Blakiston's Son & Co., Philadelphia, PA, 1914.
8. Robitaille P. M. L. Blackbody radiation and the carbon particle. *Prog. in Phys.*, 2008, v. 3, 36–55.
9. Prévost P. Mémoire sur l'équilibre du feu. *Journal de Physique*, 1791, v. 38, 314–322 (translated in Harper's Scientific Memoirs (J. S. Ames, Ed.) — The Laws of Radiation and Absorption: Memoirs of Prévost, Stewart, Kirchhoff, and Kirchhoff and Bunsen. Translated and edited by D. B. Brace, American Book Company, New York, 1901, 1–13).
10. Prévost P., Du calorique rayonnant. J. J. Paschoud, Geneva & Paris 1809 (Sections are translated in Harper's Scientific Memoirs (J. S. Ames, Ed.) — The Laws of Radiation and Absorption: Memoirs of Prévost, Stewart, Kirchhoff, and Kirchhoff and Bunsen. Translated and edited by D. B. Brace, American book company, New York, 1901, 15–20).
11. Siegel D. M. Balfour Stewart and Gustav Robert Kirchhoff: two independent approaches to Kirchhoff's law. *Isis*, 1976, v. 67(4), 565–600.
12. Robitaille P. M. L. A critical analysis of universality and Kirchhoff's law: a return to Stewart's law of thermal emission. *Prog. in Phys.*, 2008, v. 3, 30–35; arXiv: 0805.1625.
13. Quinn T. J. and Martin J. E. Cryogenic radiometry, prospects for further improvements in accuracy. *Metrologia*, 1991, v. 28, 155–161.
14. Sakuma F. and Hattori S. A practical-type fixed point blackbody furnace. *Temperature and Its Measurement and Control in Science and Industry*, 1982, v. 5, part 1, 535–539.

15. Murphy A. V., Tsai B. K., Saunders R. D. Comparative calibration of heat flux sensors in two blackbody facilities. *J. Res. Nat. Inst. Stand. Technol.*, 1999, v. 104, 487–494.
16. Murphy A. V., Tsai B. K., Saunders R. D. Transfer calibration validation tests on a heat flux sensor in the 51 mm hightemperature blackbody. *J. Res. Nat. Inst. Stand. Technol.*, 2001, v. 106, 823–831.
17. Navarro N., Bruce S. S., Carol Johnson B., Murphy A. V, Saunders R. D. Vacuum processing techniques for development of primary standard blackbodies. *J. Res. Nat. Inst. Stand. Technol.*, 1999, v. 104, 253–259.
18. Chahine K., Ballico M., Reizes J., Madadnia J. Optimization of a graphite tube blackbody heater for a thermogage furnace. *Int. J. Thermophys.*, 2008, v. 29, 386–394.
19. Hanssen L. M., Mekhontsev S. N., Zeng J., Prokhorov A. V. Evaluation of blackbody cavity emissivity in the infrared using total integrated scatter measurements. *Int. J. Thermophys.*, 2008, v. 29, 352–369.
20. Fowler J. B. A third generation water bath based blackbody source. *J. Res. Nat. Inst. Stand. Technol.*, 1995, v. 100, 591–599.
21. Schalles M., Bernhard F. Triple-fixed-point blackbody for the calibration of radiation thermometers. *Int. J. Thermophys.*, 2007, v. 28, 2049–2058.
22. Fowler J. B., Carol Johnson B., Rice J. P., Lorenz S. R. The new cryogenic vacuum chamber and black-body source for infrared calibrations at the NIST's FARCAL facility. *Metrologia*, 1998, v. 35, 323–327.
23. Fowler J. B. An oil-bath-based 293 K to 473 K blackbody source. *J. Res. Natl. Inst. Stand. Technol.*, 1996, v. 101, 629–637.
24. Geist J. Note on the quality of freezing point blackbodies. *Applied Optics*, 1971, v. 10(9), 2188–2190.
25. Geist J. Theoretical analysis of laboratory blackbodies 1: a generalized integral equation. *Applied Optics*, 1973, v. 12(6), 1325–1330.
26. Robitaille P. M. L. On the validity of Kirchhoff's law of thermal emission. *IEEE Trans. Plasma Sci.*, 2003, v. 31(6), 1263–1267.
27. Robitaille P. M. L. An analysis of universality in blackbody radiation. *Prog. in Phys.*, 2006, v. 2, 22–23; arXiv: physics/0507007.
28. DeWitt D. P. and Nutter G. D. Theory and practice of radiation thermometry. John Wiley and Sons, New York, 1988.
29. Vollmer J. Study of the effective thermal emittance of cylindrical cavities. *J. Opt. Soc. Am.*, 1957, v. 47(10), 926–932.
30. Sparrow E. M. and Heinisch R. P. The normal emittance of circular cylindrical cavities. *Appl. Opt.*, 1970, v. 9(11), 2569–2572.
31. Bauer G. and Bischoff K. Evaluation of the emissivity of a cavity source by reflection measurements. *Appl. Opt.*, 1971, v. 10(12), 2639–2643.
32. De Vos J. C. Evaluation of the quality of a blackbody. *Physica*, 1954, v. 20, 669–689.
33. De Vos J.C. A new determination of the emissivity of tungsten ribbon. *Physica*, 1954, v. 20, 690–714.
34. Ono A., Trusty R. E., and DeWitt D. P. Experimental and theoretical study on the quality of reference blackbodies formed by lateral holes on a metallic tube. *Temperature and Its Measurement and Control in Science and Industry*, 1982, v. 5, part 1, 541–550.
35. Harris L. The optical properties of metal blacks and carbon blacks. MIT and The Eppley Foundation for Research, Monograph Ser., 1, New Port, R.I., Dec. 1967.
36. Harris L., McGuiness R. T., Siegel B. M. The preparation and optical properties of gold black. *J. Opt. Soc. Am.*, 1948, v. 38, 582.
37. Paschen F. Ueber das Strahlungsgesetz des schwarzen Körpers. *Ann. Phys.*, 1901, v. 4, 277-298; Paschen F. On the distribution of energy in the spectrum of the black body at high temperatures. *Astrophys. J.*, 1900, v. 11, 288–306.
38. Lummer O. and Pringsheim E. Kritisches zur schwarzen Strahlung. *Annalen der Physik*, 1901, v. 6, 192–210.
39. Rubens H. and Kurlbaum F. Anwendung der Methode der Reststrahlen zur Prüfung der Strahlungsgesetzes. *Annalen der Physik*, 1901, v. 2, 649–666.
40. Rousseau B., Sin A., Odier P., Weiss F., Echegut P. Black body coating by spray pyrolysis. *Journal de Physique*, 2001, v. 91, Pr11.277–Pr11.281.
41. Rousseau B. Chabin M., Echegut P., Sin A., Weiss F., and Odier P. High emissivity of a rough Pr_2NiO_4 coating. *Appl. Phys. Lett.*, 2001, v. 79(22), 3633–3635.
42. Buckley H. On the radiation from the inside of a circular cylinder. *Phil. Mag.*, Ser. 7, 1927, v. 4(23), 753-762.
43. Sparrow E. M., Albers L. U., and Eckert E. R. G. Thermal radiation characteristics of cylindrical enclosures. *J. Heat Trans.*, 1962, v. 84C, 73–79.
44. Lin S. H., Sparrow E. M. Radiant interchange among curved specularly reflecting surfaces — application to cylindrical and conical cavities. *J. Heat Trans.*, 1965, v. 87C, 299–307.
45. Treuenfels E. W. Emissivity of isothermal cavities. *J. Opt. Soc. Am.*, 1963, v. 53(10), 1162–1171.
46. Sparrow E. M. and Jonsson V. K. Radiation emission characteristics of diffuse conical cavities. *J. Opt. Soc. Am.*, 1963, v. 53(7), 816–821.
47. Chandos R. J. and Chandos R. E. Radiometric properties of isothermal, diffuse wall cavity sources. *Appl. Opt.*, 1974, v. 13(9), 2142–2152.
48. Peavy B. A. A note on the numerical evaluation of thermal radiation characteristics of diffuse cylindrical and conical cavities. *J. Res. Nat. Bur. Stand. — C* (*Eng. and Instr.*), 1966, v. 70C(2), 139–147.
49. Langley S. P. The invisible solar and lunar spectrum. *Am. J. Science*, 1888, v. 36(216), 397–410.
50. Gray D. F. The observation and analysis of stellar photospheres. 2nd edition, Cambridge University Press, Cambridge, U.K., 1992, p. 101.
51. Kreith F. Principles of heat transfer. Harper & Row Publishers, New York, 1973, p. 228.
52. Rytov S. M. A theory of electrical fluctuations and thermal radiation. USSR Academy of Sciences, Moscow, 1953.

53. Rytov S. M, Kravtsov Y. A., Tatarskii V. I., Principles of statistical radiophysics, v. 3. Springer Verlag, Berlin, 1978.
54. Klyshko D. N. Photons and nonlinear optics. Gordon and Breach Scientific Publishers, New York, 1988.
55. Apresyan L. A. and Kravtsov Y. A., Radiation transfer: statistical and wave aspects. Gordon and Breach Publishers, Australia, 1996.
56. Richter F., Florian M., Henneberger K. Generalized radiation law for excited media in a nonequilibrium steady state. *Phys. Rev. B*, 2008, 205114.
57. Linsky J. L. and Mount G. H. On the validity of a generalized Kirchhoff's law for a nonisothermal scattering and absorptive medium. *Icarus*, 1972, v. 17, 193–197.
58. Robitaille P. M. L., Abduljalil A.M., Kangarlu A., Zhang X., Yu Y., Burgess R., Bair S., Noa P., Yang L., Zhu H., Palmer B., Jiang Z.,Chakeres D.M., and Spigos D. Human magnetic resonance imaging at eight tesla. *NMR Biomed.*, 1998, v. 11, 263–265.
59. Robitaille P. M. L. and Berliner L.J. Ultra high field magnetic resonance imaging. Springer, New York, 2006.
60. Robitaille P. M. L. Black-body and transverse electromagnetic (TEM) resonators operating at 340 MHz: volume RF coils for UHFMRI. *J. Comp. Assist. Tomogr.*, 1999, v. 23, 879–890.
61. Pozar D. M. Microwave engineering. John Wiley and Sons, New York, 1998.
62. Argence E. Theory of waveguides and cavity resonators. Hart Pub. Co., Oxford, 1968.
63. Roschmann P. K. High-frequency coil system for a magnetic resonance imaging apparatus. US Patent, 1988, no. 4,746,866.
64. Vaughn J. T., Hetherington H., Otu J., Pan J., Pohost G. High frequency volume coils for clinical NMR imaging and spectroscopy. *Magn. Reson. Med.*, 1994, v. 32, 206–218.
65. Kelley F. J. On Kirchhoff's law and its generalized application to absorption and emission by cavities. *J. Res. Nat. Bur. Stand. B* — (*Math. Math. Phys.*), 1965, v. 69B(3), 165–171.
66. Einstein A. The collected papers of Albert Einstein, v. 5. The Swiss years: Correspondence 1902–1914. Princeton University Press, Princeton, N.J., 1995, p. 105.
67. Einstein A. Strahlungs-emission und absorption nach der quantentheorie. *Verhandlunger der Deutschen Physikalischen Gesellschaft*, 1916, v. 18, 318–323; Einstein A. *Phys. Zs.*, 1917, v. 18, 121 (English translation by ter Haar D.: Einstein A. On the quantum theory of radiation. The old quantum theory, Pergamon Press, 1967, 167–183).
68. Robitaille P. M. L. Comment to the NRC committee on condensed matter and material physics. January 20, 2005. http://www7.nationalacademies.org/bpa/CMMP2010_Robitaille.pdf

Blackbody Radiation and the Loss of Universality: Implications for Planck's Formulation and Boltzman's Constant

Pierre-Marie Robitaille

Department of Radiology, The Ohio State University, 395 W. 12th Ave, Suite 302, Columbus, Ohio 43210, USA

E-mail: robitaille.1@osu.edu

Through the reevaluation of Kirchhoff's law (Robitaille P. M. L. *IEEE Trans. Plasma Sci.*, 2003, v. 31(6), 1263–1267), Planck's blackbody equation (Planck M. *Ann. der Physik*, 1901, v. 4, 553–356) loses its universal significance and becomes restricted to perfect absorbers. Consequently, the proper application of Planck's radiation law involves the study of solid opaque objects, typically made from graphite, soot, and carbon black. The extension of this equation to other materials may yield apparent temperatures, which do not have any physical meaning relative to the usual temperature scales. Real temperatures are exclusively obtained from objects which are known solids, or which are enclosed within, or in equilibrium with, a perfect absorber. For this reason, the currently accepted temperature of the microwave background must be viewed as an apparent temperature. Rectifying this situation, while respecting real temperatures, involves a reexamination of Boltzman's constant. In so doing, the latter is deprived of its universal nature and, in fact, acts as a temperature dependent variable. In its revised form, Planck's equation becomes temperature insensitive near 300 K, when applied to the microwave background.

With the formulation of his law of thermal emission [1], Planck brought to science a long sought physical order. Though individual materials varied widely in their radiative behaviors, Kirchhoff's law of thermal emission [2, 3] had enabled him to advance dramatic simplifications in an otherwise chaotic world [1]. Given thermal equilibrium and enclosure, the blackbody cavity seemed to impart upon nature a universal property, far removed from the confusion prevailing outside its walls [4]. Universality produced conceptual order and brought rapid and dramatic progress in mathematical physics.

In his "Theory of Heat Radiation" [4], Planck outlines the prize: the existence of the universal constants, h and k. Moreover, he is able to introduce natural units of length, mass, time, and temperature [4; §164]. He writes: "*In contrast with this it might be of interest to note that, with the aid of the two constants h and k which appear in the universal law of radiation, we have the means of establishing units of length, mass, time, and temperature, which are independent of special bodies or substances, which necessarily retain their significance for all time and for all environments, terrestrial and human or otherwise, and which may, therefore, be described as 'natural units'*" [4; §164]. Planck then presents the values of the four fundamental constants [4; §164]:

Planck's constant $h = 6.415\times10^{-27}$ g cm^2/sec,

Boltzman's constant $k = 1.34\times10^{-16}$ g cm^2/sec^2 degree,

the speed of light $c = 3.10\times10^{10}$ cm/sec,

the gravitational constant $f = 6.685\times10^{-8}$ cm^3/g sec^2.

Finally, he reveals basic units of:

length $\sqrt{fh/c^3} = 3.99\times10^{-33}$ cm,

mass $\sqrt{ch/f} = 5.37\times10^{-5}$ g,

time $\sqrt{fh/c^5} = 1.33\times10^{-43}$ s,

temperature $\frac{1}{k}\sqrt{c^5h/f} = 3.60\times10^{32}$ degree.

Planck continues: "*These quantities retain their natural significance as long as the law of gravitation and that of the propagation of light in a vacuum and the two principles of thermodynamics remain valid; they therefore must be found always the same, when measured by the most widely differing intelligences according to the most widely differing methods*" [4; §164].

The real triumph of Planck's equation [1] rested not solely on solving the blackbody problem, but rather on the universal nature of h and k. The four fundamental units of scale for time, length, mass, and temperature profoundly altered physics. It is in this light, that concern over any fundamental change in Kirchhoff's law [2, 3] and Planck's equation [1] must be viewed.

The notion that the microwave background [5] is being produced directly by the oceans of the Earth [6–9], brings with it an immediate realization that universality is lost, and Kirchhoff's law is invalid [10–14]. Blackbody radiation is not a universal process [10–14], as Planck so adamantly advocated [4]. Yet, if the microwave background truly arises from oceanic emissions [5–8], then it is not simple to reconcile a temperature at ∼3 K with a source known to have a physical temperature of ∼300 K [10]. Let us examine more closely the problem at hand, by considering Planck's formulation (1):

$$\frac{\varepsilon_\upsilon}{\alpha_\upsilon} = \frac{2h\upsilon^3}{c^2}\,\frac{1}{e^{h\upsilon/kT}-1}\,. \qquad (1)$$

In order to properly fit the microwave background using this equation, the problem rests in the kT term. It is possible, for instance, to make that assumption that an apparent temperature exists [10] and to keep the meaning of Boltzman's constant. In fact, this was the course of action initially proposed [10]. In this way, nothing was lost from the universal nature of h and k [10]. But, upon further consideration, it is clear that such an approach removes all physical meaning from temperature itself. The one alternative is to alter Boltzman's constant directly, and accept the full consequences of the loss of universality. The issue involves a fundamental understanding of how energy is distributed within matter. For the microwave background, this must focus on water [8].

Thus, let us consider a very primitive description of how energy enters, or becomes distributed, within water [8]. Water possesses many degrees of freedom and must be viewed as a complex system. At low temperatures, some of the first degrees of freedom to be fully occupied will be associated with the weak intermolecular hydrogen bond ($H_2O \cdots HOH$) [8]. These involve both stretching and bending processes, resulting in several vibrational-rotational modes. The hydrogen bond ($H_2O \cdots HOH$) has been advanced as responsible for the microwave background [8], particularly as a result of its predicted bond strength. As energy continues to enter the water system, it will start to populate other degrees of freedom, including those associated with the direct translation and rotation of individual molecules. This is in sharp contrast to graphite, for instance, because the latter never undergoes a solid-liquid phase transition [15]. Eventually, other degrees of freedom, associated with the vibrational and bending modes of the intramolecular hydroxyl bonds (H–OH) themselves, will become increasingly populated. Hydrogen bonds ($H_2O \cdots HOH$) have bond strengths which are on the order of 100 times lower than hydroxyl bonds (H–OH) [8]. Considering these complexities, it is unreasonable to believe that energy will enter the water system in a manner which ignores the existence of these degrees of freedom, particularly those associated with the liquid state.

Contrary to what Kirchhoff and Planck require for universality [1–3], these complex issues extend throughout nature. Each material is unique relative to the degrees of freedom it has available as a function of temperature [15]. Water possesses two distinct oscillators, the intermolecular hydrogen bond ($H_2O \cdots HOH$) and the intramolecular hydroxyl bond (H–OH) [7]. These two oscillatory systems have very distinct energies [8] and provide a situation which is quite removed from graphite. Kirchhoff and Planck had no means of anticipating such complexity. In fact, they were relatively unaware of the tremendous atomic variability found at the level of the lattice. As such, it is somewhat understandable that they might seek universal solutions.

In any case, it has been amply demonstrated that Kirchhoff's law is not valid [10–14]. There can be no universality. In addition, it is extremely likely that the microwave background is being produced by thermal photons emitted directly from the oceanic surface and then scattered in the Earth's atmosphere [6]. This implies that a ~300 K source is able to behave, at least over a region of the electromagnetic spectrum, as a ~3 K source. However, since the oceans are not at ~3 K, an inconsistency has been revealed in the determination of temperatures using the laws of thermal emission. The problem stems from the weakness of the hydrogen bond and the associated ease with which water enters the liquid state. Furthermore, it is evident that energy can enter the water system and be directed into its translational degrees of freedom, thereby becoming unavailable for thermal emission. This is a significant problem, which Kirchhoff and Planck did not need to consider, and of which they were unaware, when treating graphite boxes [1–4, 10]. Graphite, unlike water, cannot support convection.

In any event, the central issue remains that a ~3 K temperature has been obtained from a ~300 K source. As mentioned above, it is possible to essentially ignore the consequences of this finding by simply treating the microwave background as an apparent temperature [10], devoid of physical meaning. In this way, Planck's equation and the universal constants, survive quite nicely [10]. Conversely, if one refuses to abandon the real temperature scale, then a problem arises. In order to properly fit the microwave background with Planck's equation and a real temperature at ~300 K, then Boltzman's constant must change. In fact, it must become a temperature dependent variable, $k'(T)$. This variable must behave such that when it is multiplied by a range of temperatures near 300 K, it results in a perfectly constant value independent of temperature ($k'(T) \cdot T = P$, where P is a constant). Planck's equation thereby becomes completely insensitive to temperature fluctuations over the temperature and frequency ranges of interest, as seen in Eq. (2):

$$\frac{\varepsilon_\upsilon}{\alpha_\upsilon} = \frac{2h\upsilon^3}{c^2} \frac{1}{e^{h\upsilon/P} - 1} . \qquad (2)$$

As a result, relative to the microwave background, we move from a universal constant, k, to a temperature sensitive variable, $k'(T)$, which acts to render Planck's equation temperature insensitive. The modern value of the constant, P, for the microwave background, is approximately 3.762×10^{-16} ergs. The move away from graphite, into another Planckian system, has resulted in a profound re-evaluation of the science of thermodynamics. Boltzman's constant, therefore, remains valid only for graphite, soot, or carbon black, and those materials approaching their performance at a given frequency. Outside a certain range of temperatures, or frequencies, or materials, then other constants and/or variables, which are material specific, exist. The measure of how much energy a system can hold at a given temperature, or how temperature changes as a function of energy, is directly determined by the makeup of the system itself. The flow of heat within a system depends on all of the degrees of freedom which eventually

become available [15]. In this regard, phase transitions bring with them additional degrees of freedom, either translational or rotational, which are simply not available to the solid state [15]. Herein is found the central reason for the loss of universality: phase transitions exist. Nothing is universal, since phase transitions and any available degrees of freedom [15] are strictly dependent on the nature of matter. Hence, each material must be treated on its own accord. This is the primary lesson of the water/microwave background findings.

Physics cannot maintain a proper understanding of temperature without abandoning the universal attributes of Boltzman's constant. Otherwise, the temperature scale itself loses meaning. In order to specifically address the microwave background, Boltzman's constant, in fact, can become a temperature dependent variable. At the same time, since many materials contain covalent bonds with bond strengths near those found within graphite, it is likely that many material specific constants will, in fact, approach Boltzman's. Nonetheless, relative to the microwave background, a temperature dependent variable exists which acts to completely remove all temperature sensitivity from Planck's equation at earthly temperatures. This explains why Penzias and Wilson [5] first reported that the microwave background was devoid of seasonal variations.

As regards to Planck's constant, and the fundamental units of time, mass, and length, they appear to remain unaltered by the findings prompted by the microwave background. Perhaps they will be able to retain their universal meaning. However, a careful analysis of individual physical processes is in order, such that the consequences of the loss of universality can be fully understood.

Dedication

This work is dedicated to my wife, Patricia Anne, and to our sons, Jacob, Christophe, and Luc.

Submitted on May 28, 2009 / Accepted on June 02, 2008
First published online on June 20, 2009

References

1. Kirchhoff G. Über den Zusammenhang zwischen Emission und Absorption von Licht und Wärme. *Monatsberichte der Akademie der Wissenschaften zu Berlin*, sessions of Dec. 1859, 1860, 783–787.
2. Kirchhoff G. Über das Verhältnis zwischen dem Emissionsverögen und dem Absorptionsvermögen. der Körper für Wärme und Licht. *Poggendorfs Annalen der Physik und Chemie*, 1860, v. 109, 275–301. (English translation by F. Guthrie: Kirchhoff G. On the relation between the radiating and the absorbing powers of different bodies for light and heat. *Phil. Mag.*, 1860, ser. 4, v. 20, 1–21).
3. Planck M. Über das Gesetz der Energieverteilung im Normalspektrum. *Annalen der Physik*, 1901, v. 4, 553–563. (English translation by ter Haar D.: Planck M. On the theory of the energy distribution law in the normal spectrum. The old quantum theory. Pergamon Press, 1967, 82–90; also Planck's December 14, 1900 lecture Zur Theorie des Gesetzes der Energieverteilung in Normalspectrum, which stems from this paper, can be found in either German, or English, in: Kangro H. Classic papers in physics: Planck's original papers in quantum physics. Taylor & Francis, London, 1972, 6–14 or 38–45).
4. Planck M. The theory of heat radiation. P. Blakiston's Son & Co., Philadelphia, PA, 1914.
5. Penzias A. A. and Wilson R. W. A measurement of excess antenna temperature at 4080 Mc/s. *Astrophys. J.*, 1965, v. 1, 419–421.
6. Robitaille P. M. L. The Earth microwave background (EMB), atmospheric scattering and the generation of isotropy. *Progr. in Phys.*, 2008, v. 2, L7–L8.
7. Rabounski D. The relativistic effect of the deviation between the CMB temperatures obtained by the COBE satellite. *Progr. in Phys.*, 2007, v. 1, 24–26.
8. Robitaille P. M. L. Water, hydrogen bonding, and the microwave background. *Prog. in Phys.*, 2009, v. 2, L5–L7.
9. Rabounski D. and Borissova L. On the earthly origin of the Penzias-Wilson microwave background. *Prog. in Phys.*, 2009, v. 2, L1–L4.
10. Robitaille P. M. L. Blackbody radiation and the carbon particle. *Prog. in Phys.*, 2008, v. 3, 36–55.
11. Robitaille P. M. L. On the validity of Kirchhoff's law of thermal emission. *IEEE Trans. Plasma Sci.*, 2003, v. 31(6), 1263–1267.
12. Robitaille P. M. L. An analysis of universality in blackbody radiation. *Prog. in Phys.*, 2006, v. 2, 22–23; arXiv: physics/0507007.
13. Robitaille P. M. L. A critical analysis of universality and Kirchhoff's law: a return to Stewart's law of thermal emission. Prog. in Phys. 2008, v. 3, 30–35; arXiv: 0805.1625.
14. Robitaille P. M. L. Kirchhoff's law of thermal emission: 150 years. *Prog. in Phys.*, 2009, v. 4, 3–13.
15. Robitaille P. M. L. The little heat engine: Heat transfer in solids, liquids, and gases. *Prog. in Phys.*, 2007, v. 4, 25–33.

COBE: A Radiological Analysis

Pierre-Marie Robitaille

Department of Radiology, The Ohio State University, 395 W. 12th Ave, Suite 302, Columbus, Ohio 43210, USA

E-mail: robitaille.1@osu.edu

The COBE Far Infrared Absolute Spectrophotometer (FIRAS) operated from ∼30 to ∼3,000 GHz (1–95 cm^{-1}) and monitored, from polar orbit (∼900 km), the ∼3 K microwave background. Data released from FIRAS has been met with nearly universal admiration. However, a thorough review of the literature reveals significant problems with this instrument. FIRAS was designed to function as a differential radiometer, wherein the sky signal could be nulled by the reference horn, Ical. The null point occurred at an Ical temperature of 2.759 K. This was 34 mK above the reported sky temperature, 2.725±0.001 K, a value where the null should ideally have formed. In addition, an 18 mK error existed between the thermometers in Ical, along with a drift in temperature of ∼3 mK. A 5 mK error could be attributed to Xcal; while a 4 mK error was found in the frequency scale. A direct treatment of all these systematic errors would lead to a ∼64 mK error bar in the microwave background temperature. The FIRAS team reported ∼1 mK, despite the presence of such systematic errors. But a 1 mK error does not properly reflect the experimental state of this spectrophotometer. In the end, all errors were essentially transferred into the calibration files, giving the appearance of better performance than actually obtained. The use of calibration procedures resulted in calculated Ical emissivities exceeding 1.3 at the higher frequencies, whereas an emissivity of 1 constitutes the theoretical limit. While data from 30–60 GHz was once presented, these critical points are later dropped, without appropriate discussion, presumably because they reflect too much microwave power. Data obtained while the Earth was directly illuminating the sky antenna, was also discarded. From 300–660 GHz, initial FIRAS data had systematically growing residuals as frequencies increased. This suggested that the signal was falling too quickly in the Wien region of the spectrum. In later data releases, the residual errors no longer displayed such trends, as the systematic variations had now been absorbed in the calibration files. The FIRAS team also cited insufficient bolometer sensitivity, primarily attributed to detector noise, from 600–3,000 GHz. The FIRAS optical transfer function demonstrates that the instrument was not optimally functional beyond 1,200 GHz. The FIRAS team did not adequately characterize the FIRAS horn. Established practical antenna techniques strongly suggest that such a device cannot operate correctly over the frequency range proposed. Insufficient measurements were conducted on the ground to document antenna gain and field patterns as a full function of frequency and thereby determine performance. The effects of signal diffraction into FIRAS, while considering the Sun/Earth/RF shield, were neither measured nor appropriately computed. Attempts to establish antenna side lobe performance in space, at 1,500 GHz, are well outside the frequency range of interest for the microwave background (<600 GHz). Neglecting to fully evaluate FIRAS prior to the mission, the FIRAS team attempts to do so, on the ground, in highly limited fashion, with a duplicate Xcal, nearly 10 years after launch. All of these findings indicate that the satellite was not sufficiently tested and could be detecting signals from our planet. Diffraction of earthly signals into the FIRAS horn could explain the spectral frequency dependence first observed by the FIRAS team: namely, too much signal in the Jeans-Rayleigh region and not enough in the Wien region. Despite popular belief to the contrary, COBE has not proven that the microwave background originates from the universe and represents the remnants of creation.

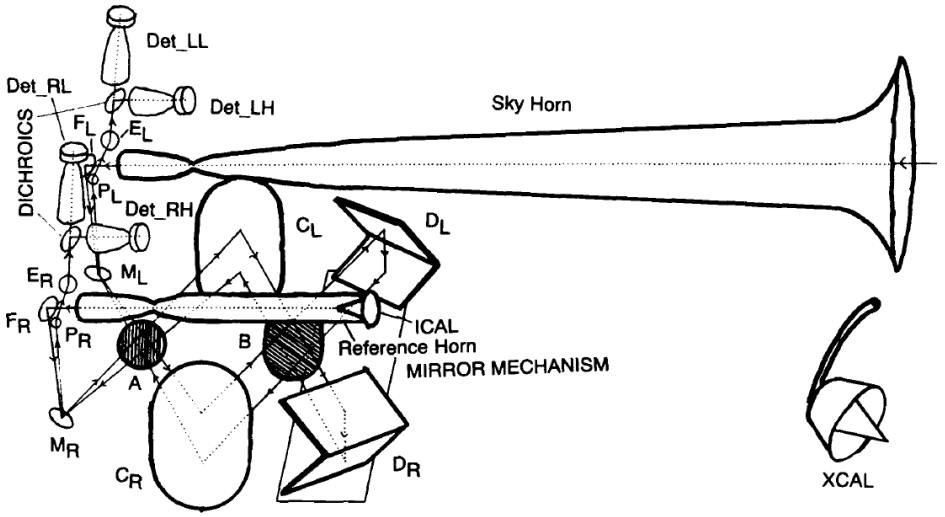

Fig. 1: Schematic representation of the COBE FIRAS instrument reproduced from [38]. The spectrometer is based on an interferometer design wherein the signal from the sky horn is being compared with that provided by the reference horn. Each of the input signals is split by grid polarizers, reflected by mirrors, and sent down the arms of the interferometer. Two output ports receive the resultant signal. An internal calibrator, Ical, equipped with two germanium resistance thermometers (GRT), provides signal to the reference horn. During calibration, the external calibrator, Xcal, is inserted into the sky horn. Xcal is monitored by three GRTs. The interferometer assembly includes a single mirror transport mechanism (MTM). Specific details can be found in [38]. No knowledge about the functioning of FIRAS, beyond that contained in this figure legend, is required to follow this work. The central elements are simply that FIRAS is made up of a sky horn, a reference horn, Ical (2 thermometers), and Xcal (3 thermometers). Reproduced by permission of the AAS.

1 Introduction

Conceding that the microwave background [1] must arise from the cosmos [2], scientists have dismissed the idea that the Earth itself could be responsible for this signal [3–7]. Most realize that the astrophysical claims are based on the laws of thermal emission [8–12]. Yet, few have ever personally delved into the basis of these laws [13–17]. At the same time, it is known that two satellites, namely COBE [18] and WMAP [19], support the cosmological interpretation [2]. As such, it seems impossible that an alternative explanation of the findings could ever prevail.

In late 2006, I prepared a detailed review of WMAP which uncovered many of the shortcomings of this instrument [20]. A range of issues were reported, including: 1) the inability to properly address the galactic foreground, 2) dynamic range issues, 3) a lack of signal to noise, 4) poor contrast, 5) yearly variability, and 6) unjustified changes in processing coefficients from year to year. In fact, WMAP brought only sparse information to the scientific community, related to the dipole and to point sources.

Nonetheless, the COBE satellite, launched in 1989, continues to stand without challenge in providing empirical proof that the microwave background did come from the universe. If COBE appears immune to criticism, it is simply because scientists outside the cosmological community have not taken the necessary steps to carefully analyze its results. Such an analysis of COBE, and specifically the Far Infrared Absolute Spectrophotometer, FIRAS, is provided in the pages which follow. Significant problems exist with FIRAS. If anything, this instrument provides tangential evidence for an earthly source, but the data was discounted. A brief discussion of the Differential Microwave Radiometers, DMR, outlines that the anisotropy maps, and the multipoles which describe them, are likely to represent a signal processing artifact.

1.1 The microwave background

When the results of the Cosmic Background Explorer (COBE) were first announced, Stephen Hawking stated that this "*was the scientific discovery of the century, if not of all time*" [21, book cover], [22, p. 236]. The Differential Microwave Radiometers (DMR) were said to have detected "*wrinkles in time*", the small anisotropies overlaid on the fabric of a nearly isotropic, or uniform, microwave background [21]. As for the COBE Far Infrared Absolute Spectrophotometer, FIRAS (see Figure 1), it had seemingly produced the most perfect blackbody spectrum ever recorded [23–45]. The blackbody curve deviated from ideality by less than 3.4×10^{-8} ergs cm^{-2} s^{-1} sr^{-1} cm [35] from ∼60–600 GHz. Eventually, the FIRAS team would publish that the "*rms deviations are less than 50 parts per million of the peak of the cosmic microwave background radiation*" [39]. As seen in Figure 2, the signal was so powerful that the error bars in its detection would form but a slight portion of the line used to draw the spectrum [39]. For its part, the Differential Microwave Radiometers (DMR), beyond the discovery of the anisotropies [21], had also confirmed the motion of the Earth through the

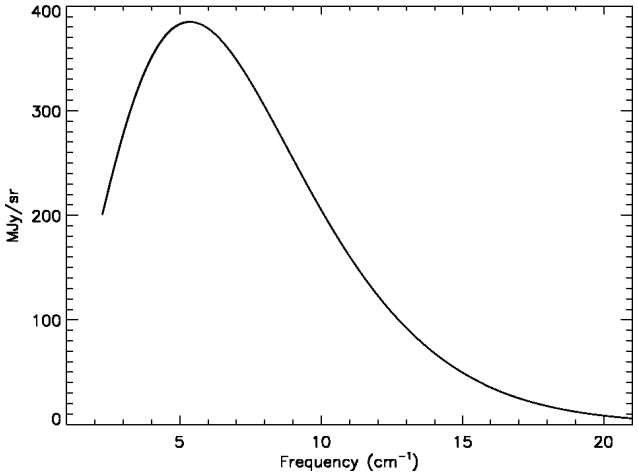

Fig. 2: Spectrum of the microwave background reproduced from [39]. This figure is well known for the claim that the error bars it contains are but a small fraction of the line width used to draw the spectrum. While this curve appears to represent a blackbody, it should be recalled that FIRAS is only sensitive to the difference between the sky and Xcal. This plot therefore reflects that the signal from the sky, after extensive calibration, is indistinguishable from that provided by Xcal. Since the latter is presumed to be a perfect blackbody, then such a spectrum is achieved for the sky. Note that the frequency axis is offset and all data below 2 cm^{-1} have been excluded. Reproduced by permission of the AAS.

local group, as established by a microwave dipole [46–49].

Over one thousand professional works have now appeared which directly utilize, or build upon, the COBE results [22, p. 247]. Yet, sparse concern can be found relative to any given aspect of the COBE project. Eventually, George Smoot and John Mather, the principle investigators for the DMR and FIRAS projects, would come to share the 2006 Nobel Prize in physics. Less than 30 years had elapsed since Arno Penzias and Robert Wilson received the same honor, in 1978, for the discovery of the $\sim$3 K microwave background [1].

Before the background was officially reported in the literature [1], the origin of the signal had already been advanced by Dicke et al. [2]. The interpretive paper [2] had immediately preceded the publication of the seminal discovery [1]. If the microwave background was thermal in origin [8–12], it implied a source at $\sim$3 K. Surely, such a signal could not come from the Earth. For the next 40 years, astrophysics would remain undaunted in the pursuit of the spectrum, thought to have stemmed from the dawn of creation. Smoot writes: "*Penzias and Wilson's discovery of the cosmic microwave background radiation was a fatal blow to the steady state theory*" [21, p. 86]. The steady state theory of the universe [50, 51] was almost immediately abandoned and astrophysics adopted Lemaître's concept of the primordial atom [52], later known as the Big Bang. Cosmologists advanced that mankind knew the average temperature of the entire universe. Thanks to COBE, cosmology was thought to have become a precision science [53, 54].

Throughout the detection history of the microwave background, it remained puzzling that the Earth itself never provided interference with the measurements. Water, after all, acts as a powerful absorber of microwave radiation. This is well understood, both at sea aboard submarines, and at home, within microwave ovens. As such, it seemed unlikely that the surface of our planet was microwave silent in every CMB experiment which preceded COBE. The only interference appeared to come from the atmosphere [55–57]. The latter was recognized as a powerful emitter of microwave radiation. The presence of water absorption/emission lines and of the water continuum, within the atmosphere, was well documented [55–57]. Nonetheless, emission from the Earth itself was overlooked.

The microwave signal is isotropic [1], while the Earth is anisotropic. The Earth experiences a broad range of real temperatures, which vary according to location and season. Yet, the background is found to be independent of seasonal variation [1]. The signal is definitely thermal in origin [9–17]. Most importantly, it is completely free from earthly contamination. The background appears to monitor a source temperature near $\sim$3 K. Earthly temperatures average $\sim$300 K and seldom fall below $\sim$200 K, even at the poles. It seems impossible that the Earth could constitute the source of this signal [3–7]. Everything can be reconsidered, only if the temperature associated with the microwave background signature is not real. Namely, that the source temperature is much higher than the temperature reported by the photons it emits. Insight in this regard can be gained by returning to the laws of thermal emission [8–12], as I have outlined [13–17].

1.2 Kirchhoff's law

One hundred and fifty years have now passed, since Kirchhoff first advanced the law upon which the validity of the microwave background temperature rests [9]. His law of thermal emission stated that radiation, at equilibrium with the walls of an enclosure, was always black, or normal [9, 10]. This was true in a manner independent of the nature of the enclosure. Kirchhoff's law was so powerful that it would become the foundation of contemporary astrophysics. By applying this formulation, the surface temperatures of all the stars could be evaluated, with the same ease as measuring the temperature of a brick-lined oven. Planck would later derive the functional form of blackbody radiation, the right-hand side of Kirchhoff's law, and thereby introduce the quantum of action [10]. However, since blackbody radiation only required enclosure and was independent of the nature of the walls, Planck did not link this process to a specific physical cause [13–17]. For astrophysics, this meant that any object could produce a blackbody spectrum. All that was required was mathematics and the invocation of thermal equilibrium. Even the requirement for enclosure was soon discarded. Processes occurring far out of equilibrium, such as the radiation of a star, and the alleged

expansion of the universe, were thought to be suitable candidates for the application of the laws of thermal emission [2]. To aggravate the situation, Kirchhoff had erred in his claim of universality [13–17]. In actuality, blackbody radiation was not universal. It was limited to an idealized case which, at the time, was best represented by graphite, soot, or carbon black [13–17]. Nothing on Earth has been able to generate the elusive blackbody over the entire frequency range and for all temperatures. Silver enclosures could never produce blackbody spectra. Kirchhoff's quest for universality was futile [13–17]. The correct application of the laws of thermal emission [8–12] requires the solid state. Applications of the laws to other states of matter, including liquids, gases, stars, and primordial atoms, constitute unjustified extensions of experimental realities and theoretical truths [13–17].

Since the source of the microwave background [1] could not possibly satisfy Kirchhoff's requirement for an enclosure [9], its $\sim$3 K temperature might only be apparent [13–17]. The temperature of the source could be very different than the temperature derived from its spectrum. Planck, indeed, advanced the same idea relative to using the laws of thermal emission to measure the surface temperature of the Sun. He wrote: "*Now the apparent temperature of the sun is obviously nothing but the temperature of the solar rays, depending entirely on the nature of the rays, and hence a property of the rays and not a property of the sun itself. Therefore it would be, not only more convenient, but also more correct, to apply this notation directly, instead of speaking of a fictitious temperature of the sun, which can be made to have a meaning only by the introduction of an assumption that does not hold in reality*" [58, §101]. Without a known enclosure, spectra appearing Planckian in nature do not necessarily have a direct link to the actual temperature of the source. The Sun operates far out of thermal equilibrium by every measure, as is evident by the powerful convection currents on its surface [59]. Furthermore, because it is not enclosed within a perfect absorber, its true surface temperature cannot be derived from the laws of thermal emission [59]. These facts may resemble the points to which Planck alludes.

1.3 The oceans of the Earth

The COBE team treats the Earth as a blackbody source of emission at $\sim$280 K [48]. Such a generalization seems plausible at first, particularly in the near infrared, as revealed by the remote sensing studies [60, 61]. However, FIRAS is making measurements in the microwave and far-infrared regions of the spectrum. It is precisely in this region that these assumptions fail. Furthermore, the FIRAS team is neglecting the fact that 70% of the planet is covered with water. Water is far from acting as a blackbody, either in the infrared or in the microwave. Using remote sensing, it has been well established that rainfall causes a pronounced drop in terrestrial brightness temperatures in a manner which is proportional to the rate of precipitation. In the microwave region, large bodies of water, like the oceans, display brightness temperatures which vary from a few Kelvin to $\sim$300 K, as a function of angle of observation, frequency, and polarization (see Figure 11.45 in [62]). Since the oceans are not enclosed, their thermal emission profiles do not necessarily correspond to their true temperatures. The oceans of the Earth, like the Sun, sustain powerful convection currents. Constantly striving for equilibrium, the oceans also fail to meet the requirements for being treated as a blackbody [13–17].

In order to understand how the oceans emit thermal radiation, it is important to consider the structure of water itself [6]. An individual water molecule is made up of two hydroxyl bonds, linking a lone oxygen atom with two adjacent hydrogens (H$-$O$-$H). These are rather strong bonds, with force constants of $\sim 8.45 \times 10^5$ dyn/cm [6]. In the gas phase, it is known that the hydroxyl bonds emit in the infrared region. The O$-$H stretch can thus be found near 3,700 cm^{-1}, while the bending mode occurs near 1,700 cm^{-1} [63]. In the condensed state, liquid water displays corresponding emission bands, near 3,400 cm^{-1} and 1,644 cm^{-1} [63, p. 220]. The most notable change is that the O$-$H stretching mode is displaced to lower frequencies [63]. This happens because water molecules, in the condensed state (liquid or solid), can interact weakly with one another, forming hydrogen bonds [63]. The force constant for the hydrogen bond ($H_2O \cdots HOH$) has been determined in the water dimer to be on the order of $\sim 0.108 \times 10^5$ dyn/cm [6, 64, 65]. But, in the condensed state, a study of rearrangement energetics points to an even lower value for the hydrogen bond force constant [66]. In any event, water, through the action of the hydrogen bond, should be emitting in the microwave and far-IR regions [6, 63]. Yet, this emission has never been detected. Perhaps, the oceanic emission from hydrogen bonds has just been mistaken for a cosmic source [2].

1.4 Ever-present water

1.4.1 Ground-based measurements

From the days of Penzias and Wilson [1], ground-based measurements of the microwave background have involved a correction for atmospheric water contributions (see [56] for an in-depth review). By measuring the emission of the sky at several angles (at least two), a correction for atmospheric components was possible. Further confidence in such procedures could be provided through the modeling of theoretical atmospheres [55, 56]. Overall, ground-based measurements were difficult to execute and corrections for atmospheric contributions could overwhelm the measurement of interest, particularly as higher frequencies were examined. The emission from atmospheric water was easy to measure, as Smoot recalls in the "parking lot testing" of a radiometer at Berkeley: "*An invisible patch of water vapor drifted overhead; the scanner showed a rise in temperature. Good: this meant the*

instrument was working, because water vapor was a source of stray radiation" [21, p. 132].

The difficulty in obtaining quality measurements at high frequencies was directly associated with the presence of the water continuum, whose amplitude displays powerful frequency dependence [55, 56]. As a result, experiments were typically moved to locations where atmospheric water was minimized. Antarctica, with its relatively low atmospheric humidity, became a preferred monitoring location [55]. The same was true for mountain tops, places like Mauna Kea and Kitt Peak [55]. Many ground-based measurements were made from White Mountain in California, at an elevation of 3800 m [55]. But, there was one circumstance which should have given cosmologists cause for concern: measurements located near the oceans or a large body of water. These were amongst the simplest of all to perform. Weiss writes: "*Temperature, pressure, and constituent inhomogeneities occur and in fact are the largest source of random noise in ground-based experiments. However, they do not contribute systematic errors unless the particular observing site is anisotropic in a gross manner — because of a large lake or the ocean in the direction of the zenith scan, for example. The atmospheric and CBR contributions are separable in this case without further measurement or modeling*" [67, p. 500]. Surely, it might be of some importance that atmospheric contributions are always a significant problem which is only minimized when large bodies of condensed water are in the immediate scan direction.

The interesting interplay between atmospheric emissions and liquid surfaces is brought to light, but in a negative fashion, in the book by Mather [22]. In describing British work in the Canary Islands, Mather writes: "*Their job was unusually difficult because Atlantic weather creates patterns in the air that can produce signals similar to cosmic fluctuations. It took the English scientists years to eliminate this atmospheric noise...*" [22, p. 246–247]. As such, astronomers recognized that the Earth was able to alter their measurements in a substantial manner. Nonetheless, the possibility that condensed water itself was responsible for the microwave background continued to be overlooked.

1.4.2 U2 planes, rockets, and balloons

As previously outlined, the presence of water vapor in the lower atmosphere makes all measurements near the Wien maximum of the microwave background extremely difficult, if not impossible, from the ground. In order to gain more elevation, astrophysicists carried their instruments skywards using U2 airplanes, rockets, and balloons [21, 22]. All too often, these measurements reported elevated microwave background temperatures. The classic example is given by the Berkeley-Nagoya experiments, just before the launch of COBE [68]. Reflecting on these experiments, Mather writes: "*A greater shock to the COBE science team, especially to me since I was in charge of the FIRAS instrument, was an announcement made in early 1987 by a Japanese-American team headed by Paul Richards, my old mentor and friend at Berkeley, and Toshio Matsumoto of Nagoya University. The Berkeley-Nagoya group had launched from the Japanese island of Kyushu a small sounding rocket carrying a spectrometer some 200 miles high. During the few minutes it was able to generate data, the instrument measured the cosmic background radiation at six wavelengths between 0.1 millimeter and 1 millimeter. The results were quite disquieting, to say the least: that the spectrum of the cosmic microwave background showed an excess intensity as great as 10 percent at certain wavelengths, creating a noticeable bump in the blackbody curve. The cosmological community buzzed with alarm*" [22, p. 206]. The results of the Berkeley-Nagoya group were soon replaced by those from COBE. The origin of the strange "bump" on the blackbody curve was never identified. However, condensation of water directly into the Berkeley-Nagoya instrument was likely to have caused the interference. In contrast, the COBE satellite was able to operate in orbit, where any condensed water could be slowly degassed into the vacuum of space. COBE did not have to deal with the complications of direct water condensation and Mather could write in savoring the COBE findings: "*Rich and Ed recognized at once that the Berkeley-Nagoya results had been wrong*" [22, p. 216]. Nonetheless, the Berkeley-Nagoya experiments had provided a vital clue to the astrophysical community.

Water seemed to be constantly interferring with microwave experiments. At the very least, it greatly increased the complexity of studies performed near the Earth. For instance, prior to flying a balloon in Peru, Smoot reports: "*It is much more humid in the tropics, and as the plane descended from the cold upper air into Lima, the chilly equipment condensed the humidity into water. As a result, water collected into the small, sensitive wave guides that connect the differential microwave radiometer's horns to the receiver. We had to take the receiver apart and dry it... Our equipment had dried, so we reassembled it and tested it: it worked*" [21, p. 151].

Still, little attention has been shown in dissecting the underlying cause of these complications [6]. Drying scientific equipment was considered to be an adequate solution to address this issue. Alternatively, scientists simply tried to protect their antenna from condensation and added small monitoring devices to detect its presence. Woody makes this apparent, relative to his experiments with Mather: "*On the ground and during the ascent, the antenna is protected from atmospheric condensation by two removable windows at the top of the horn... At the same time, a small glass mirror allows us to check for atmospheric condensation in the antenna by taking photographs looking down the throat of the horn and cone*" [69, p. 16]. Indeed, monitoring condensation has become common place in detecting the microwave background using balloons. Here is a recent excerpt from the 2006 flight of the ARCADE 2 balloon: "*A video camera mounted*

on the spreader bar above the dewar allows direct imaging of the cold optics in flight. Two banks of light-emitting diodes provide the necessary illumination. The camera and lights can be commanded on and off, and we do not use data for science analysis from times when they are on" [70]. They continue: "*The potential problem with a cold open aperture is condensation from the atmosphere. Condensation on the optics will reflect microwave radiation adding to the radiometric temperature observed by the instrument in an unknown way. In the course of an ARCADE 2 observing flight, the aperture plate and external calibrator are maintained at cryogenic temperatures and exposed open to the sky for over four hours. Figure 12 shows time averaged video camera images of the dewar aperture taken two hours apart during the 2006 flight. No condensation is visible in the 3 GHz horn aperture despite the absence of any window between the horn and the atmosphere. It is seen that the efflux of cold boiloff helium gas from the dewar is sufficient to reduce condensation in the horn aperture to below visibly detectable levels*" [70].

The fact that condensation is not visible does not imply that it is not present. Microscopic films of condensation could very well appear in the horn, in a manner undetectable by the camera. In this regard, claims of strong galactic microwave bursts, reported by ARCADE 2 [70, 71] and brought to the attention of the public [72], must be viewed with caution. This is especially true, since it can be deduced from the previous discussion, that the camera was not functional during this short term burst. In any event, it is somewhat improbable that an object like the galaxy would produce bursts on such a short time scale. Condensation near the instrument is a much more likely scenario, given the experimental realities of the observations.

It remains puzzling that greater attention is not placed on understanding why water is a source of problems for microwave measurements. Singal et al. [70], for instance, believe that condensed water is a good reflector of microwave radiation. In contrast, our naval experiences, with signal transmission by submarines, document that water is an extremely powerful absorber of microwave radiation. Therefore, it must be a good emitter [8–12].

It is interesting to study how the Earth and water were treated as possible sources of error relative to the microwave background. As a direct precursor to the COBE FIRAS horn, it is most appropriate to examine the Woody-Mather instrument [69, 73]. Woody provides a detailed error analysis, associated with the Mather/Woody interferometer-based spectrometer [69]. This includes virtually every possible source of instrument error. Both Mather and Woody view earthshine as originating from a $\sim$300 K blackbody source. They appear to properly model molecular species in the atmosphere (H_2O, O_2, ozone, etc...), but present no discussion of the expected thermal emission profile of water in the condensed state on Earth. Woody [69, p. 99] and Mather [73, p. 121] do attempt to understand the response of their antenna to the Earth. Woody places an upper limit on earthshine [69, p. 104] by applying a power law continuum to model the problem. In this case, the Earth is modeled as if it could only produce 300 K photons. Such a treatment generates an error correction which grows with increasing frequency. Woody reaches the conclusion that, since the residuals on his fits for the microwave background are relatively small, even when earthshine is not considered, then its effect cannot be very significant [69, p. 105]. It could be argued that continental emission is being modeled. Yet, the function selected to represent earthly effects overtly dismisses that the planet itself could be producing the background. The oceans are never discussed.

Though Mather was aware that the water dimer exists in the atmosphere [73, p. 54], he did not extend this knowledge to the behavior of water in the condensed state. The potential importance of the hydrogen bond to the production of the microwave background was not considered [73]. At the same time, Mather realized that condensation of water into his antenna created problems. He wrote: "*The effect of air condensing into the antenna were seen...*" [73, p. 140]. He added: "*When the second window was opened, the valve which controls the gas flow should have been rotated so that all the gas was forced out through the cone and horn. When this situation was corrected, emissions from the horn were reduced as cold helium has cooled the surfaces on which the air had condensed, and the signal returned to its normal level*" [73, p. 140–141]. Mather does try to understand the effect of diffraction for this antenna [73, p. 112–121]. However, the treatment did not model any objects beyond the horn itself.

Relative to experiments with balloons, U2 airplanes, and rockets, the literature is replete with complications from water condensation. Despite this fact, water itself continues to be ignored as the underlying source of the microwave background. It is in this light that the COBE project was launched.

1.4.3 The central question

In studying the microwave background, several important conclusions have been reached as previously mentioned. First, the background is almost perfectly isotropic: it has essentially the same intensity, independent of observation angle [1]. Second, the background is not affected by seasonal variations on Earth [1]. Third, the signal is of thermal origin [8–17]. Finally, the background spectrum (see Figure 2) is clean: it is free from earthly interference. Over a frequency range spanning nearly 3 orders of magnitude ($\sim$1–660 GHz), the microwave background can be measured without any contaminating effect from the Earth. The blackbody spectrum is "perfect" [39]. But, as seen above, liquid water is a powerful absorber of microwave radiation. Thus, it remains a complete mystery as to why cosmology overlooked that the surface of the Earth could not produce any interference in these measurements. The only issue of concern for astrophysics is the atmosphere [55, 56] and its well-known absorption in the mi-

crowave and infrared bands. The contention of this work is that, if the Earth's oceans cannot interfere with these measurements, it is precisely because they are the primary source of the signal.

2 COBE FIRAS

For this analysis, the discussion will be limited primarily to the FIRAS instrument. Only a brief treatment of the DMR will follow in section 3. The DIRBE instrument, since it is unrelated to the microwave background, will not be addressed.

2.1 General concerns

Beginning in the late 1980's, it appeared that NASA would utilize COBE as a much needed triumph for space exploration [22, 24]. This was understandable, given the recent Challenger explosion [22, 24]. Visibility and a sense of urgency were cast upon the FIRAS team. COBE, now unable to use a shuttle flight, was faced with a significant redesign stage [22, 24]. Mather outlined the magnitude of the task at hand: "*Every pound was crucial as the engineers struggled to cut the spacecraft's weight from 10,594 pounds to at most 5,025 pounds and its launch diameter from 15 feet to 8 feet*" [22, p. 195]. This urgency to launch was certain to have affected prelaunch testing. Mather writes: "*Getting COBE into orbit was now Goddard's No. 1 priority and one of NASA's top priorities in the absence of shuttle flights. In early 1987 NASA administrator Jim Fletcher visited Goddard and looked over the COBE hardware, then issued a press release stating that COBE was the centerpiece of the agency's recovery*" [22, p. 194–195]. Many issues surfaced. These are important to consider and have been highlighted in detail [22, chap. 14].

After the launch, polite open dissent soon arose with a senior group member. The entire premise of the current paper can be summarized in the discussions which ensued: "*Dave Wilkinson, the FIRAS team sceptic, argued effectively at numerous meetings that he did not believe that Ned*" (Wright) "*and Al*" (Kogut) "*had proven that every systematic error in the data was negligible. Dave's worry was that emissions from the earth might be shinning over and around the spacecraft's protective shield*" [22, p. 234]. As will be seen below, Wilkinson never suspected that the Earth could be emitting as a $\sim$3 K source. Nonetheless, he realized that the FIRAS horn had not been adequately modeled or tested. Despite these challenges, the FIRAS team minimized Wilkinson's unease. Not a single study examines the interaction of the COBE shield with the FIRAS horn. The earthshine issue was never explored and Wilkinson's concerns remain unanswered by the FIRAS team to this day.

2.2 Preflight testing

A review of the COBE FIRAS prelaunch data reveals that the satellite was not adequately tested on the ground. These concerns were once brought to light by Professor Wilkinson, as mentioned above. He writes: "*Another concern was the magnitude of 300 K Earth emission that diffracted over, or leaked through, COBE's ground screen. This had not been measured in preflight tests, only estimated from crude (by today's standards) calculations*" [74]. Unfortunately, Professor Wilkinson does not give any detailed outline of the question and, while there are signs of problems with the FIRAS data, the astrophysical community itself has not published a thorough analysis on this subject.

Professor Wilkinson focused on the Earth as a $\sim$300 K blackbody source, even if the established behavior of the oceans in the microwave and far-infrared suggested that the oceans were not radiating in this manner [62]. Wilkinson never advanced that the Earth could be generating a signal with an apparent temperature of $\sim$3 K. This means that the diffraction problems could potentially be much more important than he ever suspected. Mather did outline Wilkinson's concerns in his book as mentioned above [22, p. 234], but did not elaborate further on these issues.

Beyond the question of diffraction, extensive testing of FIRAS, assembled in the flight dewar, did not occur. Mather stated that each individual component of FIRAS underwent rigorous evaluation [22, chap. 14], however testing was curtailed for the fully-assembled instrument. For instance, Hagopian described optical alignment and cryogenic performance studies for FIRAS in the test dewar [29]. These studies were performed at room and liquid nitrogen temperatures and did not achieve the cryogenic values, $\sim$1.4 K, associated with FIRAS [29]. Furthermore, Hagopian explained: "*Due to schedule constraints, an abbreviated version of the alignment and test plan developed for the FIRAS test unit was adopted*" [29]. Vibration testing was examined in order to simulate, as much as possible, the potential stresses experienced by FIRAS during launch and flight. The issue centered on optical alignments: "*The instrument high frequency response is however, mainly a function of the wire grid beam splitter and polarizer and the dihedrals of the MTM. The instrument is sensitive to misalignments of these components on the order of a few arc seconds*" [29]. In these studies, a blackbody source was used at liquid nitrogen temperatures to test FIRAS performance, but not with its real bolometers in place. Instead, Golay cell IR detectors were fed through light pipes mounted on the dewar output ports. It was noted that: "*Generally, the instrument behaved as expected with respect to performance degradation and alignment change... These results indicate that the instrument was successfully flight qualified and should survive cryogenic and launch induced perturbations*" [29]. These experiments did not involve FIRAS in its final configuration within the flight dewar and did not achieve operational temperatures.

A description of the preflight tests undergone by COBE was also presented by L. J. Milam [26], Mosier [27], and Co-

ladonato et al. [28]. These accounts demonstrate how little testing COBE actually underwent prior to launch. Concern rested on thermal performance and flight readiness. There obviously were some RF tests performed on the ground. In Mather [22, p. 216], it was reported that the calibration file for Xcal had been obtained on Earth. This was the file utilized to display the first spectrum of the microwave background with FIRAS [22, p. 216]. Nonetheless, no RF tests for sensitivity, side lobe performance, or diffraction were discussed for the FIRAS instrument. Given that Fixsen et al. [38] cite work by Mather, Toral, and Hemmati [25] for the isolated horn, as a basis for establishing side lobe performance, it is clear that these tests were never conducted for the fully-assembled instrument. Since such studies were difficult to perform in the contaminating microwave environments typically found on the ground, the FIRAS team simply chose to bypass this aspect of preflight RF testing.

As a result, the scientific community believes that COBE was held to the highest of scientific standards during ground testing when, in fact, a careful analysis suggests that some compromises occurred. However, given the scientific nature of the project, the absence of available preflight RF testing reports implies that little took place. Wilkinson's previously noted statement echoes this belief [74].

2.2.1 Bolometer performance

The FIRAS bolometers were well designed, as can be gathered from the words of Serlemitsos [31]: "*The FIRAS bolometers were optimized to operate in two frequency ranges. The slow bolometers cover the range from 1 to 20 Hz (with a geometric average of 4.5 Hz), and the fast ones cover the range from 20–100 Hz (average 45 Hz).*" Serlemitsos continues: "*The NEP's for the FIRAS bolometers are* $\sim 4.5 \times 10^{-15}$ *W/Hz*$^{1/2}$ *at 4.5 Hz for the slow bolometers and* $\sim 1.2 \times 10^{-14}$ *W/Hz*$^{1/2}$ *at 45 Hz for the fast ones*" [31], where NEP stands for "noise equivalent power". The FIRAS bolometers were made from a silicon wafer "*doped with antimony and compensated with boron*" [31]. Serlemitsos also outlined the key element of construction: "*IR absorption was accomplished by coating the back side of the substrate with metallic film...*" made "*of 20 Å of chromium, 5 Å of chromium-gold mixture, and 30–35 Å of gold*" [31]. Such vaporized metal deposits, or metal blacks, were well known to give good blackbody performance in the far IR [75,76]. Thus, if problems existed with FIRAS, it was unlikely that they could be easily attributed to bolometer performance.

2.2.2 Grid polarizer performance

The FIRAS team also fully characterized the wire grid polarizer [30]. While the grids did "*not meet the initial specification*" their spectral performance did "*satisfy the overall system requirements*" [30].

2.2.3 Emissivity of Xcal and Ical

The FIRAS team essentially makes the assumption that the two calibrators, Xcal and Ical, function as blackbodies over the entire frequency band. Xcal and Ical are represented schematically in Figure 3 [38, 42]. Both were manufactured from Eccosorb CR-110 (Emerson and Cuming Microwave Products, Canton, MA, 1980 [77]), a material that does not possess ideal attenuation characteristics. For instance, CR-110 provides an attenuation of only 6 dB per centimeter of material at 18 GHz [78]. In Hemati et al. [79], the thermal properties of Eccosorb CR-110 are examined in detail over the frequency range for FIRAS. The authors conduct transmission and reflection measurements. They demonstrate that Eccosorb CR-110 has a highly frequency dependent decrease in the transmission profile, which varies by orders of magnitude from ∼30–3,000 GHz [79]. Hemati et al. [79] also examine normal specular reflection, which demonstrate less variation with frequency. Therefore, when absorption coefficients are calculated using the transmission equation [79], they will have frequency dependence. Consequently, Hemati et al. [79] report that the absorption coefficients for Eccosorb CR-110 vary by more than one order of magnitude over the frequency range of FIRAS.

In addition, it is possible that even these computed absorption coefficients are too high. This is because Hemati et al. [79] do not consider diffuse reflection. They justify the lack of these measurements by stating that: "*For all samples the power response was highly specular; i.e., the reflected power was very sensitive with respect to sample orientation*" [79]. As a result, any absorption coefficient which is derived from the transmission equation [79], is prone to being overestimated. It is unlikely that Eccosorb CR-110 allows no diffuse reflection of incoming radiation. Thus, Eccosorb CR-110, at these thicknesses, does not possess the absorption characteristics of a blackbody. It is only through the construction of the "trumpet mute" shaped calibrator that blackbody behavior is thought to be achieved [38].

When speaking of the calibrators, Fixsen et al. [39] state: "*The other input port receives emission from an internal reference calibrator (emissivity* ≈ 0.98*)*" and "*During calibration, the sky aperture is completely filled by the external calibrator with an emissivity greater than 0.99997, calculated and measured*" [39]. Practical experience, in the construction of laboratory blackbodies, reveals that it is extremely difficult to obtain such emissivity values over a wide frequency range. Measured emissivity values should be presented in frequency dependent fashion, not as a single value for a broad frequency range [80]. In the infrared, comparable performance is not easily achievable, even with the best materials [15, 80]. The situation is even more difficult in the far infrared and microwave.

The emissivity of the calibrators was measured, at 34 and 94 GHz, using reflection methods as described in de-

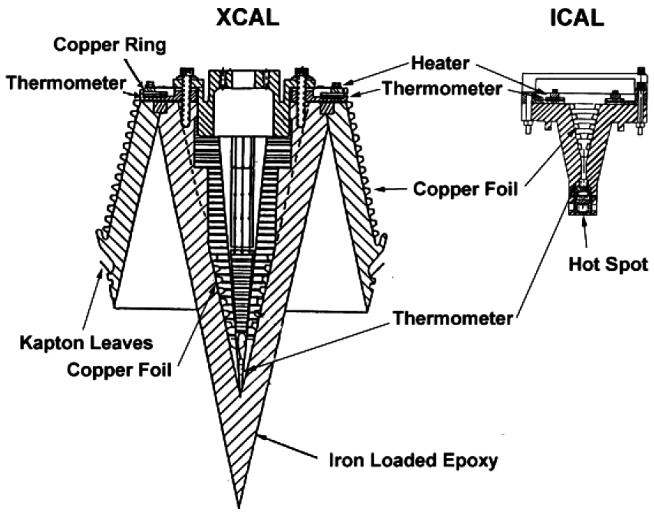

Fig. 3: Schematic representation of Xcal and Ical reproduced from [42]. Note that the calibrators are made from Eccosorb CR-110 which is backed with copper foil. Xcal, which contains three GRTs, is attached to the satellite with a movable arm allowing the calibrator to be inserted into, or removed from, the sky horn. The internal calibrator, Ical, is equipped with two GRTs and provides a signal for the reference horn. Reproduced by permission of the AAS.

tail [42]. However, these approaches are not appropriate for devices like the calibrators. In examining Figure 3, it is evident that Xcal is cast from layers of Eccosorb CR-110, backed with copper foil. For reflection methods to yield reliable results, they must address purely opaque surfaces. Eccosorb CR-110 is not opaque at these thicknesses [79] and displays significant transmission. The problem is worthy of further discussion.

In treating blackbody radiation, it is understood, from the principle of equivalence [8], that the emission of an object must be equal to its absorption at thermal and radiative equilibrium. Emission and absorption can be regarded as quantum mechanical processes. Therefore, it is most appropriate to state that, for a blackbody, or any body in radiative equilibrium, the probability of absorption, P_α, must be equal to the probability of emission, P_ε, $(P_\alpha = P_\varepsilon)$. But, given the combination of the transmittance for Eccosorb CR-110, the presence of a copper lining and the calibrator geometry, the FIRAS team has created a scenario wherein $P_\alpha \neq P_\varepsilon$. This is an interesting situation, which is permitted to exist because the copper backing on the calibrator provides a conductive path, enabling Xcal to remain at thermal equilibrium through non-radiative processes. Under these test conditions, Xcal is in thermal equilibrium, but not in radiative equilibrium. It receives incoming photons from the test signal, but can dissipate the heat, using conduction, through the copper backing. Xcal does not need to use emission to balance absorption.

If the FIRAS calibrators provide excellent reflection measurements [42], it is because of their "trumpet mute" shape and the presence of a copper back lining. Radiation incident to the device, during reflectance measurements, which is not initially absorbed, will continue to travel through the Eccosorb and strike the back of the casing. Here it will undergo normal specular reflection by the copper foil present at this location. The radiation can then re-enter the Eccosorb, where it has yet another chance of being absorbed. As a result, P_α can be effectively doubled as a consequence of this first reflection. Because of the shape of the calibrators, along with the presence of normal specular reflection on the copper, the radiation is essentially being pushed further into the calibrator where its chances of being absorbed are repeated. Consequently, P_α continues to increase with each reflection off the copper wall, or because photons are being geometrically forced to re-enter the adjacent Eccosorb wall. The situation moves in the opposite direction for P_ε and this probability therefore drops under test conditions.

Note that the copper foil has a low emissivity in this frequency range. Therefore, it is reasonable to assume that it cannot contribute much to the generation of photons. These must be generated within the Eccosorb CR-110 layers. Now, given the geometry of the "trumpet mute", there exists no means of increasing the probability of emission, P_ε. Indeed, some of the photons emitted will actually travel in the direction of the copper foil. This will lengthen their effective path out of the Eccosorb, since they exit and immediately re-enter, and increases the chance that they are absorbed before ever leaving the surface of the calibrator. Thus, P_ε experiences an effective decrease, because of the presence of the copper foil. The net result is that $P_\alpha \neq P_\varepsilon$ and the FIRAS team has not properly measured the emissivity of their calibrators using reflective methods [42]. In fact, direct measures of emissivity for these devices would demonstrate that they are not perfectly black across the frequencies of interest. Nonetheless, the devices do appear black in reflection measurements. But this is an illusion which does not imply that the calibrators are truly black when it comes to emission. Reflection measurements cannot establish the blackness of such a device relative to emission if the surface observed is not opaque. Geometry does matter in treating either emission or absorption under certain conditions. The problem is reminiscent of other logical errors relative to treating Kirchhoff's first proof for universality [16].

The FIRAS group asserts that they have verified the blackness of their calibrators with computational methods. Yet, these methods essentially "inject photons" into cavities, which otherwise might not be present [17]. Much like the improper use of detectors and reflection methods (on non-opaque surfaces), they can ensure that all cavities appear black [17]. The FIRAS calibrators are not perfectly black, but it is not clear what this implies relative to the measurements of the microwave background.

2.2.4 Leaks around Xcal

The acquisition of a blackbody spectrum from the sky is based on the performance of Xcal. For instance, Fixsen and Mather write: "*It is sometimes stated that this is the most perfect blackbody spectrum ever measured, but the measurement is actually the difference between the sky and the calibrator*" [43]. Mathematically, the process is as follows:

$$(\text{Sky} - \text{Ical}) - (\text{Xcal} - \text{Ical}) = (\text{Sky} - \text{Xcal}) .$$

Thus, Ical and all instrumental factors should ideally be negligible, contrary to what the FIRAS team experiences. Furthermore, if the calibration file with Xcal perfectly matches the sky, then a null result occurs. Since Xcal is thought to be a perfect blackbody, the derived sky spectrum is also ideal, as seen in Figure 2. It is extremely important that the calibration file, generated when Xcal is within the horn, does not contain any contamination from the sky. In the limit, should the sky dominate the calibration, a perfect blackbody shape will be recorded. This would occur because the sky is effectively compared against itself, ensuring a null.

The FIRAS team reminds us that: "*When the Xcal is in the sky horn it does not quite touch it. There is a 0.6 mm gap between the edge of the Xcal and the horn, so that the Xcal and the sky horn can be at different temperatures. Although the gap is near the flare of the horn and not in the direct line of sight of the detectors, it would result in undesirable leakage at long wavelengths because of diffraction. To ensure a good optical seal at all wavelengths, two ranks of aluminized Kapton leaves attached to the Xcal make a flexible contact with the horn*" [38] (see Figure 3). The claim that the Kapton leaves make a flexible contact with the horn, at operating temperatures, does not seem logical. The horn is operating at cryogenic temperatures ($\sim$2.7 K) and, thus, the Kapton leaves should not be considered flexible, but rather rigid, perhaps brittle. This might cause a poor contact with the horn during critical calibration events in space. The FIRAS team continues: "*An upper limit for leakage around the Xcal was determined in ground tests with a warm cryostat dome by comparing signals with the Xcal in and out of the horn. Leakage is less than 1.5×10^{-4} in the range $5 < \nu < 20$ cm^{-1} and 6.0×10^{-5} in the range $25 < \nu < 50$ cm^{-1}*" [38]. The issue of leakage around Xcal is critical to the proper functioning of FIRAS. Consequently, Mather et al. revisit the issue at length in 1999 (see section 3.5.1 in [42]). The seal does indeed appear to be good [42], but it is not certain that these particular ground tests are valid in space.

It is not clear if RF leak testing occurred while FIRAS was equipped with its specialized bolometers. As seen in section 2.2, in some preflight testing, Golay cell IR detectors had been fed through light pipes mounted on the dewar output ports. Such detectors would be unable to properly detect signals at the lowest frequencies. In fact, the FIRAS bolometers were made from metal blacks [31, 75, 76] in order to specifically provide sensitivity in the difficult low frequency range. As a result, any leak testing performed with the Golay cell IR detectors might be subject to error, since these may not have been sensitive to signal, in the region most subject to diffraction.

The FIRAS group also makes tests in flight and states: "*The Kapton levels sealing the gap between the sky horn and Xcal were tested by gradually withdrawing the Xcal from the horn. No effect could be seen in flight until it had moved 1.2 cm*" [38]. This issue is brought up, once again, by Mather et al.: "*A test was also done in flight by removing the calibrator 12 steps, or 17 mm, from the horn. Only a few interferograms were taken, but there was no sign of a change of signal level*" [42]. It is interesting that Fixsen et al. [38] claim that no effect could be seen until the horn had moved 1.2 cm. This implies that effects were seen at 1.2 cm. Conversely, Mather et al. assert that no effects were seen up to 17 mm [42]. In any case, identical results could have been obtained, even if the seal was inadequate. Perhaps this is why Fixsen et al. write: "*During calibration, the sky acts as a backdrop to the external calibrator, so residual transmission is still nearly 2.73 K radiation*" [39]. Clearly, if the seal was known to be good, there should not be any concern about "residual transmission" from the sky.

Fixsen et al. [39] rely on the sky backdrop providing a perfect blackbody spectrum behind Xcal. However, if the signal was originating from the Earth, the sky signal could be distorted as a function of frequency. This would bring error into the measurements, should the sky signal leak into the horn. From their comments, a tight seal by the Kapton leaves cannot be taken for granted. While in-flight tests, slowly removing Xcal, indicate that the spectrum changes as the calibrator was lifted out of the horn, they may not exclude that leakage exists when it is inside the horn.

It is also interesting that Mather describes significant problems with Xcal prior to launch, as follows: "*Now without gravity to help hold it in place, the calibrator popped out of the horn every time the test engineers inserted it by means of the same electronic commands they would use once COBE was in orbit. Nothing the engineers tried would keep it in place*" [22, p. 202]. In the end, the problem was caused by the flexible cable to the Xcal [22]. The cable was replaced with three thin ribbons of Kapton [22, p. 202–204]. COBE underwent one more cryogenic test, with the liquid helium dewar at 2.8 K, lasting a total of 24 days ending in June 1989 [26]. Milan's report does not provide the results of any RF testing [26], but everything must have worked. The satellite was prepared for shipment to the launch site [22, p. 202–204].

In 2002, Mather reminds us of the vibration problems with COBE: "*There were annoying vibrations at 57 and ~ 8 Hz*" [43]. On the ground, the Xcal could "pop out" of the horn if the satellite was turned on its side [22, p. 202]. Only gravity was holding Xcal in place. Still, in orbit, COBE experiences very little gravity. As such, the effects of the vi-

brations in knocking Xcal out of the horn, or in breaking the contact between the Kapton leaves and the horn, are not the same in space. A small vibration, in space, could produce a significant force against Xcal, pushing it out of the horn. Thus, all leak testing on the ground has little relevance to the situation in orbit, since both gravity and vibrations affect the Xcal position in a manner which cannot be simulated in the laboratory. The FIRAS team simply cannot be assured that Xcal did not allow leakage from the sky into the horn during calibration.

2.2.4.1 Conclusive proof for Xcal performance

When FIRAS first begins to transfer data to the Earth, a calibration file using Xcal had not been collected in space [22, p. 216]. Nonetheless, a calibration file existed which had been measured on the ground. Mather provides a wonderful account of recording the first blackbody spectrum from the microwave background [22, p. 216]. The text is so powerfully convincing that it would be easy to dismiss the search for any problems with FIRAS. Using the ground-based calibration file, the FIRAS team generates an "*absolutely perfect blackbody curve*" [22, p. 216]. However, considering all of the errors present in orbit, it is not clear how the calibration file gathered on Earth differed, if at all, from the one obtained in space. If the FIRAS team had wanted to bring forth the most concrete evidence that the situation in space, relative to Xcal, was identical to that acquired on the ground, then they could have easily displayed the difference spectrum between these two files. Ideally, no differences should be seen. But, if differences were observed, then either temperature variations, or leakage, must be assumed. In fact, the difference between the two files could have provided a clue as to the nature of the leakage into the FIRAS horn. Mather et al. feel compelled to verify the performance of Xcal on the ground 10 years after launch [42]. This suggests that the calibration files taken prior to launch did not agree with those acquired in flight.

2.2.5 Design of the FIRAS horn

In examining the FIRAS horn (see Figure 1), it is apparent that this component does not conform to accepted practices in the field of antenna design [81–83]. This device is unique, meant to operate over a phenomenal range from ∼30 to 3,000 GHz [32–45]. Since broadband horns generally span no more than 1 or 2 decades in frequency [84, 85], it is doubtful that a comparable antenna can be found in the electromagnetics literature. Even the most modern broadband horns tend to cover very limited frequency ranges and, typically, at the expense of variable gains across the band [84, 85]. Unfortunately, insufficient ground tests were conducted, to demonstrate the expected performance from 30–3,000 GHz. It is highly unlikely that FIRAS was ever able to perform as intended. The FIRAS team provides no test measurements to the contrary. These would have included gain and side lobe performances spanning the frequency spectrum. Moreover, as will be seen below (see section 2.4.3.1), FIRAS is operating less than optimally over all wavelengths. The idea of using an interferometer for these studies was elegant [32–45]. But, broadband horns with demonstrated performances, over such a range of frequencies, simply do not exist [81–85]. It is interesting in this light, that the WMAP [19] and PLANCK [86] missions have both reverted to the use of narrow band devices to sample the microwave background. As for FIRAS, it functions primarily from ∼30–600 GHz. However, even in this region, the instrument must deal with horn/shield interactions and the effects of diffraction. These effects were never appropriately considered by the FIRAS team.

The testing of the COBE FIRAS antenna pattern was inadequate. Proper tests were never performed to document the interaction of the FIRAS horn with the Sun/Earth/RFI shield. Furthermore, the team conducted no computational modeling of the horn-shield interaction as a function of frequency. This type of documentation would have been central in establishing the reliability of the FIRAS findings. Without it, the FIRAS team did not eliminate the possibility that the Earth itself is producing the microwave background. The RF shield on COBE could accomplish little more than prevent terrestrial/solar photons, in the visible or near-infrared range, from directly illuminating the dewar which contains FIRAS. The central issue for the Sun/Earth shield appears to be the conservation of helium in the dewar, not the elimination of RF interference [87]. The shield is not corrugated [81, p. 657–659] and has no special edges to prevent diffraction in the far infrared. Given that the FIRAS horn is broadband, it is extremely difficult, if not impossible, to build a good RF shield for such a device. The FIRAS team has not established that an adequate shield was constructed to prevent RF interference from the Earth. The Sun/Earth shield simply prevents direct heating of the dewar, by visible or near infrared light [87]. They comment: "*a large external conical shield protects the cryostat and instruments from direct radiation from the Sun and the Earth. The Sun never illuminates the instruments or cryostat, but the COBE orbit inclination combined with the inclination of the Earth's equator to the ecliptic do allow the Earth limb to rise a few degrees above the plane of the instrument and sunshade apertures during about one-sixth of the orbit for one-fourth of the year. During this period, the sky horn could not be cooled to 2.7 K because of the Earth limb heating*" [42]. Nowhere, in the COBE literature, is the RF performance of the "sunshade" analyzed.

2.3 FIRAS in flight

2.3.1 Side lobe performance

Fixsen et al. [38] argue that the FIRAS horn "*provides a 7° field of view with low side lobes*". They base this statement on work by Mather, Toral, and Hemmati [25]. In this paper, Mather et al. present measured and theoretical evaluations of

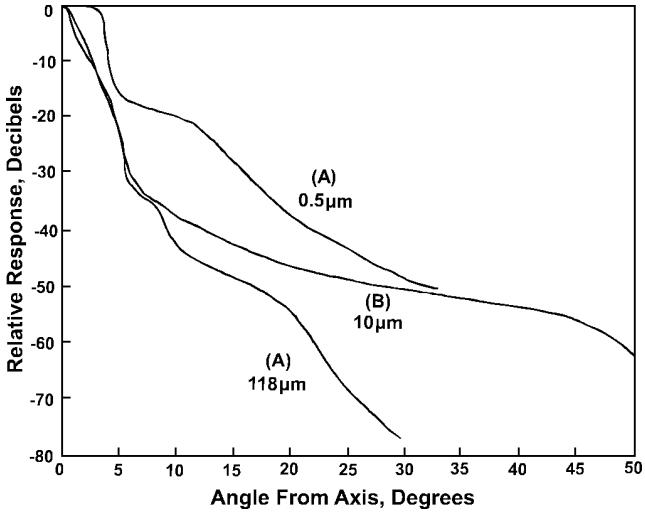

Fig. 4: Plot of the side lobe response for the FIRAS horn, without the presence of the COBE ground shield as reproduced from [25]. The sky lobe response, in preflight testing, was evaluated at three wavelengths, namely 118, 10, and 0.5 μm. Note that only the first measurement at 118 μm ($\sim$2,540 GHz) is within the frequency range of the instrument (30–3000 GHz). The latter two occur in the optical band. The side lobe performance is best at the longer wavelength, in opposition to the expected theoretical result. The FIRAS team also measures the FIRAS horn at 31.4 and 90 GHZ [25], with excellent performance (data is not reproduced herein). However, once again, these results were obtained without the interfering effects of the ground shield. Reproduced with permission of the Optical Society of America from: Mather J.C., Toral M., Hemmati H. Heat trap with flare as multimode antenna. *Appl. Optics*, 1986, v. 25(16), 2826–2830 [25].

side lobe data at 31.4 and 90 GHz [25]. As expected, the side lobes are lower at the higher frequency. The measurements conform to expected performance, at least at these frequencies. But, these tests were conducted without the RF shield and consequently have limited relevance to the actual situation in flight.

A careful examination of Figure 4 [25] is troubling. In this figure, Mather et al. [25] characterize the antenna pattern of the isolated FIRAS horn, without the COBE RF shield, at infrared and optical wavelengths (118, 10, and 0.5 μm). It is not evident why the authors present this data, as only the first wavelength, 118 μm ($\sim$2,540 GHz), is within the usable bandwidth of the instrument. Nonetheless, in Figure 4, the antenna has the strongest side lobes at the highest frequencies. For instance, at a wavelength of 0.5 μm, the antenna shows a relative response that is decreased by only 20 dB at 10° [25], as shown in Figure 4. At 118 μm, the antenna response is decreased by nearly 50 db. The authors are demonstrating that the FIRAS horn has better side lobe behavior at longer wavelengths rather than at short wavelengths. This is opposed to the expected performance. Mathematical modeling may well be impossible at these elevated frequencies. Once again, the shield was never considered.

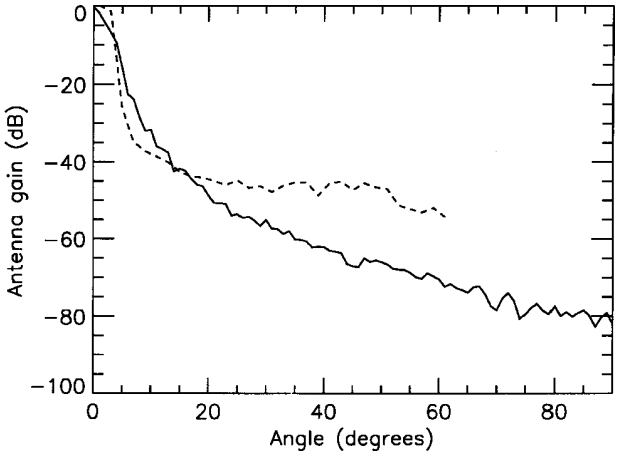

Fig. 5: Plot of the side lobe response obtained for the FIRAS shield on the ground, at 3 cm^{-1} (solid line), and in orbit, using the Moon as a source of signal, at 50 cm^{-1} (dashed line). This figure is reproduced from [38]. A detailed discussion is provided in section 2.3.1. Reproduced by permission of the AAS.

Neglecting to characterize the horn-shield interaction on the ground, the FIRAS team attempts to do so in flight. In Fixsen et al. [38], they publish Figure 5. They attempt to determine the antenna pattern in space by monitoring the Moon as a function of angle. Using this approach at 50 cm^{-1}, they conclude that the satellite provides a maximum side lobe response of "*less −38 dB beyond 15° from the center of the beam*" [38]. Such a performance is reasonable, at least at this frequency. However, the FIRAS team then compares side lobe performance at 50 cm^{-1} ($\sim$1,500 GHz) with data obtained on the ground at 3 cm^{-1} ($\sim$90 GHz). In referring to this figure in their paper, the FIRAS team writes: "*Preliminary results are shown in Figure 4, along with preflight measurements at 1 and 1.77 cm^{-1}*" [38]. Yet the figure legend itself states the following: "*Antenna pattern for the FIRAS horn as measured on the ground before launch at 3 cm^{-1} (solid line) and as measured from in flight Moon data at $\sim$50 cm^{-1} (dashed line)*" [38]. Beyond the inconsistency between the text and the figure legend, there are at least five concerns relative to this figure.

First, the data on the ground appears to have measured the FIRAS horn exclusively, not the horn with the RF shield. Second, they are comparing data at frequencies which differ by more than one order of magnitude. Third, they display none of the critical in-flight data for the lowest frequencies, namely those frequencies where one would expect the strongest effects from diffraction. Fourth, they fail to present ground data at 50 cm^{-1}. Finally, the data from Fixsen et al. [38] is also puzzling. It reveals much stronger side lobes at 50 cm^{-1} than one would have predicted at this frequency ($\sim$1,500 GHz). Note, in Figure 5, that the Moon data displays a plateau at approximately -45 dB in the range from 20–50°. This is higher than would be expected, based on the excellent side lobe response, even at a much lower 90 GHz, reported for the free

horn on the ground [25]. This plateau may simply be caused by a lack of sensitivity for the Moon at these angles. It is impossible to determine whether the plateau achieved in detection is a result of this effect. The FIRAS Explanatory Supplement suggests that the Moon can contaminate the microwave background at all frequencies [40, p. 61]. The FIRAS team does not adequately confront the issue and does not publish a work focused on side lobe behavior. Comparing ground data at ∼30 GHz, or even ∼90 GHz, with in-flight data at 1,500 GHz, has no value relative to addressing the side lobe issue.

It is also true that a loss of "Moon signal", as a function of angle, could account for the appearance of good side lobe performance. The possibility that the Moon could be reflecting terrestrial, or even solar, signals back into the FIRAS horn, through normal specular reflection, is not discussed. This process would be angle dependent and might create the illusion of reasonable side lobe behavior. The FIRAS team provides no supportive evidence from the literature that the Moon behaves as a lambertian emitter at 50 cm^{-1}. The Moon does have phases, which result in differential heating across its surface. Should the Moon not act as a lambertian emitter, the side lobe performance was not properly evaluated. This would be true, unless the satellite was rapidly turned away from the Moon while maintaining a single orbital position. But, this is unlikely to have been the case, since COBE did not have a propulsion system [22, p. 195]. Thus, the satellite was simply permitted to continue in its orbit, and the angle to the Moon thereby increased. Such a protocol might not accurately assay side lobe behavior. This is because it would depend on the absence of specular reflection from the Earth and the Sun, while requiring that the Moon is lambertian. In the end, experiments in space cannot replace systematic testing on the ground in establishing side lobe behavior.

Perhaps more troubling is that the frequencies of interest, relative to the microwave background, extend from less than 1 cm^{-1} to ∼22 cm^{-1} (<30 to ∼660 GHz). For example, the initial Penzias and Wilson measurements were made near 4 GHz [1]. Consequently, the FIRAS team is showing side lobe performance for a region outside the frequencies of interest. In fact, 1,500 GHz is the region wherein galactic dust would be sampled, not the microwave background [23]. The side lobe performance at this frequency is not relevant to the problem at hand. Furthermore, if there are problems with diffraction, they are being manifested by a distortion of signal, primarily in the lower frequency ranges. Hence, it would be critical for the FIRAS team to display in-flight data, or ground data including the shield, in order to fully document side lobe performance in this region. The data, unfortunately, is not provided.

Should access be available to the exact dimensions of the FIRAS horn and the COBE shield, it would, in principle, be possible for an independent group to verify the performance of the satellite relative to this instrument. It is true that the problem of modeling the FIRAS horn/shield interaction is extremely complex, even at 30 GHz. Nonetheless, given current computational methods, using the Geometric Theory of Diffraction, it is difficult to reconcile that the true directional sensitivity of the FIRAS horn was not modeled at any frequency. These studies would depend on obtaining the exact configuration, for the FIRAS horn/shield, and then treating the problem using computational methods. The issue cannot be treated analytically. Furthermore, this is a difficult task. It is achievable perhaps, only at the lowest frequencies of operation.

In 2002, Fixsen and Mather give a summary of the FIRAS results [43], wherein they also describe how a new instrument might be constructed. In order to address the lack of side lobe characterization, they advance that: "*we would surround the entire optical system with segmented blackbody radiators to measure the side lobe responses and ensure that the source of every photon is understood*" [43]. With COBE, the source of every photon was not understood. The side lobes were never measured in the presence of the shield. The idea of surrounding the optical system with blackbody calibrators is less than optimal. It would be best to simply analyze the horn/shield performance with preflight testing.

2.3.2 Establishing temperatures

The FIRAS team presents a dozen values for the microwave background temperature, using varying methods, as shown in Table 1. This occurs over a span of 13 years. Each time, there is a striking recalculation of error bars. In the end, the final error on the microwave background temperature drops by nearly two orders of magnitude from 60 mK to 0.65 mK. Yet, as will be seen below, in sections 2.3.3 and 2.3.4, FIRAS was unable to yield proper nulls, either with the sky and Ical, or with Xcal and Ical. Despite the subsequent existence of systematic errors, the FIRAS team minimizes error bars.

The problems with correctly establishing temperatures for Xcal and Ical were central to the mission, as these investigators recognized: "*There were two important problems. One was that the thermometers on both the Ical and Xcal did not at all agree. In fact, the disagreement among different Xcal thermometers was 3 mK at 2.7 K*" [38]. They continue: "*The disagreement between the Ical thermometers was 18 mK at 2.7 K. The heat sinking of the Ical thermometer leads was inadequate, and some of the applied heat flowed through part of the Ical*" [38].

They try to overcome the reality that the temperature monitors on the external calibrator report a systematic error. The temperature errors on Xcal are fitted with an "*arbitrary offset in the Xcal thermometer and the result was* -7.4 ± 0.2 *mK for this offset*" [38]. The FIRAS team realizes that this was "*considerably larger than the ∼1 mK expected from the preflight calibration of the thermometers*" [38]. They attribute the problem either to having improperly calibrated the thermometers before flight, or due to an unknown systematic

Reference	Temperature	Error (mK)*	Frequency (cm^{-1})
Mather et al., *ApJ*, 1990, v. 354, L37–40 [32]	2.735§	±60	1–20#
Mather et al., *ApJ*, 1994, v. 420, 439–444 [35]	2.726§	±10	2–20#
Fixsen et al., *ApJ*, 1996, v. 473, 576–587 [39]	2.730§	±1	2–21†
Fixsen et al., *ApJ*, 1996, v. 473, 576–587 [39]	2.7255¶	±0.09	2–21†
Fixsen et al., *ApJ*, 1996, v. 473, 576–587 [39]	2.717¥	±7	2–21†
Fixsen et al., *ApJ*, 1996, v. 473, 576–587 [39]	2.728**	±4	2–21†
Mather et al., *ApJ*, 1999, v. 512, 511–520 [42]	2.725§	±5	2–20‡
Mather et al., *ApJ*, 1999, v. 512, 511–520 [42]	2.7255¶	±0.085	2–21†
Mather et al., *ApJ*, 1999, v. 512, 511–520 [42]	2.722¥	±12	2–20‡
Mather et al., *ApJ*, 1999, v. 512, 511–520 [42]	2.725**	±2	2–20‡
Fixsen & Mather, *ApJ*, 2002, v. 581, 817–822 [43]	2.725	±0.65	2–20‡
Fixsen & Mather, *ApJ*, 2002, v. 581, 817–822 [43]	2.725	±1	2–20‡

* 95% confidence intervals.
§ Measurement using FIRAS microwave background lineshape. Calibration sensitive to the thermometers of the external calibrator, Xcal.
¶ Measurement using FIRAS microwave background frequency. Calibration relies on CO and C+ lines at 7.69, 11.53, 15.38, and 16.42 cm^{-1} [39].
¥ Measurement using a fit of the dipole spectrum to the 1st derivative of a Planckian function describing the microwave background with T_{cmbr} set to 2.728 K.
** Composite value obtained from analysis of three previous entries.
# Frequency range used is formally stated.
† Frequency range used is not formally stated but appears to be 2–21 cm^{-1}.
‡ Frequency range used is not formally stated but appears to be 2–20 cm^{-1}.

Table 1: Summary of microwave background temperatures obtained by the COBE FIRAS instrument.

error. They therefore assign a -4 mK offset to Xcal and raise to 5 mK its 1σ error. Though this might seem negligible, the FIRAS team is sufficiently concerned about Xcal that they attempt to recalibrate it on the ground, using a duplicate experiment, nearly ten years after launch [42]. For the present discussion, an error of at least 5 mK can be attributed to Xcal.

The FIRAS Explanatory Supplement outlines an enhanced picture relative to Ical performance [40, p. 42]. An optical temperature drift is modeled as follows:

$$T' = T + A \exp\left(t/\tau_{\mathrm{Ical}}\right) + T_{\mathrm{offset}}$$

where T' is the "raw" Ical temperature, $A = 4.26$ mK, $T_{\mathrm{offset}} = -3.054$ mK, and $\tau_{\mathrm{Ical}} = 104.3$ days [40, p. 42]. Given that FIRAS was operational for ∼259 days [40, p. 28], the drift model accounts for a 48 mK error in Ical by the time the instrument is decommissioned. Yet, in 1999, Mather et al. [42] offer a different view [40, p. 42]. While treating Ical, they write: "*An additional drift of ∼3 mK was noted in the early part of the mission*" [42]. Thus, it is likely that the equation in the supplement is simply missing a negative sign in the exponent. As a result, the ∼3 mK drift, discussed by Mather et al., can be attributed to Ical [42] along with errors of 18 mK for temperature differences between thermometers. In addition, as demonstrated in Figure 6, the emissivity modeled for Ical can exceed the theoretical upper limit of 1 over much of the FIRAS frequency range. This illustrates that the calibration model adopted by the FIRAS team contains significant shortcomings.

2.3.3 Achieving a sky null

As represented in Figure 1, FIRAS functions as a differential spectrometer, wherein the sky or the external reference, Xcal, are being constantly compared to an internal reference blackbody, Ical. When the system is functioning properly and all temperatures are equal, then a perfect null should be measured in the interferogram. This should take place whether 1) the sky is being compared to Ical set at the temperature of the sky, or 2) the external reference calibrator, Xcal, is being compared to Ical set at the same temperature.

Once COBE finally reaches orbit, the first finding is that FIRAS is unable to achieve a null when the internal reference Ical is set to the sky temperature. This is demonstrated in Figure 7 [32]. Years later, the FIRAS team discuss the situation: "*If both the sky and the Ical were blackbodies, and the interferometer were perfectly symmetrical, one could in principle null the signal from the former simply by adjusting the temperature of the latter. The temperature of the CMBR could then be read from the reference body thermometers. Unfortunately, neither of those conditions prevails*" [38]. The FIRAS team continues: "*Our Ical and instrument asymmetry com-*

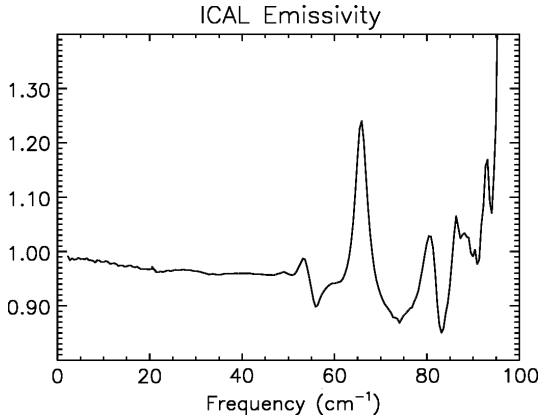

Fig. 6: Calculated emissivity for Ical as a result of calibration reproduced from the FIRAS Explanatory Supplement [40]. Note that emissivity exceeds 1, the theoretical maximum, at many frequencies. Reprinted with permission of John Mather.

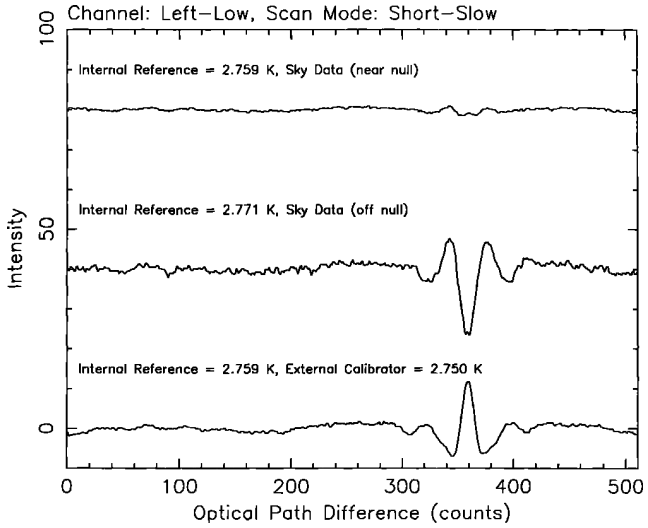

Fig. 7: Interferograms obtained in flight with the FIRAS instrument, as reproduced from [32]. The upper trace demonstrates the null condition between the sky (final reported temperature = 2.725±0.001 K [43]) and Ical set at 2.759 K. This trace is not plotted with the same vertical scaling factor as the one displayed in the central portion of the figure. Such a plot creates the illusion that a better result was achieved than actually obtained. The middle trace displays the interferogram recorded when Ical was set at 2.771 K. This indicates the magnitude of signal "off the null". The bottom interferogram was measured when comparing the two calibrators set at nearly the same temperature (Xcal = 2.759; Ical = 2.750). A null should have been obtained under these conditions, but did not occur. Once again, the vertical scale does not correspond to that used for the central trace. A correction of a factor of 3–5 should be applied to place the upper and lower interferograms on scale with the central one. This was not mentioned in the original text [32], but points to deviations from the theoretically expected results. Reproduced by permission of the AAS.

bine to produce a net reflectance of ∼4%, and Galactic emission from gas and dust contributes to the observed signal. To measure these effects, we must calibrate the instrument" [38]. Note that since the sky temperature would end up being assigned as 2.725±0.001 K [43], the upper trace in Figure 7 indicates that the null point appears with Ical at nearly 34 mK above the sky temperature (2.759–2.725 K = 34 mK). Consequently, COBE is faced with a 34 mK systematic error based on this fact. It is not clear how much of this error can be attributed to Galactic emissions. These should be primarily sensed at frequencies beyond 20 cm^{-1} [23], the cutoff of the low frequency channel [38]. As such, it is doubtful that galactic contributions can fully account for the lack of a proper null in these channels. By the end of the mission, Ical is spending most of its time near the null, at ∼2.758 K and toggling to a temperature 12 mK higher, ∼2.770 K [40, p. 28]. The FIRAS team writes: "*In addition, the temperature of Ical was toggled between a "sky null" setting to a setting 12 mK hotter, every 3–4 days, to allow instrumental gain errors to be distinguished*" [40, p. 19]. The latter is 45 mK above the temperature reported for the microwave background.

Unable to attain the expected null, the FIRAS team begins to target instrumental problems and calibration [38]. They do not envision that a null could not be achieved, because the sky was not acting as anticipated. Consider, for instance, that the Earth is producing the microwave background and that its diffracted signal is coming over the shield of the satellite. In this case, one can assume that the Earth was producing a signal with a nearly perfect Planckian [10] shape. But, at lower frequencies, the microwave background will experience more diffraction at the shield. Hence, FIRAS will be most sensitive to low frequency signals. As frequencies are increased, progressively less diffraction will occur at the shield and the FIRAS horn will become more forward directional. In so doing, it will be less sensitive to signals arising from beneath the shield. Thus, FIRAS may not sense a true Planckian curve, but a distorted spectrum displaying too much signal at the lower frequencies, and not enough signal at the higher frequencies. There may be less than the expected signal instensity along with constructive/destructive interference effects. The situation is illustrated schematically in an exaggerated fashion in Figure 8. This scenario would make it impossible to reach a null. The issue is not simply a question of temperature, but of lineshape. If two signals, arising from the sky and Ical, do not have the same lineshape, they can never be nulled. A proper null is never displayed. The underlying cause cannot be ascertained, given the nature of preflight testing, instrumental drift, and incoming signal.

In re-examining Figure 7 [32], note that the trace determining the null point is not a good null. The top trace in this figure is not plotted on the same scale as the bottom two traces, as can be deduced by examining the noise power. It needs to be multiplied by a factor of 3–5 to match the noise seen in the central trace. This gives the illusion that a better null is achieved than is actually obtained in practice. The second trace has much more noise. In fact, an analysis of noise

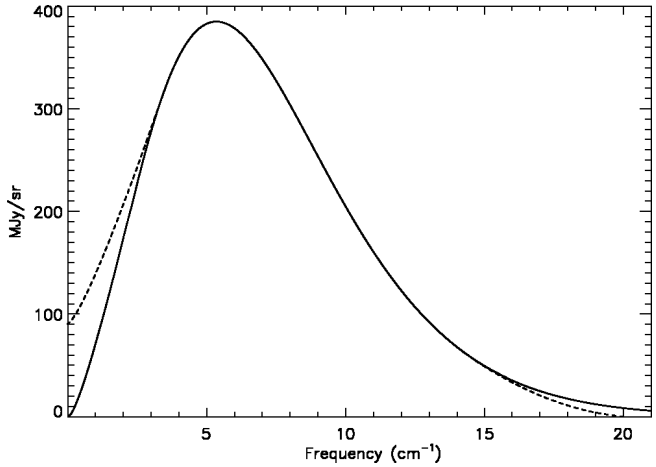

Fig. 8: Schematic representation of an ideal blackbody at 2.725 K (solid line). The dashed line is an exaggerated representation of the distortions that might occur if an earthly signal was diffracting over the FIRAS ground shield. Since diffraction might be expected to have the greatest effects at the lowest frequencies, the points in this region would be elevated. Conversely, as frequencies are increased, less diffraction should occur off the ground shield. The FIRAS horn should become more forward directional at elevated frequencies. As a result, a decreased signal might be sensed in this region. It is difficult to deduce the exact appearance of the effects from diffraction. For instance, there could actually be signs of constructive and destructive interference on the acquired spectrum. The nature of the spectrum acquired by FIRAS would also depend on the extent that the sky signal was diffracting into the FIRAS horn during calibration with Xcal, due to leakage. In the limit of severe leakage, FIRAS would report a perfect blackbody spectrum from the sky, even with diffraction occurring at the ground shield. Further details are provided in the text.

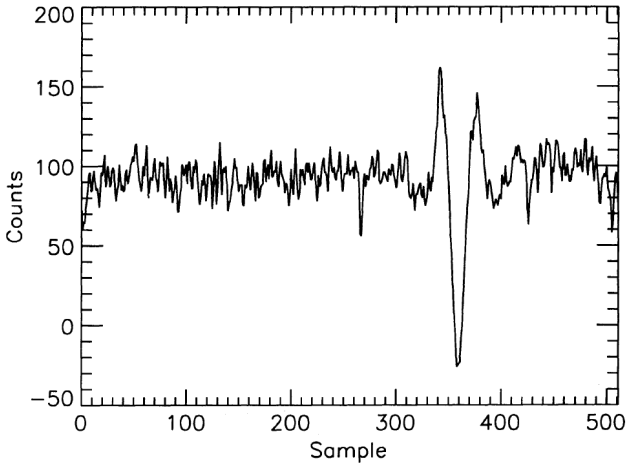

Fig. 9: FIRAS interferogram acquired between the sky and Ical, as reproduced from [38]. The signal is being generated just slightly "off the null". Apparently, the point at 355 can be perfectly nulled [38], but it is doubtful that such a result can be obtained while maintaining the null condition over all other points. The FIRAS team does not present a perfect null. A spectrum acquired "just off the null" yields little scientific information. Reproduced by permission of the AAS.

power from these traces establishes that the FIRAS team is not maintaining a constant vertical amplification. This should not have escaped the eye of the reviewers. Correct scaling factors should have been provided in the figure legend.

In any case, the null is not clean. The FIRAS team, for instance, shows a second interferogram in Fixsen et al. [38], reproduced herein as Figure 9. In the figure legend, they state that the peak at 355 can be nulled within detector noise levels. However, they fail to demonstrate the corresponding interferogram. It is certain that the point at 355 can be nulled. But, it is essential that all the points in the spectrum are simultaneously nulled. The FIRAS team has never been able to present such an interferogram. Moreover, if a proper null exists, they should not display data "just off the null". These interferograms are not useful as measures of instrument performance. The issue is not simply one of temperature match. For, if two blackbodies are brought to the same temperature, then ideally, the null must be perfect. Lineshape differences, generated by diffraction on the shield, could account for the discrepancies noted.

Unable to reach a perfect null with the sky and dismissing lineshape effects, the FIRAS team is left to implicate instrument design [38]. This is because they believe that a perfectly Planckian background must be found in the sky in front of FIRAS. The idea that an ideal blackbody spectrum, produced by the Earth, could have been distorted by diffraction over the shield, is not entertained. As a result, they cite that the Ical provides a 4% reflectance, to partially account for the lack of a proper null [38].

2.3.4 Achieving a null when $T_{\mathrm{Ical}} = T_{\mathrm{Xcal}}$

In analyzing the bottom trace in Figure 7, it is evident that a null cannot be achieved, when Xcal is set at nearly the same temperature as Ical (Xcal = 2.750 K, Ical = 2.759 K). Unfortunately, the FIRAS team does not publish a sufficient number of interferograms to enable the complete dissection of this question. On the surface, failure to locate a null, when $T_{\mathrm{Ical}} = T_{\mathrm{Xcal}}$, would support the idea that the problem was instrumental. After all, a second failure to establish a solid null is being reported. The FIRAS team might have been able to supply proof of this contention, using a combination of interferograms with Xcal and Ical at differing temperatures. As it is, no proof exists that Ical was the sole problem with FIRAS. Again, failure to attain a null, when $T_{\mathrm{Ical}} = T_{\mathrm{Xcal}}$, could also be supported by technical issues with leakage around Xcal.

It is vital to understand the exact temperatures for Xcal and Ical, when a null spectrum is achieved by the two calibrators. However, such data is not presented by the FIRAS team. Furthermore, it is not certain that they were ever able to obtain a null. In order to properly address this issue, the critical data is found in the null spectrum between Xcal and Ical on the ground. It is not known if the null imbalance was documented for FIRAS using preflight tests. The data have

not been published, but are critical to understanding the inability to reach a null between the sky and Ical, as discussed in section 2.3.3. Without it, the FIRAS team cannot defend the hypothesis that galactic contributions, for instance, were responsible for this shortcoming. It is obvious that the galaxy may not be invoked for the lack of a null between the two reference blackbodies. Therefore, for a proper evaluation of these questions, ground data, obtained between Xcal and Ical, should be provided.

2.4 Data processing

Initially, the FIRAS team publishes a spectrum from 1–21 cm^{-1} [32]. That spectrum was said to deviate from the intensity of a blackbody by less than 1%. Then, in 1994, Mather et al. [35] advance a new set of data, wherein the intensity deviates from a blackbody by less than 0.03%. The error bar in setting the absolute temperature, using Xcal, drops precipitously from 60 mK to 10 mK (see Table 1). Fixsen et al. [39], in 1996, then report that the "*rms deviations are less than 50 parts per million of the peak of the cosmic microwave background radiation*". In 1999, Mather et al. apparently again increase the rms deviation and assert that the deviation of the CMB from the theoretical blackbody is less than 0.01% [42]. Finally, in 2002, Fixsen and Mather [43] advance that "*the measured deviation from this spectrum are 50 parts per million (PPM, rms) of the peak brightness of the CMBR spectrum, within the uncertainty of the measurement*". Using technology established in the 1970's, the FIRAS team reported a spectral precision well beyond that commonly achievable today in the best radiometry laboratories of the world.

Figure 2 [39] is famous for the observation that the uncertainties are a small fraction of the line thickness. This figure is unusually drawn, as the frequency axis is offset. This makes it less apparent that data is not being shown below 2 cm^{-1}. The final result was obtained with the calibration procedures outlined by Fixsen et al. [38]. In the end, the FIRAS team transfers the error from the spectrum of interest into the calibration file, as will be discussed in detail below. Using this approach, it would be possible, in principle, to attain no deviations whatsoever from the perfect theoretical blackbody. Given enough degrees of freedom and computing power, errors begin to lose physical meaning. The calibration file became a repository for everything that did not work with FIRAS. The only problem was that it was now impossible to dissect what the FIRAS microwave background spectrum really looked like. Along these lines, the most serious concern was the omission of data, as discussed in section 2.4.3.

2.4.1 FIRAS calibration

In order to provide data for in-flight calibration, the FIRAS team controls the temperature of four key sources of emission, 1) the internal calibrator, 2) the external calibrator, 3) the sky horn, and 4) the reference horn. The emissivity of each of these devices could be modified on demand in the temperature range from 2–25 K [38]. Other parts of the instrument are approximated as Planckian functions [10], presumably because they are isothermal [38]. Cheng describes the calibration process: "*Calibration is accomplished by removing all known instrument effects from the raw spectra. This requires a model of the instrument, with all known imperfections, and sufficient calibration data to establish the model parameters. The measured instrument state for the sky data can then be used to predict the instrument characteristics based on the model which is then used to calibrate the sky data... The emissivity of various internal components in the instrument are determined by varying their temperatures while observing a constant input signal (e.g. from the external calibrator). These components include the sky horn, reference horn, internal reference load, dihedral mirrors, collimator, and the detector itself. The temperature of the first three components can be varied by command so that determining their emissivity is straightforward. The emissivity of the other components are determined by temperature variations during several cryostat temperature transients which occurred early on in the mission*" [34].

A critical aspect of the calibration procedure is that the external calibrator, Xcal, is treated as providing a perfect blackbody signal to the rest of the instrument. This approximation may not be justified, given the discussion in section 2.2.3. There are also complications, if the seal between the horn and the calibrator is not perfect, due to vibration, as addressed in section 2.2.4. The idea of approximating the thermal behavior of the dihedral mirrors, collimator, and detectors with Planck functions, as Fixsen describes [38], does not rest on solid grounds. Each material should ideally have been measured in the laboratory, as real materials do not behave as blackbody sources [80]. For instance, the FIRAS team describes harmonic responses in the instrument when radiation passes through the system more than once. This proves that the interior components of the instrument cannot be modeled as perfect blackbodies. They do provide reflective surfaces. It is noted that $\sim$20% of the input signal fails to reach the output [38]. This is a large number, which represents frequency dependent losses. However, no frequency dependence is mentioned, presumably because the loss for each interferogram cannot be dissected in these terms. Both second and third order harmonics were thought to be significant at the 0.1% level [38]. They also report that the frequency scale for FIRAS does not quite agree with that determined using known spectral lines. In order to correct the situation, they make a 0.5% adjustment with "*the remainder being absorbed by a 4 mK adjustment in the absolute temperature scale*" [38].

The discussion relative to the bolometers highlights how modeling can misrepresent the actual behavior of a device. The FIRAS team writes: "*The total of nine parameters with their uncertainties and covariance matrix were determined*

from these tests. The agreement with the determination of the parameters from the FIRAS in-orbit calibration is poor, with normalized χ^2's of 80 to 800 in various fits for 9 DOF (degrees of freedom). This is probably due to a deficit in the bolometer model" [38]. In the final analysis, the in-flight calibration procedure is viewed as correct, and the disagreement with pre-flight data appears to be disregarded. This demonstrates how the COBE calibration procedures have become essentially detached from any experimental findings recorded on the ground before flight.

The calibration process brings many more degrees of freedom for setting error bars and temperatures. Mather et al. thus write: "*However, the calibration process corrects other effects of the error to the first order...*" [42]. Calibration involves: "*comparison of the sky with an ideal movable external blackbody calibrator (Xcal) that can fill the aperture of the sky horn. The rest of the calibration process is used to measure gains and offsets that apply if the calibrator spectrum does not match the sky spectrum*" [43]. As a result, the FIRAS team can achieve a perfect fit to the sky spectrum. They have sufficient degrees of freedom to accomplish the task by invoking the calibration procedure. The inversion matrix required for the calibration fits is "*of such large rank (∼4,000)*" that it "*is not generally tractable*" [38]. The FIRAS team was "*able to invert this matrix by taking advantage of its special form... This made inversion possible, though still not speedy*" [38].

Relative to error analysis, very large degrees of freedom (DOF) were invoked. The FIRAS team writes: "*The normalized χ^2 resulting from this fit is 2.8218 (27873 DOF) for the left low detector, short slow stroke data ($2.27 < \nu < 21.54$ cm^{-1}), and 4.53 for (159353 DOF) for the right high detector, short slow stroke data ($2.27 < \nu < 96.28$ cm^{-1})*" [38]. Moreover, it can be deduced that the values are rather high for χ^2/DOF, particularly when operating away from the null position. Cheng [34] reports higher than expected χ^2/DOF values, of 4 to 10, for the low and high frequency channels when discussing the calibration data. Apparently [34], it is only when considering calibration files near the null condition that χ^2/DOF values near 1 are reached [39]. Of course, it is easier to fit data near the null, for the precise reason that the spectrum contains little power in this range. It is solely by examining the performance of the calibration model away from the null, that any real insight can be harnessed relative to the reliability of this method. However, such data appears to give even higher χ^2/DOF values than obtained near the null [34]. This is not a good sign, relative to the validity of this approach. The inability to find good χ^2/DOF values off the null might be reflecting leakage around Xcal, for instance. This could become more apparent when Xcal and Ical are at very different temperatures.

Fixsen et al. [39] do describe excellent χ^2/DOF performance in their Figure 1 (not reproduced herein). An analysis of Table 1 in [39] reveals that χ^2/DOF are generally on the order of 2 or more. Nonetheless, it is noticeable that the χ^2/DOF, listed in this work (see Table 1 in [39]), have improved substantially over those found 2 years earlier (see Table 2 in [38]). It is not clear if this represents anything but better insight into how χ^2/DOF values could be minimized. In the end, there is too much flexibility in these approaches. This places at risk all physically meaningful experimental findings, reflecting systematic errors.

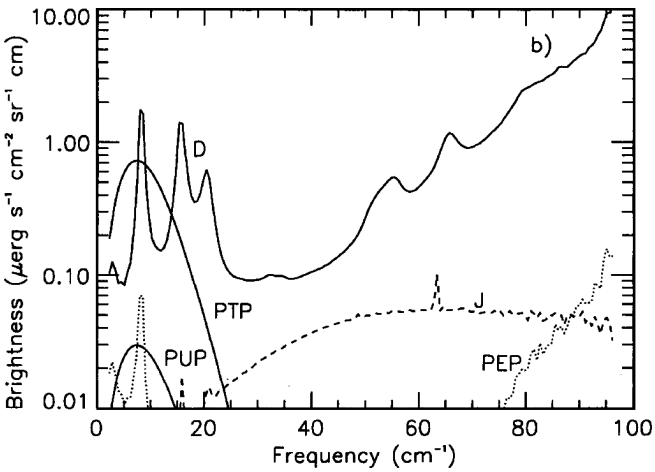

Fig. 10: Plot of various error terms for the FIRAS high frequency channel for a typical sky point, as reproduced from [38]. Separate fits are obtained for each point in the sky. This allows for far too many degrees of freedom in the FIRAS calibration stage. Curve D represents the error arising from detector sensitivity. Note the resonances at ∼7, 16, and 20 cm^{-1}. These may correspond to CO lines in the galaxy. Such resonances should not be found on functions representing detector sensitivity. They are not found in the detector functions at low frequency [38]. The dashed line, which is not labeled in the original work, represents the calculated errors from the galaxy as can be established using Figure 13. Note that there is little error contribution from the galaxy, below 20 cm^{-1}. As such, the FIRAS team cannot attribute the failure to achieve a proper null to the presence of contaminating galactic signal in this frequency region. The dotted line, PEP, accounts for error associated with various temperatures within the instrument. Once again, a resonance line is observed at ∼7 cm^{-1}. Such a resonance line should not be found on this function. It would, however, permit the FIRAS team to vary the error in this region when trying to correct for contributions from galactic CO. PTP accounts for errors in the absolute temperature scale. PUP error depends on the absolute temperature state of the instrument and is most sensitive to Ical. PUP and PTP are given a blackbody appearance without proper justification by the FIRAS team (see text for additional details). Reproduced by permission of the AAS.

A treatment by Fixsen et al. [38] of the error terms for FIRAS reveals that the FIRAS team considered nearly every possible source of instrumental contribution, while discounting the possibility that errors existed in the shape of the blackbody provided by the sky itself. Such a systematic error could exist if diffraction effects were important.

Figure 10 is a reproduction of Figure 9b in [38]. For

the low frequency channel (figure not displayed), the major term is referred to as PTP. It represents the uncertainty in the absolute temperature scale. The peak brightness of a 2.7 K blackbody is approximately 120 μergs cm^{-2} s^{-1} sr^{-1} cm [38]. As a result, this error term absorbs about 0.5% of the deviation from the peak of a blackbody. The most important error term for the high frequency channel, D, accounts for detector noise. The PUP error is linked to the temperature state of the instrument and is primarily dependent on Ical. The PEP error depends on the temperatures of various emitters in the instrument. "*These are: Ical 2.76±0.006 K, MTM 2.0±0.4 K, horns 2.75±0.005 K, mirrors 1.56±0.02 K, and bolometers 1.52±0.017 K*" [38]. The FIRAS team writes that the PEP and PUP error terms are well approximated by Planckian functions. This claim, however, is without foundation. In fact, there are no references provided for assigning a Planckian shape [10] to either PTP or PUP. Assigning such shapes to these two terms will help determine the appearance of the other terms. The entire procedure is without scientific basis [80]. It is particularly concerning that the FIRAS team generates such error functions for each point in the sky. Instrument error should not be dependent on the scan direction. At the same time, it is true that the instrument experiences temperature fluctuations over time: "*Further tests of the calibration are obtained by searching the calibrated map of the sky for features relating to changes of the instrument state. The largest such changes occurred during the time from 1990 May to August. In this time period, it was impossible to keep both the Earth and the Sun below the Sun screen, and the Earth illuminated the top of the instrument during part of the orbit. The data taken with the Earth above the instrument were rejected in the maps, but the thermal transient produced by the heat of the Earth was large and long. As a result, we raised the set point of the horn temperature controllers to as high as 6 K to achieve stability*" [38]. Direct visualization of the Earth did impact the COBE results, but the data were rejected. Yet, if the Earth was truly silent over the frequency of interest, there could be no reason to reject this data. Heating by the Earth could simply be accounted for in a manner similar to that used for other parts of the orbit. The FIRAS team believes that the heat transient in the instrument, as a consequence of direct infrared heating, was the only effect. However, it would have been most interesting to examine the resulting sky interferograms. Perhaps these actually contained direct physical proof that the Earth had emitted the microwave background.

In any case, note the nature of the error term, D, for the high frequency channels. Essentially, there are resonance lines at ∼7, ∼16, and ∼20 cm^{-1}. These features seem to correspond to the presence of the CO lines in the galaxy [39]. Such lines should not be found within detector noise error. In addition, curve D for the high frequency channels approaches 10 μergs cm^{-2} s^{-1} sr^{-1} cm, at 95 cm^{-1}. This is an extremely powerful contribution from this term, given that the maximal power of the microwave background itself is on the order of 120 μergs cm^{-2} s^{-1} sr^{-1} cm.

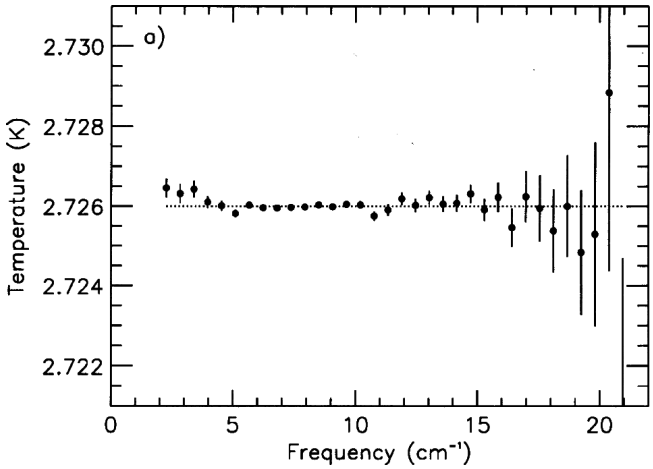

Fig. 11: Calculated residual errors in the microwave background, as reproduced from [35]. These residuals were generated, using a conservative approach, by increasing the statistical errors, forcing χ^2 to 32 [35]. Nonetheless, note the systematic increase in the residuals beyond 15 cm^{-1}. There is a slight trend towards signal loss in this region as well. In addition, the points below 5 cm^{-1}, slowly begin to rise away from the reported temperature, and represent signs of excessive signal in this region of the spectrum. The residuals are presented once again in 2001 [44]. At this time, systematic variations have been absorbed by the calibration files and the residuals are now random and of insignificant importance. Reproduced by permission of the AAS.

2.4.2 Analysis of residual errors

When Mather et al. [35] publish the 1994 FIRAS data release, several unexpected findings are revealed. Figure 1 of this work [35], a presentation of the CMBR residuals, is reproduced as Figure 11. There are two interesting aspects of this figure. First, there is a pronounced increase in the error bars associated with the residuals, as the frequencies are raised beyond 15 cm^{-1}. This increase in variability is systematic, and consequently may represent a real finding. In fact, there is a slight trend towards decreased temperatures as a function of frequency beyond 15 cm^{-1}. Second, at the lower frequencies, the data points begin to rise. The FIRAS team comments as follows: "*pending further detailed study of possible instrument faults at these low frequencies, we cannot speculate on their nature. We emphasize that the size of the apparent deviations is greatest at those frequencies where diffractive effects, interferogram baseline curvature, and very low spectral resolving power and wide spectral sidebands cause the greatest difficulties in calibration*" [35]. The authors therefore "*conservatively increase the statistical errors by a factor, forcing χ^2 to exactly 32, the number of degrees of freedom in the fit*" [35]. Nonetheless, they eventually publish

new residuals [44], which have now lost the systematic variations displayed in Figure 11. This shows the power of the fitting methods applied.

The FIRAS team believes that they fully understand all systematic errors and that their fits are justified. However, this is not the case. The fact that an excellent fit can be found, given sufficient degrees of freedom, is well recognized in science. The question remains how well justified were the bases for the fits. Adequate justification is based on a complete understanding of the instrument on the ground with calibrated test procedures. This approach was not utilized. Instead, fits are obtained by adjusting gains, offsets, and functions, which have a weak foundation, other than their ability to result in minimal residual errors for the sky. Furthermore, the FIRAS team has not shown that it can minimize residuals, using their final calibrations across all ranges of temperatures for Xcal, Ical, the sky horn, and the reference horn. Without explicit demonstration that the final calibrations apply to all possible interferograms, the analysis of residuals for the sky alone have little value. It is a complement of all residuals, for all conditions, which is important to visualize, for this alone might help establish the reliability of the approach in the absence of sufficient pre-flight testing.

2.4.3 Data omission

The FIRAS data set from 1994 contains a more serious concern: all of the observations at frequencies below 2 cm^{-1} are now excluded [35]. Moreover, there is a rise in the residuals below 4 cm^{-1} which cannot be accounted for by their error bars. This region is usually the easiest to monitor due to the low frequency range. Never again is the data below 2 cm^{-1} re-included in the FIRAS data set. It is only through reading the accompanying calibration work by Fixsen et al. [38], that one might postulate on the causes behind the loss of this data. A single sentence is presented when discussing the reference horn: "*However, the measured emission is higher than predicted, particularly at the lowest frequencies*" [38].

Though FIRAS was designed to cover the region from 1–2 cm^{-1}, the FIRAS team omits the data below 2 cm^{-1} and ignores the excessive signal. They do not discuss the cause of this anomaly, unless Wilkinson's concerns about earthshine were a reaction to this problem [74]. At the same time, given the use of calibration files to correct FIRAS, it may have been that the FIRAS team could not envision a means to account for the spectral behavior below 2 cm^{-1}. On the surface, ignoring this data might not appear so serious. After all, the entire spectrum beyond 2 cm^{-1} was reported.

Given that diffraction of a terrestrial signal would produce distortions in the measurement of the microwave background, which include excessive signal at low frequencies and decreased signal as frequencies increase, the dismissal of this data cannot be taken lightly. The FIRAS team also forsakes all data acquired when the Earth was directly illuminating FIRAS [38], as previously discussed in section 2.4.1. While infrared heating of the instrument did occur at this time, it is not evident that such heating could not be modeled. This is the type of evidence that may have pointed to an earthly source for the microwave background.

2.4.4 Error bars

Despite the presence of systematic errors, the FIRAS team is able to essentially sidestep the recordings of their thermometers and overcome their inaccuracy. E. S. Cheng summarizes the overall approach of the group: "*Since the FIRAS is a far more sensitive thermometer that the GRT's (germanium resistance thermometers), especially at temperatures above 3 K, the thermometer readings can be adjusted, using the calibration data, to provide maximal internal consistency and a refined temperature calibration*" [34]. As such, the readings of the physical thermometers could be given less weight.

Initially, it is not evident if they are aware that errors in the thermometers limit the ultimate temperature that can be reported for the microwave background. In 1996, Fixsen et al. arrive at a microwave background temperature of 2.730 ± 0.001 K (see Table 1), which relies on Xcal (see page 581, section 4.1, in [39]). Then, three years later, in 1999, the FIRAS team writes: "*A 5 mK error in the temperature determination of Xcal leads directly to a 5 mK error in the temperature determination of the CMBR*" [42]. The team apparently realized that it was impossible for Fixsen et al. [39] to claim a 1 mK error bar for this measurement in 1996. But, they continue to discount the 18 mK error between the Ical thermometers [38].

In order to fully restrict the error bars on the determination of the microwave background, the COBE group therefore moves to adopt two additional methods which, at least on the surface, are independent of Xcal. In the first instance, they determine the temperature by calibrating the frequencies of the background, using lines from CO and C+ [39]. Few details are provided relative to this approach; however, it may rely on accurately defining a Wien maximum and extracting the temperature from Wien's law [11]. The method is solid, on the surface at least. Nonetheless, it will depend on correctly setting the peak in the microwave background data, which may in turn depend on Ical and/or Xcal. The ability to detect a proper Wien maximum [11] would also be sensitive to interference effects caused by diffraction on the COBE shield, should the signal originate from the Earth. As a result, it is not clear that the frequency method holds any less systematic error than that directly relying on Xcal.

Alternatively, the group also uses the existence of a dipole to extract a monopole temperature [39]. In this way, they can build on the findings of the DMR relative to the dipole value [46–49]. Once again, the method may appear more accurate, but is also subject to many of the same problems as that based on Xcal. If the use of frequency calibration, or of

the dipole, seems less prone to systematic error, it may simply be because these have escaped detection by the FIRAS team. It is well established, not only in physics, but across the sciences, that systematic errors can be extremely difficult, even impossible, to detect [88]. Consequently, one must not dismiss those systematic errors which are evident.

Using a combination of these three methods, the FIRAS team finally arrives at a microwave background temperature of 2.725±.00065 K [43]. Beyond undetected systematic errors, this number circumvents much of the planning built into Xcal and Ical. It also neglects the excessive signal detected below 2 cm^{-1}. Relative to error bars, the result obtained, using an average of many methods, was analogous to ignoring the existence of known temperature error in the reference calibrators Xcal and Ical. The existence of imperfect nulls was also dismissed, as were all interferograms obtained while the Earth was directly illuminating FIRAS.

In the absence of proper pre-flight testing, it is impossible to account, with certainty, for all possible source of systematic errors associated with inability to find a null. Data processing methods do not address the fundamental issue. The FIRAS team believes that it has fully understood all systematic errors and that they can be removed from the final error report. But, systematic errors are best treated through the proper design and testing of scientific instruments on the ground. This was not achieved. The calibration procedure creates the illusion that all systematic error can be taken into account, after completion of data acquisition. This is not a prudent approach to systematic error, especially since they can be nearly impossible to identify [88, p. 93–95]. It is best to report all known systematic errors within the final error bar.

In failing to achieve a clear null, FIRAS is pointing to something on the order of a 34 mK error. The overall error in Xcal was ∼5 mK. The error difference between the Ical thermometers is 18 mK and the drift for Ical is 3 mK. A frequency correction of ∼4 mK exists. Some of these errors may be related and could be added quadratically [88, p. 93–95]. Direct addition provides a worse case scenario of ∼64 mK [88, p. 93–95]. As such, using direct addition, ∼64 mK appears to be a good lower limit on the accuracy of the FIRAS data set, from 2–20 cm^{-1}. This treatment would discount attempts to lower the error bar to 1 mK in the final FIRAS report [43]. In fact, ∼64 mK is not far from the 60 mK error initially used by the FIRAS team [32]. At the same time, the group asserts that their data is "*indistinguishable from a blackbody*" [37]. A cursory examination would suggest that this was the case (see Figure 2). An understanding of calibration process has provided the explanation.

2.4.5 The optical transfer function

The FIRAS team first presents the optical transfer function in the Explanatory Supplement, in 1997 [40]. This function is critical in processing FIRAS data files [40, p. 50] and it is reproduced herein as Figure 12. For an ideal spectrometer, the optical transfer function would be unity over the entire frequency range. That is, for every photon which enters the system, one photon is recorded by the detector. This situation does not occur in practice, and transfer functions will deviate from ideality. But, the transfer function for FIRAS is much less than ideal. At the lowest frequencies (<20 cm^{-1}), the transfer function contains a very strange and unexplained oscillation. The FIRAS team does not comment on the cause of this feature. Nonetheless, since the reciprocal of the transfer function is used to process data, this oscillation is significant. Although difficult to ascertain, this feature might be a sign of signal diffraction into the horn. In any event, the discontinuity near 20 cm^{-1} is due to the filter cutoff between the low and high frequency channels.

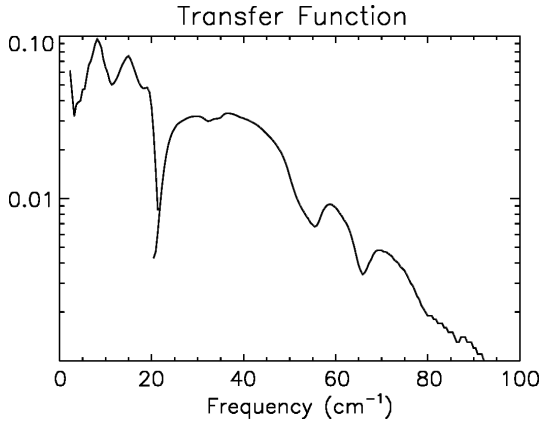

Fig. 12: Illustration of the Optical Transfer Function for FIRAS, as reproduced from the Explanatory Supplement [40]. The features near 20 cm^{-1} are due to the position of the filter cutoff. Nonetheless, this does act to provide a substantial correction for signal beyond the Wien maximum and between 15 and 20 cm^{-1}. Note the oscillation present below this frequency range. It is not clear why such features should be present on this optical transfer function. These might represent the effect of constructive and destructive interference. It is impossible to truly ascertain their cause with the data provided. Most importantly, the optical transfer function is decreasing exponentially. This is not characteristic of a properly functioning spectrophotometer. This figure reveals that the FIRAS instrument is suboptimal, beyond ∼30 cm^{-1}. Reprinted with permission of John Mather.

The most noteworthy feature of the optical transfer function for FIRAS is that only 1 photon in 10 is being detected, at best. In addition, the plot is on a logarithmic scale. Such behavior is highly unusual and demonstrates that the FIRAS instrument is not linear. It is also not sensitive at the higher frequencies. As a result, when the optical transfer function is applied to process data beyond 30 cm^{-1}, it results in a pronounced amplification of spectral noise. This is revealed in Figure 13 [41], where noise in the fits is amplified beyond 40 cm^{-1}. This constitutes a solid illustration that the FIRAS instrument, for practical purposes, is subfunctional in this frequency range.

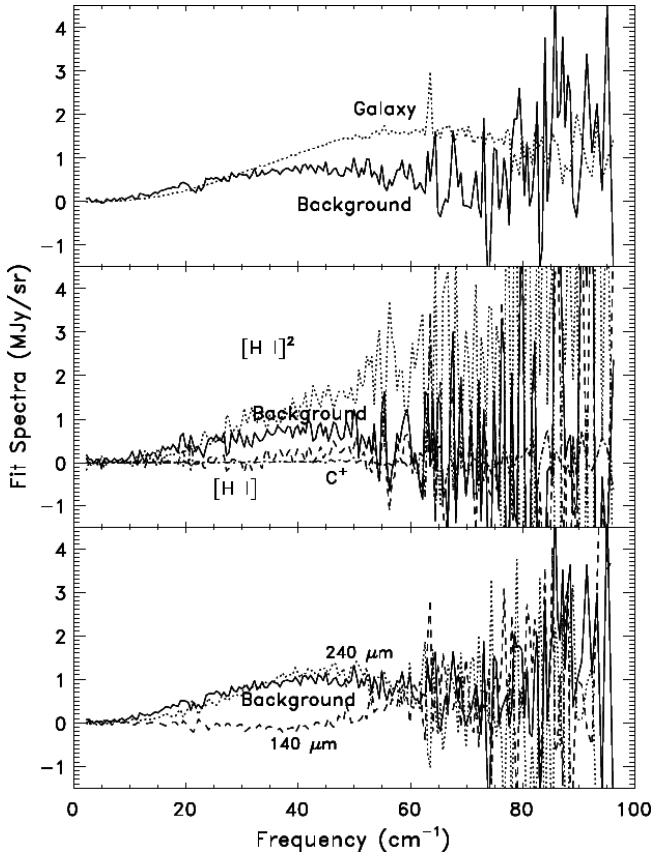

Fig. 13: Fit spectra calculated across the high frequency region using the FIRAS instrument, as reproduced from [41]. Note the tremendous increase in random errors beyond 30 cm^{-1}. This indicates that the spectrometer is suboptimal, in this frequency range. Reproduced by permission of the AAS.

2.4.6 Comments made by other authors

Several Italian authors [89–91] have been interested in the calibration of the FIRAS instrument as Fixsen and Mather highlight [42]. Giorgi, for instance, suggests that there could be an asymmetry of as much as 5% in the two input arms of FIRAS [89]. Fixsen and Mather point out that the measured asymmetry is only 1–3% [42]. In defending FIRAS data, Fixsen and Mather write: "*However, one must also consider the source of any reflection. The Xcal is part of a closed cavity composed of the calibrator, the sky horn, a small gap between the calibrator and the sky, and a small aperture leading to the spectrometer horn. Consequently, the radiation reflected by the calibrator must have originated either from itself, the sky horn, the sky through the gap, or the small aperture to the spectrometer. Three of these sources are effectively at the temperature of the CMB. As the most emissive of the four, the source of most of the reflected radiation is the calibrator itself... Moreover, since both the horn and the Xcal temperatures were set to match the CMB temperature, the only source of radiation that could be reflected by the calibrator and that was not at the CMB temperature is the small aperture leading to the spectrometer*" [42]. Such a statement cannot be justified. It is not clear that the sky is at the temperature of the CMB. Should the signal originate from the Earth, it would undergo differential diffraction as a function of frequency, as it travels over the RF shield and into the horn. This would lead to a spectrum which is not blackbody, and the measured sky spectrum would not be at the exact temperature of the microwave background. It would be distorted. Fixsen and Mather cannot assume that the sky is a blackbody at the temperature of the CMB. That is what they are trying to determine.

Work by Battistelli et al. [90] is centered on a computational analysis of Xcal, in order to further refine cosmological parameters. The text does not constitute a criticism of FIRAS. The emissivity values obtained for Xcal, are nearly ideal. Salvaterra and Burigana [91] examine a range of issues in detail, but the text does not raise any real concerns relative to FIRAS.

3 The Differential Microwave Radiometers (DMR)

The COBE satellite is also equipped with Differential Microwave Radiometers, the DMR. These constitute three pairs of narrow band antennae operating at 31.5, 53, and 90 GHz [46]. The DMR are mounted directly on the sides of the helium dewar containing the FIRAS and DIRBE instruments [45]. A detailed treatment of the DMR will not be presented, as many of the issues relative to the DMR have already been addressed relative to the WMAP satellite [20]. It is clear that the DMR has measured a dipole. This result is highly significant.

Of all the concerns which the DMR shares with WMAP, the central issue remains the processing of data and the extraction of the multipoles [20]. These are the "*wrinkles on the fabric of time*" [21]. Before the multipoles can be analyzed, the signal from both the dipole and galactic foreground must be removed. Importantly, as Smoot discusses in his popular book [21], these investigators also remove the quadrupole signal from the underlying maps. It is only at this stage that the multipoles become visible. Smoot writes: "*We were confident that the quadrupole was a real cosmic signal... By late January and early February, the results were beginning to gel, but they still did not quite make sense. I tried all kinds of different approaches, plotting data in every format I could think of, including upside down and backwards, just to try a new perspective and hoping for a breakthrough. Then I thought, why not throw out the quadrupole — the thing I'd been searching for all those years — and see if nature had put anything else there!*" [21, 276–277]. After removing the quadrupole, the multipoles finally appeared. Smoot then comments [21, 279]: "*Why, I puzzled, did I have to remove the quadrupole to see the wrinkles?*"

The answer to this question is one of data processing.

The raw maps do not contain any systematic signal variations on their own [21, 276–279]. The signals were random in nature. However, when Smoot and his colleagues imposed a systematic removal of signal, they produced a systematic remnant. In essence, the act of removing the quadrupole created the multipoles and the associated systematic anisotropy. Once the quadrupole was removed, the multipoles appeared as extremely consistent variations on the maps. As previously mentioned, these findings have no relevance to cosmology and are purely an artifact of signal processing. Citing from previous work [20]: "*Apparent anisotropy must not be generated by processing*". The sky does have anisotropy. But this anisotropy is likely to remain random, as Smoot initially observed in his data set, before removal of the quadrupole.

4 Conclusion

Through this analysis, unexpected problems with FIRAS and the DMR data have been brought to light. With regard to FIRAS, many issues exist. They include: 1) lack of gain and side lobe characterization for the FIRAS horn, 2) absence of diffraction modeling involving the interaction between FIRAS and the shield, 3) rudimentary pre-flight testing, 4) failure to document side lobe performance, in space, at frequencies relevant to the microwave background, 5) inappropriate evaluation of Xcal emissivities, 6) inability to ensure that leakage did not occur around Xcal in flight, given the vibrations present, the lack of gravity, and the nature of the Kapton leaves, 7) existence of a suboptimal transfer function for the instrument, 8) the presence of systematic errors, for the Xcal and Ical thermometers, 9) inability to achieve a proper null between the sky and Ical, 10) inability to reach a proper null between Xcal and Ical, 11) excessive degrees of freedom during the calibration process, 12) lack of justification for the error functions PTP and PUP, 13) inappropriate minimization of error bars, 14) omission of data below 2 cm^{-1} from all final data releases, and 15) omission of data when the Earth was directly illuminating FIRAS.

Given the systematic errors on Xcal, Ical, the frequency drift, and the null temperature, it is reasonable to ascertain that the FIRAS microwave background temperature has a significant error bar. As such, an error on the order of 64 mK represents a best case scenario, especially in light of the dismissal/lack of data at low frequency. The report of a microwave temperature of 2.725 ± 0.001 K [43] does not accurately reflect the extent of the problems with the FIRAS instrument. Furthermore, the absolute temperature of the microwave background will end up being higher than 2.725 K, when measured without the effect of diffraction, and when data below 2 cm^{-1} is included. Contrary to popular belief, the FIRAS instrument did not record the most perfect blackbody spectrum in the history of science.

Relative to the DMR, the problems mirror, to a large extent, those I voiced earlier with WMAP [20]. The most pressing questions are centered on the ability to remove the quadrupole from the maps of the sky. In so doing, it is clear that a systematic residual will be created, which can easily be confounded for true multipoles. In the end, the methods to process the anisotropy maps are likely to be "creating anisotropy" where none previously existed.

It also remains fascinating that the astrophysical community has not expressed greater anxiety relative to the difficulties produced by water, in the lower atmosphere. This is perhaps the most serious area of concern. It is certainly true that the Earth is bathed in a field with an apparent temperature near 3 K. The existence of the dipole is also firmly established. Cosmology holds that the monopole signal [1] represents a remnant of creation. Conversely, I maintain, along with my colleagues [5, 7], that it is being produced by the oceans of the Earth. Through this work, it is my hope that others will begin to see that there are legitimate issues with the FIRAS and DMR results on COBE. The thermal emission of water, in the microwave and far infrared, remains incompletely characterized. Our planet has never been eliminated as the source of the microwave background. In the end, the PLANCK satellite [86] should reveal that the Penzias and Wilson monopole [1] was never present in the depth of the Cosmos. The signal belongs to the Earth.

Acknowledgement

John Mather is recognized for granting permission to reproduce figures on behalf of the COBE team.

Dedication

This work is dedicated to Professor A. J. Christoforidis for the faith he demonstrated relative to my work these many years and for conferring upon me the privilege of becoming a professor of radiology.

Submitted on June 24, 2009 / Accepted on July 03, 2009
First published online on July 16, 2009

References

1. Penzias A.A. and Wilson R.W. A measurement of excess antenna temperature at 4080 Mc/s. *Astrophys. J.*, 1965, v. 1, 419–421.
2. Dicke R.H., Peebles P.J.E., Roll P.G., and Wilkinson D.T. Cosmic black-body radiation. *Astrophys. J.*, 1965, v. 1, 414–419.
3. Robitaille P.-M.L. A radically different point of view on the CMB. In: *Questions of Modern Cosmology — Galileo's Legacy*, ed. by M. D'Onofrio and C. Burigana, Springer, New York, N.Y., 2009.
4. Robitaille P.M.L. The Earth microwave background (EMB), atmospheric scattering and the generation of isotropy. *Prog. in Phys.*, 2008, v. 2, L7–L8.

5. Rabounski D. The relativistic effect of the deviation between the CMB temperatures obtained by the COBE satellite. *Prog. in Phys.*, 2007, v. 1, 24–26.
6. Robitaille P.M.L. Water, hydrogen bonding, and the microwave background. *Prog. in Phys.*, 2009, v. 2, L5–L7.
7. Rabounski D. and Borissova L. On the earthly origin of the Penzias-Wilson microwave background. *Prog. in Phys.*, 2009, v. 2, L1–L4.
8. Stewart B. An account of some experiments on radiant heat, involving an extension of Prévost's theory of exchanges. *Trans. Royal Soc. Edinburgh*, 1858, v. 22(1), 1–20 (also found in Harper's Scientific Memoirs, edited by J. S. Ames: The Laws of Radiation and Absorption: Memoirs of Prévost, Stewart, Kirchhoff, and Kirchhoff and Bunsen, translated and edited by D. B. Brace, American Book Company, New York, 1901, 21–50).
9. Kirchhoff G. Über das Verhältnis zwischen dem Emissionsvermögen und dem Absorptionsvermögen. der Körper für Wärme und Licht. Poggendorfs Annalen der Physik und Chemie, 1860, v. 109, 275–301 (English translation by F. Guthrie: Kirchhoff G. On the relation between the radiating and the absorbing powers of different bodies for light and heat. *Phil. Mag.*, 1860, ser. 4, v. 20, 1–21).
10. Planck M. Über das Gesetz der Energieverteilung im Normalspektrum. *Annalen der Physik*, 1901, v. 4, 553–563 (English translation by ter Haar D.: Planck M. On the theory of the energy distribution law in the normal spectrum. The old quantum theory. Pergamon Press, 1967, 82–90; also Planck's December 14, 1900 lecture *Zur Theorie des Gesetzes der Energieverteilung in Normalspectrum*, which stems from this paper, can be found in either German, or English, in: Kangro H. Classic papers in physics: Planck's original papers in quantum physics. Taylor & Francis, London, 1972, 6–14 or 38–45).
11. Wien W. Über die Energieverteilung in Emissionspektrum eines schwarzen Körpers. *Ann. Phys.*, 1896, v. 58, 662–669.
12. Stefan J. Über die Beziehung zwischen der Warmestrahlung und der Temperature. *Sitzungsberichte der mathematischnaturwissenschaftlichen Classe der kaiserlichen Akademie der Wissenschaften Wien*, 1879, v. 79, 391–428.
13. Robitaille P.M.L. On the validity of Kirchhoff's law of thermal emission. *IEEE Trans. Plasma Sci.*, 2003, v. 31(6), 1263–1267.
14. Robitaille P.M.L. An analysis of universality in blackbody radiation. *Prog. in Phys.*, 2006, v. 2, 22–23; arXiv: physics/0507007.
15. Robitaille P.M.L. Blackbody radiation and the carbon particle. *Prog. in Phys.*, 2008, v. 3, 36–55.
16. Robitaille P.M.L. A critical analysis of universality and Kirchhoff's law: a return to Stewart's law of thermal emission. *Prog. in Phys.*, 2008, v. 3, 30–35; arXiv: 0805.1625.
17. Robitaille P.M.L. Kirchhoff's law of thermal emission: 150 years. *Prog. in Phys.*, 2009, v. 4, 3–13.
18. COBE website, http://lambda.gsfc.nasa.gov/product/cobe
19. WMAP website, http://map.gsfc.nasa.gov
20. Robitaille P.-M.L. WMAP: A radiological analysis. *Prog. in Phys.*, 2007, v. 1, 3–18.
21. Smoot G. and Davidson K. Wrinkles in time: witness to the birth of the Universe. Harper Perennial, New York, N.Y., 1993.
22. Mather J.C. and Boslough J. The very first light. Basic Books, New York, N.Y., 1996.
23. Mather J.C. COBE-explorer of the primeval explosion. *Astronautics & Aeronautics*, 1978, v. 16, 60–66.
24. NASA. Redesign of the Cosmic Background Explorer (COBE), Academy of Program/Project & Engineering Leadership (available online through NASA).
25. Mather J.C., Toral M., Hemmati H. Heat trap with flare as multimode antenna. *Appl. Optics*, 1986, v. 25(16), 2826–2830.
26. Milan L.J. Test facility requirements for the thermal vacuum thermal balance test of the cosmic background explorer. *Journal IES*, 1991, March/April, 27–33.
27. Mosier C.L. Thermal design of the cosmic background explorer cryogenic optical assembly. *AIAA*, *Aerospace Sciences Meeting*, 29th, Reno, NV, Jan. 7–10, 1991, 1–6.
28. Coladonato R.J., Irish S.M, and Mosier C.L. Cryogenic Optical Assembly (COA) cooldown analysis for the Cosmic Background Explorer (COBE). *Third Air Force/NASA Symposium on Recent Advances in Multidisciplinary Analysis and Optimization*, 1990, 370–377.
29. Hagopian J.G. FIRAS optical alignment and performance during vibration qualification and cryogenic cycling. *Cryogenic Optical Systems and Instruments III*: Proceedings of the SPIE, 1989, v. 973, 117–131.
30. Barney R.D. and Magner T.J. FIRAS wire grid characterization techniques. *Cryogenic Optical Systems and Instruments III*: Proceedings of the SPIE, 1989, v. 973, 139–146.
31. Serlemitos A.T. Flight worthy infrared bolometers with high throughput and low NEP. *Cryogenic and Optical Systems III*: *Proceedings of the SPIE*, 1989, v. 973, 314–321.
32. Mather J.C., Cheng E.S., Eplee R.E., Isaacman R.B., Meyer S.S., Shafer R.A., Weiss R., Wright E.L., Bennett C.L., Boggess N., Dwek E., Gulkis S., Hauser M.G., Janssen M., Kelsall T., Lubin P.M., Moseley S.H., Murdock T.L., Silverberg R.F., Smoot G.F., and Wilkinson D.T. A preliminary measurement of the cosmic microwave background spectrum by the cosmic background explorer (COBE) satellite. *Astrophys. J.*, 1990, v. 354, L37–L40.
33. Mather J.C., Fixsen D.J., and Shafer R.A. Design for the COBE Far Infrared Absolute Spectrophotometer (FIRAS). *Proc. SPIE*, 1993, v. 2019, 168–179; http://lambda.gsfc.nasa.gov/data/cobe/firas/doc/FES4_APP_B.PS
34. Cheng E.S. Far-infrared cosmology measurements — the FIRAS spectrum and other curious results. *Astronomical Soc. Pac. Conf. Ser. Observational Cosmology*, 1993, v. 51, 501–511.
35. Mather J.C., Cheng E.S., Cottingham D.A., Eplee R.E., Fixsen D.J., Hewagama T., Isaacman R.B, Jensen K.A., Meyer S.S., Noerdlinger P.D., Read S.M., Rosen L.P., Shafer R.A., Wright E.L., Bennett C.L., Boggess N.W., Hauser M.G., Kelsall T., Moseley S.H., Silverberg R.F., Smoot G.F., Weiss R, and Wilkinson D.T. Measurement of the cosmic microwave background spectrum by the COBE FIRAS Instrument. *Astrophys. J.*, 1994, v. 420, 439–444.

36. Fixsen D.J.,Cheng E.S., Cottingham D.A., Eplee R.E., Isaacman R.B., Mather J.C., Meyer S.S., Noerdlinger P.D., Shafer R.A., Weiss R., Wright E.L., Bennett C.L., Boggess N.W., Kelsall T., Moseley S.H., Silverberg R.F., Smoot G.F., and Wilkinson D.T. Cosmic microwave background dipole spectrum measured by COBE FIRAS. *Astrophys. J.*, 1994, v. 420, 445–449.
37. Wright E.L., Mather J.C., Fixsen D.J., Kogut A., Shafer R.A., Bennett C.L., Boggess N.W., Cheng E.S., Silverberg R.F., Smoot G.F., and Weiss R. Interpretation of the COBE FIRAS CMBR spectrum. *Astrophys. J.*, 1994, v. 420, 450–456.
38. Fixsen D.J., Cheng E.S., Cottingham D.A., Eplee R.E., Hewagama T., Isaacman R.B, Jensen K.A., Mather J.C., Massa D.L., Meyer S.S., Noerdlinger D.P., Read S.M., Rosen L.P., Shafer R.A., Trenholme A.R., Weiss R., Bennett C.L., Boggess N.W., Wilkinson D.T., and Wright E.L. Calibration of the COBE FIRAS instrument. *Astrophys. J.*, 1994, v. 420, 457–473.
39. Fixsen D.J., Cheng E.S., Gales J.M, Mather J.C., and Shafer R.A., and Wright E.L. The cosmic microwave background spectrum from the full COBE FIRAS data set. *Astrophys. J.*, 1996, v. 473, 576–587.
40. Brodd S., Fixsen D.J., Jensen K.A., Mather J.C., and Shafer R.A. Cosmic background explorer (COBE) Far Infrared Absolute Spectrophotometer (FIRAS) Explanatory Supplement. NASA, 1997; lambda.gsfc.nasa.gov/data/cobe/firas/doc/FES4_ABSPREF.PS
41. Fixsen D.J., Dwek E., Mather J.C., Bennett C.L., Shafer R.A. The spectrum of the extragalactic far-infrared background from the COBE FIRAS observations. *Astrophys. J.*, 1998, v. 508, 123–128.
42. Mather J.C., Fixsen D.J., Shafer R.A., Mosier C., and Wilkinson D.T. Calibrator design for the COBE far infrared absolute spectrometer (FIRAS). *Astrophys. J.*, 1999, v. 512, 511–520.
43. Fixsen D.J. and Mather J.C. The spectral results of the far-infrared absolute spectrophotometer instrument on COBE. *Astrophys. J.*, 2002, v. 581, 817–822.
44. Wright E. Cosmic microwave background. Encyclopedia of Astronomy and Astrophysics (Paul Murdin, Ed.), Institute of Physics Publishing, Bristol, U.K., 2001, v. 1, 524–530.
45. Boggess N.W., Mather J.C., Weiss R., Bennett C.L., Cheng E.S., Dwek E., Gulkis S., Hauser M.G., Janssen M.A., Kelsall T., Meyer S.S., Moseley S.H., Murdock T.L., Shafer R.A., Silverberg R.F., Smoot G.F., Wilkinson D.T., and Wright E.L. The COBE mission: its design and performance two years after launch. *Astrophys. J.*, 1992, v. 397, 420–429.
46. Smoot G., Bennett C., Weber R., Maruschak J., Ratliff R., Janssen M., Chitwood J., Hilliard L., Lecha M., Mills R., Patschke R., Richards C., Backus C., Mather J., Hauser M., Weiss R., Wilkinson D., Gulkis S., Boggess N., Cheng E., Kelsall T., Lubin P., Meyer S., Moseley H., Murdock T., Shafer R., Silverberg R., and Wright E. COBE Differential Microwave Radiometers: Instrument design and implementation. *Astrophys. J.*, 1990, v. 360, 685–695.
47. Smoot G.F., Bennett C.L., Kogut A., Wright E.L., Aymon J., Boggess N.W., Cheng E.S., de Amici G., Gulkis S., Hauser M.G., Hinshaw G., Jackson P.D., Janssen M., Kaita E., Kelsall T., Keegstra P., Lineweaver C., Loewenstein K., Lubin P., Mather J., Meyer S.S., Moseley S.H., Murdock T., Rokke L., Silverberg R.F., Tenorio L., Weiss R., and Wilkinson D.T. Structure in the COBE differential microwave radiometer first-year maps. *Astrophys. J. Letters*, 1992, v. 396(1), L1–L5.
48. Bennett C.L., Kogut A., Hinshaw G., Banday A.J., Wright E.L., Gorski K.M., Wilkinson D.T., Weiss R., Smoot G.F., Meyer S.S., Mather J.C., Lubin P., Loewenstein K., Lineweaver C., Keegstra P., Kaita E., Jackson P.D., and Cheng E.S. Cosmic temperature fluctuations from two years of COBE differential microwave radiometers observations. *Astrophys. J.*, 1994, v. 436, 423–442.
49. Bennett C.L., Banday A.J., Gorski K.M., Hinshaw G., Jackson P., Keegstra P., Kogut A., Smoot G.F., Wilkinson D.T., and Wright E.L. Four-Year COBE DMR Cosmic Microwave Background Observations: Maps and Basic Results. *Astrophys. J.*, 1996, v. 464, L1–L4 and plates L1–L3.
50. Hoyle F. A new model for the expanding universe. *Monthly Not. Roy. Astron. Soc.*, 1948, v. 108(5), 372–382.
51. Bondi H. and Gold T. The steady-state theory of the expanding universe. *Monthly Not. Roy. Astron. Soc.*, 1948, v. 108(3), 252–270.
52. Lemaitre G. Un univers homogène de masse constante et de rayon croissant, rendant compte de la vitesse radiale des nébuleuses extragalactiques. *Annales de la Société scientifique de Bruxelles*, 1927, v. 47, 49–59.
53. Guth A.H. Inflation and the new era of high precision cosmology. *MIT Physics Annual*, 2002, 28–39.
54. Smoot G.F. Our age of precision cosmology. *Proceedings of the 2002 International Symposium on Cosmology and Particle Astrophysics* (CosPA 02), X.G. He and K.W. Ng, Editors, World Scientific Publications, London, U.K., 2003, 314–326.
55. Danese L. and Partidge R.B. Atmospheric Emission Models: Confrontation between Observational Data and Predictions in the 2.5–300 GHz Frequency Range. *Astrophys. J.*, 1989, v. 342, 604–615.
56. Partridge R.B. 3 K: the Cosmic Microwave Background Radiation. Cambridge University Press, Cambridge, 1995, p. 103–160.
57. Lay O.P and Halverson N.W. The Impact of Atmospheric Fluctuations on Degree-Scale Imaging of the Cosmic Microwave Background. *Astrophys. J.*, 2000, v. 543, 787–798.
58. Planck M. The theory of heat radiation. P. Blakiston's Son & Co., Philadelphia, PA, 1914.
59. Robitaille P.-M.L. The solar photosphere: evidence for condensed matter. *Prog. in Phys.*, 2006, v. 2, 17–21.
60. Sabins F.F. Remote sensing: principles and applications. W. H. Freeman and Company, San Francisco, CA, 1978.
61. Lillesand T.M., Kiefer R.W., and Chipman J.W. Remote sensing and image interpretation (6th Edition). John Wiley and Sons, Hoboken, N.J., 2008.
62. Ulaby F.T., Moore R.K., and Fung A.K. Microwave remote sensing active and passive — Volume 2: Radar remote sensing and surface scattering and emission theory. London, Addison-Wesley Publishing Company, 1982, p. 880–884.

63. Maréchal Y. The hydrogen bond and the water molecule: the physics and chemistry of water, aqueous and bio-media. Elsevier, Amsterdam, 2007.
64. Dyke T.R. and Muenter J.S. Microwave spectrum and structure of hydrogen bonded water dimer. *J. Chem. Phys.*, 1974, v. 60, 2929–2930.
65. Dyke T.R., Mack K.M., and Muenter J.S. The structure of water dimer from molecular beam electric resonance spectroscopy. *J. Chem. Phys.*, 1977, v. 66, 498–510.
66. Smith J.D., Cappa C.D., Wilson K.R., Messer B.M., Cohen R.C., and Saykally R.J. Energetics of hydrogen bond network rearrangements in liquid water. *Science*, 2004, v. 306, 851–853.
67. Weiss R. Measurements of the cosmic background radiation. *Ann. Rev. Astron. Astrophys.*, 1980, v. 18, 489–535.
68. Matsumoto T., Hayakawa S., Matsuo H., Murakami H., Sato S., Lange A.E., and Richards P.L. The submillimeter spectrum of the cosmic background radiation. *Astrophys. J.*, 1988, v. 329, 567–571.
69. Woody D.P. An observation of the submillimeter cosmic background spectrum. University of California, Berkeley, 1975.
70. Singal J., Fixsen D.J., Kogut A., Levin S., Limon M., Lubin P., Mirel P., Seiffert M. Villela T., Wollack E. and Wuensche C.A. The ARCADE 2 instrument. arXiv: 0901.0546.
71. 71.Kogut A., Fixsen D.J., Levin S.M., Limon M., Lubin P.M., Mirel P., Seiffert M., Singal J., Villela T., Wollack E., and Wuensche C.A. ARCADE 2 observations of galactic radio emission. arXiv: 0901.0562.
72. Atkinson N. Cosmic radio noise booms six times louder than expected. Universe Today, January 7, 2000, http://www.universetoday.com/2009/01/07/cosmic-radio-noise-booms-six-times-louder-than-expected/
73. Mather J.C. Far infrared spectrometry of the Cosmic Background Radiation. University of California, 1974.
74. Wilkinson D. The microwave background anisotropies: observations. *PNAS*, 1998, v. 95(1), 29–34.
75. Harris L. The optical properties of metal blacks and carbon blacks. MIT and The Eppley Foundation for Research, Monograph Ser. 1, New Port, R.I., Dec. 1967.
76. Harris L., McGuiness R.T., and Siegel B.M. The preparation and optical properties of gold black. *J. Opt. Soc. Am.*, 1948, v. 38, 582.
77. Emerson and Cuming Microwave Products (Canton, MA). Technical Bulletin 2–6 (revised).
78. Emerson and Cuming Microwave Products. Technical Reference: ECCOSORB® CR Two-Part Castable Load Absorber Series. http://www.eccosorb.com/file/958/cr.pdf
79. Hemmati H., Mather J.C., and Eichhorn W.L. Submillimeter and millimeter wave characterization of absorbing materials. *Appl. Optics*, 1985, v. 24, 4489–4492.
80. Touloukian Y.S. and DeWitt D.P. Thermal radiative properties of nonmetallic solids. Vol. 8. In: *Thermophysical Properties of Matter*, IFI/Plenum, New York, N.Y., 1972.
81. Kraus J.D. Antennas. McGraw-Hill Book Company, New York, N.Y., 1988.
82. Balanis C. Modern antenna handbook. John Wiley and Sons, Inc., Hoboken, N.J., 2008.
83. Johnson R.C. Antenna engineering handbook. McGraw-Hill Company, New York, N.Y., 1993.
84. Shen Z. and Feng C. A new dual-polarized broadband horn antenna. *IEEE Ant. Wireless Prop. Lett.*, 2005, v. 4, 270–273.
85. Bruns C., Leuchtmann P., and Vahldieck R. Analysis and simulation of a 1–18 GHz broadband double-ridged horn antenna. *IEEE Trans. Electromagn. Comp.*, 2003, v. 45(1), 55–60.
86. PLANCK website, http://www.rssd.esa.int/index.php?project=PLANCK&page=index.
87. Bard S., Stein J., and Petrick S.W. Advanced radiative cooler with angled shields. Spacecraft radiative transfer and temperature control (T.E. Horton, Ed). *Prog. Astronautics & Aeronautics*, 1982, v. 83, 249–258.
88. Taylor J.R. An introduction to error analysis: the study of uncertainties in physical measurements. University Science Books, Mill Valley, CA, 1982.
89. Giorgi P.G. Influence of the angular response on Fourier absolute spectrometry the case of COBE-FIRAS. *Infrared Phys. Tech.*, 1995, v. 36, 749–753.
90. Battistelli E.S., Fulcoli V., and Macculi C. The CMBR spectrum: new upper limits for the distortion parameters y and μ. *New Astronomy*, 2000, v. 5, 77–90.
91. Salvatera R. and Burigana C. A joint study of early and late spectral distortions of the cosmic microwave background and of the millimetric foreground. *Mon. Not. Royal Astron. Soc.*, 2002, v. 336(2), 592–610.

Active Galactic Nuclei: the Shape of Material Around Black Holes and the Witch of Agnesi Function. Asymmetry of Neutrino Particle Density

Gary C. Vezzoli

Department of Science and Mathematics, Lebanon College, Hanover Street, Lebanon, NH 03766, USA
Senior Research Consultant Physicist, Institute for the Basic Sciences, West Windsor, VT 05089, USA

E-mail: vezzoli2005@yahoo.com

A mathematical representation is given and physically described for the shape of the very hot material that immediately surrounds a black hole and the warm material located at a greater distance from the black hole, as related to active galactic nuclei. The shape of the material surrounding the black hole is interpreted in terms of asymmetry of the neutrino flux. Detailed experimental measurements on radioactive decay influenced by astrophysical events are given to support this interpretation.

1 Introduction

Recent work [1] that examined over 200 active galactic nuclei has shown that all have a common shape of the material surrounding the black hole core, and that this shape seems to be independent of the size of the black hole. The Active galactic nuclei (AGN) are cores of galaxies that are energized by disks of hot material that act as ingress/feeder to supermassive black holes. the shape of the hot material that surrounds the black hole was inferred from the observation of x-rays that emanate from very hot material that is close to the black hole, and from infra-red radiation that derives from warm material much further from the core of the black hole.

Through comparing the ratio of x-rays to infrared radiation, the contour shape of the black hole is indirectly mapped [1]. The results are shown in Fig. 1. Inspection of the inferred topology of the surrounding material indicates that although approximate symmetry is shown across the vertical axis, the horizontal axis shows no indication whatsoever of mirror plane symmetry, and thus the upper and lower regions of the 2-d projection must derive from very different functional representations. Stars, planets, and moons do not show a significant asymmetry, other than equatorial bulge. The non-symmetry of the material surrounding the black hole appears thus at first surprising, however, when considered in terms of a collision-induced gravity model [2], the asymmetry could be hypothesized to be a consequence of observing the black hole from a location closer to the centre of the universe where the neutrino flux density is far greater than at position coordinates that are associated with the expansion of the periphery region of the universe, even though that locus of positions is considered unbounded. Asymmetries, such as shown in Fig. 1 are generally thought to be associated with tidal effects — and in the case at hand, this would mean gravitational interactions, such as a form of lensing. Although there is a consideration of the red shift associated with the receding of the galaxies, the cores of which are powered by disks of very hot material "feeding" the supper massive black hole, I do not think that the asymmetry shown in Fig. 1 arises purely from considerations of Relativity, but instead arises at least to some significant level from collision criteria [2].

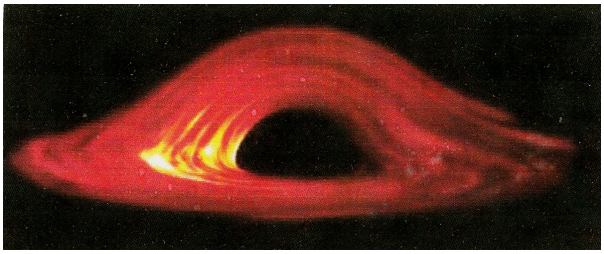

Fig. 1: Material shape near black hole. Courtesy of Anna Morton, moderator of 4D WorldX Yahoo Science Groups. See [1].

2 Analysis and interpretation

The event horizon associated with a black hole refers to the surface that surrounds the black hole, having the property that any visible light cannot escape from the super dense mass because of the strength of the gravitational field [3]. In terms of collision-induced gravity, the term "field" is *not* employed because gravity is considered to be particle-based and the escape-inability of photons at energies less than x-rays is due the increase in collision cross-section between neutrinos and photons that accompanies the super dense packing of mass in a black hole that has developed from a neutron star. The accretion disc of a black hole refers to how accretion onto a neutron star takes place from from a matter input from the Roche lobe of a primary star in the binary system. This passing of matter when occurring from the primary to the secondary star through a Lagrangian point [4] establishes a non-symmetry, but of a different form than that of the black hole shown in Fig. 1, yet these asymmetries may be ultimately related through the physical processes associated with the involvement of the black hole. The vertical asymmetry of the material that surrounds the black hole may also arise from the phenomena that are associated with the periodic ejecta of

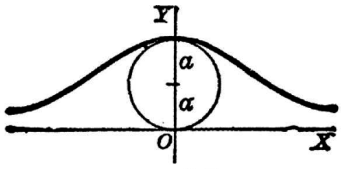

$$y = \frac{8a^3}{x^2 + 4a^2}$$

$$\begin{cases} x = 2a \cot \phi \\ y = 2a \sin^2 \phi \end{cases}$$

Fig. 2: The Witch of Agnesi function.

material from the black hole, which may be influenced by the magnetic properties of the super dense collapsed star. The comparatively slight asymmetry in the horizontal direction must relate to inhomogeneous temperatures and non-isotropic mass distributions of the black hole because of specific local conditions at the $xyzt$ spatial-temporal location of the highly dense aggregating of matter.

The 2-d geometry shown in Fig. 1 above the horizontal axis that passes through the extrema of the inferred contoured distribution of mass, shows the appearance of the mathematical function known as the Witch of Agnesi. (The term "witch" is an involvement of a misnomer, caused by an incorrect translation of the work of Maria Agnesi who developed the function geometrically in 1768). The Agnesi function (Fig. 2) is generally given by, $y = [(8a^3)/(x^2 + 4a^2)]$, where a is the radius of the circle that is utilized to geometrically form the functional curve. In polar coordinates the Agnesi function is given by $x = 2a \cot \phi$, and $y = 2 \sin^2 \phi$. The function can be generated geometrically by rotating the radius of the circle whereby the y-coordinate of the function is the y-value of the radial vector as it sweeps the associated circle, and the x-coordinate is the x-value of the ordered pair that represents the intersection of the extrapolation of the radial vector with the line, $y = a$. Although many world class mathematicians explored the geometric development of this function, including Fermat, no application in astrophysics to the author's knowledge was established for what became known as the Witch of Agnesi function, until now — general applications of the function being confined to probability theory.

Some properties of the Agnesi function are associated with gravitational criteria, such as the x-squared term appearing in the denominator, and suggestive of an inverse square relationship, which in Newtonian gravity derives from Newton's postulate of a central force, which he interpreted from Kepler's First Law of Planetary Action-namely that the orbits of the planet must be elliptical from consideration of years of visual data of Tycho Brahe. The inverse square relationship in the collision-induced gravity model/theory derives from the properties of a flux, as in the photon inverse-square light intensity fall-off, or the equivalent for the distance dependency of the amplitude/intensity of magnetic or electrostatic properties. The relationship of the sweeping rotating radius of the function-forming circle, and its extension to intersect the line

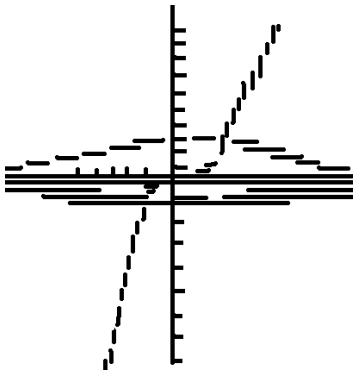

Fig. 3: Representation of the shape of material near a black hole using Agnesi function contours and quadratic function.

$y = a$ can be arguably topologically associated with the notion of accretion and event horizon, and *continuous* processes. The asymptotes of the function (the positive and negative x-axes) relate to the convergence of the shape of the constituent material as temperature decreases because of distance from the "donut" core of the black hole.

The region of Fig. 1 below the horizontal axis can in 2-d projection be well represented by a wide parabola that opens upward. Thus the combined representation of the 2-d geometry shown in Fig. 1 requires the use of a two-function coalescence, and implies the involvement of two different physical phenomena, whereby the quadratic is typically associated with gravitational interactions but the Agnesi function is not.

Using the Agnesi function, and varying the value of the radius, a, combined with the parabola, $y = ax^2 - k$, where a is a very small positive constant $\ll 1$, the contoured representation shown in Fig. 3 is readily developed. The knee shaped curve given also in Fig. 3 represents the calculation of volume of integration of the region surrounding the black hole as a function of the position coordinate, x, showing a threshold effect above which the volume increases rapidly with high slope. The volume function involves an arc tangent term which which is consistent with involvement of an event horizon.

It has been proposed [5] that when emission from an inner accretion disk around a black hole is occulted by a companion star, the observed light curve becomes asymmetric at ingress and egress on a time scale of 0.1–1 sec. The light-curve analysis is claimed [5] to provide a means of verifying the relativistic properties of the accretion flow which is based on both the Special Relativity and General Relativity that is associated with black holes. It is reported [5] that the "skewness" for the eclipsing light curve is approximately zero for what are called slim disks because the innermost part is self-occulted by the outer rim of the disk. This self occulting is a very important property of the black hole, yet these criteria do not uniquely and exclusively seem capable of explaining the major asymmetry shown in the geometry inferred from the x-ray and infra-red data [1] given in Fig. 1.

1	425
2	415
2	390
4	462
5	420
6	420
7	405
8	406
9	421
10	429
11	410
12	415
13	392
14	420
15	430
16	412
17	411
18	418
19	420
20	410
21	391
22	420
23	440
24	421
25	395
26	421
27	422
28	437
29	437
30	402
31	404
32	402
33	430

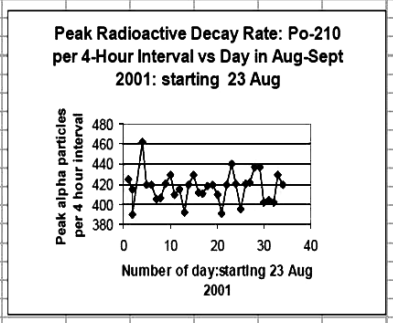

Fig. 4: Radioactive decay data for Po-210 during August-September 2001 measured at Harvard University using the Rad-7 solid-state detector.

On the other hand, it has been reported [6] that propagation of fermions in curved space-time generates gravitational interaction due to the coupling of its spin with space time curvature connection, and causes a CPT violating term in the Lagrangian, generating an asymmetry between the left-handed and the right-handed partners under the CPT transformation. (CPT refers to charge conjugation, space reversal, and time interval, and thus deals with parity). It is interpreted [6] that in the case of neutrinos this property can generate neutrino asymmetry in the Universe, causing the dispersion energy relation for the neutrino and its anti-neutrino to be different giving rise to differences in their number density, and associated with the left-hand helicity of the neutrino. These effects may have an influence in contributing to the asymmetry shown in Fig. 1. It has also been shown [7] that particle interactions in the black-hole accretion disks cause an excess production of positrons as compared to electrons, however, this disparity alone, without emission directionality considerations, does not constitute a non-conservation of parity.

Although the behaviour of each type of galaxy or AGN is *dependent* upon the angle of observation relative to the accretion plane of the black hole core, the asymmetry shown in Fig. 1 is common to all 200 AGN's that were studied in [1], yet the angles of observation relative to the accretion zones had to be different, and the azimuths from the observation coordinates also had to be different.

Our own work [8] has suggested that near the periphery of the current universe, gravitational interactions must have a net repulsive, rather than attractive, dependence — this owing to the far lower neutrino flux in the far distant regions of the universe ($\sim 10^{50}$ km). Thus, though arguably at very small length scales ($\ll 0.1$ mm), gravitational interactions may be described by an inverse fourth dependence [9], and at typical solar system and galactic length scales by inverse square dependence, yet at length scales of 10^n km (where $n > 40$), the dependence is likely *not* to be attractive at all, and instead repulsive near the outer zones of the universe. Thus, relative to the line of centres (a curved Riemannian arc) of the earth born measurement laboratory and the very distant black holes, the neutrino flux that is emanating from the outer regions of the universe, and opposing the escape of both x-rays and infra-red radiation toward the observer, has a higher particle density, than the neutrino flux that is *opposing* (due to collisions and associated net exchange of total momenta) the escape of electromagnetic radiation in the direction of the periphery of the universe. This higher level of particles per square centimetre per second escaping toward the periphery of the universe diffuses in curved directions because of the collision basis of gravity, and the net result contributes to the asymmetry detected by the observer, as in Fig. 1, and shown functionally in Figs. 2 and 3.

3 Supporting evidence for the significance of the neutrino flux

In a work previously published in this journal [10] I presented the explanation of the physical cause of the decades of radioactive decay data histograms determined by Shnoll et al. [11–13] which reported characteristic histograms for the decay of Pu-239 which were periodic over a 24 h interval (the solar day, thus the spin of the Earth), a ∼28 day interval (the lunar month, thus the period of the Moon), and the sidereal year, and also reported characteristic histograms of radioactive decay rate associated with a New Moon and a total solar eclipse. My explanation [10] was based on the Moon and/or the Earth periodically interrupting through scattering and capture some of the neutrinos that emanated from the Sun, and which would have otherwise transferred their momentum to the radioactive source, the decay rate of which was being studied in the experiments (taking place in Moscow, and aboard two research ships that travelled all over the world, including the polar regions). Also, the Sun and Moon intercept neutrinos emanating from deep space.

The Shnoll work [11–13] prompted me to lease a Rad-7 solid-state detector through Dr. Derek Lane-Smith at Durridge Corporation (Bedford, MA) for the purpose of exploring further the Shnoll conclusions. The Rad-7 detector is utilized worldwide as the principle detector of alpha particles decaying from radon gas, and as such is ideally suited also to study the daughter isotopes of Radon. Amongst these, Po-210 has the ideal half life compatible with the purposes of my work. The detector was set up for a 4 week period at the Farlow Herbarium at Harvard University, where I was a research affiliate at the time, conducting work at the Arnold Ar-

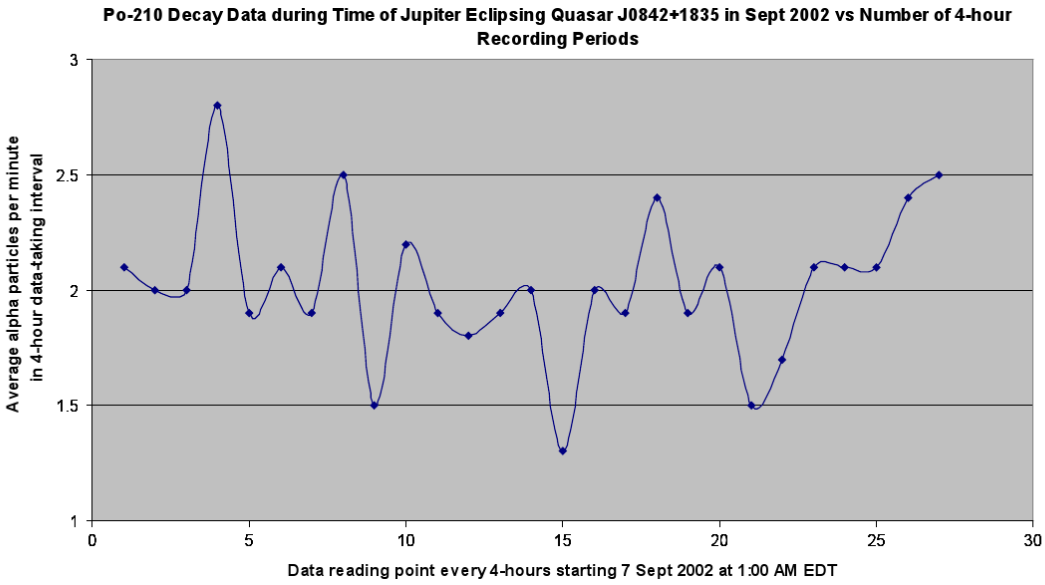

Fig. 5: Data showing three decreases in radioactive decay data of Po-210, 24 hours apart, corresponding to period of 6–10 AM Sept. 7–10 during time interval of Jupiter eclipsing quasar JO842+1835. Reproduced from [16].

boretum, studying the negative geotropism of a heavy vine, Aristolochia macrophylla. Although, conclusions could not be definitely established regarding a diurnal variation of the radioactive decay, a clear peak was observed in the 12:00–4:00 PM time interval on 26 August 2001, far exceeding two-sigma in alpha particles per 4 hour interval. These data are given in Fig. 4, and are digitally reproduced from [14]. It was not until over a year later that I learned that on 26–27 August 2001, radiation from the explosion of supernova SN 2001 dz (in UGC 47) reached the Earth [15]. A supernova explosion is associated with a very significant release of neutrinos, and I interpret that the radioactive alpha particle decay rate peak, shown in Fig. 4, is a consequence of the impingement of the neutrinos, associated with the supernova explosion burst, upon the radioactive isotope source which then pertubed and further de-stabilized a nucleus that was already unstable due to the ratio of neutrons to protons.

During the period September 7–11, 2002, the planet Jupiter eclipsed the deep space quasar JO842+1835, and measurements of alpha particle decay rate were conducted by Dr. Lane-Smith in the Boston area at my request. The averaged data are given in Fig. 5 (digitally reproduced from [16]), showing a decrease in decay rate from approximately 6:00AM to 10:00 AM every 24 hours during the 3-day time interval of the eclipsing event. This variation is attributed to the rotation of the Earth such that once per day Jupiter, interrupted the particle-path from the deep-space quasar to the earth laboratory where the radioactive source was located for the experiment. This interruption of neutrinos, due to the nucleons of Jupiter scattering and inelastically capturing some small, but non-trivial, proportion of particles and/or radiation causes a decrease in radioactive decay rate because of the consequent decrease in the particle flux transferring momentum to the nuclei of Po-210. The x-axis scale is the number of four-hour periods in to the experiment starting at 1:00 AM EDT Sept 7, 2002, and showing decreases at abscissa values of 9, 15, and 21 — these being six 4-hr intervals (24 h) apart.

On 4 Dec 2002, a total solar eclipse occurred, during which the radioactive decay rate of Co-60 was measured at Pittsburg State University in southeastern Kansas [17], and the radioactive decay rate of Po-210 [18] was measured in the Boston area, both at/near the time of totality in southern Australia. The decay data [14] are plotted in Fig. 6, and show dips in decay rate at the time when the umbra of the eclipse was closest to the location of the source isotopes (on the opposite side of the Earth from totality). The inset shows very recent data [19] on the decay of Cs-137 during the annular solar eclipse of 26 January 2009, also in southeast Kansas, at the time when the eclipse was at peak darkness in Australia, also showing a dip in decay rate when the umbra passed closest to the source isotope (time = 4.06 days into the experiment). The 2009 data plot (inset) shows also the envelope of the negative percent changes. The circled data points are analogous to the leading-edge signal and the trailing-edge signal that corresponded to dips in gravity upon first contact and upon last contact associated with the total solar eclipse in China in March 1997 (see [20, 20]). These consistent decreases in decay rate (using three different isotopes) during two different solar eclipses can only be explained by the mass of the Moon and the mass of the Earth interupting the flux of neutrinos coming from the Sun, and thus some of the neutrinos associated with the flux, never reaching the source isotope. Hence these scattered and captured neutrinos do *not* cause any further de-stabilization of the weak cohesive interaction of mesons and of gluons that hold the nucleus intact/together, normally ascribed to the weak force — an internal interaction

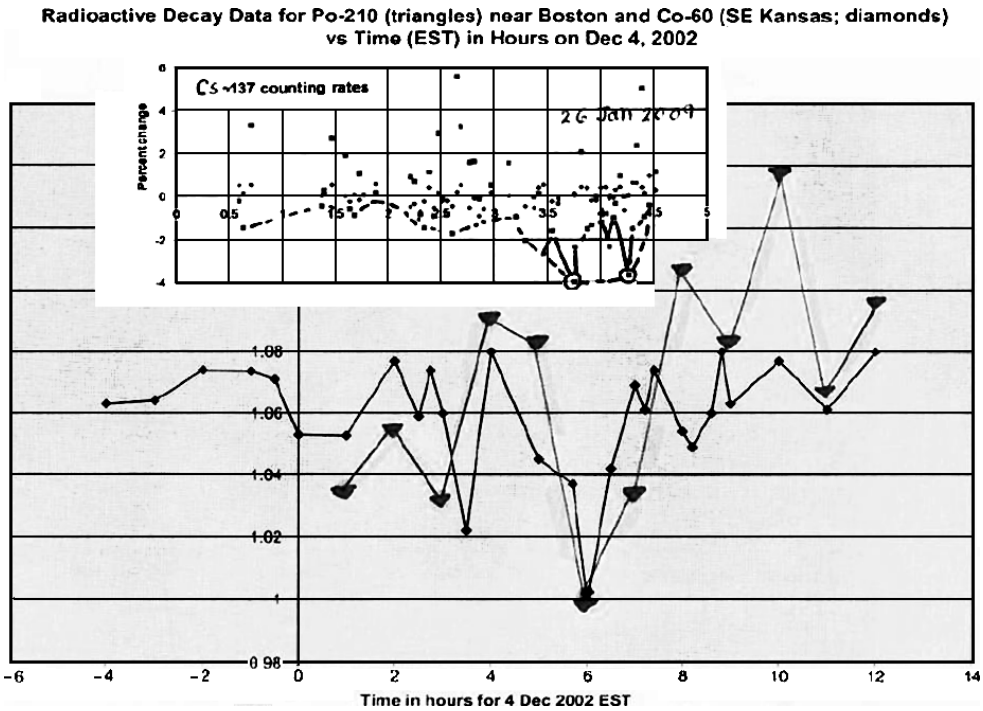

Fig. 6: Decrease in radioactive decay rate for Co-60 and for Po-210 during total eclipse of 4 Dec. 2002, and decrease in radioactive decay rate for Cs-137 during annular solar eclipse of 26 Jan. 2009.

— but now shown to depend upon momenta transfer from externally impinging particles including primarily the muon neutrino and the electron neutrino.

Additional supporting data regarding the significance of the neutrino flux on radioactivity, and highly supportive of my own work and interpretations given herein, are as follows:

1. A major multi-year study by Purdue University researchers at Brookhaven National Laboratory clearly show that the radioactive decay rates of many isotopes correlate very well with the distance of the source isotope from the Sun, as well as changes in radioactive decay rate correlated with major solar flares [22].
2. Positron annihilation measurements [23] that show periodic variation with the phases of the Moon, yielding peaks associated with the New Moon (which approximates a solar eclipse), and troughs correlated with the presence of the Full Moon. The source of positrons in this study was Na-22, and the dependent variable of the experiment measured the yield of molecular iodine (I_2). Thus the peaks in $I_2\%$ correlated with the presence of the New Moon, and hence the interference by the Moon of a flow of particles from the Sun and from space. The data also showed a general trend increase in I_2 production over the course of the months of the experiment (November through February), that the authors tentatively attribute to seasonal changes of the distance between the Earth and the Sun. The exact phenomena causing the peaks is not yet established since in this case an interruption of neutrino flow by the Moon enhances positronium production. It is possible that the peaks are due to more molecular iodine being produced associated with a different collision cross-section caused by change-in-flavor of the neutrino due to collision with nucleons of the Moon.
3. Periodic oscillations have been reported [24] in Pm-142 which show an oscillating sinusoidal decay for electron capture (as contrasted to a conventionally established exponential decay) which the authors attribute to modulations caused by the oscillation of neutrinos between two different mass states (flavors), that of the electron neutrino emitted in the original decay, and that of the muon neutrino which is observed in decays of the muon (a particle 200 times more massive than the electron).
4. The standard deviation of decay rate of radioactive isotopes is periodic with respect to the phases of the Moon, being maximum at Full Moon (whereby external particle impingement from the Sun is unobstructed) and minimum at New Moon (whereby external particle impingement is obstructed by the Moon [25]), akin an eclipse condition.

4 Conclusion

Thus based on all of the above considerations, in the current work, the asymmetry in neutrino flux is identified as the prin-

cipal cause of the non-symmetry shown in Fig. 1, owing to neutrino-photon collisions in the AGN or black hole regimes where the collision cross-sections of neutrinos and photons is many orders of magnitude higher than in the solar system regime. This conclusion is supported by our previous experimental work using both very-close-proximity gravitational pendula, and a magnetic pendulum system, interrogated by laser scattering, showing asymmetry in gravitational particle/wave impinging flux in the X-Y plane as compared to the zed (Z) direction [16].

Note added in proof

Recent work by G. C. Vezzoli and R. Morgan has shown that the 1444 minute annually periodic histogram reported by Shnol and Rubenstein in this journal for the period 24 July 2005 into August correlates with the NASA report of the Sun beginning the occulting of Saturn on that date; and thus also correlates with the work of Vezzoli reporting a dip in gravity on 18 May 2001 when earth, Sun, and Saturn were in syzygy [15]. The Morgan-Vezzoli work will be reported in a Letter-to-the-Editor of this journal authored by Morgan.

Acknowledgements

The author wishes to gratefully acknowledge the assistance, collegial cooperation, fruitful discussions of Prof. C. Blatchley, Dr. Derek Lane-Smith, Dr. William Stanley, Sandra Smalling, and the faculty, administration, staff, and students at Lebanon College.

Submitted on February 24, 2009 / Accepted on June 03, 2009

References

1. McKernan B. American Museum of Natural History and Manhattan Community College, City University of New York, 17 Dec 2008 See also Kaku M. and Thompson J. Beyond Einstein. Anchor, Random House, New York, 1995.
2. Stanley W. and Vezzoli G.C. Induced gravity model based on external impinging neutrinos: calculation of G in terms of collision phenomena and inferences to inertial mass and atomic-quantization. *arXiV: astro-ph/0102109*
3. The new physics. Ed. by P. Davies, Cambridge University Press, 1989.
4. Longair M. *Ibid.*, p.141
5. Watarai K-Y. Ecipsing light-curve asymmetry for black hole accretion flows. *Publ. Astron. Soc. Jpn.*, 2005, v. 57(5), 827–833.
6. Banibrata M. Neutrino asymmetry around black holes. *Modern Physics Letters A*, 2005, v. 20(28), 2145–2155.
7. Akujar C.E. Contribution of black hole accretion disks to symmetric lepton production. *Astrophysics and Space Science*, 1984, v. 100, 1–2, 413–415.
8. Vezzoli G.C. Note on indication of nano local short range order in liquid iron from analysis of recovered products from molten state: geophysical inferences from the materials science, *Mat. Res. Innov.*, 2002, v. 5, 222–225.
9. Hoyle C.D. *Phys. Rev. Lett.*, 2001, v. 86(8), 1418.
10. Vezzoli G.C. On the explaination of the physical cause of the Shnoll characteristic histograms and observed fluctuations. *Progress in Physics*, 2008, v. 2, 158–161.
11. Shnoll S., Kolombet V., Pozharski E., Zenchenko T., Zvereva I., and Konradov A. Realization of discrete states during fluctuations in macroscopic processes. *Physics-Uspekhi*, 1998, v. 162(10), 1139–1140.
12. Shnoll S., Zenchenko T., Zenchenko K., Pozharski E., Kolombet V., and Konradov A. Regular variation of the fine structure of statistical distributions as a consequence of cosmophysical agents. *Physics-Uspekhi*, 2000, v. 43(2), 205–209.
13. Shnoll S., Zenchenko K., Shapovalov S., Gorshkov S., Makarevich., and Troshichev O.A. The specific form of histograms presenting the distribution of data of alpha decay measurements appears simultaneously in the moment of New Moon in different points from Artic to Antartic. arXiv: physics/0412152.
14. Vezzoli G.C. Radioactive decay of Po-210 and Co-60 at two U.S. Observation Stations in the Path of the Umbra/Penumbra of the total eclipse of the Sun of December 4, 2002 in Southern Australia. *Infinite Energy*, 2005, v. 11(61), 48–53.
15. Photograph of this supernova was taken by T. Boles and G. M. Hurst in Basingstoke, England, August 27–28 2001. The supernova SN 2001 is described at website http://www.theastronomer.org/supernovae.html. Code symbols are SN 2001dw-20010825-tb.jpg or SN 2001dz.
16. Vezzoli G.C. Gravitational data during the syzygy of May 18, 2001 and related studies. *Infinite Energy*, 2004, v. 9(53), 18–27.
17. Co-60 was conducted by Professor C. Blatchley at Pittsburg State University during time interval of total solar eclipse of 4 Dec 2002 showing a decrease in decay rate at the time of totality in Southern Australia. Dr. Blatchley asked me to point out in this citation that he is not certain whether his data are supportive of my conclusions because of inherent noise effects and barometric effects that relate to these type of radioactive decay measurements.
18. Po-210 study was conducted by Dr. Derek Lane-Smith of Durridge Corporation in Bedford, MA, during time interval of total solar eclipse of 4 Dec 2002 showing a decrease in radioactive decay rate at the time of totality in southern Australia.
19. Cs-137 decay study was conducted by Professor C. Blatchley at Pittsburg State University during the time interval of the annular solar eclipse of 26 January 2009, indicating a small decrease in decay rate at the time of totality in Australia, corresponding to 4.06 days since the beginning of the experimental measurements. Dr. Blatchley does not share the same opinion as the author regarding the significance of the Cs-137 radioactive decay data as related to the total physics of a solar eclipse, partly because the detected signal does not show a variation exceding two-sigma. However, it must be pointed out that the variation in the measuring of a property such as radioactive decay, or gravity, during totality of a solar eclipse must indeed necessarily

be extremely small. Regarding gravity, this variation was measured to be about 10 microgal (see Refs. 21 and 22).

20. Wang Q., Yang X., Wu C., Guo H., Liu H., and Hua C. Precise measurement of gravity variation during a total solar eclipse. *Phys. Rev. D.*, 2000, v. 62, 041101R.
21. Yang X. and Wang Q. Gravity anomaly during the Mohe total solar eclipse and new constraint on gravitational shielding parameter. *Astrophysics and Space Science*, 2002, v. 285, 245–253; Yang X. Private communications, 2005–2007.
22. Jenskin J., Fischbach E., Buncher J., Gruenwald J., Krause D., and Mattes J. Evidence for correlations between nuclear decay rates and earth-Sun distance. arXiv: 00808.3283.
23. Vikin B.P. Gravitational pertubations as a possible cause for instability in the measurements of positron annihilation. *Progress in Physics*, 2008, v. 2, 76–77.
24. Litvinov Y.A. et al. *Phys. Rev. Lett.*, 2008, v. 664, 162–168.
25. Goleminov N. Private communications, 2006.

Combining NASA/JPL One-Way Optical-Fiber Light-Speed Data with Spacecraft Earth-Flyby Doppler-Shift Data to Characterise 3-Space Flow

Reginald T. Cahill

School of Chemistry, Physics and Earth Sciences, Flinders University, Adelaide 5001, Australia
E-mail: Reg.Cahill@flinders.edu.au

We combine data from two high precision NASA/JPL experiments: (i) the one-way speed of light experiment using optical fibers: Krisher T.P., Maleki L., Lutes G.F., Primas L.E., Logan R.T., Anderson J.D. and Will C.M. *Phys. Rev. D*, 1990, v. 42, 731–734, and (ii) the spacecraft earth-flyby Doppler shift data: Anderson J.D., Campbell J.K., Ekelund J.E., Ellis J. and Jordan J.F. *Phys. Rev. Lett.*, 2008, v. 100, 091102, to give the solar-system galactic 3-space average speed of 486 km/s in the direction RA $= 4.29^{\rm h}$, Dec $= -75.0^{\circ}$. Turbulence effects (gravitational waves) are also evident. Data also reveals the 30 km/s orbital speed of the Earth and the Sun inflow component at 1AU of 42 km/s and also 615 km/s near the Sun, and for the first time, experimental measurement of the 3-space 11.2 km/s inflow of the Earth. The NASA/JPL data is in remarkable agreement with that determined in other light speed anisotropy experiments, such as Michelson-Morley (1887), Miller (1933), Torr and Kolen (1981), DeWitte (1991), Cahill (2006), Munera (2007), Cahill and Stokes (2008) and Cahill (2009).

1 Introduction

In recent years it has become clear, from numerous experiments and observations, that a dynamical 3-space* exists [1, 2]. This dynamical system gives a deeper explanation for various observed effects that, until now, have been successfully described, but not explained, by the Special Relativity (SR) and General Relativity (GR) formalisms. However it also offers an explanation for other observed effects not described by SR or GR, such as observed light speed anisotropy, bore hole gravity anomalies, black hole mass spectrum and spiral galaxy rotation curves and an expanding universe without dark matter or dark energy. Herein yet more experimental data is used to further characterise the dynamical 3-space, resulting in the first direct determination of the inflow effect of the Earth on the flowing 3-space. The 3-space flow is in the main determined by the Milky Way and local galactic cluster. There are also components related to the orbital motion of the Earth and to the effect of the Sun, which have already been extracted from experimental data [1].

The postulate of the invariance of the free-space speed of light in all inertial frames has been foundational to the physics of the 20th Century, and so to the prevailing physicist's paradigm. Not only did it provide computational means essential for the standard model of particle physics, but also provided the spacetime ontology, which physicists claim to be one of the greatest of all discoveries, particularly when extended to the current standard model of cosmology, which assumes a curved spacetime account of not only gravity but also of the universe, but necessitating the invention of dark matter and dark energy.

*The nomenclature *3-space* is used to distinguish this dynamical 3-dimensional space from other uses of the word *space*.

It s usually assumed that the many successes of the resulting Special Theory of Relativity mean that there could be very little reason to doubt the validity of the invariance postulate. However the spacetime formalism is just that, a formalism, and one must always be careful in accepting an ontology on the basis of the postulates, as in the case of the speed of light, because the postulate never stipulated how the speed of light was to be measured, in particular how clock retardation and length contraction effects were to be corrected. In contrast to the spacetime formalism Lorentz gave a different neo-Galilean formalism in which space and time were not mixed, but where the special relativity effects were the consequence of absolute motion with respect to a real 3-space. Recently [3] the discovery of an exact linear mapping between the Minkowski-Einstein spacetime class of coordinates and the neo-Galilean class of time and space coordinates was reported. In the Minkowski-Einstein class the speed of light is invariant by construction, while in the Galilean class the speed is not invariant. Hence statements about the speed of light are formalism dependent, and the claim that the successes of SR implies that the speed of light is invariant is bad logic. So questions about of the speed of light need to be answered by experiments.

There have been many experiments to search for light speed anisotropy, and they fall generally into two classes — those that successfully detected anisotropy and those that did not. The reasons for this apparent disparity are now understood, for it is important to appreciate that because the speed of light is invariant in SR — as an essential part of that formalism, then SR cannot be used to design or analyse data from light speed anisotropy experiments. The class of experiments that failed to detect anisotropy, such as those using vacuum Michelson interferometers, say in the form of reso-

nant vacuum cavities [4], suffer a design flaw that was only discovered in 2002 [5,6]. Essentially there is a subtle cancellation effect in the original Michelson interferometer, in that two unrelated effects exactly cancel unless the light passes through a dielectric. In the original Michelson interferometer experiments the dielectric happened, fortuitously, to be a gas, as in [7–11,15], and then the sensitivity is reduced by the factor $k^2 = n^2 - 1$, where n is the refractive index of the gas, compared to the sensitivity factor $k^2 = 1$ used by Michelson in his calculation of the instrument's calibration constant, using Newtonian physics. For air, with $n = 1.00029$, this factor has value $k^2 = 0.00058$ which explained why the original Michelson-Morley fringe shifts were much smaller than expected. The physics that Michelson was unaware of was the reality of the Lorentz-Fitzgerald contraction effect. Indeed the null results from the resonant vacuum cavities [4] experiments, in comparison with their gas-mode versions, gives explicit proof of the reality of the contraction effect*. A more sensitive and very cheap detector is to use optical fibers as the light carrying medium, as then the cancellation effect is overcome [16]. Another technique to detect light speed anisotropy has been to make one-way speed measurements; Torr and Kolen [12], Krisher *et al.* [18], DeWitte [13] and Cahill [14]. Another recently discovered technique is to use the Doppler shift data from spacecraft earth-flybys [19]. Using the spacetime formalism results in an unexplained earth-flyby Doppler shift anomaly, Anderson *et al.* [20], simply because the spacetime formalism is one that explicitly specifies that the speed of the EM waves is invariant, but only wrt a peculiar choice of space and time coordinates.

Here we combine data from two high precision NASA/JPL experiments: (i) the one-way speed of light experiment using optical fibers: Krisher *et al.* [18], and (ii) the spacecraft earth-flyby Doppler shift data: Anderson *et al.* [20], to give the solar-system galactic 3-space average speed of 486 km/s in the direction RA $= 4.29^{\mathrm{h}}$, Dec $= -75^{\circ}$. Turbulence effects (gravitational waves) are also evident. Various data reveal the 30 km/s orbital speed of the Earth and the Sun inflow component of 615 km/s near the Sun, and 42 km/s at 1AU, and for the first time, experimental evidence of the 3-space inflow of the Earth, which is predicted to be 11.2 km/s at the Earth's surface. The optical-fiber and restricted flyby data give, at this stage, only an average of 12.4 ± 5 km/s for the Earth inflow — averaged over the spacecraft orbits, and so involving averaging wrt distance from earth and RF propagation angles wrt the inflow†. The optical fiber — flyby data is in remarkable agreement with the spatial flow characteristics as determined in other light speed anisotropy experiments, such as Michelson-Morley (1887), Miller (1933), DeWitte (1991), Torr and Kolen (1981), Cahill (2006), Munera (2007), Cahill and Stokes (2008) and Cahill (2009). The NASA data enables an independent calibration of detectors for use in light speed anisotropy experiments and related gravitational wave detectors. These are turbulence effects in the flowing 3-space. These fluctuations are in essence gravitational waves, and which were apparent even in the Michelson-Morley 1887 data [1,2,21].

2 Flowing 3-space and emergent quantum gravity

We give a brief review of the concept and mathematical formalism of a dynamical flowing 3-space, as this is often confused with the older dualistic space and aether ideas, wherein some particulate aether is located and moving through an unchanging Euclidean space — here both the space and the aether were viewed as being ontologically real. The dynamical 3-space is different: here we have only a dynamical 3-space, which at a small scale is a quantum foam system without dimensions and described by fractal or nested homotopic mappings [1]. This quantum foam is not embedded in any space — the quantum foam is all there is and any metric properties are intrinsic properties solely of that quantum foam. At a macroscopic level the quantum foam is described by a velocity field $\mathbf{v}(\mathbf{r}, t)$, where $\mathbf{r}$ is merely a 3-coordinate within an embedding space. This space has no ontological existence — it is merely used to (i) record that the quantum foam has, macroscopically, an effective dimension of 3, and (ii) to relate other phenomena also described by fields, at the same point in the quantum foam. The dynamics for this 3-space is easily determined by the requirement that observables be independent of the embedding choice, giving, for zero-vorticity dynamics and for a flat embedding space‡

$$\left.\begin{aligned} &\nabla \cdot \left(\frac{\partial \mathbf{v}}{\partial t} + (\mathbf{v} \cdot \nabla)\mathbf{v} \right) + \\ &\qquad + \frac{\alpha}{8} \left((\mathrm{tr} D)^2 - \mathrm{tr}(D^2) \right) = -4\pi G \rho \,, \\ &\nabla \times \mathbf{v} = \mathbf{0}, \qquad D_{ij} = \frac{1}{2} \left(\frac{\partial v_i}{\partial x_j} + \frac{\partial v_j}{\partial x_i} \right), \end{aligned}\right\} \quad (1)$$

where $\rho(\mathbf{r}, t)$ is the matter and EM energy densities expressed as an effective matter density. Borehole g measurements and astrophysical blackhole data has shown that $\alpha \approx 1/137$ is the fine structure constant to within observational errors [1, 2, 24, 25]. For a quantum system with mass

*As well the null results from the LIGO-like and related vacuum-mode Michelson interferometers are an even more dramatic confirmation. Note that in contrast the LISA space-based vacuum interferometer does not suffer from the Lorentz contraction effect, and as a consequence would be excessively sensitive.

†A spacecraft in an eccentric orbit about the Earth would permit, using the high-precision Doppler shift technology, a detailed mapping of the 3-space inflow.

‡It is easy to re-write (1) for the case of a non-flat embedding space, such as an S^3, by introducing an embedding 3-space-metric $g_{ij}(\mathbf{r})$, in place of the Euclidean metric δ_{ij}. A generalisation of (1) has also been suggested in [1] when the vorticity is not zero. This vorticity treatment predicted an additional gyroscope precession effect for the GPB experiment, R. T. Cahill, *Progress in Physics*, 2007, v. 3, 13–17.

m the Schrödinger equation is uniquely generalised [24] with the new terms required to maintain that the motion is intrinsically wrt to the 3-space, and not wrt to the embedding space, and that the time evolution is unitary

$$i\hbar\frac{\partial\psi(\mathbf{r},t)}{\partial t}=-\frac{\hbar^2}{2m}\nabla^2\psi(\mathbf{r},t)- -i\hbar\left(\mathbf{v}\cdot\nabla+\frac{1}{2}\nabla\cdot\mathbf{v}\right)\psi(\mathbf{r},t)\,. \tag{2}$$

The space and time coordinates $\{t,x,y,z\}$ in (1) and (2) ensure that the separation of a deeper and unified process into different classes of phenomena — here a dynamical 3-space (quantum foam) and a quantum matter system, is properly tracked and connected. As well the same coordinates may be used by an observer to also track the different phenomena. However it is important to realise that these coordinates have no ontological significance — they are not real. The velocities $\mathbf{v}$ have no ontological or absolute meaning relative to this coordinate system — that is in fact how one arrives at the form in (2), and so the "flow" is always relative to the internal dynamics of the 3-space. A quantum wave packet propagation analysis of (2) gives the acceleration induced by wave refraction to be [24]

$$\mathbf{g}=\frac{\partial\mathbf{v}}{\partial t}+(\mathbf{v}\cdot\nabla)\mathbf{v}+(\nabla\times\mathbf{v})\times\mathbf{v}_R\,, \tag{3}$$

$$\mathbf{v}_R(\mathbf{r}_\circ(t),t)=\mathbf{v}_\circ(t)-\mathbf{v}(\mathbf{r}_\circ(t),t)\,, \tag{4}$$

where $\mathbf{v}_R$ is the velocity of the wave packet relative to the 3-space, and where $\mathbf{v}_\circ$ and $\mathbf{r}_\circ$ are the velocity and position relative to the observer, and the last term in (3) generates the Lense-Thirring effect as a vorticity driven effect. Together (2) and (3) amount to the derivation of gravity as a quantum effect, explaining both the equivalence principle ($\mathbf{g}$ in (3) is independent of m) and the Lense-Thirring effect. Overall we see, on ignoring vorticity effects, that

$$\nabla\cdot\mathbf{g}=-4\pi G\rho-\frac{\alpha}{8}\left((\mathrm{tr}D)^2-\mathrm{tr}(D^2)\right), \tag{5}$$

which is Newtonian gravity but with the extra dynamical term whose strength is given by α. This new dynamical effect explains the spiral galaxy flat rotation curves (and so doing away with the need for "dark matter"), the bore hole g anomalies, the black hole "mass spectrum". Eqn. (1), even when $\rho=0$, has an expanding universe Hubble solution that fits the recent supernovae data in a parameter-free manner without requiring "dark matter" nor "dark energy", and without the accelerating expansion artifact [25,26]. However (5) cannot be entirely expressed in terms of $\mathbf{g}$ because the fundamental dynamical variable is $\mathbf{v}$. The role of (5) is to reveal that if we analyse gravitational phenomena we will usually find that the matter density ρ is insufficient to account for the observed $\mathbf{g}$. Until recently this failure of Newtonian gravity has been explained away as being caused by some unknown and undetected "dark matter" density. Eqn. (5) shows that to the contrary it is a dynamical property of 3-space itself. Here we determine various properties of this dynamical 3-space from the NASA optical-fiber and spacecraft flyby Doppler anomaly data.

Significantly the quantum matter 3-space-induced "gravitational" acceleration in (3) also follows from maximising the elapsed proper time wrt the wave-packet trajectory $\mathbf{r}_\circ(t)$, see [1],

$$\tau=\int dt\sqrt{1-\frac{\mathbf{v}_R^2(\mathbf{r}_\circ(t),t)}{c^2}} \tag{6}$$

and then taking the limit $v_R/c\to 0$. This shows that (i) the matter 'gravitational' geodesic is a quantum wave refraction effect, with the trajectory determined by a Fermat least proper-time principle, and (ii) that quantum systems undergo a local time dilation effect — which is used later herein in connection with the Pound-Rebka experiment. A full derivation of (6) requires the generalised Dirac equation.

3 3-space flow characteristics and the velocity superposition approximation

This paper reports the most detailed analysis so far of data from various experiments that have directly detected the 3-space velocity field $\mathbf{v}(\mathbf{r},t)$. The dynamics in (1) is necessarily time-dependent and having various contributing effects, and in order of magnitude: (i) galactic flows associated with the motion of the solar system within the Milky Way, as well as flows caused by the supermassive black hole at the galactic center and flows associated with the local galactic cluster, (ii) flows caused by the orbital motion of the Earth and of the inflow caused by the Sun, and (iii) the inflow associated with the Earth. An even smaller flow associated with the Moon is not included in the analysis. It is necessary to have some expectations of the characteristics of the flow expected for an earth based observer. First consider an isolated spherical mass density $\rho(r)$, with total mass M, then (1) has a stationary flow solution, for $r>R$, i.e outside of the mass,

$$\mathbf{v}(\mathbf{r})=-\hat{\mathbf{r}}\sqrt{\frac{2GM(1+\frac{\alpha}{2}+\dots)}{r}} \tag{7}$$

which gives the matter acceleration from (3) to be

$$\mathbf{g}(\mathbf{r})=-\hat{\mathbf{r}}\frac{GM(1+\frac{\alpha}{2}+\dots)}{r^2} \tag{8}$$

corresponding to a gravitational potential, via $\mathbf{g}=-\nabla\boldsymbol{\Phi}$,

$$\Phi(\mathbf{r})=-\frac{GM(1+\frac{\alpha}{2}+\dots)}{r}\,. \tag{9}$$

This special case is Newton's law of gravity, but with some 0.4% of the effective mass being caused by the α- dynamics term. The inflow (7) would be applicable to an isolated and stationary sun or earth. At the surface of the Sun

this predicts an inflow speed of 615 km/s, and 42 km/s at the Earth distance of 1AU. For the Earth itself the inflow speed at the Earth's surface is predicted to be 11.2 km/s. When both occur and when both are moving wrt the asymptotic 3-space, then numerical solutions of (1) are required. However an approximation that appears to work is to assume that the net flow in this case may be approximated by a vector superposition [27]

$$\mathbf{v} = \mathbf{v}_{galactic} + \mathbf{v}_{sun} - \mathbf{v}_{orbital} + \mathbf{v}_{earth} + \dots \qquad (10)$$

which are, in order, translational motion of the Sun, inflow into the Sun, orbital motion of the Earth (the orbital motion produces an apparent flow in the opposite direction — hence the -ve sign; see Fig. 4), inflow into the Earth, etc. The first three have been previously determined from experimental data, and here we more accurately and using new data determine all of these components. However this superposition cannot be completely valid as (1) is non-linear. So the superposition may be at best approximately valid as a time average only. The experimental data has always shown that the detected flow is time dependent, as one would expect, as with multi-centred mass distributions no stationary flows are known. This time-dependence is a turbulence effect — it is in fact easily observed and is seen in the Michelson-Morley 1887 data [2]. This turbulence is caused by the presence of any significant mass, such as the galaxy, sun, earth. The NASA/JPL data discussed herein again displays very apparent turbulence. These wave effects are essentially *gravitational waves*, though they have characteristics different from those predicted from GR, and have a different interpretation. Nevertheless for a given flow $\mathbf{v}(\mathbf{r}, t)$, one can determine the corresponding induced spacetime metric $g_{\mu\nu}$ which generates the same matter geodesics as from (5), with the proviso that this metric is not determined by the Hilbert-Einstein equations of GR. Significantly vacuum-mode Michelson interferometers cannot detect this phenomenon, which is why LIGO and related detectors have not seen these very large wave effects.

4 Gas-mode Michelson interferometer

The Michelson interferometer is a brilliant instrument for measuring $\mathbf{v}(\mathbf{r}, t)$, but only when operated in dielectric mode. This is because two different and independent effects exactly cancel in vacuum mode; see [1, 2, 5]. Taking account of the geometrical path differences, the Fitzgerald-Lorentz arm-length contraction and the Fresnel drag effect leads to the travel time difference between the two arms, and which is detected by interference effects*, is given by

$$\Delta t = k^2 \frac{L v_P^2}{c^3} \cos\big(2(\theta - \psi)\big), \qquad (11)$$

*The dielectric of course does not cause the observed effect, it is merely a necessary part of the instrument design physics, just as mercury in a thermometer does not *cause* temperature.

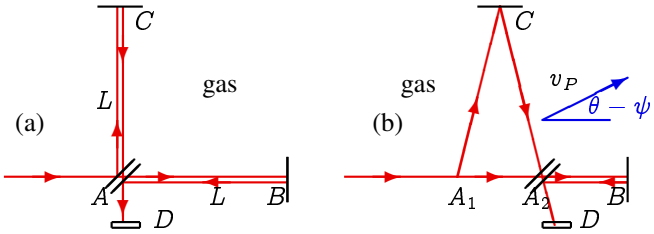

Fig. 1: Schematic diagrams of the gas-mode Michelson Interferometer, with beamsplitter/mirror at A and mirrors at B and C mounted on arms from A, with the arms of equal length L when at rest. D is the detector screen. In (a) the interferometer is at rest in space. In (b) the 3-space is moving through the gas and the interferometer with speed v_P in the plane of the interferometer and direction $\delta = \theta - \psi$ relative to AB arm. Interference fringes are observed at D when mirrors C and D are not exactly perpendicular. As the interferometer is rotated in the plane shifts of the fringes are seen in the case of absolute motion, but only if the apparatus operates in a gas. By measuring fringe shifts the speed v_P may be determined. In general the v_P direction has angle θ wrt the local meridian, and the arm AB has angle ψ relative to the local meridian, so that $\delta = \theta - \psi$ is angle between $\mathbf{v}_P$ and one-arm. The difference in travel times Δt is given in (11), but with temperature changes and non-orthogonal mirrors by (12). In vacuum the fringes do not shift during rotation .

where ψ specifies the direction of $\mathbf{v}(\mathbf{r}, t)$ projected onto the plane of the interferometer, giving projected value v_P, relative to the local meridian, and where $k^2 = (n^2 - 2) \times \times (n^2 - 1)/n$. Neglect of the relativistic Fitzgerald-Lorentz contraction effect gives $k^2 \approx n^3 \approx 1$ for gases, which is essentially the Newtonian theory that Michelson used.

However the above analysis does not correspond to how the interferometer is actually operated. That analysis does not actually predict fringe shifts, for the field of view would be uniformly illuminated, and the observed effect would be a changing level of luminosity rather than fringe shifts. As Michelson and Miller knew, the mirrors must be made slightly non-orthogonal with the degree of non-orthogonality determining how many fringe shifts were visible in the field of view. Miller experimented with this effect to determine a comfortable number of fringes: not too few and not too many. Hicks [22] developed a theory for this effect – however it is not necessary to be aware of the details of this analysis in using the interferometer: the non-orthogonality reduces the symmetry of the device, and instead of having period of 180° the symmetry now has a period of 360°, so that to (11) we must add the extra term $a \cos(\theta - \beta)$ in

$$\Delta t = k^2 \frac{L(1 + e\theta) v_P^2}{c^3} \cos\big(2(\theta - \psi)\big) + \\ + a(1 + e\theta) \cos(\theta - \beta) + f\,. \qquad (12)$$

The term $1 + e\theta$ models the temperature effects, namely that as the arms are uniformly rotated, one rotation taking several minutes, there will be a temperature induced change in the length of the arms. If the temperature effects are linear

in time, as they would be for short time intervals, then they are linear in θ. In the Hick's term the parameter a is proportional to the length of the arms, and so also has the temperature factor. The term f simply models any offset effect. Michelson and Morley and Miller took these two effects into account when analysing his data. The Hick's effect is particularly apparent in the Miller and Michelson-Morley data.

The interferometers are operated with the arms horizontal. Then in (12) θ is the azimuth of one arm relative to the local meridian, while ψ is the azimuth of the absolute motion velocity projected onto the plane of the interferometer, with projected component v_P. Here the Fitzgerald-Lorentz contraction is a real dynamical effect of absolute motion, unlike the Einstein spacetime view that it is merely a spacetime perspective artifact, and whose magnitude depends on the choice of observer. The instrument is operated by rotating at a rate of one rotation over several minutes, and observing the shift in the fringe pattern through a telescope during the rotation. Then fringe shifts from six (Michelson and Morley) or twenty (Miller) successive rotations are averaged to improve the signal to noise ratio, and the average sidereal time noted. Some examples are shown in Fig. 2, and illustrate the incredibly clear signal. The ongoing claim that the Michelson-Morely experiment was a null experiment is disproved. And as well, as discussed in [1, 2, 21], they detected gravitational waves, *viz* 3-space turbulence in 1887. The new data analysed herein is from one-way optical fiber and Doppler shift spacecraft experiments. The agreement between these and the gas-mode interferometer techniques demonstrate that the Fitzgerald-Lorentz contraction effect is a real dynamical effect. The null results from the vacuum-mode interferometers [4] and LIGO follow simply from having $n = 1$ giving $k^2 = 0$ in (11).

5 Sun 3-space inflow from Miller interferometer data

Miller was led to the conclusion that for reasons unknown the existing theory of the Michelson interferometer did not reveal true values of v_P, and for this reason he introduced the parameter k, with $\overline{k}$ herein indicating his numerical values. Miller had reasoned that he could determine both $\mathbf{v}_{galactic}$ and $\overline{k}$ by observing the interferometer-determined v_P and ψ over a year because the known orbital speed of the Earth about the Sun of 30 km/s would modulate both of these observables, giving what he termed an aberration effect as shown in Fig. 11, and by a scaling argument he could determine the absolute velocity of the solar system. In this manner he finally determined that $|\mathbf{v}_{galactic}| = 208$ km/s in the direction $(\alpha = 4^{\mathrm{h}}54^{\mathrm{m}}, \delta = -70^{\circ}33')$. However now that the theory of the Michelson interferometer has been revealed an anomaly becomes apparent. Table 2 shows $v = v_M/k_{air}$, the speed determined using (11), for each of the four epochs. However Table 3 also shows that $\overline{k}$ and the speeds $\overline{v} = v_M/\overline{k}$ determined by the scaling argument are considerably different. We denote by v_M the notional speeds determined from (11) using the Michelson Newtonian-physics value of $k = 1$. The v_M values arise after taking account of the projection effect. That $\overline{k}$ is considerably larger than the value of k_{air} indicates that another velocity component has been overlooked. Miller of course only knew of the tangential orbital speed of the Earth, whereas the new physics predicts that as-well there is a 3-space radial inflow $\mathbf{v}_{sun} = 42$ km/s at 1AU. We can approximately re-analyse Miller's data to extract a first approximation to the speed of this inflow component. Clearly it is $v_R = \sqrt{v_{sun}^2 + v_{orbital}^2}$ that sets the scale, see Fig. 4 and not $v_{orbital}$, and because $\overline{k} = v_M/v_{orbit}$ and $k_{air} = v_M/v_R$ are the scaling relations, then

$$v_{sun} = v_{orbital}\sqrt{\frac{v_R^2}{v_{orbital}^2} - 1} = v_{orbital}\sqrt{\frac{\overline{k}^2}{k_{air}^2} - 1}\,. \quad (13)$$

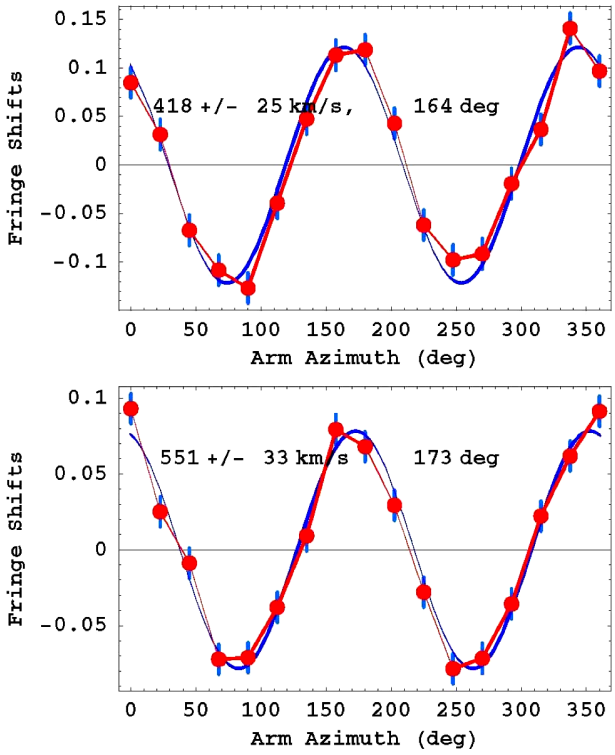

Fig. 2: (a) A typical Miller averaged-data from September 16, 1925, $4^{\mathrm{h}}40'$ Local Sidereal Time (LST) — an average of data from 20 turns of the gas-mode Michelson interferometer. Plot and data after fitting using (12), and then subtracting both the temperature drift and Hicks effects from both, leaving the expected sinusoidal form. The error bars are determined as the rms error in this fitting procedure, and show how exceptionally small were the errors, and which agree with Miller's claim for the errors. (b) Best result from the Michelson-Morley 1887 data — an average of 6 turns, at 7^{h} LST on July 11, 1887. Again the rms error is remarkably small. In both cases the indicated speed is v_P — the 3-space speed projected onto the plane of the interferometer. The angle is the azimuth of the 3-space speed projection at the particular LST. The speed fluctuations from day to day significantly exceed these errors, and reveal the existence of 3-space flow turbulence — i.e gravitational waves.

Epoch 1925/26	v_M	$\overline{k}$	$v = v_M/k_{air}$	$\overline{v} = v_M/\overline{k}$	$v = \sqrt{3}\overline{v}$	v_{sun}
February 8	9.3 km/s	0.048	385.9 km/s	193.8 km/s	335.7 km/s	51.7 km/s
April 1	10.1	0.051	419.1	198.0	342.9	56.0
August 1	11.2	0.053	464.7	211.3	366.0	58.8
September 15	9.6	0.046	398.3	208.7	361.5	48.8

Table 1: The $\overline{k}$ anomaly: $\overline{k} \gg k_{air} = 0.0241$, as the 3-space inflow effect. Here v_M and $\overline{k}$ come from fitting the interferometer data using Newtonian physics (with $v_{orbital} = 30$ km/s used to determine $\overline{k}$), while v and $\overline{v}$ are computed speeds using the indicated scaling. The average of the Sun inflow speeds, at 1AU, is $v_{sun} = 54 \pm 6$ km/s, compared to the predicted inflow speed of 42 km/s from (7). From column 4 we obtain the average galactic flow of $v = 417 \pm 50$ km/s, compared with the NASA-data determined flow of 486 km/s.

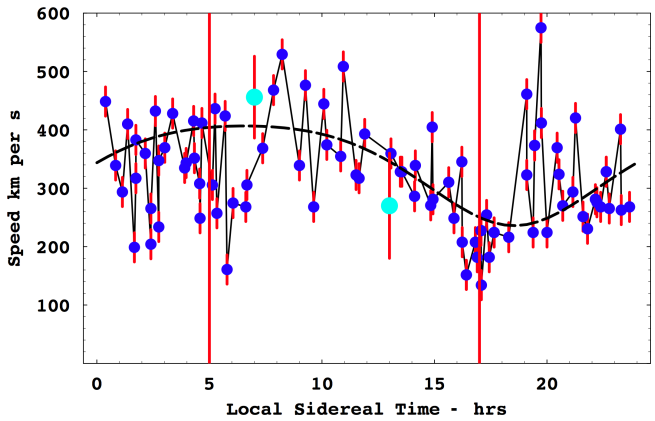

Fig. 3: Speeds v_P, of the 3-space velocity $\mathbf{v}$ projected onto the horizontal plane of the Miller gas-mode Michelson interferometer located atop Mt.Wilson, plotted against local sidereal time in hours, for a composite day, with data collected over a number of days in September 1925, [8]. The data shows considerable fluctuations, from hour to hour, and also day to day, as this is a composite day. The dashed curve shows the non-fluctuating best-fit variation over one day, as the Earth rotates, causing the projection onto the plane of the interferometer of the velocity of the average direction of the space flow to change. The maximum projected speed of the curve is 417 km/s (using the STP air refractive index of $n = 1.00029$ in (11) (atop Mt. Wilson the better value of $n = 1.00026$ is suggested by the NASA data), and the min/max occur at approximately 5hrs and 17hrs local sidereal time (Right Ascension). Note from Fig. 11 and Table 2 that the Cassini flyby in August gives a RA$= 5.15^{\text{h}}$, close to the RA apparent in the above plot. The error bars are determined by the method discussed in Fig. 2. The green data points, with error bars, at 7^{h} and 13^{h} are from the Michelson-Morley 1887 data, from averaging (excluding only the July 8 data for 7^{h} because it has poor S/N), and with same rms error analysis. The fiducial time lines at 5^{h} and 17^{h} are the same as those shown in Figs. 6 and 11. The speed fluctuations are seen to be much larger than the statistically determined errors, confirming the presence of turbulence in the 3-space flow, i.e gravitational waves, as first seen in the Michelson-Morley experiment.

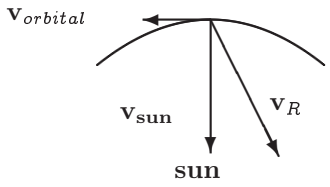

Fig. 4: Orbit of earth about the Sun defining the plane of the ecliptic with tangential orbital velocity $\mathbf{v}_{orbital}$ and the Sun inflow velocity $\mathbf{v}_{sun}$. Then $\mathbf{v}_R = \mathbf{v}_{sun} - \mathbf{v}_{orbital}$ is the velocity of the 3-space relative to the Earth, but not showing the $\mathbf{v}_{galactic}$ contribution.

Using the $\overline{k}$ values in Table 1 and the value* of k_{air} we obtain the v_{sun} speeds shown in Table 1, which give an averaged speed of 54 ± 6 km/s, compared to the predicted inflow speed of 42 km/s. Of course this simple re-scaling of the Miller results is not completely valid because the direction of $\mathbf{v}_R$ is of course different to that of $\mathbf{v}_{orbital}$, nevertheless the Sun inflow speed of $v_{sun} = 54 \pm 5$ km/s at 1AU from this analysis is reasonably close to the predicted value of 42 km/s.

6 Generalised Maxwell equations and the Sun 3-space inflow light bending

One of the putative key tests of the GR formalism was the gravitational bending of light by the Sun during the 1915 solar eclipse. However this effect also immediately follows from the new 3-space dynamics once we also generalise the Maxwell equations so that the electric and magnetic fields are excitations of the dynamical space. The dynamics of the electric and magnetic fields must then have the form, in empty space,

$$\left.\begin{aligned} \nabla \times \mathbf{E} &= -\mu \left(\frac{\partial \mathbf{H}}{\partial t} + \mathbf{v} \cdot \nabla \mathbf{H} \right), \quad \nabla \cdot \mathbf{E} = \mathbf{0}, \\ \nabla \times \mathbf{H} &= \epsilon \left(\frac{\partial \mathbf{E}}{\partial t} + \mathbf{v} \cdot \nabla \mathbf{E} \right), \quad \nabla \cdot \mathbf{H} = \mathbf{0}, \end{aligned}\right\} \tag{14}$$

*We have not modified this value to take account of the altitude effect or temperatures atop Mt.Wilson. This weather information was not recorded by Miller. The temperature and pressure effect is that $n = 1.0 + 0.00029 \frac{P}{P_0} \frac{T_0}{T}$, where T is the temperature in $0\,\text{K}$ and P is the pressure in atmospheres. $T_0 = 273\text{K}$ and $P_0 = 1\text{atm}$. The NASA data implies that atop Mt. Wilson the air refractive index was probably close to $n = 1.00026$.

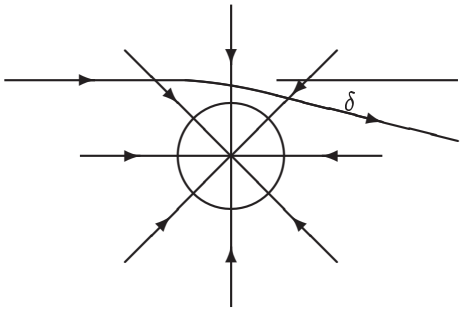

Fig. 5: Shows bending of light through angle δ by the inhomogeneous spatial inflow, according to the minimisation of the travel time in (18). This effect permits the inflow speed at the surface of the Sun to be determined to be 615 km/s. The inflow speed into the Sun at the distance of the Earth from the Sun has been extracted from the Miller data, giving 54 ± 6 km/s.

which was first suggested by Hertz in 1890 [23], but with $\mathbf{v}$ being a constant vector field. Suppose we have a uniform flow of space with velocity $\mathbf{v}$ wrt the embedding space or wrt an observer's frame of reference. Then we can find plane wave solutions for (14):

$$\mathbf{E}(\mathbf{r},t) = \mathbf{E}_0 e^{i(\mathbf{k}\cdot\mathbf{r}-\omega t)} \quad \mathbf{H}(\mathbf{r},t) = \mathbf{H}_0 e^{i(\mathbf{k}\cdot\mathbf{r}-\omega t)} \qquad (15)$$

with

$$\omega(\mathbf{k},\mathbf{v}) = c|\vec{\mathbf{k}}| + \mathbf{v}\cdot\mathbf{k} \quad \text{where} \quad c = 1/\sqrt{\mu\epsilon}\,. \qquad (16)$$

Then the EM group velocity is

$$\mathbf{v}_{EM} = \vec{\nabla}_k\,\omega(\mathbf{k},\mathbf{v}) = c\hat{\mathbf{k}} + \mathbf{v}\,. \qquad (17)$$

So the velocity of EM radiation $\mathbf{v}_{EM}$ has magnitude c only with respect to the space, and in general not with respect to the observer if the observer is moving through space. These experiments show that the speed of light is in general anisotropic, as predicted by (17). The time-dependent and inhomogeneous velocity field causes the refraction of EM radiation. This can be computed by using the Fermat least-time approximation. Then the EM ray paths $\mathbf{r}(t)$ are determined by minimising the elapsed travel time:

$$\tau = \int_{s_i}^{s_f} \frac{ds\left|\dfrac{d\mathbf{r}}{ds}\right|}{|c\,\hat{\mathbf{v}}_R(s) + \mathbf{v}(\mathbf{r}(\mathbf{s}),\mathbf{t}(\mathbf{s})|}\,, \qquad (18)$$

$$\mathbf{v}_R = \left(\frac{d\mathbf{r}}{dt} - \mathbf{v}(\mathbf{r}(\mathbf{t}),\mathbf{t})\right), \qquad (19)$$

by varying both $\mathbf{r}(s)$ and $t(s)$, finally giving $\mathbf{r}(t)$. Here s is a path parameter, and $\mathbf{v}_R$ is the 3-space vector tangential to the path. For light bending by the Sun inflow (7) the angle of deflection is

$$\delta = 2\,\frac{v^2}{c^2} = \frac{4GM(1+\frac{\alpha}{2}+\dots)}{c^2 d} + \dots \qquad (20)$$

where v is the inflow speed at distance d and d is the impact parameter. This agrees with the GR result except for the α correction. Hence the observed deflection of 8.4×10^{-6} radians is actually a measure of the inflow speed at the Sun's surface, and that gives $v = 615$ km/s, in agreement with (7). These generalised Maxwell equations also predict gravitational lensing produced by the large inflows associated with the new "black holes" in galaxies.

7 Torr and Kolen RF one-way coaxial cable experiment

A one-way coaxial cable experiment was performed at the Utah University in 1981 by Torr and Kolen [12]. This involved two rubidium vapor clocks placed approximately 500 m apart with a 5 MHz sinewave RF signal propagating between the clocks via a nitrogen filled coaxial cable buried in the ground and maintained at a constant pressure of $\sim$2 psi. Torr and Kolen observed variations in the one-way travel time, as shown in Fig. 7 by the data points. The theoretical predictions for the Torr-Kolen experiment for a cosmic speed of 480 km/s in the direction ($\alpha = 5^{\mathrm{h}}, \delta = -70^{\circ}$), and including orbital and in-flow velocities, are shown in Fig. 7. The maximum/minimum effects occurred, typically, at the predicted times. Torr and Kolen reported fluctuations in both the magnitude, from 1–3 ns, and time of the maximum variations in travel time, just as observed in all later experiments — namely wave effects.

8 Krisher *et al.* one-way optical-fiber experiment

The Krisher *et al.* one-way experiment [18] used two hydrogen maser oscillators with light sent in each direction through optical fiber of length approximately 29 km. The optical fiber was part of the NASA DSN Deep Space Communications Complex in the Mojave desert at Goldstone, California. Each maser provided a stable 100-MHz output frequency. This signal was split, with one signal being fed directly into one channel of a Hewlett-Packard Network Analyzer. The other signal was used to modulate a laser carrier signal propagated along a 29 km long ultrastable fiber optics link that is buried five feet underground. This signal was fed into the second channel of the other Network Analyzer at the distant site. Each analyzer is used to measure the relative phases of the masers, ϕ_1 and ϕ_2. The data collection began on November 12 1988 at 20:00:00 (UTC), with phase measurements made every ten seconds until November 17 1988 at 17:30:40 (UTC). Figs. 6(a) and (f) shows plots of the phase difference $\phi_1 - \phi_2$ and phase sum $\phi_1 + \phi_2$, in degrees, after removing a bias and a linear trend, as well as being filtered using a Fast Fourier Transform. The data is plotted against local sidereal time. In analysing the phase data the propagation path was taken to be along a straight line between the two masers, whose longitude and latitude are given by $(243^\circ 12' 21''.65,\ 35^\circ 25' 33''.37)$ and $(243^\circ 06' 40''.37,\ 35^\circ 14' 51''.82)$. Fig. 6

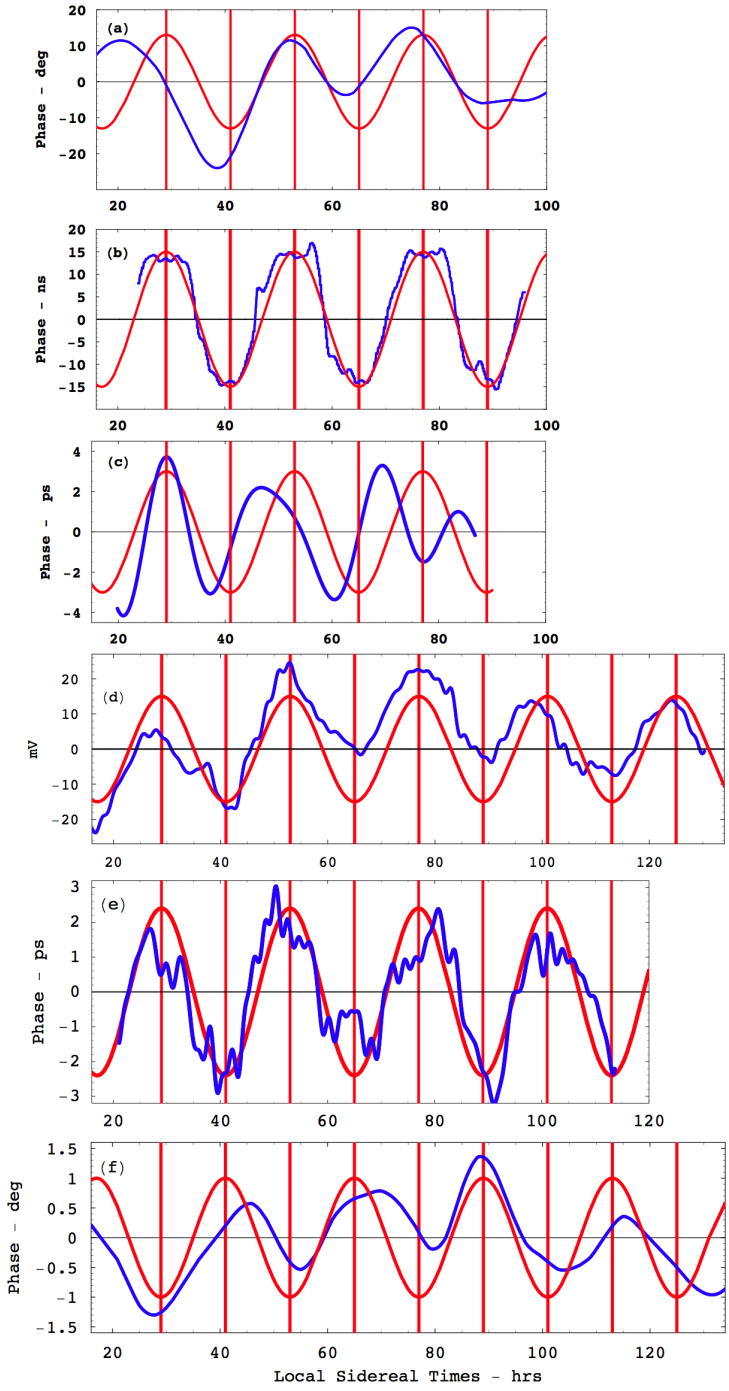

Fig. 6: Data from five different EM speed anisotropy experiments showing earth rotation wrt local preferred frame, as shown by sidereal time phasing, together with wave effects. In all cases a zero bias was removed and low-pass filtering was applied. **(a)**: Krisher [18] optical fiber phase difference data $\phi_1 - \phi_2$, in degrees. **(b)**: DeWitte [13] RF coaxial cable phase data, in ns. The DeWitte cable ran NS. **(c):** Cahill [14] hybrid optical-fiber/RF coaxial-cable data, in ps, from August 2006. Cable ran NS. **(d):** Cahill [16, 17] optical-fiber Michelson interferometer, in photodiode mV, from September 18, 2007. **(e):** Cahill RF coaxial-cable data, in ps, from May 2009. Cable ran NS. **(f)**: Krisher [18] optical fiber phase sum data $\phi_1 + \phi_2$, in degrees. In each case the (red) sinusoidal curves shows the phase expected for a RA of 5^{h}, but with arbitrary magnitudes. The vertical lines are at local sidereal times of 5^{h} and 17^{h}, on successive days, corresponding to the RAs shown in red in Fig. 11. The Krisher data gives a local sidereal time of 4.96^{h}, corresponding to a RA of 6.09^{h} for November — caused by the 42° azimuth angle of the optical fiber to the local meridian. This RA was used in combination with the spacecraft earth-flyby Doppler shift data. Note the amplitude and phase fluctuations in all the data — these are gravitational wave effects.

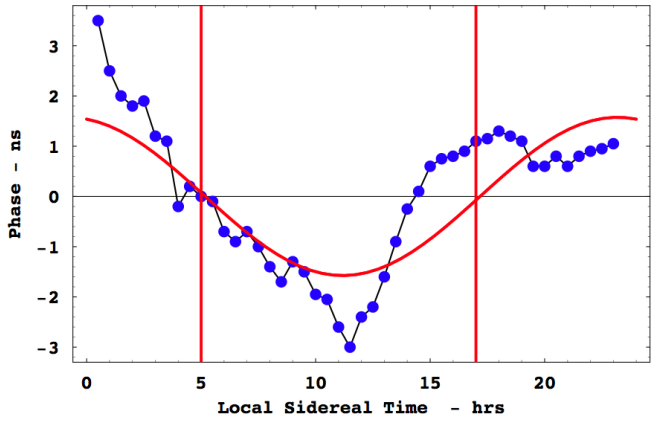

Fig. 7: Data from the 1981 Torr-Kolen experiment at Logan, Utah [12]. The data shows variations in travel times (ns), for local sidereal times, of an RF signal travelling through 500 m of coaxial cable orientated in an EW direction. Actual days are not indicated but the experiment was done during February-June 1981. Results are for a typical day. For the 1st of February the local time of 12:00 corresponds to 13:00 sidereal time. The predictions are for February, for a cosmic speed of 480 km/s in the direction ($\alpha = 5.0^{\mathrm{h}}, \delta = -70^{\circ}$), and including orbital and in-flow velocities but without theoretical turbulence. The vertical lines are at local sidereal times of 5^{h} and 17^{h}, corresponding to the RAs shown in red in Figs. 6 and 11.

shows as well the corresponding phase differences from other experiments. Krisher only compared the phase variations with that of the Cosmic Microwave Background (CMB), and noted that the phase relative to the local sidereal time differed from CMB direction by 6 hrs, but failed to notice that it agreed with the direction discovered by Miller in 1925/26 and published in 1933 [8]. The phases from the various experiments show that, despite very different longitudes of the experiments and different days in the year, they are in phase when plotted against local sidereal times. This demonstrates that the phase cycles are caused by the rotation of the Earth relative to the stars — that we are observing a galactic phenomenon, being that the 3-space flow direction is reasonably steady wrt the galaxy*. Nevertheless we note that all the phase data show fluctuations in both the local sidereal time for maxima/minima and also fluctuations in magnitude. These wave effects first appeared in experimental data of Michelson and Morley in 1887.

From the November Krisher data in Figs. 6(a) and (f) the Right Ascension of the 3-space flow direction was obtained from the local sidereal times of the maxima and minima, giving a RA of 6.09^{h}, after correcting the apparent RA of 4.96^{h} for the 42° inclination of the optical fiber to the local meridian. This RA was used in combination with the spacecraft earth-flyby Doppler shift data, and is shown in Fig. 11.

The magnitudes of the Krisher phases are not used in determining the RA for November, and so are not directly used in this report. Nevertheless these magnitudes provide a check on the physics of how the speed of light in optical fibers is affected by the 3-space flow. The phase differences $\phi_1 - \phi_2$ in Fig. 6a, which correspond to a 1st order in v/c experiment in which the Fresnel drag effect must be taken into account, are shown to be consistent with the determined speed for November, noting that the use of phase comparators does not allow the determination of multiple 360° contributions to the phase differences. The analysis of the Krisher phase sum $\phi_1 + \phi_2$ in Fig. 6f, which correspond to a 2nd order in v/c experiment, requires the Lorentz contraction of the optical fibers. as well as the Fresnel drag effect, to be taken into account. The physics of optical fibers in relation to this and other 3-space physics will be discussed more fully elsewhere.

*The same effect is observed in Ring Lasers [29] — which detect a sidereal period of rotation of the Earth, and not the solar period. Ring Lasers cannot detect the 3-space direction, only a rate of rotation.

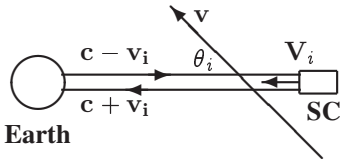

Fig. 8: Asymptotic flyby configuration in earth frame-of-reference, with spacecraft (SC) approaching Earth with velocity $\mathbf{V}_i$. The departing asymptotic velocity will have a different direction but the same speed, as no force other than conventional Newtonian gravity is assumed to be acting upon the SC. The dynamical 3-space velocity is $\mathbf{v}(\mathbf{r}, t)$, though taken to be time independent during the Doppler shift measurement, which causes the outward EM beam to have speed $c - v_i(r)$, and inward speed $c + v_i(r)$, where $v_i(r) = v(r)\cos(\theta_i)$, with θ_i the angle between $\mathbf{v}$ and $\mathbf{V}$. A similar description applies to the departing SC, labeled $i \to f$.

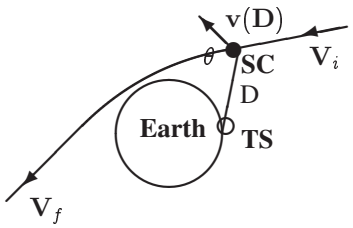

Fig. 9: Spacecraft (SC) earth flyby trajectory, with initial and final asymptotic velocity $\mathbf{V}$, differing only by direction. The Doppler shift is determined from Fig. 8 and (32). The 3-space flow velocity at the location of the SC is $\mathbf{v}$. The line joining Tracking Station (TS) to SC is the path of the RF signals, with length D. As SC approaches earth $\mathbf{v}(D)$ changes direction and magnitude, and hence magnitude of projection $v_i(D)$ also changes, due to earth component of 3-space flow and also because of RF direction to/from Tracking Station. The SC trajectory averaged magnitude of this earth in-flow is determined from the flyby data and compared with theoretical prediction.

9 3-space flow from Earth-flyby Doppler shifts

The motion of spacecraft relative to the Earth are measured by observing the direction and Doppler shift of the transponded RF transmissions. This gives another technique to determine

the speed and direction of the dynamical 3-space as manifested by the light speed anisotropy [19]. The repeated detection of the anisotropy of the speed of light has been, until recently, ignored in analysing the Doppler shift data, causing the long-standing anomalies in the analysis [20]. The use of the Minkowski-Einstein choice of time and space coordinates does not permit the analysis of these Doppler anomalies, as they mandate that the speed of the EM waves be invariant.

Because we shall be extracting the Earth inflow effect we need to take account of a spatially varying, but not time-varying, 3-space velocity. In the Earth frame of reference, see Fig. 8, and using clock times from earth-based clocks, let the transmitted signal from earth have frequency f. The time for one RF maximum to travel distance D to SC from earth is, see Fig. 9,

$$t_1 = \int_0^D \frac{dr}{c - v_i(r)} \,. \tag{21}$$

The next RF maximum leaves time $T = 1/f$ later and arrives at SC at time, taking account of SC motion,

$$t_2 = T + \int_0^{D-VT} \frac{dr}{c - v_i(r)} \,. \tag{22}$$

The period at the SC of the arriving RF is then

$$T' = t_2 - t_1 = T + \int_D^{D-VT} \frac{dr}{c - v_i(r)} \approx \approx \frac{c - v_i(D) - V}{c - v_i(D)}\, T \,. \tag{23}$$

Essentially this RF is reflected* by the SC. Then the 1st RF maximum takes time to reach the Earth

$$t_1' = -\int_{D-VT}^0 \frac{dr}{c + v_i(r)} \tag{24}$$

and the 2nd RF maximum takes time

$$t_2' = T' - \int_{D-VT-VT'}^0 \frac{dr}{c + v_i(r)} \,. \tag{25}$$

Then the period of the returning RF at the Earth is

$$\begin{aligned} T'' &= t_2' - t_1' = \\ &= T' + \int_{D-VT}^{D-VT-VT'} \frac{dr}{c + v_i(r)} \approx \\ &\approx \frac{c + v_i(D) - V}{c + v_i(D)}\, T' . \end{aligned} \tag{26}$$

Then overall we obtain the return frequency to be†

$$f'' = \frac{1}{T''} = \frac{c + v_i(D)}{c + v_i(D) - V} \cdot \frac{c - v_i(D)}{c - v_i(D) - V}\, f \,. \tag{27}$$

*In practice a more complex protocol is used.

†This corrects the corresponding expression in [19], but without affecting the final results.

Ignoring the projected 3-space velocity $v_i(D)$, that is, assuming that the speed of light is invariant as per the usual literal interpretation of the Einstein 1905 light speed postulate, we obtain instead

$$f'' = \frac{c^2}{(c - V)^2}\, f \,. \tag{28}$$

The use of (28) instead of (27) is the origin of the putative anomalies. Expanding (28) we obtain

$$\frac{\Delta f}{f} = \frac{f'' - f}{f} = \frac{2V}{c} \,. \tag{29}$$

However expanding (27) we obtain, for the same Doppler shift,

$$\frac{\Delta f}{f} = \frac{f'' - f}{f} = \left(1 + \frac{v(D)^2}{c^2}\right) \frac{2V}{c} + \dots \tag{30}$$

It is the prefactor to $2V/c$ missing from (29) that explains the spacecraft Doppler anomalies, and also permits yet another determination of the 3-space velocity $\mathbf{v}(D)$, *viz* at the location of the SC. The published data does not give the Doppler shifts as a function of SC location, so the best we can do at present is to use a SC trajectory-averaged $v(D)$, namely $\overline{v}_i$ and $\overline{v}_f$, for the incoming and outgoing trajectories, as further discussed below.

From the observed Doppler shift data acquired during a flyby, and then best fitting the trajectory, the asymptotic hyperbolic speeds $V_{i\infty}$ and $V_{f\infty}$ are inferred from (29), but incorrectly so, as in [20]. These inferred asymptotic speeds may be related to an inferred asymptotic Doppler shift

$$\frac{\Delta f_{i\infty}}{f} = \frac{f'_\infty - f}{f} = \frac{2V_{i\infty}}{c} + \dots \tag{31}$$

which from (30) gives

$$V_{i\infty} \equiv \frac{\Delta f_{i\infty}}{f} \cdot \frac{c}{2} = \left(1 + \frac{\overline{v}_i^2}{c^2}\right) V + \dots \tag{32}$$

where V is the actual asymptotic speed. Similarly after the flyby we obtain

$$V_{f\infty} \equiv \frac{\Delta f_{f\infty}}{f} \cdot \frac{c}{2} = \left(1 + \frac{\overline{v}_f^2}{c^2}\right) V + \dots \tag{33}$$

and we see that the "asymptotic" speeds $V_{i\infty}$ and $V_{f\infty}$ must differ, as indeed reported in [20]. We then obtain the expression for the so-called flyby anomaly

$$\Delta V_\infty = V_{f\infty} - V_{i\infty} = \frac{\overline{v}_f^2 - \overline{v}_i^2}{c^2}\, V \tag{34}$$

where here $V \approx V_\infty$ to sufficient accuracy, where V_∞ is the average of $V_{i\infty}$ and $V_{f\infty}$, The existing data on $\mathbf{v}$ permits *ab*

initio predictions for ΔV_∞. As well a separate least-squares-fit to the individual flybys permits the determination of the average speed and direction of the 3-space velocity, relative to the Earth, during each flyby. These results are all remarkably consistent with the data from the various laboratory experiments that studied $\mathbf{v}$. We now indicate how $\overline{v}_i$ and $\overline{v}_f$ were parametrised during the best-fit to the flyby data. In (10) $\mathbf{v}_{galactic} + \mathbf{v}_{sun} - \mathbf{v}_{orbital}$ was taken as constant during each individual flyby, with $\mathbf{v}_{sun}$ inward towards the Sun, with value 42 km/s, and $\mathbf{v}_{orbital}$ as tangential to earth orbit with value 30 km/s — consequentially the directions of these two vectors changed with day of each flyby. The earth inflow $\mathbf{v}_{earth}$ in (10) was taken as radial and of an unknown fixed trajectory-averaged value. So the averaged direction but not the averaged speed varied from flyby to flyby, with the incoming and final direction being approximated by the (α_i, δ_i) and (α_f, δ_f) asymptotic directions shown in Table 2. The predicted theoretical variation of $v_{earth}(R)$ is shown in Fig. 10. To best constrain the fits to the data the flyby data was used in conjunction with the RA from the Krisher optical fiber data. This results in the aberration plot in Fig. 11, the various flyby data in Table 2, and the Earth in-flow speed determination in Fig. 12. The results are in remarkable agreement with the results from Miller, showing the extraordinary skill displayed by Miller in carrying out his massive interferometer experiment and data analysis in 1925/26. The only effect missing from the Miller analysis is the spatial in-flow effect into the Sun, which affected his data analysis, but which has been partially corrected for in Sect. 5. Miller obtained a galactic flow direction of $\alpha = 4.52$ hrs, $\delta = -70.5^\circ$, compared to that obtained herein from the NASA data of $\alpha = 4.29$ hrs, $\delta = -75.0^\circ$, which differ by only $\approx 5^\circ$.

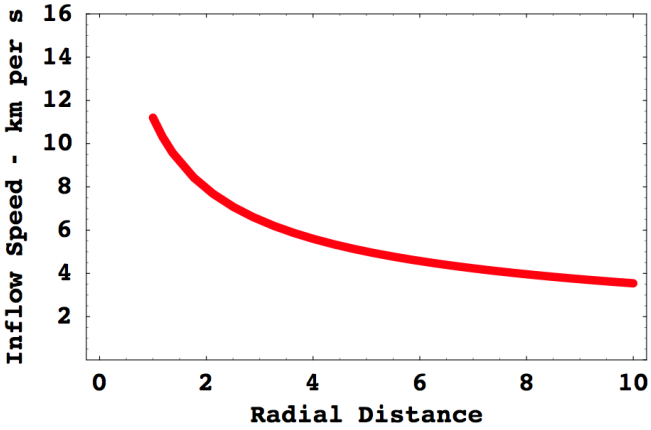

Fig. 10: Earth 3-space inflow speed vs distance from earth in earth radii, as given in (7), plotted only for $R > 1.0$. Combining the NASA/JPL optical fiber RA determination and the flyby Doppler shift data has permitted the determination of the angle- and distance-averaged inflow speed, to be 12.4 ± 5km/s.

10 Earth 3-space inflow: Pound and Rebka experiment

The numerous EM anisotropy experiments discussed herein demonstrate that a dynamical 3-space exists, and that the speed of the earth wrt this space exceeds 1 part in 1000 of c, namely a large effect. Not surprisingly this has indeed been detected many times over the last 120 years. The speed of nearly 500 km/s means that earth based clocks experience a real, so-called, time dilation effect from (6) of approximately 0.12 s per day compared to cosmic time. However clocks may be corrected for this clock dilation effect because their speed v though space, which causes their slowing, is measurable by various experimental methods. This means that the absolute or cosmic time of the universe is measurable. This very much changes our understanding of time. However because of the inhomogeneity of the Earth 3-space in-flow component the clock slowing effect causes a differential effect for clocks at different heights above the Earth's surface. It was this effect that Pound and Rebka reported in 1960 using the Harvard tower [28]. Consider two clocks at heights h_1 and h_2, with $h = h_2 - h_1$, then the frequency differential follows from (6),

$$\begin{aligned}
\frac{\Delta f}{f} &= \sqrt{1 - \frac{v^2(h_2)}{c^2}} - \sqrt{1 - \frac{v^2(h_1)}{c^2}} \approx \\
&\approx \frac{v^2(h_1) - v^2(h_2)}{2c^2} + \cdots = \\
&= \frac{1}{2c^2}\frac{dv^2(r)}{dr}\,h + \cdots = \\
&= \frac{g(r)\,h}{c^2} + \cdots = \\
&= -\frac{\Delta\Phi}{c^2} + \ldots
\end{aligned} \tag{35}$$

using (3) with $\mathbf{v}\cdot\nabla\mathbf{v} = \nabla\left(\frac{v^2}{2}\right)$ for zero vorticity $\nabla\times\mathbf{v} = \mathbf{0}$, and ignoring any time dependence of the flow, and where finally, $\Delta\Phi$ is the change in the gravitational potential. The actual process here is that, say, photons are emitted at the top of the tower with frequency f and reach the bottom detector with the same frequency f — there is no change in the frequency. This follows from (23) but with now $V = 0$ giving $T = T'$. However the bottom clock is running slower because the speed of space there is faster, and so this clock determines that the falling photon has a higher frequency, ie. appears blue shifted. The opposite effect is seen for upward travelling photons, namely an apparent red shift as observed by the top clock. In practice the Pound-Rebka experiment used motion induced Doppler shifts to make these measurements using the Mössbauer effect. The overall conclusion is that Pound and Rebka measured the derivative of v^2 wrt to height, whereas herein we have measured that actual speed, but averaged wrt the SC trajectory measurement protocol. It is important to note that the so-called "time dilation" effect is really a "clock slowing" effect — clocks are simply slowed by their movement through 3-space. The Gravity Probe A

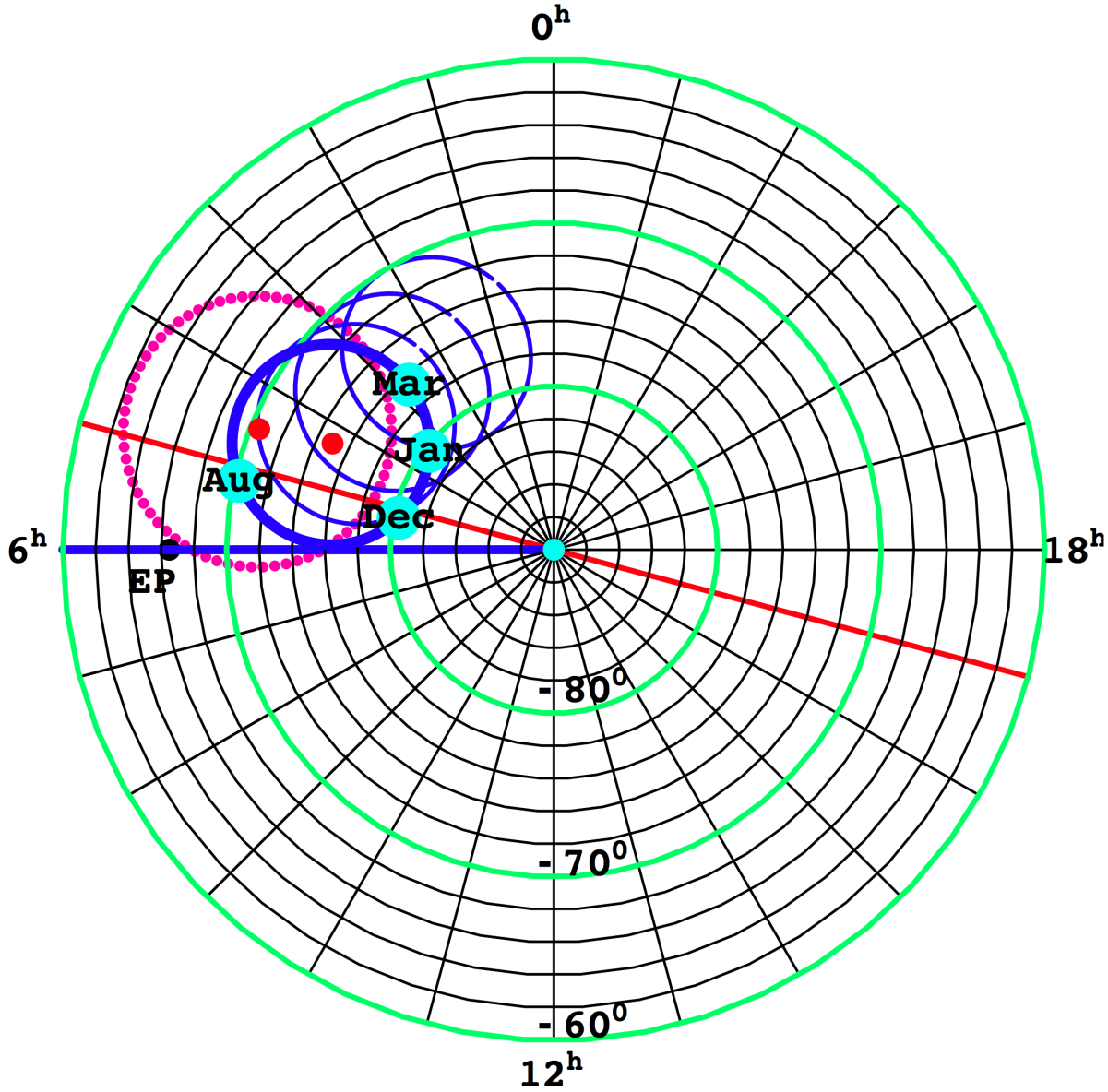

Fig. 11: South celestial sphere with RA and Dec shown. The red dotted circle shows the Miller aberration path discovered in 1925/26, from [8]. The red point at $\alpha = 4.52$ hrs, $\delta = -70.5^\circ$ shows the galactic flow direction determined by Miller, after removing earth-orbit aberration effect. The dark blue circle shows the aberration path from best-fitting the Earth-flyby Doppler shift data and using the optical-fiber RA data point for November from Krisher [18], see Fig. 12. This corresponds to a best fit averaged earth inflow speed of 12.4 ± 5km/s. The blue aberration paths show the best-fit if (a) upper circle: earth inflow speed = 0 km/s, (b) = 4.0 km/s, (c) = 8.0 km/s and (d) = 12.4 km/s (thick blue circle). The actual 3-space flow directions are shown by light-blue background to labels for the flybys in Aug, Dec, Jan and Mar, and given in Table 2. The red point at $\alpha = 4.29$ hrs, $\delta = -75.0^\circ$ shows the optical-fiber/earth-flyby determined galactic flow direction, also after removal of earth-orbit aberration effect, and is only 5° from the above mentioned Miller direction. The miss-fit angle $\Delta\theta$ between the best-fit RA and Dec for each flyby is given in Table 2, and are only a few degrees on average, indicating the high precision of the fit. This plot shows the remarkable concordance between the NASA/JPL determined 3-space flow characteristics and those determined by Miller in 1925/26. It must be emphasised that the optical-fiber/flyby aberration plot and galactic 3-space flow direction is obtained completely independently of the Miller data. The blue line at $6.09^{\rm h}$ is the orientation corrected Krisher RA, and has an uncertainty of $\pm 1^{\rm h}$, caused by wave/turbulence effects. The fiducial RA of $5^{\rm h}$ and $17^{\rm h}$, shown in red, are the fiducial local sidereal times shown in Figs. 3, 6 and 7. The point EP is the pole of the ecliptic. The speed and declination differences between the Miller and NASA data arise from Miller being unaware of the Sun 3-space inflow effect — correcting for this and using an air refractive index of $n = 1.00026$ atop Mt. Wilson increases the Miller data determined speed and moves the declination slightly southward, giving an even better agreement with the NASA data. Here we have merely reproduced the Miller aberration plot from [8].

Parameter	GLL-I	GLL-II	NEAR	Cassini	Rosetta	M'GER
Date	Dec 8, 1990	Dec 8, 1992	Jan 23, 1998	Aug 18, 1999	Mar 4, 2005	Aug 2, 2005
V_∞ km/s	8.949	8.877	6.851	16.010	3.863	4.056
α_i deg	266.76	219.35	261.17	334.31	346.12	292.61
δ_i deg	-12.52	−34.26	−20.76	−12.92	−2.81	31.44
α_f deg	219.97	174.35	183.49	352.54	246.51	227.17
δ_f deg	−34.15	−4.87	−71.96	−4.99	−34.29	−31.92
α_v hrs	5.23	5.23	3.44	5.18	2.75	4.89
δ_v deg	−80.3	−80.3	−80.3	−70.3	−76.6	−69.5
v km/s	490.6	490.6	497.3	478.3	499.2	479.2
(O) ΔV_∞ mm/s	3.92±0.3	−4.6±1.0	13.46±0.01	−2±1	1.80±0.03	0.02±0.01
(P) ΔV_∞ mm/s	4.07	−5.26	13.45	−0.76	0.86	−4.56
(P) $\Delta\theta$ deg	1	1	2	4	5	—

Table 2: Earth flyby parameters from [20] for spacecraft Galileo (GLL: flybys I and II), NEAR, Cassini, Rosetta and MESSENGER (M'GER). V_∞ is the average osculating hyperbolic asymptotic speed, α and δ are the right ascension and declination of the incoming (i) and outgoing (f) osculating asymptotic velocity vectors, and (O) ΔV_∞ is the putative "excess speed" anomaly deduced by assuming that the speed of light is isotropic in modeling the Doppler shifts, as in (31). The observed (O) ΔV_∞ values are from [20], and after correcting for atmospheric drag in the case of GLL-II, and thruster burn in the case of Cassini. (P) ΔV_∞ is the predicted "excess speed", using (34), after least-squares best-fitting that data using (34): α_v and δ_v and v are the right ascension, declination and the 3-space flow speed for each flyby date, which take account of the Earth-orbit aberration and earth inflow effects, and correspond to a galactic flow with $\alpha = 4.29$ hrs, $\delta = -75.0^\circ$ and $v = 486$ km/s in the solar system frame of reference. $\Delta\theta$ is the error, in the best fit, for the aberration determined flow direction, from the nearest flyby flow direction. In the fitting the MESSENGER data is not used, as the data appears to be anomalous.

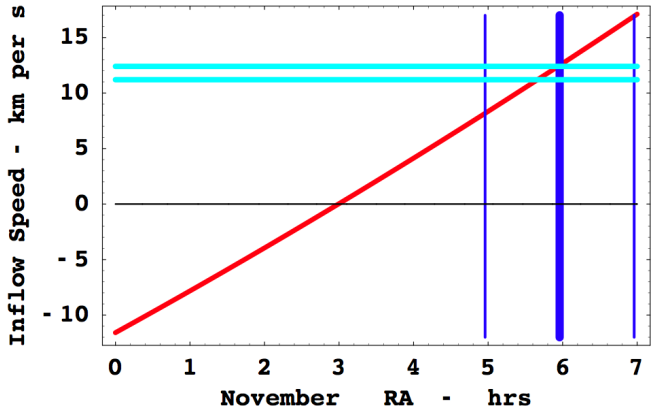

Fig. 12: The weighted angle- and distance-averaged earth 3-space inflow speed v_{earth}, see Fig. 10, as determined from NASA data, upper green plot. Uses the averaged Right Ascension from the Krisher *et al.* data for November, $\alpha = 4.96^{\rm h}$, but corrected to $\alpha = 6.09^{\rm h}$ for orientation effect of the optical fiber, shown by the thick blue line, with uncertainty range from wave effects shown by two thin blue lines, compared with the predicted RA from fitting the flyby data, as shown in Fig. 11. The red plot shows that prediction for various averaged inflow speeds, with +ve speeds being an inflow, while -ve speeds are an outflow. The earth flyby aberration fits for $v_{earth} = 0, +4.0, +8.0$ and $+12.4$ km/s are shown in Fig. 11. Theory gives that the inflow speed is $+11.2$km/s at the Earth's surface — shown by lower green plot. So the detected averaged inflow speed seems to be in good agreement with an expected averaged value. This is the first detection of the Earth's spatial inflow, and the acceleration of this flow is responsible for the Earth's gravity. Note that the flyby data clearly mandates an inflow (+ve values in this figure and not an out-flow — having -ve values).

experiment [33] also studied the clock slowing effect, though again interpreted differently therein, and again complicated by additional Doppler effects.

11 CMB direction

The Cosmic Microwave Background (CMB) velocity is often confused with the Absolute Motion (AM) velocity or light-speed anisotropy velocity as determined in the experiments discussed herein. However these are unrelated and in fact point in very different directions, being almost at 90° to each other, with the CMB velocity being 369 km/s in direction $(\alpha = 11.2^{\rm h}, \delta = -7.22^\circ)$. The CMB velocity vector was first determined in 1977 by Smoot *et al.* [30].

The CMB velocity is obtained by defining a frame of reference in which the thermalised CMB 3°K radiation is isotropic, that is by removing the dipole component, and the CMB velocity is the velocity of the Earth in that frame. The CMB velocity is a measure of the motion of the solar system relative to the last scattering surface (a spherical shell) of the universe some 13.4Gyrs in the past. The concept here is that at the time of decoupling of this radiation from matter that matter was on the whole, apart from small observable fluctuations, on average at rest with respect to the 3-space. So the CMB velocity is not motion with respect to the *local* 3-space now; that is the AM velocity. Contributions to the AM velocity would arise from the orbital motion of the solar system within the Milky Way galaxy, which has a speed of some 250 km/s, and contributions from the motion of the Milky

Way within the local cluster, and so on to perhaps super clusters, as well as flows of space associated with gravity in the Milky Way and local galactic cluster etc. The difference between the CMB velocity and the AM velocity is explained by the spatial flows that are responsible for gravity at the galactic scales.

12 Conclusions

We have shown that the NASA/JPL optical fiber and spacecraft earth flyby data give another independent determination of the velocity of the solar system through a dynamical 3-space. The resulting direction is in remarkable agreement with the direction determined by Miller in 1925/26 using a gas-mode Michelson interferometer. The Miller speed requires a better knowledge of the refractive index of the air atop Mt. Wilson, where Miller performed his experiments, but even using the STP value we obtain reasonable agreement with the NASA/JPL determined speed. Using an air refractive index of 1.00026 in place of the STP value of 1.00029 would bring the Miller speed into agreement with the NASA data determined speed. As well the NASA/JPL data has permitted the first direct measurement of the flow of 3-space into the Earth, albeit averaged over spacecraft trajectory during their flybys. This is possible because the inflow component is radially inward and so changes direction relative to the other flow components during a flyby, making the flyby Doppler shifts sensitive to the inflow speed.

It must be emphasised that the long-standing and repeated determinations of the anisotropy of vacuum EM radiation is not in itself in contradiction with the Special Relativity formalism — rather SR uses a different choice of space and time variables from those used herein, a choice which by construction mandates that the speed of EM radiation in vacuum be invariant wrt to that choice of coordinates [3]. However that means that the SR formalism cannot be used to analyse EM radiation anisotropy data, and in particular the flyby Doppler shift data.

The discovery of absolute motion wrt a dynamical 3-space has profound implications for fundamental physics, particularly for our understanding of gravity and cosmology. It shows that clocks, and all oscillators, whether they be classical or quantum, exhibit a slowing phenomenon, determined by their absolute speed though the dynamical 3-space. This "clock slowing" has been known as the "time dilation" effect — but now receives greater clarity. It shows that there is an absolute or cosmic time, and which can be measured by using any clock in conjunction with an absolute speed detector — many of which have been mentioned herein, and which permits the "clock slowing" effect to be compensated. This in turn implies that the universe is a far more coherent and non-locally connected process than previously realised, although a model for this has been proposed [1]. It also shows that the now standard discussion of the limitations of simultaneity were really misleading — being based on the special space and time coordinates invoked in the SR formalism, and that simultaneity is a fact of the universe, albeit an astounding one.

As well successful absolute motion experiments have always shown wave or turbulence phenomena, and at a significant scale. This is a new phenomena that is predicted by the dynamical theory of 3-space. Ongoing development of new experimental techniques to detect and characterise these wave phenomena will be reported elsewhere.

Submitted on June 18, 2009 / Accepted on July 10, 2009

References

1. Cahill R.T. Process physics: from information theory to quantum space and matter. Nova Science Pub., New York, 2005.
2. Cahill R.T. Dynamical 3-space: a review. In: *Ether Space-time and Cosmology: New Insights into a Key Physical Medium*, Duffy M. and Lévy J., eds., *Apeiron*, 2009, 135–200.
3. Cahill R.T. Unravelling Lorentz covariance and the spacetime formalism. *Progress in Physics*, 2008, v. 4, 19–24.
4. Braxmaier C. *et al. Phys. Rev. Lett.*, 2002, v. 88, 010401; Müller H. *et al. Phys. Rev. D*, 2003, v. 68, 116006-1-17; Müller H. *et al. Phys. Rev. D*, 2003, v. 67, 056006; Wolf P. *et al. Phys. Rev. D*, 2004, v. 70, 051902-1-4; Wolf P. *et al. Phys. Rev. Lett.*, 2003, v. 90, 060402; Lipa J.A. *et al. Phys. Rev. Lett.*, 2003, v. 90, 060403.
5. Cahill R.T. and Kitto K. Michelson-Morley experiments revisited. *Apeiron*, 2003, v. 10(2), 104–117.
6. Cahill R.T. The Michelson and Morley 1887 experiment and the discovery of absolute motion. *Progress in Physics*, 2005, v. 3, 25–29.
7. Michelson A.A. and Morley E.W. *Am. J. Sc.*, 1887, v. 34, 333–345.
8. Miller D.C. *Rev. Mod. Phys.*, 1933, v. 5, 203–242.
9. Illingworth K.K. *Phys. Rev.*, 1927, v. 3, 692–696.
10. Joos G. *Ann. d. Physik*, 1930, v. 7, 385.
11. Jaseja T.S. *et al. Phys. Rev. A*, 1964, v. 133, 1221.
12. Torr D.G. and Kolen P. In: *Precision Measurements and Fundamental Constants*, Taylor, B.N. and Phillips, W.D. eds. *Natl. Bur. Stand. (U.S.), Spec. Pub.*, 1984, 617, 675.
13. Cahill R.T. The Roland DeWitte 1991 experiment. *Progress in Physics*, 2006, v. 3, 60–65.
14. Cahill R.T. A new light-speed anisotropy experiment: absolute motion and gravitational waves detected. *Progress in Physics*, 2006, v. 4, 73–92.
15. Munéra H.A. *et al.* In: *Proceedings of SPIE*, 2007, v. 6664, K1–K8, eds. Roychoudhuri C. *et al.*
16. Cahill R.T. Optical-fiber gravitational wave detector: dynamical 3-space turbulence detected. *Progress in Physics*, 2007, v. 4, 63–68.
17. Cahill R.T. and Stokes F. Correlated detection of sub-mHz gravitational waves by two optical-fiber interferometers. *Progress in Physics*, 2008, v. 2, 103–110.

18. Krisher T.P., Maleki L., Lutes G.F., Primas L.E., Logan R.T., Anderson J.D. and Will C.M. Test of the isotropy of the one-way speed of light using hydrogen-maser frequency standards. *Phys. Rev. D*, 1990, v. 42, 731–734.

19. Cahill R.T. Resolving spacecraft Earth-flyby anomalies with measured light speed anistropy. *Progress in Physics*, 2008, v. 4, 9–15.

20. Anderson J.D., Campbell J.K., Ekelund J.E., Ellis J. and Jordan J.F. Anomalous orbital-energy changes observed during spacecraft flybys of Earth. *Phys. Rev. Lett.*, 2008, v. 100, 091102.

21. Cahill R.T. Quantum foam, gravity and gravitational waves. In: *Relativity, Gravitation, Cosmology: New Developments*, Dvoeglazov V., ed., Nova Science Pub., New York, 2009.

22. Hicks W.M. *Phil. Mag.*, 1902, v. 3, 9–42.

23. Hertz H. On the fundamental equations of electro-magnetics for bodies in motion. *Wiedemann's Ann.*, 1890, v. 41, 369; Electric waves. Collection of scientific papers. Dover Publ., New York, 1962.

24. Cahill R.T. Dynamical fractal 3-space and the generalised Schrödinger equation: equivalence principle and vorticity effects. *Progress in Physics*, 2006, v. 1, 27–34.

25. Cahill R.T. A quantum cosmology: no dark matter, dark energy nor accelerating Universe. arXiv: 0709.2909.

26. Cahill R.T. Unravelling the dark matter — dark energy paradigm. *Apeiron*, 2009, v. 16, no. 3, 323–375.

27. Cahill, R.T. The dynamical velocity superposition effect in the quantum-foam theory of gravity. In: *Relativity, Gravitation, Cosmology: New Developments*, Dvoeglazov V., ed., Nova Science Pub., New York, 2009.

28. Pound R.V. and Rebka Jr. G.A. *Phys. Rev. Lett.*, 1960, v. 4(7), 337–341.

29. Schreiber K.U., Velikoseltsev A., Rothacher M., Klügel T., Stedman G.E. and Wilsthire D.L. Direct measurement of diurnal polar motion by ring laser gyroscopes. *J. Geophys. Res.*, 2004, v. 109, B06405; arXiv: physics/0406156.

30. Smoot G.F., Gorenstein M.V. and Muller R.A. *Phys. Rev. Lett.*, 1977, v. 39(14), 898.

31. Cahill R.T. 3-space inflow theory of gravity: boreholes, black-holes and the fine structure constant. *Progress in Physics*, 2006, v. 2, 9–16.

32. Cahill R.T. Dark matter as a quantum foam in-flow effect. In: *Trends in Dark Matter Research*, ed. J. Val Blain, Nova Science Pub., NY, 2005, 95–140.

33. Vessot R.F.C. *et al.* Test of relativistic gravitation with a space-borne hydrogen maser. *Rev. Mod. Phys.*, 1980, v. 45, 2081.

Geometry of Space-Time

Ulrich E. Bruchholz

Schillerstrasse 36, D-04808 Wurzen, Germany

E-mail: Ulrich.Bruchholz@t-online.de; http://www.bruchholz-acoustics.de

The geometry of the space-time is deduced from gravitational and electromagnetic fields. We have to state that Rainich's "already unified field theory" is the ground work of the proposed theory. The latter is deduced independently on Rainich. Rainich's analogies are brilliantly validated. His formulae are verified this way. Further reaching results and insights demonstrate that Rainich's theory is viable. In final result, we can formulate an enhanced equivalence principle. It is the equivalence of Newton's force with the Lorentz force.

To the memory of John Archibald Wheeler, who foresaw this simple idea.

1 The predecessor

George Yuri Rainich already saw the analogies of the electromagnetic with the gravitational field. Since Einstein's equivalence principle implies a geometric approach of gravitation [1], electromagnetism has to be geometry too. Not enough, Rainich also saw that the electromagnetic field tensor is performed from the congruences of two dual surfaces. It is the analogy of the curvature vector of the current path, performed from the main normal, see on generalized Frenet formulae in [2].

One can well pursue Rainich's way in his papers from 1923 to 1924. First, he tried to find a non-Riemannian geometry for the electromagnetic vacuum field [3]. Later, he saw that Riemannian geometry is sufficient to describe electromagnetism [4, 5]. Rainich's identities (also called algebraic Rainich conditions) are deduced without special techniques in [6]. Present paper provides a further derivation of Rainich's identities, additionally identifying the concrete geometry.

Since a full geometric approach precludes sources, Rainich concluded a central role of singularities. However, it is deduced in [7] that this role is commonly overestimated. The singularities pass for a bar to the geometric approach. It is shown in [7] that formal singularities are in areas (according to observer's coordinates), which are not locally imaged. The related boundaries specify the discrete values of the integration constants from field equations [7].

2 The derivation

The first precursor is to see in [8]. The derivation follows the steps according to the chapter "Geometric interpretation of the Ricci tensor — the Ricci main directions" in [2]. As well, we shall see that the space-time involves a vital difference to other manifolds.

The known source-free Einstein-Maxwell equations

$$R_{ik} = \kappa \left(\frac{1}{4}\, g_{ik} F_{ab} F^{ab} - F_{ia} F_k{}^a \right), \tag{1}$$

$$F^{ia}{}_{;a} = 0\,, \tag{2}$$

$$F_{ij,k} + F_{jk,i} + F_{ki,j} = 0 \tag{3}$$

involve a special kind of Riemannian geometry, what is explained as follows.

The Ricci main directions (written in terms according to Eisenhart [2]) follow from

$$\det \left| R_{ik} + \rho g_{ik} \right| = 0 \tag{4}$$

with the solutions*

$$\rho_{|1} = \rho_{|4} = +\rho_0\,, \quad \rho_{|2} = \rho_{|3} = -\rho_0 \tag{5}$$

with

$$\rho_0{}^2 = R_1{}^a R^1{}_a = R_2{}^a R^2{}_a = R_3{}^a R^3{}_a = R_4{}^a R^4{}_a\,, \tag{6}$$

what leads directly to Rainich's identities

$$R_i{}^a R^k{}_a = \delta_i^k \rho_0{}^2 = \frac{1}{4}\, \delta_i^k R_a{}^b R^a{}_b\,. \tag{7}$$

Characteristical are the two double-roots, that means: There are two dual surfaces of the congruences

$$e_{|1}{}^i e_{|4}{}^k - e_{|1}{}^k e_{|4}{}^i \quad \text{and} \quad e_{|2}{}^i e_{|3}{}^k - e_{|2}{}^k e_{|3}{}^i$$

with minimal and maximal mean Riemannian curvature. $e_{|1} \ldots e_{|4}$ are the vectors of an orthogonal quadruple (vierbein) in those "main surfaces". At single roots we had 4 main directions. But we will see that the main surfaces are a spe-

*Where ρ_0 has a negative value, what has to do with the special signature of the space-time.

ciality of the space-time. With the obtained solutions we get

$$\left.\begin{aligned} g_{ik} &= e_{|1\_i}e_{|1\_k} + e_{|2\_i}e_{|2\_k} + \\ &\quad + e_{|3\_i}e_{|3\_k} - e_{|4\_i}e_{|4\_k}\,, \\ \frac{R_{ik}}{\rho_0} &= -e_{|1\_i}e_{|1\_k} + e_{|2\_i}e_{|2\_k} + \\ &\quad + e_{|3\_i}e_{|3\_k} + e_{|4\_i}e_{|4\_k}\,. \end{aligned}\right\} \tag{8}$$

If we set

$$c_{|ik} = -c_{|ki} = F_{ab}e_{|i}{}^{a}e_{|k}{}^{b} \tag{9}$$

follows from elementary calculations

$$\left.\begin{aligned} &-\kappa\left((c_{|23})^2 + (c_{|14})^2\right) = 2\rho_0\,, \\ &c_{|12} = c_{|34} = c_{|13} = c_{|24} = 0\,. \end{aligned}\right\} \tag{10}$$

With it, the field tensor

$$\begin{aligned} F_{ik} = &-c_{|14}\left(e_{|1\_i}e_{|4\_k} - e_{|1\_k}e_{|4\_i}\right) + \\ &+ c_{|23}\left(e_{|2\_i}e_{|3\_k} - e_{|2\_k}e_{|3\_i}\right) \end{aligned} \tag{11}$$

is performed from the main surfaces. Rainich knew also these relations [4, 5].

3 Conclusions

Montesinos and Flores [9] deduce the electromagnetic energy-momentum tensor via Noether's theorem [10]. That means, the Ricci tensor must have just the form according to Eqn. (1). Therefore, the geometry with the main surfaces is necessary for the space-time. Since the electromagnetic field tensor is performed by the main surfaces, it is a curve parameter of the current path like the curvature vector (which is performed by the main normal, and is the geometric expression of both gravitation and accelerated motion), as Rainich already saw. We can formulate an enhanced equivalence principle this way. It is the equivalence of the Lorentz force with Newton's force. Because the test body means a current point on the path, i.e. all forces to the test body come from curve parameters.

Montesinos and Flores [9] derived a symmetric energy-momentum tensor from three different theories, with the result that sources have to vanish in each case. That means:

1. The Maxwell theory is sufficient, because it runs as demonstrated in [7], even also regarding quantization. Non-Riemannian ansatzes are not needed;
2. Any ansatz with distributed charges or masses is false in principle. This error was helpful in classical theories before Einstein, which were separately handled. Now, such error turns up to be counterproductive.

It appears inviting to specify metrics first via Eqn. (7) (see [6]), but this method has narrow limits. The electromagnetic integration constants (charge, magnetic momentum) come from Maxwell's equations. The geometric theory of fields [7] unifies electromagnetism with gravitation natural way.

Submitted on June 23, 2009 / Accepted on July 17, 2009

References

1. Einstein A. Grundzüge der Relativitätstheorie. A back-translation from the Four Lectures on Theory of Relativity. Akademie-Verlag Berlin, Pergamon Press Oxford, Friedrich Vieweg & Sohn Braunschweig, 1969.
2. Eisenhart L.P. Riemannian geometry. Princeton University Press, Princeton, 1949.
3. Rainich G.Y. The electromagnetic field and curvature. *Proc. N.A.S.*, 1923, v. 9, 404–406.
4. Rainich G.Y. Electrodynamics in the general relativity theory. *Proc. N.A.S.*, 1924, v. 10, 124–127.
5. Rainich G.Y. Second note on electrodynamics in the general relativity theory. *Proc. N.A.S.*, 1924, v. 10, 294–298.
6. Caltenco Franca J.H., López-Bonilla J.L., Peña-Rivero R. The algebraic Rainich conditions. *Progress in Physics*, 2007, v. 3, 34–35.
7. Bruchholz U.E. Key notes on a geometric theory of fields. *Progress in Physics*, 2009, v. 2, 107–113.
8. Bruchholz U. Zur Berechnung stabiler elektromagnetischer Felder. *Z. elektr. Inform.- u. Energietechnik*, Leipzig, 1980, Bd. 10, 481–500.
9. Montesinos M. and Flores E. Symmetric energy-momentum tensor in Maxwell, Yang-Mills, and Proca theories obtained using only Noether's theorem. arXiv: hep-th/0602190.
10. Noether E. Invariante Variationsprobleme. *Nachr. d. König. Gesellsch. d. Wiss. zu Göttingen, Math-phys. Klasse*, 1918, 235–257 (English translation by M. A. Tavel in: *Transport Theory and Statistical Physics*, 1971, v. 1(3), 183–207; arXiv: physics/0503066).

Derivation of Planck's Constant from Maxwell's Electrodynamics

Ulrich E. Bruchholz

Schillerstrasse 36, D-04808 Wurzen, Germany

E-mail: Ulrich.Bruchholz@t-online.de; http://www.bruchholz-acoustics.de

Like Planck deduced the quantization of radiation energy from thermodynamics, the same is done from Maxwell's theory. Only condition is the existence of a geometric boundary, as deduced from author's Geometric theory of fields.

Let us go from Maxwell's equations of the vacuum that culminate in wave equations for the electric potential

$$\Box\varphi = 0 \tag{1}$$

and

$$\Box\mathcal{A} = 0 \tag{2}$$

for the magnetic vector potential.

Take the wave solution from Eqn. (2), in which the vector potential consists of a single component vertical to the propagation direction

$$A_y = A_y\Big(\omega\cdot(t-x)\Big), \tag{3}$$

where $c = 1$ (normalization), ω is a constant (identical with the circular frequency at the waves), x means the direction of the propagation, A_y is an *arbitrary* real function of $\omega\cdot(t-x)$ (independent on y, z).

The field strengthes respectively flow densities (which are the same in the vacuum) become

$$E_y = \frac{\partial A_y}{\partial t} = \omega {A_y}'\Big(\omega\cdot(t-x)\Big), \tag{4}$$

and

$$B_z = -\frac{\partial A_y}{\partial x} = \omega {A_y}'\Big(\omega\cdot(t-x)\Big), \tag{5}$$

where ${A_y}'$ means the total derivative.

The energy density of the field results in

$$\eta = \frac{\varepsilon_\circ}{2}\cdot({E_y}^2 + {B_z}^2) = \omega^2\varepsilon_\circ {A_y}'^2\Big(\omega\cdot(t-x)\Big), \tag{6}$$

where $\varepsilon_\circ$ means the vacuum permitivity.

The geometric theory of fields allows geometric boundaries from the non-linearities in the equations of this theory [1]. If one assumes such a boundary, like those in stationary solutions of the non-linear equations, the included energy becomes the volume integral within this boundary

$$\iiint \eta\,\mathrm{d}(t-x)\,\mathrm{d}y\,\mathrm{d}z = \\ = \omega\,\varepsilon_\circ \iiint {A_y}'^2\Big(\omega\cdot(t-x)\Big)\,\mathrm{d}\Big(\omega\cdot(t-x)\Big)\,\mathrm{d}y\,\mathrm{d}z\,. \tag{7}$$

This volume integral would be impossible without the boundary, because the linear solution, being alone, is not physically meaningful for the infinite extension.

We can write the last equation as

$$E = \omega\,\hbar \tag{8}$$

(E means here energy), or

$$E = h\,\nu\,, \tag{9}$$

because the latter volume integral has a constant value. The known fact that this value is always the same means also that only one solution exists with ω as a parameter.

Keep the calculation for the concrete value. This can be done only in numerical way, and might be a great challenge. The value of the above volume integral has to become $\hbar/\varepsilon_\circ$. With it, the fundamental relation of Quantum Mechanics follows from classical fields.

Summarizingly, the derivation involves two predictions:

1. Photon has a geometric boundary. That may be the reason that photon behaves as a particle;
2. There is only one wave solution.

Submitted on June 23, 2009 / Accepted on July 23, 2009

References

1. Bruchholz U.E. Key notes on a geometric theory of fields. *Progress in Physics*, 2009, v. 2, 107–113.

Changes in the Shape of Histograms Constructed from the Results of ^{239}Pu Alpha-Activity Measurements Correlate with the Deviations of the Moon from the Keplerian Orbit

Sergei N. Shapovalov*, Ilya A. Rubinstein†, Oleg A. Troshichev*, and Simon E. Shnoll‡

*St. Petersburg Arctic and Antarctic Institute, 38 Bering Str., St. Petersburg 199397, Russia
†Skobeltsin's Institute of Nuclear Physics, Moscow State University, Moscow 119991, Russia
‡Department of Physics, Moscow State University, Moscow 119992, Russia
‡Inst. of Theor. and Experim. Biophysics, Russian Acad. of Sci., Pushchino, Moscow Region, 142290, Russia
‡Puschino State University, Prospect Nauki 3, Pushchino, Moscow Region, 142290, Russia

E-mail: shapovalov@aari.nw.ru; shnoll@mail.ru

We have found that the shape of the histograms, constructed on the basis of the results of radioactivity measurements, changes in correlation with the distortions of the lunar Keplerian orbit (due to the gravitational influence of the Sun). Taking into account that the phenomenon of "macroscopic fluctuations" (regular changes in the fine structure of histograms constructed from the results of measurements of natural processes) does not depend on the nature of the process under study, one can consider the correlation of the histogram shape with the Moon's deviations from the Keplerian orbit to be independent from the nature of the process the histograms were obtained on.

1 Introduction

In the last decades, the studies of solar-terrestrial relations, which were initiated by A. L. Chizhevsky [1, 2], rest upon the concept that these relations have an electromagnetic origin [3–9]. A supposition that the solar-terrestrial relations could be of gravitational nature — when the matter at issue are *physico-chemical*, *chemical* and *biochemical* processes — would raise objections, as the energy change upon gravitational disturbances is much less than that observed in the processes mentioned. As for correlations of *physiological* processes with tidal forces (see, for example, [10–12]), they can be explained on the basis of complex indirect mechanisms.

Nevertheless, there were reports [13–21] on a strong correlation between variation of some physical and biochemical processes and deviations of the Moon from the Keplerian orbit (evection, variation and annual inequality; see [30]). The conclusion was that gravitational disturbances should play an essential role in these phenomena. The processes that correlations were revealed for were very different in their nature: there were fluctuations of "computer time", ^{239}Pu α-activity, the rate of a model chemical redox reaction, the content of haemoglobin in erythrocytes, and urea secretion.

There is no trivial explanation to the fact that physical and biochemical processes, which are little affected by tidal forces, correlate with changes of the lunar orbit.

As shown for the processes of diverse nature, the spectrum of their amplitude fluctuations (i.e., the shape of the corresponding histograms) correlates with a number of cosmophysical factors [22–28]. The change of energy in those processes (noise in electronic circuits, α-decay, chemical reactions) varies by tens orders of magnitude, yet the correlations are the same. Evidently, we deal with correlations of a non-energy nature. So we can suggest that the correlations of various processes with the distortions of the lunar orbit reported in [13–21] have a non-energy nature as well.

Thereby we have checked if changes in the shape of histograms constructed from the results of ^{239}Pu α-activity measurements correlate with the deviations of the Moon from the Keplerian orbit. The measurements were carried out at Novo-Lazarevskaya station (Antarctida) and in Pushchino in 2003–2008. Analysing regularities in the change of the histogram shape, we found periods corresponding to the periodical deviations of the Moon from the Keplerian orbit: variation (14.8 days) and evection (31.8 days). The correlations are analogous to those reported earlier [13–21], which suggests a common and very general nature of all these phenomena.

2 Materials and methods

The measurements of ^{239}Pu α-activity were performed at Novo-Lazarevskaya station (Antarctida) and in Pushchino in 2003–2008. α-Activity was monitored continuously, with a second interval, using devices constructed by one of the authors (I. A. Rubinstein). The analysis of data consists in pairwise comparing of histograms constructed from the results of measurements. Histograms were constructed either for 60-point segments of one-second measurements (1-min histograms) or for 60-point segments of one-minute measurements (1-h histograms). All the operations of histogram construction and analysis, as well as calculation of intervals between similar histograms and plotting the corresponding dis-

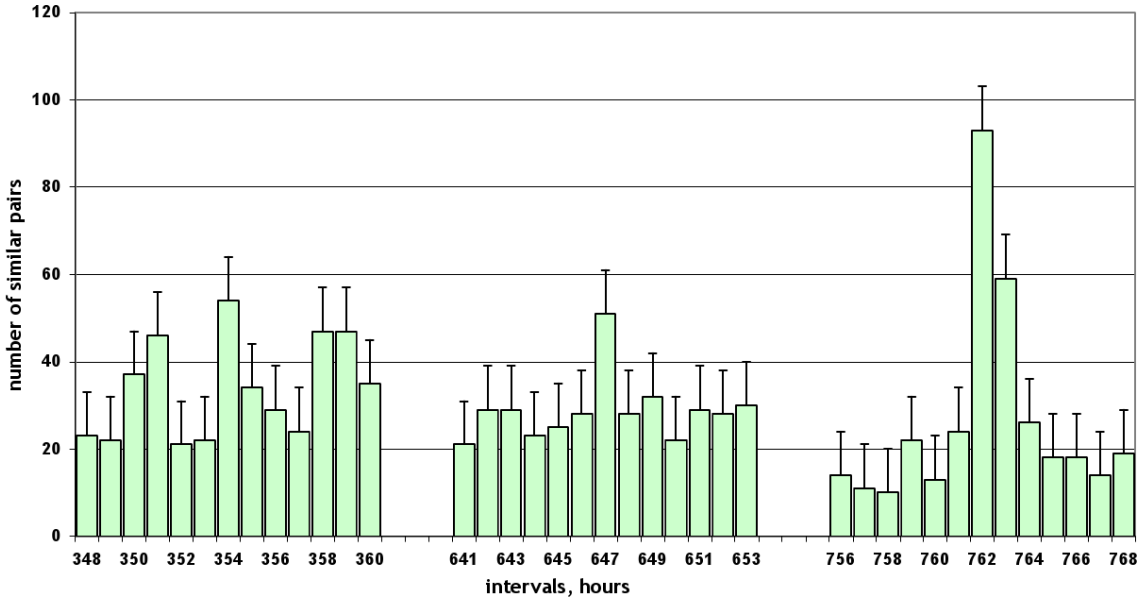

Fig. 1: Comparing 1-h histograms reveals periods equal to 350–354 h (in the region of variation, 14.8 days), 647 h (in the region of the 27-day period) and 762 h (in the region of evection, 31.8 days). In the figure, the number of similar histogram pairs (y-axis) is plotted versus the interval between similar histograms (x-axis, h).

tributions, were conducted with the aid of a computer program written by E. V. Pozharsky [22]. The decision of two histograms to be or not to be similar was made by an expert upon visual evaluation. A detailed description of all the procedures (measurements, histogram construction and analysis) can be found in [22].

3 Results

3.1 The shape of histograms changes with the periods of evection and variation

Figs. 1 and 2 show the results of our search for periodical changes in the shape of histograms constructed from the Antarctic data (Novo-Lazarevskaya station; since May 26, 2005 till the end of the year). We compared series of both 1-min and 1-h histograms in the regions of the putative periods: 762±6 h (a 31-day period, evection), 648±6 h (a 27-day period) and 355±6 h (a 15-day period, variation).

All the expected periods can be seen in Fig. 1. However, the period that corresponds to evection is, *ceteris paribus*, much more pronounced. To be sure that the periods revealed are not artefacts, we repeated the analysis many times with different data. Fig. 2 shows the summary result of five other experiments, in which we compared 1-h histograms constructed from the data obtained on April–October, 2004.

Along with 1-h histograms, we also compared 1-min ones. Fig. 3 shows the results of this analysis, which was made in the region of evection period.

As can be seen in Fig. 3, the 60-fold increase in "resolution" does not change the character of the distribution: there is a sharp extremum, which corresponds to the evection period. It is very surprising. Evection is a rather slow process: its period equals to 31.8 days. Naturally, one minute (out of 45779!) is by no means enough for evection to manifest itself — the distortion of the Keplerian orbit will be negligible. So we believe that the clear periodicity in the alteration of the histogram shape cannot be explained by a slow change of the "effecting force".

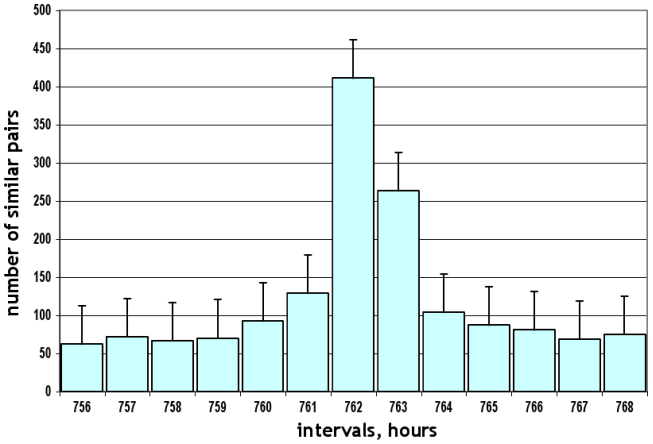

Fig. 2: Determination of the evection period by comparing 1-h histograms constructed from the results of ^{239}Pu α-activity measurements on April–October, 2004 (a summary result of five experiments). Axes are defined as in Fig. 1.

3.2 "Palindrome effects" in the evection periods

It seems that the apparently paradoxal narrowness of the extrema we see in the above figures has a relation to the sharp spatial anisotropy of our world [26–29]. Many observations

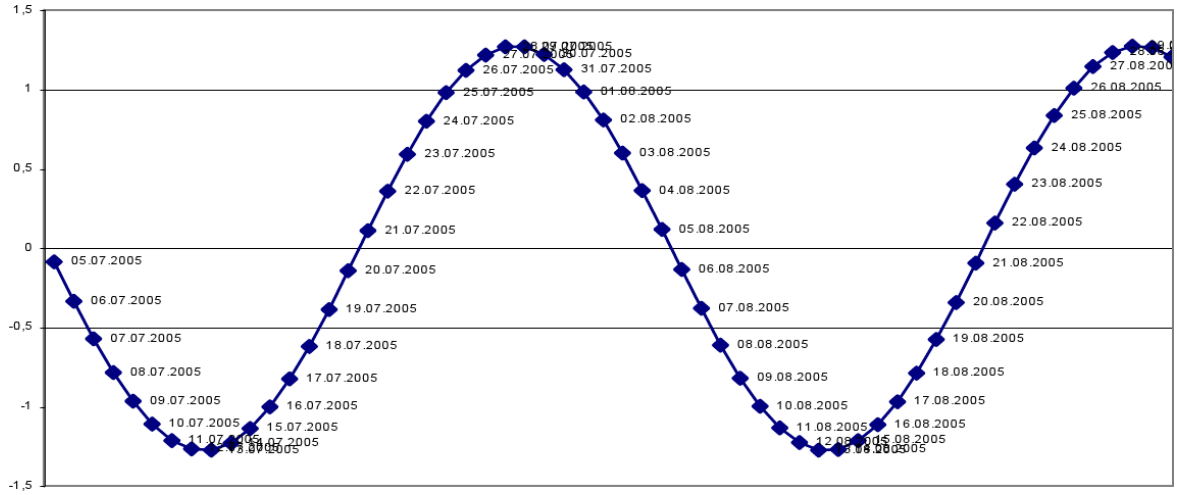

Fig. 4: Evection phenomenon (periodical change of the extent of distortion of the lunar Keplerian orbit) on July–August, 2005. Evection maxima in 2005: May 26, June 26, July 27, August 28–29, September 29–30, November 1 and December 2. Evection minima in 2005: June 10, July 11–12, August 12–13, September 13–14, October 15–16 and November 16.

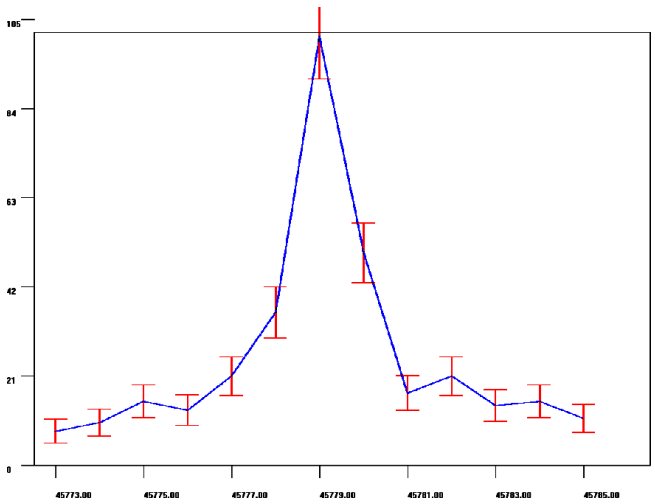

Fig. 3: Comparing 1-min histograms gave an evection period equal to 45779 min (31.79 days). Axes are defined as in Fig. 1.

confirmed this supposition — in particular, the experiments that made use of collimators, isolating narrowly directed beams of α-particles [24–25]. This anisotropy is stable, which is evidenced by the high probability of a certain histogram shape to reappear every time the laboratory has the same orientation towards the sphere of fixed stars. With the Earth rotating about its axis and moving along the circumsolar orbit, the laboratory will repeatedly pass through such points of the same star-related orientation. A manifestation of stable anisotropy of our space is the phenomenon of "palindromes", which is the high probability of a series of "daytime" histograms to be similar to the inverse series of the "nighttime" ones. In the nighttime, the rotation of the Earth is co-directed with its movement along the sircumsolar orbit, this being the opposite in the daytime. As a result, the sequence of "star-orientation points" that the laboratory passes through in the nighttime will be reversibly scanned by the laboratory in the daytime. Accordingly, series of daytime histograms were found to be opposite to the correspondent series of the nighttime ones [27, 28], with the "day-" and "nighttime" being accurately defined as the local time since 6:00 to 18:00 (daytime) and since 18:00 to 6:00 of the next day (nighttime). Figuratively speaking, the rotating Earth consecutively reads the same text first in the direct and then in the inverse order, and the result is the same — as in the phrase "step on no pets".

As it turned out, the histogram series that correspond to the "direct" and "inverse" halfs of the evection cycle are also "palindromes".

The periodical changes of the lunar Keplerian orbit in the evection cycles that correspond to the periods of our measurements are given in Fig. 4. According to this graph, we prepared series of 1-h histograms constructed from the results of ^{239}Pu α-activity measurements. The series were divided into the "odd" and "even" ones, corresponding to the descending and ascending halfs of the evection periods respectively (each half lasting 381.6 h or, more precisely, 22896 min). Then we compared the "odd" series to the "even" ones pairwise, with the even series being of two types: direct and inverse (with the direct and inverse sequence of histograms).

As shown in Fig. 5, there is a high probability of an "even" histogram to be similar to the "odd" one of the same order number when the series of "odd" histograms is inverse. Without inversion, the similarity is much less probable. This is a typical palindrome.

4 Discussion

Thus, the shape of histograms constructed from the results of radioactivity measurements changes in correlation with the distortions of the lunar Keperian orbit caused by the gravita-

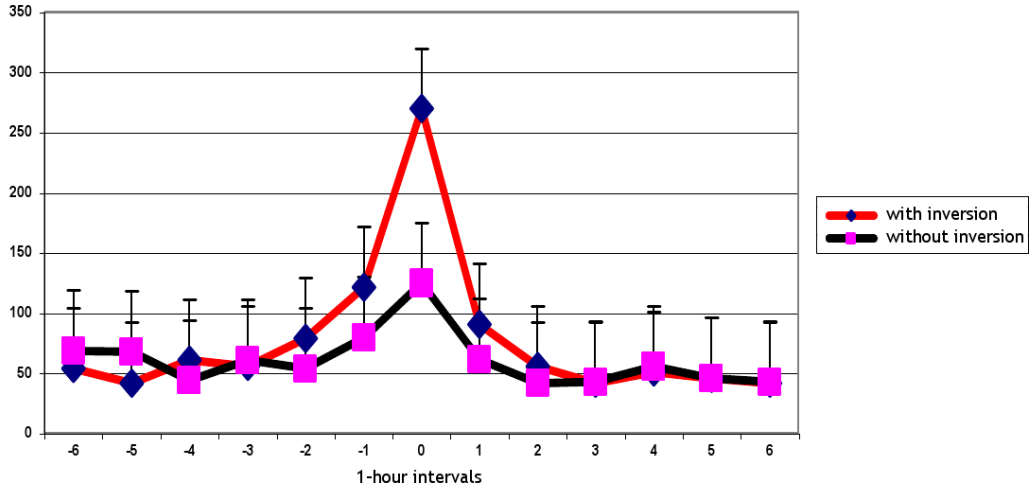

Fig. 5: The palindrome effect. When a series of consecutive 1-h histograms of the 1st (descending) half of the evection period is compared to the corresponding series of the 2nd (ascending) half, the high probability of histograms of the same order number to be similar is observed only in the case of *inversion* of the 2nd histogram series. The figure shows a summary result of analysis of four different sets of data obtained in the period since May 26 to October 1, 2005 at Novo-Lazarevskaya station.

tional influence of the Sun. It changes in the same manner as the processes reported in [13–21]. Taking into account that the phenomenon of "macroscopic fluctuations" (i.e., regular changes in the fine structure of histograms constructed from the results of measurements of natural processes) does not depend on the nature of the process studied [26, 28], one can consider the correlation of the histogram shape with the deviations of the Moon from the Keplerian orbit to be independent of the process nature as well. Since gravitational forces would have no direct impact on physico-chemical and biological processes in terms of energy, the correlations revealed can be considered as resulting from gravitation-induced disturbances in the space geometry. These disturbances, changes of space curvature — to formulate in general, changes of the spacial-temporal scale — should equally manifest themselves in the processes of any nature. The data on strong correlations revealed for the fluctuations of "computer time" [13–21] might be an illustration of such alterations of the spacial-temporal scale.

The phenomena of half-day and half-year palindromes were explained by the repetition of a certain orientation of the Earth towards the Sun [27] and the sphere of fixed stars [28] respectively. Adopting an analogous explanation to the palindrome with the period equal to that of evection (31.8 days) assumes a strong spatial anisotropy caused by the Moon.

Acknowledgements

S. E. Shnoll is thankful to M. N. Kondrashova for permanent discussions and spiritual support. The authors thank their colleagues for valuable discussions. We also appreciate help from the side of T. A. Zenchenko and K. I. Zenchenko, in conducting measurements and maintaining a computer bank of experimental results. We are pleased to thank A. V. Agafonoff for creative English translation. S. E. Shnoll is greatly indebted to D. Rabounski for deep understanding of our results and mental support.

Submitted on July 02, 2009 / Accepted on July 28, 2009

References

1. Chizhevsky A.L. Physical factors of the historical process. Kaluga, 1924 (*in Russian*).
2. Chizhevsky A.L. Terrestrial echo of solar storms. Mysl' Press, Moscow, 1976 (*in Russian*).
3. Vladimirsky B.M. Solar activity and the biosphere: an interdisciplinary problem. *Priroda*, 1994, v. 9, 15–19 (*in Russian*).
4. Solar activity and life. Zinante Press, Riga, 1967 (*in Russian*).
5. Effect of solar activity on the Earth's biosphere. Gnevyshev M. N. and Ol' A. I. (eds.), Nauka Press, Moscow, 1971 (*in Russian*).
6. Sidyakin V.T., Temur'yants N.A., Makeev V.B. and Vladimirsky B.M. Cosmic ecology. Naukova Dumka Press, Kiev, 1985 (*in Russian*).
7. Vladimirsky B.M. and Temur'yants N.A. Effect of solar activity on the biosphere-noosphere. MNEPU Press, Moscow, 2000 (*in Russian*).
8. See numerous papers in *Biofizika* (*in Russian*): no. 3 and 4 (1992); no. 4 and 5 (1995); no. 4 and 5 (1998); no. 7 (2004).
9. Glybin L.Ya. Cosmo-physical aspects of diurnal cyclicity: a concept of temporal organization of the life of human society. *Biofizika*, 1992, v. 37(3), 559–565 (*in Russian*).
10. Dubrov A.P. Lunar rhythms in a human: a brief essay on selenomedicine. Meditsina Press, Moscow, 1990 (*in Russian*).
11. Raybstein B.A., Voinov V.I., Kydryashev V.E. and Chepasov V.I. On the correlation of medical characterisitics with fluc-

tuations of natural gravitational fields. *Biofizika*, 1992, v. 7(3), 524–532 (*in Russian*).

12. Bortnikova G.I. The effect of tidal forces on the periodicity of adrenocortical and thyroidal activity in dogs. *Biofizika*, 1992, v. 7(3), 533–540 (*in Russian*)
13. Gorshkov E.S., Shapovalov S.N., Sokolovsky V.V. and Troshichev O.A. On the detection of impulse cosmophysical radiation. *Biofizika*, 2000, v. 45(5), 947–949 (*in Russian*).
14. Gorshkov E.S., Shapovalov S.N., Sokolovsky V.V. and Troshichev O.A. On the gravitational conditionality of rate fluctuations in the reaction of unithiol oxidation by nitrite ions. *Biofizika*, 2000, v. 45(4), 631–635 (*in Russian*).
15. Shapovalov S.N., Gorshkov E.S., Troshichev O.A., Borisova T.D. and Frank-Kamenetsky A.V. Stochastic fluctuations in the readings of measuring devices: effects of cosmophysical influence? *Biofizika*, 2001, v. 46(6), 819–822 (*in Russian*).
16. Shapovalov S.N. Principles of physical indication of cosmogeophysical ecological factors of non-electromagnetic nature. PhD Thesis, AANII and RGGMU Press, St. Petersburg, 2003 (*in Russian*).
17. Shapovalov S.N., Gorshkov E.S., Troshichev O.A., Borisova T.D., Frank-Kamenetsky A.V. Effects of non-electromagnetic disturbances from the Sun in "computer time" instability. *Biophysics*, 2004, v. 49(1), S79–S84.
18. Sokolovsky V.V., Gorshkov E.S., Ivanov V.V., Shapovalov S.N. and Troshichev O.A. Relation of the regular gravitational field variations to biochemical processes observed in vitro and in vivo. *Biophysics*, 2004, v. 49(1), S85–S91.
19. Shapovalov S.N., Gorshkov E.S., Troshichev O.A. Cosmophysical effects observed in impulses of the microphotocolorimeter current. *Biophysics*, 2004, v. 49(1), S119–S122.
20. Troshichev O.A., Gorshkov E.S., Shapovalov S.N., Sokolovskii V.V. , Ivanov V.V., Vorobeitchikov V.M. Variation of the gravitational field as a motive power for rhythmics of biochemical processes. *Advances in Space Research*, 2004, v. 34, 1619–1624.
21. Shapovalov S.N., Troshichev O.A., Povazhny V.I., Sokolovsky V.V., Vorobeychikov V.M., Gorshkov E.S., Lozovsky V.T. and Alexandrova A.B. Cosmophysical regularities in the photoeffect experiment. *Meteorologichesky Vestnik*, 2008, v. 1(1), 1–23 (*in Russian*).
22. Shnoll S.E., Kolombet V.A., Pozharsky E.V., Zenchenko T.A., Zvereva I.M. and Konradov A.A. On the cosmophysical conditionality of "macroscopic fluctuations". *Biofizika*, 1998, v. 43(5), 909–915 (*in Russian*).
23. Shnoll S.E., Rubinstein I.A., Zenchenko K.I., Zenchenko T.A., Udaltsova N.V., Konradov A.A., Shapovalov S.N., Makarevich A.V., Gorshkov E.S. and Troshichev O.A. Dependence of "macroscopic fluctuations" on geographical coordinates (on the basis of materials of the Arctic (2000) and Antarctic (2001) expeditions). *Biofizika*, 2003, v. 48(6), 1123–1131 (*in Russian*).
24. Shnoll S.E., Zenchenko K.I., Berulis I.I., Udaltsova N.V., Zhirkov S.S. and Rubinstein I.A. Dependence of "macroscopic fluctuations" on cosmophisical factors. Space anisotropy. *Biofizika*, 2004, v. 49(1), 132–139 (*in Russian*)
25. Shnoll S.E., Rubinshtejn I.A., Zenchenko K.I., Shlekhtarev V.A., Kaminsky A.V., Konradov A.A. and Udaltsova N.V. Experiments with rotating collimators cutting out pencil of alpha-particles at radioactive decay of Pu-239 evidence sharp anisotropy of space. *Progress in Physics*, 2004, v. 1, 81–84.
26. Shnoll S.E. Changes in fine structure of stochastic distributions as a consequence of space-time fluctuations. *Progress in Physics*, 2006, v. 2, 39–45.
27. Shnoll S.E., Pancheluga V.A. and Shnoll A.E. The palindrom effect. *Progress in Physics*, 2008, v. 2, 151–153.
28. Shnoll S.E. The "scattering of the results of measurements" of processes of diverse nature is determined by the Earth's motion in the inhomogeneous space-time continuum. The effect of "half-year palindromes". *Progress in Physics*, 2009, v. 1, 3–7.
29. Shnoll S.E. and Rubinstein I.A. "Regular changes in the fine structure of histograms reaveled in the experiments with collimators which isolate beams of alpha-particles flying at certain directions". *Progress in Physics*, 2009, v. 2, 33–95.
30. Astronomical calendar (invariant part). Nauka Press, Moscow, 1981 (*in Russian*).

Astrophysically Satisfactory Solutions to Einstein's R-33 Gravitational Field Equations Exterior/Interior to Static Homogeneous Oblate Spheroidal Masses

Chifu Ebenezer Ndikilar

Physics Department, Gombe State University, P.M.B. 127, Gombe, Gombe State, Nigeria
E-mail: ebenechifu@yahoo.com

In this article, we formulate solutions to Einstein's geometrical field equations derived using our new approach. Our field equations exterior and interior to the mass distribution have only one unknown function determined by the mass or pressure distribution. Our obtained solutions yield the unknown function as generalizations of Newton's gravitational scalar potential. Thus, our solution puts Einstein's geometrical theory of gravity on same footing with Newton's dynamical theory; with the dependence of the field on one and only one unknown function comparable to Newton's gravitational scalar potential. Our results in this article are of much significance as the Sun and planets in the solar system are known to be more precisely oblate spheroidal in geometry. The oblate spheroidal geometries of these bodies have effects on their gravitational fields and the motions of test particles and photons in these fields.

1 Introduction

After the publication of A. Einstein's geometrical theory of gravitation in 1915/1916, the search for exact solutions to its inherent geometrical field equations for various mass distributions began [1]. Four well known approaches have so far been proposed.

The first approach is to seek a mapping under which the metric tensor assumed a simple form, such as the vanishing of the off-diagonal components.With sufficiently clever assumptions of this sort, it is often possible to reduce the Einstein field equations to a much simpler system of equations, even a single partial differential equation (as in the case of stationary axisymmetric vacuum solutions, which are characterised by the Ernst equation) or a system of ordinary differential equations (this led to the first exact analytical solution — the famous Schwarzschild's solution [2]). A special generalization of the Schwarzschild's metric is the Kerr metric. This metric describes the geometry of space time around a rotating massive body.

The second method assumes that the metric tensor has symmetries-assumed forms of the Killing vectors. This led to the solution found by Weyl and Levi-Civita [3–6]. The third approach required that the metric tensor leads to a particular type of the classifications of Weyl and Riemann — Christoffel tensors. These are often stated interms of Petrov classification of the possible symmetries of the Weyl tensor or the Segre classification of the possible symmetries of the Ricci tensor. This leds to plane fronted wave solutions [3–6]. It is worth remarking that even after the symmetry reductions in the three methods above, the reduced system of equations is often difficult to solve. The fourth approach is to seek Taylor series expansion of some initial value hyper surface, subject to consistent initial value data. This method has not proved successful in generating solutions [3–6].

Recently [7–12], we introduced our own method and approach to formulation of exact analytical solutions as an extension of Schwarzschild's method. In this article, we show how exact analytical solutions of order c^{-2} (where c is the speed of light in vacuum) can be constructed in gravitational fields interior and exterior to static homogeneous oblate spheroids placed in empty space. For the sake of mathematical convenience we choose to use the 3rd (R_{33}) field equation [7].

2 Exterior field equation

The covariant metric tensor in the gravitational field of a static homogeneous oblate spheroid in oblate spheroidal coordinates (η, ξ, ϕ) has been obtained [7, 12] as

$$g_{00} = \left(1 + \frac{2}{c^2} f(\eta, \xi)\right), \tag{2.1}$$

$$g_{11} = -\frac{a^2}{1+\xi^2-\eta^2} \times \times \left[\eta^2 \left(1 + \frac{2}{c^2} f(\eta, \xi)\right)^{-1} + \frac{\xi^2(1+\xi^2)}{(1-\eta^2)}\right], \tag{2.2}$$

$$g_{12} \equiv g_{21} = -\frac{a^2\eta\xi}{1+\xi^2-\eta^2} \left[1 - \left(1 + \frac{2}{c^2} f(\eta, \xi)\right)^{-1}\right], \tag{2.3}$$

$$g_{22} = -\frac{a^2}{1+\xi^2-\eta^2} \times \times \left[\xi^2 \left(1 + \frac{2}{c^2} f(\eta, \xi)\right)^{-1} + \frac{\eta^2(1-\eta^2)}{(1+\xi^2)}\right], \tag{2.4}$$

$$g_{33} = -a^2(1+\xi^2)(1-\eta^2), \tag{2.5}$$

$$g_{\mu\nu} = 0; \text{ otherwise}, \tag{2.6}$$

$$g^{00}=\left[1+\frac{2}{c^2}f(\eta,\xi)\right]^{-1} \tag{2.7}$$

$$g^{11}=\frac{-\left(1-\eta^2\right)\left(1+\xi^2-\eta^2\right)\left[\eta^2\left(1-\eta^2\right)+\xi^2\left(1+\xi^2\right)\left(1+\frac{2}{c^2}f(\eta,\xi)\right)^{-1}\right]}{a^2\left(1+\frac{2}{c^2}f(\eta,\xi)\right)^{-1}\left[\eta^2\left(1-\eta^2\right)+\xi^2\left(1+\xi^2\right)\right]^2} \tag{2.8}$$

$$g^{12}\equiv g^{21}=\frac{-\eta\xi\left(1-\eta^2\right)\left(1+\xi^2\right)\left(1+\xi^2-\eta^2\right)\left[1-\left(1+\frac{2}{c^2}f(\eta,\xi)\right)^{-1}\right]}{a^2\left(1+\frac{2}{c^2}f(\eta,\xi)\right)^{-1}\left[\eta^2\left(1-\eta^2\right)+\xi^2\left(1+\xi^2\right)\right]^2} \tag{2.9}$$

$$g^{22}=\frac{-\left(1+\xi^2\right)\left(1+\xi^2-\eta^2\right)\left[\xi^2\left(1+\xi^2\right)+\eta^2\left(1-\eta^2\right)\left(1+\frac{2}{c^2}f(\eta,\xi)\right)^{-1}\right]}{a^2\left(1+\frac{2}{c^2}f(\eta,\xi)\right)^{-1}\left[\eta^2\left(1-\eta^2\right)+\xi^2\left(1+\xi^2\right)\right]^2} \tag{2.10}$$

$$g^{33}=-\left[a^2\left(1+\xi^2\right)\left(1-\eta^2\right)\right]^{-1} \tag{2.11}$$

$$g^{\mu\nu}=0 \text{ otherwise} \tag{2.12}$$

$$\begin{aligned}
&-g^{00}g^{00}g_{00,12}-g^{00}g^{11},_2\,g_{00,1}-g^{00}g^{12}g_{00,22}-g^{00}g^{12},_2\,g_{00,2}-g^{00}g^{21},_2\,g_{00,1}-\\
&-g^{00}g^{22}g_{00,22}-g^{00}g^{22},_2\,g_{00,2}-g^{00}g^{11}g^{22}g_{00,1}g_{22,1}-g^{00}g^{11}g^{33}g_{00,1}g_{33,1}-\\
&-g^{00}g^{12}g^{12}g_{00,2}g_{12,1}-g^{00}g^{12}g^{33}g_{00,2}g_{33,1}-g^{00}g^{11}g^{21}g_{00,1}g_{11,2}-\\
&-g^{00}g^{21}g^{12}g_{00,1}g_{12,2}-g^{00}g^{21}g^{33}g_{00,1}g_{33,2}-\tfrac{1}{2}\,g^{00}g^{22}g^{33}g_{00,2}g_{33,2}-\\
&-g^{00}g^{11}g_{00,11}-g^{11}g^{00},_1\,g_{00,1}-g^{11}g^{12},_1\,g_{11,2}-2g^{11}g^{22}g_{22,11}-g^{11}g^{22},_1\,g_{22,1}-\\
&-g^{11}g^{33},_1\,g_{33,1}+4g^{11}g^{21}g_{11,12}+g^{11}g^{21},_2\,g_{11,1}+4g^{11}g^{22}g_{12,12}-2g^{11}g^{22}g_{11,22}+\\
&+g^{11}g^{22},_2\,g_{11,2}-g^{11}g^{11}g^{22}g_{11,2}g_{12,1}+g^{00}g^{11}g^{22}g_{00,2}g_{12,1}-g^{00}g^{11}g^{22}g_{00,2}g_{11,2}+\\
&+g^{11}g^{22}g^{22}g_{12,1}g_{22,1}-\tfrac{1}{2}\,g^{11}g^{22}g^{22}g_{11,2}g_{22,1}+g^{11}g^{22}g^{33}g_{12,1}g_{33,2}-\\
&-\tfrac{1}{2}\,g^{11}g^{22}g^{33}g_{11,2}g_{33,2}+\tfrac{1}{2}\,g^{11}g^{21}g^{22}g_{11,1}g_{22,1}-g^{11}g^{21}g^{21}g_{11,2}g_{11,2}+\\
&+g^{11}g^{21}g^{12}g_{11,2}g_{12,1}-g^{22}g^{00}g_{00,12}-g^{22}g^{00},_2\,g_{00,1}-g^{22}g^{11},_2\,g_{00,1}-g^{22}g^{11},_2\,g_{11,2}-\\
&-g^{22}g^{12},_2\,g_{22,1}-g^{22}g^{33}g_{33,22}-g^{22}g^{33},_2\,g_{33,2}+g^{22}g^{12},_1\,g_{22,2}+g^{22}g^{11},_1\,g_{12,2}-\\
&-g^{22}g^{11},_1\,g_{22,1}+\tfrac{1}{2}\,g^{00}g^{22}g^{22}g_{00,2}g_{22,2}-g^{12}g^{12}g^{22}g_{11,2}g_{22,2}+\\
&+\tfrac{1}{2}\,g^{00}g^{12}g^{22}g_{00,1}g_{22,2}+\tfrac{1}{2}\,g^{11}g^{12}g^{22}g_{11,1}g_{22,2}+\tfrac{1}{2}\,g^{12}g^{22}g^{33}g_{22,2}g_{33,1}-\\
&-g^{11}g^{22}g^{22}g_{12,2}g_{22,1}+g^{00}g^{11}g^{22}g_{00,1}g_{12,2}+g^{11}g^{11}g^{22}g_{11,1}g_{12,2}+g^{11}g^{22}g^{33}g_{12,2}g_{33,1}+\\
&+\tfrac{1}{2}\,g^{11}g^{22}g^{22}g_{11,2}g_{22,2}+g^{12}g^{12}g^{22}g_{12,2}+\tfrac{1}{2}\,g^{12}g^{12}g^{22}g_{22,1}g_{22,1}-\\
&-\tfrac{1}{2}\,g^{12}g^{22}g^{33}g_{12,2}g_{33,2}+\tfrac{1}{2}\,g^{12}g^{22}g^{33}g_{22,1}g_{33,2}+g^{33}g^{11},_1\,g_{33,1}+g^{33}g^{12},_1\,g_{33,2}+\\
&+2g^{21}g^{33}g_{33,12}-g^{33}g^{21},_2\,g_{33,1}-g^{22}g^{33}g_{33,22}-g^{33}g^{22},_2\,g_{33,2}-g^{11}g^{22}g^{33}g_{22,1}g_{33,1}-\\
&-g^{12}g^{12}g^{33}g_{12,1}g_{33,2}-\tfrac{1}{2}\,g^{12}g^{22}g^{33}g_{22,1}g_{33,2}-g^{21}g^{21}g^{33}g_{12,2}g_{33,1}-\\
&-\tfrac{1}{2}\,g^{21}g^{22}g^{33}g_{22,2}g_{33,1}-\tfrac{1}{2}\,g^{00}g^{22}g^{33}g_{00,2}g_{33,2}-\tfrac{1}{2}\,g^{11}g^{22}g^{33}g_{11,2}g_{33,2}+\\
&+g^{00}g^{12}g_{00,12}+2g^{12}g^{00},_2\,g_{00,1}+2g^{12}g^{11},_2\,g_{11,1}+4g^{12}g^{12}g_{12,12}+4g^{12}g^{12},_2\,g_{12,1}-2g^{12}g^{12}g_{11,22}-\\
&-2g^{12}g^{12},_2\,g_{11,2}+2g^{12}g^{33},_2\,g_{33,1}+2g^{12}g^{11},_1\,g_{11,2}+2g^{12}g^{12}g_{22,11}+2g^{12}g^{12},_1\,g_{22,1}+\\
&+g^{00}g^{11}g^{12}g_{00,1}g_{11,2}+g^{00}g^{12}g^{12}g_{00,1}g_{22,1}+g^{00}g^{12}g^{21}g_{00,2}g_{11,2}+g^{11}g^{12}g^{21}g_{11,2}g_{11,2}+\\
&+g^{12}g^{12}g^{12}g_{11,2}g_{22,1}+g^{12}g^{21}g^{33}g_{11,2}g_{33,2}+g^{12}g^{12}g^{33}g_{22,1}g_{33,1}-g^{11}g^{12}g^{21}g_{11,1}g_{12,2}-\\
&-g^{12}g^{21}g^{12}g_{11,1}g_{22,2}-g^{12}g^{21}g^{22}g_{12,1}g_{22,2}-g^{11}g^{12}g^{22}g_{11,2}g_{22,1}+g^{12}g^{12}g^{22}g_{11,2}g_{22,2}=0
\end{aligned} \tag{2.18}$$

and the contravariant metric tensor is as shown in formulas (2.7)–(2.12), where $f(\eta,\xi)$ is an unknown function determined by the mass distribution. From this covariant metric tensor, we can then construct our field equations for the gravitational field after formulating the Coefficients of affine connection, Riemann Christoffel tensor, Ricci tensor and the Einstein tensor [7–12]. After the above steps, it can be shown that the exterior R_{33} field equation in this gravitational field is given as;

$$R_{33} - \frac{1}{2} R g_{33} = 0 . \tag{2.13}$$

or more explicitly interms of the affine connections, Ricci tensor and covariant metric tensor as;

$$\begin{aligned} &-\Gamma^1_{33}\Gamma^0_{10} - \Gamma^2_{33}\Gamma^0_{20} - \Gamma^1_{33,1} - \Gamma^1_{33}\Gamma^1_{11} - \Gamma^2_{33}\Gamma^1_{21}\Gamma^3_{31}\Gamma^1_{33} - \\ &- \Gamma^2_{33,2} - \Gamma^1_{33}\Gamma^2_{12} - \Gamma^2_{33}\Gamma^2_{22} + \Gamma^3_{32}\Gamma^2_{33} - \frac{1}{2} R g_{\alpha\beta} = 0 \end{aligned} \tag{2.14}$$

with the symbols and numbers having their usual meaning and

$$R = g^{00}R_{00} + g^{11}R_{11} + 2g^{12}R_{12} + g^{22}R_{22} + g^{33}R_{33} . \tag{2.15}$$

Now, multiplying equation (2.13) by $2g^{33}$ and using the fact that $g^{33}g_{33} = 1$ yields

$$2g^{33}R_{33} - R = 0 . \tag{2.16}$$

Writing the expression for the curvature scalar,R as in equation (2.15) gives;

$$\begin{aligned} &-g^{00}R_{00} - g^{11}R_{11} - 2g^{12}R_{12} - \\ &- g^{22}R_{22} + g^{33}R_{33} = 0 . \end{aligned} \tag{2.17}$$

Writing the various terms of the field equation (2.17) explicitly in terms of the metric tensor gives our field equation explicitly as (2.18).

Now, we realize that our covariant metric tensor (2.1)–(2.6) can be written equally as

$$g_{\mu\nu}(\eta,\xi) = h_{\mu\nu}(\eta,\xi) + f_{\mu\nu}(\eta,\xi) , \tag{2.19}$$

where $h_{\mu\nu}$ are the well known pure empty space components and $f_{\mu\nu}$ are the contributions due to the oblate spheroidal mass distribution. Consequently, as the mass distribution decays out; $f_{\mu\nu} \to 0$ and hence $g_{\mu\nu} \to h_{\mu\nu}$. Therefore, the metric tensor reduces to the pure empty space metric tensor as the distribution of mass decays out. Also,

$$g^{\mu\nu}(\eta,\xi) = h^{\mu\nu}(\eta,\xi) + f^{\mu\nu}(\eta,\xi) , \tag{2.20}$$

where $h^{\mu\nu}$ are the well known pure empty space components and $f^{\mu\nu}$ are the contributions due to the oblate spheroidal mass distribution. Thus it can be shown that for this field, the non zero metric components can be written as;

$$h_{00} = 1 , \tag{2.21}$$

$$h_{11} = -\frac{a^2\left(\eta^2+\xi^2\right)}{1-\eta^2} , \tag{2.22}$$

$$h_{22} = -\frac{a^2\left(\eta^2+\xi^2\right)}{1+\eta^2} , \tag{2.23}$$

$$h_{33} = -a^2\left(1+\eta^2\right)\left(1+\xi^2\right) , \tag{2.24}$$

$$f_{00} = \frac{2}{c^2} f , \tag{2.25}$$

$$f_{11} = -\frac{a^2\eta^2}{\left(1-\eta^2+\xi^2\right)} \sum_{n=1}^{\infty} \binom{-1}{n} \frac{2^n}{c^n} f^n , \tag{2.26}$$

$$f_{12} \equiv f_{21} = -\frac{a^2\eta\xi}{\left(1-\eta^2+\xi^2\right)} \sum_{n=1}^{\infty} \binom{-1}{n} \frac{2^n}{c^n} f^n , \tag{2.27}$$

$$f_{22} = -\frac{a^2\xi^2}{\left(1-\eta^2+\xi^2\right)} \sum_{n=1}^{\infty} \binom{-1}{n} \frac{2^n}{c^n} f^n , \tag{2.28}$$

also,

$$h^{00} = \frac{1}{h_{00}} , \tag{2.29}$$

$$h^{11} = \frac{1}{h_{11}} , \tag{2.30}$$

$$h^{22} = \frac{1}{h_{22}} , \tag{2.31}$$

$$h^{33} = \frac{1}{h_{33}} , \tag{2.32}$$

$$f^{00} = \sum_{n=1}^{\infty} \binom{-1}{n} \frac{2^n}{c^n} f^n , \tag{2.33}$$

$$f^{11} = -\frac{f_{11}}{(h_{11})^2} + 0\left(c^{-4}\right) , \tag{2.34}$$

$$f^{12} \equiv f^{21} = -\frac{f_{12}}{h_{11}h_{22}} + 0\left(c^{-4}\right) , \tag{2.35}$$

$$f^{22} = -\frac{f_{22}}{(h_{22})^2} + 0\left(c^{-4}\right) . \tag{2.36}$$

To begin the explicit formulation of the R_{33} field equation we note, first of all, that all the terms of order c^0 cancel out identically since the empty space time metric tensor $h_{\mu\nu}$ independently satisfies the homogeneous R_{33} field equation. Therefore the lowest order of terms we expect in the exterior R_{33} field equation is c^{-2}. Hence in order to formulate the exterior R_{33} field equation of order c^{-2}, let us decompose our covariant metric tensor $g_{\mu\nu}$ into pure empty space part $h_{\mu\nu}$ (of order c^0 only) and the nonempty space part $f_{\mu\nu}$ (of order c^{-2} or higher). Similarly, let our contravariant metric tensor $g^{\mu\nu}$ be decomposed into pure empty space part $h^{\mu\nu}$ (of order c^0 only) and the nonempty space part $f^{\mu\nu}$ (of order c^{-2} or higher). Substituting explicit expressions for equations (2.19) and (2.20) into equation (2.18) and neglecting all terms of order c^0, the exterior R_{33} field equation can be written as (2.37), where the coefficients are given as (2.38)–(2.58).

$$S_1(\eta,\xi)\,f_{22,11}+S_2(\eta,\xi)\,f_{00,11}+S_3(\eta,\xi)\,f_{12,12}+S_4(\eta,\xi)\,f_{00,12}+S_5(\eta,\xi)\,f_{11,22}+$$
$$+S_6(\eta,\xi)\,f_{00,22}+S_7(\eta,\xi)\,f_{00,1}+S_8(\eta,\xi)\,f_{12,1}+S_9(\eta,\xi)\,f_{22,1}+S_{10}(\eta,\xi)\,f^{11},_1+$$
$$+S_{11}(\eta,\xi)\,f^{12},_1+S_{12}(\eta,\xi)\,f^{22},_1+S_{13}(\eta,\xi)\,f_{00,2}+S_{14}(\eta,\xi)\,f_{11,2}+S_{15}(\eta,\xi)\,f_{12,2}+ \tag{2.37}$$
$$+S_{16}(\eta,\xi)\,f_{22,2}+S_{17}(\eta,\xi)\,f^{12},_2+S_{18}(\eta,\xi)\,f^{22},_2+S_{19}(\eta,\xi)\,f^{11}+S_{20}(\eta,\xi)\,f^{12}+$$
$$+S_{21}(\eta,\xi)\,f^{22}=0$$

$$S_1(\eta,\xi)=-2h^{11}h^{22} \tag{2.38}$$

$$S_2(\eta,\xi)=-h^{11} \tag{2.39}$$

$$S_3(\eta,\xi)=4h^{11}h^{22} \tag{2.40}$$

$$S_4(\eta,\xi)=-h^{11}-h^{22} \tag{2.41}$$

$$S_5(\eta,\xi)=-2h^{11}h^{22} \tag{2.42}$$

$$S_6(\eta,\xi)=-h^{22} \tag{2.43}$$

$$S_7(\eta,\xi)=-h^{11},_2-h^{11}h^{22}h_{22,1}-h^{11}h^{33}h_{33,1} \tag{2.44}$$

$$S_8(\eta,\xi)=h^{11}h^{22},_2+h^{11}h^{22}\left(h^{33}h_{33,2}+h^{22}h_{22,1}-h^{11}h_{11,2}\right) \tag{2.45}$$

$$S_9(\eta,\xi)=-h^{11}h^{22}\left(h^{33}h_{33,1}+\tfrac{1}{2}\,h^{22}h_{11,2}\right)-h^{22}h^{11},_1-h^{11}h^{22},_1 \tag{2.46}$$

$$S_{10}(\eta,\xi)=-h^{22}h_{22,1}+h^{33}h_{33,1} \tag{2.47}$$

$$S_{11}(\eta,\xi)=h^{22}h_{22,2}+h^{33}h_{33,2} \tag{2.48}$$

$$S_{12}(\eta,\xi)=-h^{11}h_{22,1} \tag{2.49}$$

$$S_{13}(\eta,\xi)=-h^{22},_2-h^{22}h^{33}h_{33,2}+\tfrac{1}{2}\,h^{22}h^{22}h_{22,2}-h^{11}h^{22}h_{11,2} \tag{2.50}$$

$$S_{14}(\eta,\xi)=-h^{11}h^{22},_2-h^{22}h^{11},_2+\frac{1}{2}\,h^{11}h^{22}\left(-h^{22}h_{22,1}+h^{22}h_{22,2}-h^{33}h_{33,2}\right) \tag{2.51}$$

$$S_{15}(\eta,\xi)=h^{22}h^{11},_1+h^{11}h^{22}\left(h^{33}h_{33,1}+h^{11}h_{11,1}-h^{22}h_{22,1}\right) \tag{2.52}$$

$$S_{16}(\eta,\xi)=\tfrac{1}{2}\,h^{11}h^{22}h^{22}h_{11,2} \tag{2.53}$$

$$S_{17}(\eta,\xi)=h^{11}h_{11,1}-h^{22}h_{22,1}-h^{33}h_{33,1} \tag{2.54}$$

$$S_{18}(\eta,\xi)=-h^{11}h_{11,1}-h^{33}h_{33,2} \tag{2.55}$$

$$S_{19}(\eta,\xi)=-h^{22}h^{33}h_{33,2}-h^{22}h^{33}h_{33,1}+h^{22}h^{22}h_{11,2}h_{22,2}-$$
$$-h^{22}h^{33}h_{11,2}h_{33,2}-\tfrac{1}{2}\,h^{22}h^{22}h_{11,2}h_{22,1}-h^{22},_2\,h_{11,2}-2h^{22}h_{11,22}-h^{33},_1\,h_{33,1}- \tag{2.56}$$
$$-h^{22},_1\,h_{22,1}-2h^{22}h_{22,11}$$

$$S_{20}(\eta,\xi)=4h^{11}h_{11,12}+\tfrac{1}{2}\,h^{11}h^{22}h_{11,1}\left(h_{22,1}+h_{22,2}\right)+$$
$$+\tfrac{1}{2}\,h^{22}h^{33}h_{22,1}h_{33,2}+2h^{33}h_{33,12}-\tfrac{1}{2}\,h^{22}h^{33}h_{22,1}+2h^{11},_2\,h_{11,1}+2h^{33},_2\,h_{33,1}+ \tag{2.57}$$
$$+2h^{11},_1\,h_{11,2}-h^{11}h^{22}h_{11,2}h_{22,1}$$

$$S_{21}(\eta,\xi)=-\tfrac{1}{2}\,h^{11}h^{33}h_{33,2}+h^{11}h^{22}h_{11,2}h_{22,2}-h^{11}h^{22}h_{11,2}h_{22,1}-$$
$$-\tfrac{1}{2}\,h^{11}h^{33}h_{11,2}h_{33,2}-2h^{33}h_{33,22}-h^{11}h^{33}h_{33,1}-h^{11},_2\,h_{11,2}-h^{33},_2\,h_{33,2}- \tag{2.58}$$
$$-h^{11},_1\,h_{22,1}-2h^{11}h_{22,11}-2h^{11}h_{11,22}\,.$$

$$K_1(\eta,\xi) f_{\eta\eta} + K_2(\eta,\xi) f_{\eta\xi} + K_3(\eta,\xi) f_{\xi\xi} + K_4(\eta,\xi) f_\eta + K_5(\eta,\xi) f_\xi + K_6(\eta,\xi) f = 0 \tag{2.59}$$

$$K_1(\eta,\xi) = \frac{2\left(1-\eta^2\right)\left(1-\eta^2+\xi^2\right) - 2a^4\xi^2\left(\eta^2+\xi^2\right)}{a^2c^2\left(\eta^2+\xi^2\right)\left(1-\eta^2+\xi^2\right)} \tag{2.60}$$

$$K_2(\eta,\xi) = \frac{4\left(\eta^2+\xi^2\right)\left(1-\eta^2+\xi^2\right) - 8\eta\xi\left(1-\eta^4\right)}{a^2c^2\left(\eta^2+\xi^2\right)^2\left(1-\eta^2+\xi^2\right)} \tag{2.61}$$

$$K_3(\eta,\xi) = \frac{2\left(1+\eta^2\right)}{a^2c^2\left(\eta^2+\xi^2\right)} \tag{2.62}$$

$$\begin{aligned} K_4(\eta,\xi) = {} & \frac{-8a^2\eta\xi^2 S_1(\eta,\xi) + 2a^2\xi^2 S_9(\eta,\xi)}{c^2\left(1-\eta^2+\xi^2\right)^2} - \frac{8\xi\left(1-\eta^4\right)\left(1-\eta^2-\xi^2\right)}{a^2c^2\left(\eta^2+\xi^2\right)^2\left(1-\eta^2+\xi^2\right)^2} + \\ & + \frac{2a^2\eta^2 S_{10}(\eta,\xi)}{c^2\left(h_{11}\right)^2\left(1-\eta^2+\xi^2\right)} + \frac{2a^2\eta\xi S_{11}(\eta,\xi)}{c^2 h_{11}h_{22}\left(1-\eta^2+\xi^2\right)} - \frac{2a^2\xi^2 S_{12}(\eta,\xi)}{c^2\left(h_{22}\right)^2\left(1-\eta^2+\xi^2\right)} \end{aligned} \tag{2.63}$$

$$\begin{aligned} K_5(\eta,\xi) = {} & \frac{-8\xi\left(1+\eta^2+\xi^2\right)}{a^2c^2\left(\eta^2+\xi^2\right)^2\left(1-\eta^2+\xi^2\right)^2} + \frac{16\eta^2\xi\left(1-\eta^4\right)}{a^2c^2\left(\eta^2+\xi^2\right)^2\left(1-\eta^2+\xi^2\right)} + \frac{2\left[S_9(\eta,\xi)+S_{13}(\eta,\xi)\right]}{c^2} + \\ & + \frac{2a^2\eta\xi\left[-S_8(\eta,\xi)-S_{15}(\eta,\xi)+\xi S_{16}(\eta,\xi)\right]}{c^2\left(h_{11}\right)^2\left(1-\eta^2+\xi^2\right)} + + \frac{2a^2\eta\xi S_{17}(\eta,\xi)}{c^2 h_{11}h_{22}\left(1-\eta^2+\xi^2\right)} - \frac{2a^2\xi^2 S_{17}(\eta,\xi)}{c^2\left(h_{22}\right)^2\left(1-\eta^2+\xi^2\right)} \end{aligned} \tag{2.64}$$

$$\begin{aligned} K_6(\eta,\xi) = {} & \frac{-4a^2\xi^2\left(1+3\eta^2+\xi^2\right)}{c^2\left(1-\eta^2+\xi^2\right)^3} - \frac{8\left(1-\eta^4\right)\left(1-\eta^4-\xi^4-10\eta^2\xi^2\right)}{a^2c^2\left(\eta^2+\xi^2\right)^2\left(1-\eta^2+\xi^2\right)^3} + \frac{8\eta^2\left(1-\eta^2\right)}{a^2c^2\left(\eta^2+\xi^2\right)\left(1-\eta^2+\xi^2\right)^2} + \\ & + \frac{2a^2\left[-\eta\left(1+\eta^2+\xi^2\right)S_8(\eta,\xi) + 2\eta\xi^2 S_9(\eta,\xi) - \eta\left(1-\eta^2-\xi^2\right)S_{15}(\eta,\xi) + 2\xi\left(1-\eta^2\right)S_{16}(\eta,\xi)\right]}{c^2\left(1-\eta^2+\xi^2\right)^2} - \\ & - \frac{-2a^2\eta^2\left(h_{11}\right)^2{}_{,1}\,S_{10}(\eta,\xi)}{c^2\left(h_{11}\right)^4\left(1-\eta^2+\xi^2\right)} + \frac{2a^2\eta^2\left[2\left(1+\xi^2\right)S_{10}(\eta,\xi) - S_{19}(\eta,\xi)\right]}{c^2\left(h_{11}\right)^2\left(1-\eta^2+\xi^2\right)} + \frac{2a^2\xi\left(1+\eta^2+\xi^2\right)S_{11}(\eta,\xi)}{c^2 h_{11}h_{22}} - \\ & - \frac{2a^2\eta\xi\left[\left(h_{11}h_{22}\right)_{,1}S_{11}(\eta,\xi)\right]}{c^2\left(h_{11}h_{22}\right)^2\left(1-\eta^2+\xi^2\right)} + \frac{2a^2\xi\left[\left(h_{22}\right)^2{}_{,1}\,S_{12}(\eta,\xi) - \xi\left(h_{22}\right)^2{}_{,2}\,S_{18}(\eta,\xi)\right]}{c^2\left(h_{22}\right)^4\left(1-\eta^2+\xi^2\right)} + \\ & + \frac{2a^2\left[\left(1-\eta^2-\xi^2\right)S_{17}(\eta,\xi) - \eta\xi\left(1-\eta^2+\xi^2\right)S_{20}(\eta,\xi)\right]}{c^2\left(h_{11}h_{22}\right)\left(1-\eta^2+\xi^2\right)^2} - \\ & - \frac{2a^2\xi\left[\eta\xi S_{12}(\eta,\xi) - 2\left(1-\xi^2\right)^2 S_{18}(\eta,\xi) - \xi S_{21}(\eta,\xi)\right]}{c^2\left(h_{22}\right)^2\left(1-\eta^2+\xi^2\right)^2} \end{aligned} \tag{2.65}$$

Substituting the explicit expressions for the nonempty space parts $f_{\mu\nu}$ and $f^{\mu\nu}$ into equation (2.37), simplifying and grouping like terms yields (2.59), where the terms consisting it are (2.60)–(2.65).

Equation (2.59) is thus our exact explicit R_{33} exterior field equation to the order c^{-2}. We can now conveniently formulate astrophysical solutions for the equation in the next section; which are convergent in the exterior space time of a homogeneous massive oblate spheroid placed in empty space.

3 Formulation of R-33 exterior solution

In the exterior oblate spheroidal space time [7]:

$$\xi \geqslant \xi_0 \quad \text{and} \quad -1 \leqslant \eta \leqslant 1; \quad \xi_0 = constant \tag{3.1}$$

Let us now seek a solution for the R_{33} field equation (2.59) in the form of the power series

$$f(\eta,\xi) = \sum_{n=0}^{\infty} P_n^+(\xi)\,\eta^n. \tag{3.2}$$

where P_n^+ is a function to be determined for each value of n. Substituting the proposed function into the field equation and taking into consideration the fact that $\{\eta^n\}_{n=0}^{\infty}$ is a linearly independent set, we can thus equate the coefficients of η^n on both sides of the obtained equation. From the coefficients of η^0, we obtain the equation

$$\begin{aligned} 0 = {} & K_1(\eta,\xi) P_2^+(\xi) + K_2(\eta,\xi)\left[P_1^+(\xi)\right]' + \\ & + K_3(\eta,\xi)\left[P_0^+(\xi)\right]'' + K_4(\eta,\xi) P_1^+(\xi) + \\ & + K_5(\eta,\xi)\left[P_0^+(\xi)\right]' + K_6(\eta,\xi) P_0^+(\xi) \end{aligned} \tag{3.3}$$

or more explicitly

$$\begin{aligned} 0 = {} & a^3\xi^3\left(1+\xi^2-a^2\xi^4\right)P_2^+(\xi) + \\ & + 2a^3\xi^3\left(1+\xi^2\right)^2\left[P_1^+(\xi)\right]' + a^3\xi^2\left(1+\xi^2\right)P_1^+(\xi) + \\ & + a^3\xi^3\left(1+\xi^2\right)^2\left[P_0^+(\xi)\right]'' + \left(1+\xi^2\right)\times \\ & \times\left(-1-2a^2\xi^2-\xi^2-a^2\xi^3+4a^2\xi^5\right)\left[P_0^+(\xi)\right]' + \\ & + \left[2a^3\xi\left(4-2\xi^2-a^4\xi^4-a^4\xi^6\right)\right]P_0^+(\xi). \end{aligned} \tag{3.4}$$

Equation (3.4) is the first recurrence differential equation for the unknown functions. All the other recurrence differential equations can thus follow, yielding infinitely many recurrence differential equations that can be used to determine all the unknown functions.

The following profound points can thus be made. Firstly, equation (3.4) determines P_2^+ in terms of P_0^+ and P_1^+, similarly the other recurrence differential equations will determine the other unknown functions $P_3^+, \dots$ in terms of P_0^+ and P_1^+. Secondly, we note that we have the freedom to choose our arbitrary functions to satisfy the physical requirements or needs of any particular distribution or area of application.

Let us now recall that for any gravitational field [7, 13],

$$g_{00} \cong 1 + \frac{2}{c^2}\,\Phi \tag{3.5}$$

where Φ is Newton's gravitational scalar potential for the field under consideration. Thus we can then deduce that the unknown function in our field equation can be given approximately as

$$f(\eta,\xi) \cong \Phi^+(\eta,\xi) \tag{3.6}$$

where $\Phi^+(\eta,\xi)$ is Newton's gravitational scalar potential exterior to a homogeneous oblate spheroidal mass. Recently [14], it has been shown that

$$\Phi^+(\eta,\xi) = B_0 Q_0(-i\xi)\,P_0(\eta) + B_2 Q_2(-i\xi)\,P_2(\eta) \tag{3.7}$$

where Q_0 and Q_2 are the Legendre functions linearly independent to the Legendre polynomials P_0 and P_2 respectively; B_0 and B_2 are constants.

Let us now seek our exact analytical exterior solution (3.4) to be as close as possible to the approximate exterior solution (3.7). Now since the approximate solution possesses no term in the first power of η, let us choose

$$P_0^+(\xi) = B_0 Q_0(-i\xi)\,P_0 + B_2 Q_2(-i\xi) \tag{3.8}$$

and

$$P_1^+(\xi) \equiv 0\,. \tag{3.9}$$

Hence, we can write P_2^+ in terms of P_0^+ as

$$\begin{aligned} P_2^+(\xi) = &-\frac{\left(1+\xi^2\right)^2}{\left(1+\xi^2-a^2\xi^4\right)}\left[P_0^+(\xi)\right]'' - \\ &-\frac{2\left(1+\xi^2\right)\left(3a^2\xi^2+4a^2\xi^5-\xi^2-1\right)}{a^2\xi^3}\left[P_0^+(\xi)\right]' - \\ &-2\left[\frac{1-2a^3\xi^2-a^7\xi^4-a^7\xi^6+a^3}{a^3\xi^2\left(1+\xi^2-a^2\xi^4\right)}\right]P_0^+(\xi)\,. \end{aligned} \tag{3.10}$$

We now remark that the first three terms of our series solution converge everywhere in the exterior space time. We also remark that our solution of order c^0 may be written as

$$f(\eta,\xi) = \Phi^+(\eta,\xi) + \Phi_0^+(\eta,\xi) \tag{3.11}$$

where $\Phi^+(\eta,\xi)$ is the corresponding Newtonian gravitational scalar potential given by (3.7) and $\Phi_0^+(\eta,\xi)$ is the pure Einsteinian or general relativistic or post Newtonian correction of order c^0.

Hence, we deduce that our exterior analytical solution is of the general form

$$f(\eta,\xi) = \Phi^+(\eta,\xi) + \Phi_0^+(\eta,\xi) + \sum_{n=1}^{\infty}\Phi_{2n}^+(\eta,\xi)\,. \tag{3.12}$$

4 Formulation of interior R-33 field equation and solution

For the interior space time, Einstein's field equations are well known to be given as;

$$R_{\mu\nu} - \frac{1}{2}\,R g_{\mu\nu} = -\frac{8\pi G}{c^4}\,T_{\mu\nu} \tag{4.1}$$

where $T_{\mu\nu}$ is the energy momentum tensor.

Now, let us assume that the homogeneous mass distribution is a "perfect fluid". Thus, we can define the energy momentum tensor as

$$T_{\mu\nu} = (\rho_0 + P_0)\,u_\mu u_\nu - P_0 g_{\mu\nu} \tag{4.2}$$

where ρ_0 is the proper mass density and P_0 is the proper pressure and u_μ is the velocity four vector. Hence, the five non trivial interior field equations can be written as;

$$R_{00} - \frac{1}{2}\,R g_{00} = -\frac{8\pi G}{c^4}\left[(\rho_0 + P_0)\,u_0 u_0 - P_0 g_{00}\right], \tag{4.3}$$

$$R_{11} - \frac{1}{2}\,R g_{11} = \frac{8\pi G}{c^4}\,P_0 g_{11}\,, \tag{4.4}$$

$$R_{12} - \frac{1}{2}\,R g_{12} = \frac{8\pi G}{c^4}\,P_0 g_{12}\,, \tag{4.5}$$

$$R_{22} - \frac{1}{2}\,R g_{22} = \frac{8\pi G}{c^4}\,P_0 g_{22}\,, \tag{4.6}$$

$$R_{33} - \frac{1}{2}\,R g_{33} = \frac{8\pi G}{c^4}\,P_0 g_{33}\,. \tag{4.7}$$

Now, we formulate the solution of (4.7). For the sake of mathematical convenience, we assume in this article that the pressure is negligible compared to the mass density and hence

$$P_0 \cong 0\,. \tag{4.8}$$

Multiplying equation (4.7) by $2g^{33}$ and using the fact that $g^{33}g_{33} = 1$ we obtain precisely as in the section 2;

$$-g^{00}R_{00} - g^{11}R_{11} - g^{22}R_{22} + g^{33}R_{33} - 2g^{12}R_{12} = 0\,. \tag{4.9}$$

Similarly, we obtain the interior equation explicitly as

$$\begin{aligned} &K_1(\eta,\xi)\,f_{\eta\eta} + K_2(\eta,\xi)\,f_{\eta\xi} + K_3(\eta,\xi)\,f_{\xi\xi} + \\ &+ K_4(\eta,\xi)\,f_\eta + K_5(\eta,\xi)\,f_\xi + K_6(\eta,\xi)\,f = 0\,. \end{aligned} \tag{4.10}$$

We now remark that, for the interior field we are required to formulate interior solutions of (4.10) convergent in the range

$$0 \leqslant \xi \leqslant \xi_0 , \qquad -1 \leqslant \eta \leqslant 1. \tag{4.11}$$

Let us thus seek a series solution of the form;

$$f^- (\eta, \xi) = \sum_{n=0}^{\infty} Z_n^- (\eta) \, \xi^n. \tag{4.12}$$

where Z_n^- are unknown functions to be determined. Now, using the fact that $\{\xi^n\}_{n=0}^{\infty}$ is a linearly independent set, we may equate coefficients on both sides and hence obtain the equations satisfied by Z_n^-. We proceed similarly as in the case of the exterior solution to obtain recurrence differential equations that determine the explicit expression for our exact analytical solution. Equating the coefficients of ξ^0, we obtain the first recurrence differential equation as

$$\begin{aligned} & K_1 (\eta, \xi) \left[Z_0^- (\eta) \right]'' + K_2 (\eta, \xi) \left[Z_1^- (\eta) \right]' + \\ & + K_3 (\eta, \xi) \, Z_2^- (\eta) + K_4 (\eta, \xi) \left[Z_0^- (\eta) \right]' + \\ & + K_5 (\eta, \xi) \, Z_1^- (\eta) + K_6 (\eta, \xi) \, Z_0^- (\eta) = 0 . \end{aligned} \tag{4.13}$$

In a similar manner, the other recurrence differential equations follow.

We can now proceed as in the previous section to choose the most astrophysically satisfactory solution to be as close as possible to the approximate solution. The gravitational scalar potential interior to a homogeneous oblate spheroid is well known [14] to be given as

$$\Phi^- (\eta, \xi) = \left[A_0 - \frac{1}{2} A_2 P_2(\eta) \right] - 3/2 A_2 P_2(\eta) \, \xi^2, \tag{4.14}$$

where P_2 is Legendre's polynomial of order 2 and A_0, A_2, are constants.

Since (4.14) converges for all values in the interval (4.11), it is very satisfactory for us to choose;

$$Z_0^- (\eta) = A_0 - \frac{1}{2} A_2 P_2(\eta) \tag{4.15}$$

and

$$Z_1^- (\eta) \equiv 0 . \tag{4.16}$$

Thus the first recurrence differential equation determines Z_2^- in terms of Z_0^-. Similarly, all the other recurrence differential equations will determine all the other functions in terms of Z_0^-. Hence we obtain our unique astrophysically most satisfactory interior solution. It is obvious that this unique solution will converge, precisely as the first two terms. Moreover, it is obvious that our unique solution reduces to the corresponding pure Newtonian gravitational scalar potential in the limit of the first two terms. This solution may be written as

$$f^- (\eta, \xi) = \Phi^- (\eta, \xi) + \Phi_0^- (\eta, \xi) \tag{4.17}$$

where $\Phi^- (\eta, \xi)$ is the corresponding Newtonian gravitational scalar potential given by (4.14) and $\Phi_0^- (\eta, \xi)$ is the pure instructively Einstenian (or general relativistic or post Newtonian correction) of order c^0.

Proceeding exactly as above we may derive all the corresponding solutions of all the other non-trivial interior Einstein's field equations for the sake of mathematical completeness, comparison with those of the R_{33} equation and theoretical applications where and when necessary in Physics. It is clearly obvious how to extend the derivation of the interior Einstein field equations above to include any given pressure function $P_0 (\eta, \xi)$, wherever and whenever necessary and useful in physical theory.

5 Conclusions

Interestingly, the single dependent function f in our mathematically most simple and astrophysically most satisfactory solution turns out as the corresponding well known pure Newtonian exterior/interior gravitational scalar potential augmented by hitherto unknown pure Einsteinian (or general relativistic or post-Newtonian) gravitational scalar potential terms of orders c^0, c^{-2}, c^{-4}, ... Hence, this article has revealed a hitherto unknown sense in which the exterior/interior Einstein's geometrical gravitational field equations are obtained as a generalization or completion of Newton's dynamical gravitational field equations.

With the formulation of our mathematically most simple and astrophysically most satisfactory solutions in this article, the way is opened up for the formulation and solution of the general relativistic equations of motion for all test particles in the gravitational fields of all static homogeneous distributions of mass within oblate spheroidal regions in the universe. And precisely because these equations contain the pure Newtonian as well as post-Newtonian gravitational scalar potentials all their predictions shall be most naturally comparable to the corresponding predictions from the pure Newtonian theory. This is most satisfactory indeed.

It is now obvious how our work in this article may by emulated to (i) derive a mathematically most simple structure for all the metric tensors in the space times exterior or interior to any distribution of mass within any region having any of the 14 regular geometries in nature, (ii) formulate all the nontrivial Einstein geometrical gravitational field equations and derive all their general solutions and (iii) derive astrophysically most satisfactory unique solutions for application to the motions of all test particles and comparison with corresponding pure Newtonian results and applications. Therefore our goal in this article has been completely achieved: to use the case of a spheroidal distribution of mass to show how the much vaunted Einstein's geometrical gravitational field equations may be solved exactly and analytically for any given distribution of mass within any region having any geometry.

Finally, we conclude that at very long last — 93 years after the publication of the laws of General Relativity by Einstein in 1915 — we have found a method and process for (1) deriving a unique approximate astrophysically most satisfactory solutions for the space times exterior and interior to every distribution of mass within any region having any of the 14 regular geometries in nature, in terms of the corresponding pure Newton's gravitational scalar potential, without even formulating the field equation; and (2) systematically formulating and solving the geometrical gravitational field equations in the space times of all distributions of mass in nature.

Acknowledgenent

The author is highly indebted to Prof. S. X. K. Howusu of the Physics Department, Kogi State University, Nigeria for his immense inspiration, guidance; and for the use of his R_{11} solution method to formulate the solution in this article.

Submitted on June 29, 2009 / Accepted on August 03, 2009

References

1. Bergmann P.G. Introduction to the Theory of Relativity. Prentice Hall, New Delhi, 1987.
2. Schwarzschild K. Über das Gravitationsfeld eines Massenpunktes nach der Einsteinschen Theorie. *Sitzungsberichte der Koniglich Preussischen Akademie der Wissenschaften*, 1916, 189–196 (published in English as: Schwarzschild K. On the gravitational field of a point mass according to Einstein's theory. *The Abraham Zelmanov Journal*, 2008, v. 1, 10–19).
3. Finster F., Kamran N., Smoller J. and Yau S.T. Decay of solutions of the wave equation in the Kerr geometry. *Communications in Mathematical Physics*, 2006, v. 264, 465–503.
4. Anderson L., Elst V., Lim W.C. and Uggla C. Assymptotic silence of generic cosmological singularities. *Physical Review Letters*, 2001, v. 94, 51–101.
5. MacCallum M.A.H. Finding and using exact solutions of the Einstein equation. arxiv: 0314.4133.
6. Stephani H., Kramer D., MacCallum M.A.H., Hoenselars C., Herlt E. Exact solutions of Einstein's field equations. 2nd ed., Cambridge Univ. press, London, 2003.
7. Howusu S.X.K. The 210 astrophysical solutions plus 210 cosmological solutions of Einstein's geometrical gravitational field equations. Jos University Press, Jos, 2007.
8. Chifu E.N. and Howusu S.X.K. Gravitational radiation and propagation field equation exterior to astrophysically real or hypothetical time varying distributions of mass within regions of spherical geometry. *Physics Essays*, 2009, v. 22(1), 73–77.
9. Chifu E.N. and Howusu S.X.K. Einstein's equation of motion for a photon in fields exterior to astrophysically real or imaginary spherical mass distributions who's tensor field varies with azimuthal angle only. *Journal of the Nigerian Association of Mathematical Physics*, 2008, v. 13, 363–366.
10. Chifu E.N., Howusu S.X.K. and Lumbi L.W. Relativistic mechanics in gravitational fields exterior to rotating homogeneous mass distributions within regions of spherical geometry. *Progress in Physics*, 2009, v. 3, 18–23.
11. Chifu E.N and Howusu S.X.K. Solution of Einstein's geometrical field equations exterior to astrophysically real or hypothetical time varying distributions of mass within regions of spherical geometry. *Progress in Physics*, 2009 v. 3,45–48.
12. Chifu E.N., Usman A. and Meludu O.C. Orbits in homogeneous oblate spheroidal gravitational space time. *Progress in Physics*, 2008, v. 3, 49–53.
13. Weinberg S. Gravitation and cosmology. J. Wiley, New York, 1972, p. 175–188.
14. Howusu S.X.K. Gravitational fields of spheroidal bodies-extension of gravitational fields of spherical bodies. *Galilean Electrodynamics*, 2005, v. 16(5), 98–100.

A New Finslerian Unified Field Theory of Physical Interactions

Indranu Suhendro
E-mail: spherical_symmetry@yahoo.com

In this work, we shall present the foundational structure of a new unified field theory of physical interactions in a geometric world-space endowed with a new kind of Finslerian metric. The intrinsic non-metricity in the structure of our world-geometry may have direct, genuine connection with quantum mechanics, which is yet to be fully explored at present. Building upon some of the previous works of the Author, our ultimate aim here is yet another quantum theory of gravity (in just four space-time dimensions). Our resulting new theory appears to present us with a novel Eulerian (intrinsically motion-dependent) world-geometry in which the physical fields originate.

1 Introduction

This work is a complementary exposition to our several previous attempts at the geometrization of matter and physical fields, while each of them can be seen as an independent, self-contained, coherent unified field theory.

Our primary aim is to develop a new foundational world-geometry based on the intuitive notion of a novel, fully naturalized kind of Finsler geometry, which extensively mimics the Eulerian description of the mechanics of continuous media with special emphasis on the world-velocity field, in the sense that the whole space-time continuum itself is taken to be globally dynamic on both microscopic and macroscopic scales. In other words, the world-manifold itself, as a whole, is not merely an ambient four-dimensional geometric background, but an open (self-closed, yet unbounded), co-moving, self-organizing, self-projective entity, together with the individual particles (objects) encompassed by its structure.

2 Elementary construction of the new world-geometry

Without initial recourse to the common structure of Finsler geometry, whose exposition can easily be found in the literature, we shall build the essential geometric world-space of our new theory somewhat from scratch.

We shall simply start with an intuitive vision of intrinsically motion-dependent objects, whose fuzzy Eulerian behavior, on the microscopic scale, is generated by the structure of the world-geometry in the first place, and whose very presence, on the macroscopic scale, affects the entire structure of the world-geometry. In this sense, the space-time continuum itself has a dynamic, non-metric character at heart, such that nothing whatsoever is intrinsically "fixed", including the defining metric tensor itself, which evolves, as a structural entity of global coverage, in a self-closed (self-inclusive) yet unbounded (open) manner.

In the present theory, the Universe is indeed an evolving, holographic (self-projective) four-dimensional space-time continuum U_4 with local curvilinear coordinates x^α and an intrinsically fuzzy (quantum-like), possibly degenerate, non-metric field ψ. As such, U_4 may encompass all possible metric-compatible (sub-)universes, especially those of the General Theory of Relativity. In this sense, U_4 may be viewed as a Meta-Universe, possibly without admitting any apparent boundary between its microscopic (interior) and macroscopic (exterior) mechanisms, as we shall see.

If we represent the metric-compatible part of the geometric basis of U_4 as $g_\alpha(x)$, then, following our unification scenario, the total geometric basis of our generally non-metric manifold shall be given by

$$\begin{aligned} g_\alpha(x,u) &= g_\alpha(x) + \psi_\alpha u \\ g^\alpha(x,u) &= \left(g_\alpha(x,u)\right)^{-1} \\ \left\langle g_\alpha(x,u), g^\beta(x,u)\right\rangle &= \delta^\beta_\alpha \end{aligned}$$

where $u = \frac{dx^\alpha}{ds} g_\alpha(x,u)$ is the world-velocity field along the world-line

$$s(x,u) = \int \sqrt{g_{\alpha\beta}(x,u)\, dx^\alpha dx^\beta}$$

(with $g_{\alpha\beta}(x,u)$ being the components of the generalized metric tensor to be subsequently given below), and where δ^β_α are the components of the Kronecker delta. (Needless to say, the Einstein summation convention is applied throughout this work as usual.) Here the inner product is indicated by $\langle \dots, \dots \rangle$. We then have

$$\frac{\partial}{\partial x^\beta} g_\alpha(x,u) = \frac{\partial}{\partial x^\beta} g_\alpha(x) + u \frac{\partial \psi_\alpha}{\partial x^\beta} + \psi_\alpha \nabla_\beta u,$$

where ∇ denotes the gradient, that is, the covariant derivative.

The components of the symmetric, bilinear metric tensor $g(x,u)$ for the given geometric basis are readily given by

$$\begin{aligned} g_{\alpha\beta}(x,u) &= \langle g_\alpha(x,u), g_\beta(x,u)\rangle \\ g_{\alpha\lambda}(x,u)\, g^{\beta\lambda}(x,u) &= \delta^\beta_\alpha . \end{aligned}$$

As such, we obtain

$$g_{\alpha\beta}(x,u) = g_{\alpha\beta}(x) + 2\,\hat{u}_{(\alpha}\psi_{\beta)} + \phi^2(x,u)\,\psi_\alpha\,\psi_\beta .$$

As usual, round brackets enclosing indices indicate symmetrization; subsequently, anti-symmetrization shall be indicated by square brackets. In the above relation, $\hat{u}_\alpha = \langle u, g_\alpha(x)\rangle$ and

$$\phi^2(x,u) = g_{\alpha\beta}(x,u)\, u^\alpha u^\beta$$

is the squared length of the world-velocity vector, which varies from point to point in our world-geometry. As we know, this squared length is equal to unity in metric-compatible Riemannian geometry.

The connection form of our world-geometry is obtained through the inner product

$$\Gamma^\lambda_{\alpha\beta}(x,u) = \left\langle g^\lambda(x,u), \frac{\partial}{\partial x^\beta} g_\alpha(x,u)\right\rangle.$$

In an explicit manner, we see that

$$\Gamma^\lambda_{\alpha\beta}(x,u) = \Gamma^\lambda_{\alpha\beta}(x) + \left(\frac{\partial \psi_\alpha}{\partial x^\beta}\right) u^\lambda + \psi_\alpha \nabla_\beta u^\lambda.$$

In accordance with our previous unified field theories (see, for instance, [1–5]), the above expression must generally be asymmetric, with the torsion being given by the anti-symmetric form

$$\Gamma^\lambda_{[\alpha\beta]}(x,u) = \Gamma^\lambda_{[\alpha\beta]}(x) + \frac{1}{2}\left(\frac{\partial \psi_\alpha}{\partial x^\beta} - \frac{\partial \psi_\beta}{\partial x^\alpha}\right) u^\lambda + \frac{1}{2}\left(\psi_\alpha \nabla_\beta u^\lambda - \psi_\beta \nabla_\alpha u^\lambda\right).$$

In contrast to the case of a Riemannian manifold (without background embedding), we have the following unique case:

$$\nabla_\beta g_\alpha(x,u) \equiv \frac{\partial}{\partial x^\beta} g_\alpha(x,u) - \Gamma^\lambda_{\alpha\beta}(x,u)\, g_\lambda(x,u) = \frac{1}{2}\psi_\alpha \psi_\lambda \left(\nabla_\beta u^\lambda\right)\psi$$

for which, additionally, $\Gamma^\lambda_{\alpha\beta}(x)\ \psi_\lambda = 0$. Consequently, the covariant derivative of the world-metric tensor fails to vanish in the present theory, as we obtain the following non-metric expression:

$$\nabla_\lambda g_{\alpha\beta}(x,u) = \psi_\alpha \psi_\beta \psi_\sigma \nabla_\lambda u^\sigma.$$

At this point, in order to correspond with Finsler geometry in a manifest way, we shall write

$$\nabla_\lambda g_{\alpha\beta}(x,u) = \Phi_{\alpha\beta\sigma} \nabla_\lambda u^\sigma$$

and

$$g_{\alpha\beta}(x,u) = \frac{1}{2}\frac{\partial^2}{\partial u^\alpha \partial u^\beta}\phi^2(x,u)$$

in such a way that the following conditions are satisfied:

$$\Phi_{\alpha\beta\lambda} = \psi_\alpha \psi_\beta \psi_\lambda,$$

$$\frac{1}{2}\Phi_{\alpha\beta\lambda} = \frac{1}{2}\Phi_{(\alpha\beta\lambda)} = \frac{1}{2}\frac{\partial}{\partial u^\lambda} g_{\alpha\beta}(x,u) = \frac{1}{4}\frac{\partial^3}{\partial u^\alpha \partial u^\beta \partial u^\lambda}\phi^2(x,u),$$

$$\Phi_{\alpha\beta\lambda}\, u^\lambda = 0,$$

$$\psi_\alpha\, u^\alpha = 0.$$

Once the velocity field is known, the Hessian form of the metric tensor enables us to write, in the momentum representation for a geometric object with mass m (initially at rest, locally),

$$g_{\alpha\beta}(x,u) = \frac{1}{2} m^2 \frac{\partial^2}{\partial p^\alpha \partial p^\beta}\phi^2(x,u),$$

$$p^\alpha = m\, u^\alpha$$

such that, with $\phi^2(x,u)$ being expressed in parametric form, physical geometry, that is, the existence of a geometric object in space-time, is essentially always related to mass and its energy content.

Taking into account the projective angular tensor given by

$$\Omega_{\alpha\beta}(x,u) = g_{\alpha\beta}(x,u) - \frac{1}{\phi^2(x,u)} u_\alpha u_\beta,$$

$$\Omega_{\alpha\lambda}(x,u)\ \Omega^{\beta\lambda}(x,u) = \delta^\beta_\alpha - \frac{1}{\phi^2(x,u)} u_\alpha u^\beta,$$

$$\Omega_{\alpha\beta}(x,u)\ u^\beta = 0,$$

where n is the number of dimensions of the geometric space (in our case, of course, $n = 4$), in the customary Finslerian way, it can easily be shown that

$$\Phi_{\alpha\beta\lambda} = \frac{1}{n}\left(\Omega_{\alpha\beta}(x,u)\ \Phi_\lambda + \Omega_{\beta\lambda}(x,u)\ \Phi_\alpha + \Omega_{\lambda\alpha}(x,u)\ \Phi_\beta - \frac{1}{\Phi_\sigma \Phi^\sigma}\Phi_\alpha \Phi_\beta \Phi_\lambda\right),$$

$$\Phi_\alpha = g^{\sigma\rho}(x,u)\ \Phi_{\sigma\rho\alpha} = 2\frac{\partial}{\partial u^\alpha}\ln\sqrt{\det\left(g(x,u)\right)},$$

$$\frac{\partial}{\partial u^\alpha}\ln\sqrt{\det\left(g(x,u)\right)} = \frac{1}{2} g^{\rho\sigma}(x,u)\frac{\partial}{\partial u^\alpha} g_{\rho\sigma}(x,u)$$

for which, in our specific theory, we have, with $\psi^2 = g_{\alpha\beta}(x,u)\ \psi^\alpha \psi^\beta$,

$$\Phi_{\alpha\beta\lambda} = \frac{\psi^2}{n}\left(\Omega_{\alpha\beta}(x,u)\ \psi_\lambda + \Omega_{\beta\lambda}(x,u)\ \psi_\alpha + \Omega_{\lambda\alpha}(x,u)\ \psi_\beta - \frac{1}{\psi^2}\psi_\alpha \psi_\beta \psi_\lambda\right).$$

We may note that, along the world-line, for the intrinsic geodesic motion of a particle given by the parallelism

$$\frac{Du^\alpha}{Ds} = \left(\nabla_\beta u^\alpha\right) u^\beta = 0,$$

the Finslerian condition

$$\frac{D}{Ds}\, g_{\alpha\beta}\,(x,u) = 0$$

is always satisfied, along with the supplementary condition

$$\frac{D}{Ds}\, \phi^2\,(x,u) = 0\,.$$

Consequently, we shall also have

$$\frac{D}{Ds}\, \Omega_{\alpha\beta}\,(x,u) = 0\,.$$

It is essential to note that, unlike in Weyl geometry, we shall not expect to arrive at the much simpler gauge condition $\nabla_\lambda\, g_{\alpha\beta}\,(x,u) = g_{\alpha\beta}\,(x,u)\; A_\lambda\,(\psi)$. Instead, we shall always employ the following alternative general form:

$$\nabla_\lambda\, g_{\alpha\beta}\,(x,u) = \frac{1}{\phi^2\,(x,u)}\left(\delta_u\, g_{\alpha\beta} - 2\,\hat{u}_{(\alpha}\;\psi_{\beta)}\right)\;\psi_\sigma\,\nabla_\lambda\, u^\sigma$$

where, as we can easily see, the diffeomorphic structure of the metric tensor for the condition of non-metricity of our world-geometry is manifestly given by

$$\delta_u\, g_{\alpha\beta} \equiv g_{\alpha\beta}\,(x,u) - g_{\alpha\beta}\,(x) =$$
$$= 2\,\hat{u}_{(\alpha}\,\psi_{\beta)} + \phi^2\,(x,u)\;\psi_\alpha\,\psi_\beta$$

3 Explicit physical (Eulerian) structure of the connection form

Having recognized the structural non-metric character of our new world-geometry in the preceding section, we shall now seek to outline the explicit physical structure of the connection form for the purpose of building a unified field theory.

We first note that the non-metric connection form of our theory can always be given by the general expression

$$\Gamma^\lambda_{\alpha\beta}\,(x,u) = \frac{1}{2}\, g^{\lambda\sigma}\,(x,u)\left(\frac{\partial}{\partial\, x^\beta}\, g_{\sigma\alpha}\,(x,u) -\right.$$
$$- \frac{\partial}{\partial x^\sigma}\, g_{\alpha\beta}\,(x,u) + \frac{\partial}{\partial\, x^\alpha}\, g_{\beta\sigma}\,(x,u)\Big) +$$
$$+\; \Gamma^\lambda_{[\alpha\beta]}\,(x,u) - g^{\lambda\sigma}\,(x,u)\left(g_{\alpha\rho}\,(x,u)\,\Gamma^\rho_{[\sigma\beta]}\,(x,u) +\right.$$
$$+\; g_{\beta\rho}\,(x,u)\,\Gamma^\rho_{[\sigma\alpha]}\,(x,u)\Big) +$$
$$+\; \frac{1}{2}\, g^{\lambda\sigma}\,(x,u)\left(\nabla_\beta\, g_{\sigma\alpha}\,(x,u) -\right.$$
$$-\; \nabla_\sigma\, g_{\alpha\beta}\,(x,u) + \nabla_\alpha\, g_{\beta\sigma}\,(x,u)\Big)\,.$$

Then, using the results given in the previous section, in direct relation to our previous metric-compatible unification theory of gravity, electromagnetism, material spin, and the nuclear interaction [4], where the electromagnetic field and material spin are generated by the torsion field, we readily obtain

$$\Gamma^\lambda_{\alpha\beta}\,(x,u) = \frac{1}{2}\, g^{\lambda\sigma}\,(x,u)\left(\frac{\partial}{\partial\, x^\beta}\, g_{\sigma\alpha}\,(x,u) -\right.$$
$$- \frac{\partial}{\partial\, x^\sigma}\, g_{\alpha\beta}\,(x,u) + \frac{\partial}{\partial\, x^\alpha}\, g_{\beta\sigma}\,(x,u)\Big) +$$
$$+\; \frac{e}{2\, m\, c^2}\,\phi^2\,(x,u)\left(F_{\alpha\beta}\, u^\lambda - F^\lambda{}_\alpha\, u_\beta - F^\lambda{}_\beta\, u_\alpha\right) +$$
$$+\; S^\lambda_{\alpha\beta} - g^{\lambda\sigma}\,(x,u)\left(g_{\alpha\rho}\,(x,u)\; S^\rho_{\sigma\beta} + g_{\beta\rho}\,(x,u)\; S^\rho_{\sigma\alpha}\right) +$$
$$+\; \frac{1}{2}\, g^{\lambda\sigma}(x,u)\,\psi_\rho(\psi_\sigma\,\psi_\alpha\,\nabla_\beta\, u^\rho - \psi_\alpha\,\psi_\beta\,\nabla_\sigma\, u^\rho +$$
$$+\; \psi_\beta\,\psi_\sigma\,\nabla_\alpha\, u^\rho)\,.$$

Here it is interesting to note that even when $\psi = 0$, which gives a metric-compatible ("classical") case, our connection form already explicitly depends on the world-velocity (in addition to position), hence the unified field theory of physical interactions outlined in [4] can somehow already be considered as being a Finslerian one despite the fact that it is metric-compatible.

We recall, still from [4], that the electromagnetic field F and the material spin field S have a common geometric origin, which is the structural torsion of the space-time manifold, and are essentially given by the following expressions:

$$F_{\alpha\beta} = 2\,\frac{m\, c^2}{e}\,\Gamma^\lambda_{[\alpha\beta]}\, u_\lambda\,,$$
$$S^\lambda_{\alpha\beta} = S^\lambda{}_\alpha\, u_\beta - S^\lambda{}_\beta\, u_\alpha\,,$$
$$S^{\alpha\beta}\, u_\beta = 0,\, S^{\alpha\beta} = S^{[\alpha\beta]}\,,$$
$$\Gamma^\lambda_{[\alpha\beta]} = \frac{e}{2\, m\, c^2}\, F_{\alpha\beta}\, u^\lambda + S^\lambda_{\alpha\beta}\,,$$

where m is the (rest) mass, e is the electric charge, and c is the speed of light in vacuum, such that the physical fields are intrinsic to the space-time geometry itself, as manifest in generalized geodesic equation of motion $\frac{Du^\alpha}{Ds} = 0$, which naturally yields the general relativistic equation of motion of a charged, massive particle in the gravitational field

$$m\, c^2\left(\frac{du^\alpha}{ds} + \Delta^\alpha_{\beta\lambda}\, u^\beta\, u^\lambda\right) = e\, F^\alpha{}_\beta\, u^\beta\,,$$
$$\Delta^\alpha_{\beta\lambda} = \frac{1}{2}\, g^{\alpha\sigma}\left(\frac{\partial\, g_{\sigma\beta}}{\partial\, x^\lambda} - \frac{\partial\, g_{\beta\lambda}}{\partial\, x^\sigma} + \frac{\partial\, g_{\lambda\sigma}}{\partial\, x^\beta}\right).$$

In other words, the physical fields other than gravity (chiefly, the electromagnetic field) can also be represented as part of the internal structure of the free-fall of a particle. Just like gravity, being fully geometrized in our theory, these non-holonomic (vortical) fields are no longer external entities merely added into the world-picture in order to interact with

gravity and the structure of space-time itself, thereby essentially fulfilling the geometrization program of physics as stated, for example, in [6].

Correspondingly, the nuclear (Yang-Mills) interaction is essentially given in our theory as an internal electromagnetic interaction by

$$F^i_{\alpha\beta} = 2\,\omega^i_\lambda\,\Gamma^\lambda_{[\alpha\beta]}\,,$$

$$F_{\alpha\beta} = \frac{m\,c^2}{e}\,F^i_{\alpha\beta}\,u_i\,(i=1,2,3)\,,$$

where ω^i_α are the components of the tetrad (projective) field relating the global space-time to the internal three-dimensional space of the nuclear interaction.

In this direction, we may also define the extended electromagnetic field, which explicitly depends on the world-velocity, through

$$\tilde{F}_{\alpha\beta}\,(x,u) = \phi^2\,(x,u)\,F_{\alpha\beta} = 2\,\phi^2\,(x,u)\,\frac{mc^2}{e}\,\Gamma^\lambda_{[\alpha\beta]}\,u_\lambda\,.$$

4 Substantial structure of covariant differentiation in $\mathbf{U_4}$

Given an arbitrary world-tensor $T\,(x,u)$ at any point in our Finslerian world-geometry, we have the following elementary substantial derivatives:

$$\frac{d}{d\tau}\,T^{\alpha\beta\ldots\gamma}_{\rho\sigma\ldots\lambda}\,(x,u) =$$
$$= \frac{\partial}{\partial x^\eta}\left(T^{\alpha\beta\ldots\gamma}_{\rho\sigma\ldots\lambda}\,(x,u)\right)\frac{dx^\eta}{d\tau} + \frac{\partial}{\partial u^\eta}\left(T^{\alpha\beta\ldots\gamma}_{\rho\sigma\ldots\lambda}\,(x,u)\right)\frac{\partial u^\eta}{\partial\tau}\,,$$

$$\frac{d}{dx^\eta}T^{\alpha\beta\ldots\gamma}_{\rho\sigma\ldots\lambda}\,(x,u) =$$
$$= \frac{\partial}{\partial x^\eta}T^{\alpha\beta\ldots\gamma}_{\rho\sigma\ldots\lambda}\,(x,u) + \frac{\partial}{\partial u^\delta}\left(T^{\alpha\beta\ldots\gamma}_{\rho\sigma\ldots\lambda}\,(x,u)\right)\frac{\partial u^\delta}{\partial x^\eta}\,,$$

where τ is a global parameter.

In this way, the substantial structure of covariant differentiation in U_4 shall be given by

$$\tilde{\nabla}_\eta\,T^{\alpha\beta\ldots\gamma}_{\rho\sigma\ldots\lambda}\,(x,u) =$$
$$= \frac{\partial}{\partial\,x^\eta}\,T^{\alpha\beta\ldots\gamma}_{\rho\sigma\ldots\lambda}\,(x,u) + \frac{\partial}{\partial\,u^\varsigma}\left(T^{\alpha\beta\ldots\gamma}_{\rho\sigma\ldots\lambda}\,(x,u)\right)\frac{\partial\,u^\varsigma}{\partial\,x^\eta} +$$
$$+\,\Gamma^\alpha_{\delta\eta}\,(x,u)\,T^{\delta\beta\ldots\gamma}_{\rho\sigma\ldots\lambda}\,(x,u) + \Gamma^\beta_{\delta\eta}\,(x,u)\,T^{\alpha\delta\ldots\gamma}_{\rho\sigma\ldots\lambda}\,(x,u) + \ldots +$$
$$+\,\Gamma^\gamma_{\delta\eta}\,(x,u)\,T^{\alpha\beta\ldots\delta}_{\rho\sigma\ldots\lambda}\,(x,u) - \Gamma^\delta_{\rho\eta}\,(x,u)\,T^{\alpha\beta\ldots\gamma}_{\delta\sigma\ldots\lambda}\,(x,u) -$$
$$-\,\Gamma^\delta_{\sigma\eta}\,(x,u)\,T^{\alpha\beta\ldots\gamma}_{\rho\delta\ldots\lambda}\,(x,u) - \ldots - \Gamma^\delta_{\lambda\eta}\,(x,u)\,T^{\alpha\beta\ldots\gamma}_{\rho\sigma\ldots\delta}\,(x,u)$$

along with the more regular (point-oriented) form

$$\nabla_\eta\,T^{\alpha\beta\ldots\gamma}_{\rho\sigma\ldots\lambda}\,(x,u) = \frac{\partial}{\partial\,x^\eta}\,T^{\alpha\beta\ldots\gamma}_{\rho\sigma\ldots\lambda}\,(x,u) +$$
$$+\,\Gamma^\alpha_{\delta\eta}\,(x,u)\,T^{\delta\beta\ldots\gamma}_{\rho\sigma\ldots\lambda}\,(x,u) + \Gamma^\beta_{\delta\eta}\,(x,u)\,T^{\alpha\delta\ldots\gamma}_{\rho\sigma\ldots\lambda}\,(x,u) + \cdots +$$
$$+\,\Gamma^\gamma_{\delta\eta}\,(x,u)\,T^{\alpha\beta\ldots\delta}_{\rho\sigma\ldots\lambda}\,(x,u) - \Gamma^\delta_{\rho\eta}\,(x,u)\,T^{\alpha\beta\ldots\gamma}_{\delta\sigma\ldots\lambda}\,(x,u) -$$
$$-\,\Gamma^\delta_{\sigma\eta}\,(x,u)\,T^{\alpha\beta\ldots\gamma}_{\rho\delta\ldots\lambda}\,(x,u) - \cdots - \Gamma^\delta_{\lambda\eta}\,(x,u)\,T^{\alpha\beta\ldots\gamma}_{\rho\sigma\ldots\delta}\,(x,u)\,.$$

Turning our attention to the world-metric tensor, we see that the expression

$$\tilde{\nabla}_\lambda\,g_{\alpha\beta}\,(x,u) = \frac{\partial}{\partial\,x^\lambda}\,g_{\alpha\beta}\,(x,u) + \frac{\partial}{\partial\,u^\sigma}\,(g_{\alpha\beta}\,(x,u))\,\frac{\partial\,u^\sigma}{\partial\,x^\lambda} -$$
$$-\,\Gamma^\rho_{\alpha\lambda}\,(x,u)\,g_{\rho\beta}\,(x,u) - \Gamma^\rho_{\beta\lambda}\,(x,u)\,g_{\alpha\rho}\,(x,u)$$

may enable us to establish a rather indirect metricity-like condition. This can be done by invoking the condition

$$\Phi_{\alpha\beta\sigma}\Gamma^\sigma_{\rho\lambda}\,(x,u)\,u^\lambda = 0$$

and by setting

$$\tilde{\nabla}_\lambda\,g_{\alpha\beta}\,(x,u) = 0\,.$$

Now, with the help of the already familiar relations

$$\frac{\partial}{\partial\,u^\lambda}\,g_{\alpha\beta}\,(x,u) = \Phi_{\alpha\beta\lambda}\,,$$

$$g^{\alpha\beta}\,(x,u)\,\frac{\partial}{\partial\,u^\lambda}\,g_{\alpha\beta}\,(x,u) = 2\frac{\partial}{\partial\,u^\lambda}\,\ln\,\sqrt{\det\,(g\,(x,u))}$$

we shall again have

$$\nabla_\lambda\,g_{\alpha\beta}\,(x,u) = \Phi_{\alpha\beta\sigma}\,\nabla_\lambda\,u^\sigma\,.$$

5 Generalized curvature forms

We are now equipped enough with the basic structural relations to investigate curvature forms in our theory. In doing so, we shall derive a set of generalized Bianchi identities corresponding to a peculiar class of field equations, including some possible conservation laws (in rather special circumstances).

In a direct customary manner, we have the extended expression

$$\left(\tilde{\nabla}_\nu\,\tilde{\nabla}_\mu - \tilde{\nabla}_\mu\,\tilde{\nabla}_\nu\right)T^{\alpha\beta\ldots\gamma}_{\rho\sigma\ldots\lambda}\,(x,u) =$$
$$= \left(\nabla_\nu\,\nabla_\mu - \nabla_\mu\,\nabla_\nu\right)T^{\alpha\beta\ldots\gamma}_{\rho\sigma\ldots\lambda}\,(x,u) +$$
$$+\,\frac{\partial}{\partial\,u^\eta}\left(\nabla_\mu T^{\alpha\beta\ldots\gamma}_{\rho\sigma\ldots\lambda}\,(x,u)\right)\frac{\partial\,u^\eta}{\partial\,x^\nu} -$$
$$-\,\frac{\partial}{\partial\,u^\eta}\left(\nabla_\nu T^{\alpha\beta\ldots\gamma}_{\rho\sigma\ldots\lambda}\,(x,u)\right)\frac{\partial\,u^\eta}{\partial\,u^\mu} +$$
$$+\,\nabla_\nu\left(\frac{\partial}{\partial\,u^\eta}\left(T^{\alpha\beta\ldots\gamma}_{\rho\sigma\ldots\lambda}\,(x,u)\right)\frac{\partial\,u^\eta}{\partial\,x^\mu}\right) -$$
$$-\,\nabla_\mu\left(\frac{\partial}{\partial\,u^\eta}\left(T^{\alpha\beta\ldots\gamma}_{\rho\sigma\ldots\lambda}\,(x,u)\right)\frac{\partial\,u^\eta}{\partial\,x^\nu}\right) +$$
$$+\,\frac{\partial}{\partial\,u^\delta}\left(\frac{\partial}{\partial\,u^\eta}\left(T^{\alpha\beta\ldots\gamma}_{\rho\sigma\ldots\lambda}\,(x,u)\right)\frac{\partial\,u^\eta}{\partial\,x^\mu}\right)\frac{\partial\,u^\delta}{\partial\,x^\nu} -$$
$$-\,\frac{\partial}{\partial\,u^\delta}\left(\frac{\partial}{\partial\,u^\eta}\left(T^{\alpha\beta\ldots\gamma}_{\rho\sigma\ldots\lambda}\,(x,u)\right)\frac{\partial\,u^\eta}{\partial\,x^\nu}\right)\frac{\partial\,u^\delta}{\partial\,x^\mu}$$

for which the essential part is

$$\begin{aligned}
&\left(\nabla_\nu\,\nabla_\mu-\nabla_\mu\,\nabla_\nu\right)T^{\alpha\beta\ldots\gamma}_{\rho\sigma\ldots\lambda}\left(x,u\right)=\\
&=R^{\eta}{}_{\rho\mu\nu}\left(x,u\right)T^{\alpha\beta\ldots\gamma}_{\eta\sigma\ldots\lambda}\left(x,u\right)+\\
&+R^{\eta}{}_{\sigma\mu\nu}\left(x,u\right)T^{\alpha\beta\ldots\gamma}_{\rho\eta\ldots\lambda}\left(x,u\right)+\ldots+\\
&+R^{\eta}{}_{\lambda\mu\nu}\left(x,u\right)T^{\alpha\beta\ldots\gamma}_{\rho\sigma\ldots\eta}\left(x,u\right)-\\
&-R^{\alpha}{}_{\eta\mu\nu}\left(x,u\right)T^{\eta\beta\ldots\gamma}_{\rho\sigma\ldots\lambda}\left(x,u\right)-\\
&-R^{\beta}{}_{\eta\mu\nu}\left(x,u\right)T^{\alpha\eta\ldots\gamma}_{\rho\sigma\ldots\lambda}\left(x,u\right)-\\
&-\ldots-R^{\gamma}{}_{\eta\mu\nu}\left(x,u\right)T^{\alpha\beta\ldots\eta}_{\rho\sigma\ldots\lambda}\left(x,u\right)-\\
&-2\,\Gamma^{\eta}_{[\mu\nu]}\left(x,u\right)\nabla_\eta\,T^{\alpha\beta\ldots\gamma}_{\rho\sigma\ldots\lambda}\left(x,u\right).
\end{aligned}$$

Here the world-curvature tensor, that is, the generalized, Eulerian Riemann tensor, is given by

$$\begin{aligned}
&R^{\alpha}{}_{\beta\rho\sigma}\left(x,u\right)=\frac{\partial}{\partial\,x^\rho}\,\Gamma^{\alpha}_{\beta\sigma}\left(x,u\right)-\frac{\partial}{\partial\,x^\sigma}\,\Gamma^{\alpha}_{\beta\rho}\left(x,u\right)+\\
&+\Gamma^{\lambda}_{\beta\sigma}\left(x,u\right)\Gamma^{\alpha}_{\lambda\rho}\left(x,u\right)-\,\Gamma^{\lambda}_{\beta\rho}\left(x,u\right)\Gamma^{\alpha}_{\lambda\sigma}\left(x,u\right)
\end{aligned}$$

for which the corresponding curvature form of mobility may simply be given by

$$\begin{aligned}
&\tilde{R}^{\alpha}{}_{\beta\rho\sigma}\left(x,u\right)=\frac{\partial}{\partial\,x^\rho}\,\Gamma^{\alpha}_{\beta\sigma}\left(x,u\right)+\frac{\partial}{\partial\,u^\lambda}\left(\Gamma^{\alpha}_{\beta\sigma}\left(x,u\right)\right)\frac{\partial\,u^\lambda}{\partial\,x^\rho}-\\
&-\frac{\partial}{\partial\,x^\sigma}\,\Gamma^{\alpha}_{\beta\rho}\left(x,u\right)-\frac{\partial}{\partial\,u^\lambda}\left(\Gamma^{\alpha}_{\beta\rho}\left(x,u\right)\right)\frac{\partial\,u^\lambda}{\partial\,x^\sigma}+\\
&+\Gamma^{\lambda}_{\beta\sigma}\left(x,u\right)\Gamma^{\alpha}_{\lambda\rho}\left(x,u\right)-\Gamma^{\lambda}_{\beta\rho}\left(x,u\right)\Gamma^{\alpha}_{\lambda\sigma}\left(x,u\right).
\end{aligned}$$

We can now write the following fundamental decomposition:

$$\begin{aligned}
&R^{\alpha}{}_{\beta\rho\sigma}\left(x,u\right)=B^{\alpha}{}_{\beta\rho\sigma}\left(x,u\right)+M^{\alpha}{}_{\beta\rho\sigma}\left(x,u\right)+\\
&+N^{\alpha}{}_{\beta\rho\sigma}\left(x,u\right)+U^{\alpha}{}_{\beta\rho\sigma}\left(x,u\right),\\
&B^{\alpha}{}_{\beta\rho\sigma}\left(x,u\right)=\frac{\partial}{\partial\,x^\rho}\,\Delta^{\alpha}_{\beta\sigma}\left(x,u\right)-\frac{\partial}{\partial\,x^\sigma}\,\Delta^{\alpha}_{\beta\rho}\left(x,u\right)+\\
&+\Delta^{\lambda}_{\beta\sigma}\left(x,u\right)\Delta^{\alpha}_{\lambda\rho}\left(x,u\right)-\,\Delta^{\lambda}_{\beta\rho}\left(x,u\right)\Delta^{\alpha}_{\lambda\sigma}\left(x,u\right),\\
&M^{\alpha}{}_{\beta\rho\sigma}\left(x,u\right)=\breve{\nabla}_\rho\,K^{\alpha}_{\beta\sigma}\left(x,u\right)-\breve{\nabla}_\sigma\,K^{\alpha}_{\beta\rho}\left(x,u\right)+\\
&+K^{\lambda}_{\beta\sigma}\left(x,u\right)K^{\alpha}_{\lambda\rho}\left(x,u\right)-\,K^{\lambda}_{\beta\rho}\left(x,u\right)K^{\alpha}_{\lambda\sigma}\left(x,u\right),\\
&N^{\alpha}{}_{\beta\rho\sigma}\left(x,u\right)=\breve{\nabla}_\rho\,Q^{\alpha}_{\beta\sigma}\left(x,u\right)-\breve{\nabla}_\sigma\,Q^{\alpha}_{\beta\rho}\left(x,u\right)+\\
&+Q^{\lambda}_{\beta\sigma}\left(x,u\right)Q^{\alpha}_{\lambda\rho}\left(x,u\right)-\,Q^{\lambda}_{\beta\rho}\left(x,u\right)Q^{\alpha}_{\lambda\sigma}\left(x,u\right),\\
&U^{\alpha}{}_{\beta\rho\sigma}\left(x,u\right)=K^{\lambda}_{\beta\sigma}\left(x,u\right)Q^{\alpha}_{\lambda\rho}\left(x,u\right)-K^{\lambda}_{\beta\rho}\left(x,u\right)Q^{\alpha}_{\lambda\sigma}\left(x,u\right)+\\
&+Q^{\lambda}_{\beta\sigma}\left(x,u\right)K^{\alpha}_{\lambda\rho}\left(x,u\right)-Q^{\lambda}_{\beta\rho}\left(x,u\right)K^{\alpha}_{\lambda\sigma}\left(x,u\right),
\end{aligned}$$

where the Eulerian Levi-Civita connection, the Eulerian contorsion tensor, and the connection of non-metricity are respectively given by

$$\begin{aligned}
&\Delta^{\lambda}_{\alpha\beta}\left(x,u\right)=\frac{1}{2}\,g^{\lambda\sigma}\left(x,u\right)\Big(\frac{\partial}{\partial\,x^\beta}\,g_{\sigma\alpha}\left(x,u\right)-\frac{\partial}{\partial\,x^\sigma}\,g_{\alpha\beta}\left(x,u\right)+\\
&+\,\frac{\partial}{\partial\,x^\alpha}\,g_{\beta\sigma}\left(x,u\right)\Big),\\
&K^{\lambda}_{\alpha\beta}\left(x,u\right)=\Gamma^{\lambda}_{[\alpha\beta]}\left(x,u\right)-\\
&-\,g^{\lambda\sigma}\left(x,u\right)\left(g_{\alpha\rho}\left(x,u\right)\,\Gamma^{\rho}_{[\sigma\beta]}\left(x,u\right)+g_{\beta\rho}\left(x,u\right)\,\Gamma^{\rho}_{[\sigma\alpha]}\left(x,u\right)\right),\\
&Q^{\lambda}_{\alpha\beta}\left(x,u\right)=\frac{1}{2}\,g^{\lambda\sigma}\left(x,u\right)\Big(\nabla_\beta\,g_{\sigma\alpha}\left(x,u\right)-\nabla_\sigma\,g_{\alpha\beta}\left(x,u\right)+\\
&+\,\nabla_\alpha\,g_{\beta\sigma}\left(x,u\right)\Big),
\end{aligned}$$

such that $\breve{\nabla}$ represents covariant differentiation with respect to the symmetric connection $\Delta\left(x,u\right)$ alone. The curvature tensor given by $B\left(x,u\right)$ is, of course, the Eulerian Riemann-Christoffel tensor, generalizing the one of the General Theory of Relativity which depends on position alone.

Of special interest, for the world-metric tensor, we note that

$$\begin{aligned}
&\left(\nabla_\sigma\,\nabla_\rho-\nabla_\rho\,\nabla_\sigma\right)g_{\alpha\beta}\left(x,u\right)=R_{\alpha\beta\rho\sigma}\left(x,u\right)+R_{\beta\alpha\rho\sigma}\left(x,u\right)-\\
&-\,2\,\Gamma^{\lambda}_{[\rho\sigma]}\left(x,u\right)\nabla_\lambda\,g_{\alpha\beta}\left(x,u\right)
\end{aligned}$$

where, with the usual notation, $R_{\alpha\beta\rho\sigma}\left(x,u\right)=g_{\alpha\lambda}\left(x,u\right)R^{\lambda}{}_{\beta\rho\sigma}\left(x,u\right)$. That is, more specifically, while keeping in mind that

$$\Phi_{\alpha\beta\lambda}=\frac{\partial}{\partial\,u^\lambda}\,g_{\alpha\beta}\left(x,u\right)=\psi_\alpha\,\psi_\beta\,\psi_\lambda\,,$$

we have

$$\begin{aligned}
&\left(\nabla_\sigma\,\nabla_\rho-\nabla_\rho\,\nabla_\sigma\right)g_{\alpha\beta}\left(x,u\right)=R_{\alpha\beta\rho\sigma}\left(x,u\right)+\\
&+R_{\beta\alpha\rho\sigma}\left(x,u\right)-\,2\,\Gamma^{\lambda}_{[\rho\sigma]}\left(x,u\right)\Phi_{\alpha\beta\gamma}\,\nabla_\lambda\,u^\gamma.
\end{aligned}$$

As such, we have a genuine homothetic curvature given by

$$\begin{aligned}
&H_{\alpha\beta}\left(x,u\right)=R^{\lambda}{}_{\lambda\alpha\beta}\left(x,u\right)=\\
&=\breve{\nabla}_\alpha\,Q_\beta\left(x,u\right)-\breve{\nabla}_\beta\,Q_\alpha\left(x,u\right)=\\
&=\frac{\partial}{\partial\,x^\alpha}\,Q_\beta\left(x,u\right)-\frac{\partial}{\partial\,x^\beta}\,Q_\alpha\left(x,u\right),\\
&Q_\alpha\left(x,u\right)=Q^{\lambda}_{\lambda\alpha}\left(x,u\right)=\frac{1}{2}\,g^{\lambda\beta}\left(x,u\right)\nabla_\alpha\,g_{\lambda\beta}\left(x,u\right)=\\
&=\psi^2\,\psi_\beta\,\nabla_\alpha\,u^\beta\,.
\end{aligned}$$

Upon setting

$$\theta_\alpha\left(x,u\right)=\frac{1}{2}\,\psi_\beta\,\nabla_\alpha\,u^\beta,$$

we have

$$\begin{aligned}
&H_{\alpha\beta}\left(x,u\right)=\psi^2\Big(\frac{\partial}{\partial\,x^\alpha}\,\theta_\beta\left(x,u\right)-\frac{\partial}{\partial\,x^\beta}\,\theta_\alpha\left(x,u\right)-\\
&-\,2\Big(\theta_\alpha\left(x,u\right)\frac{\partial\ln\psi}{\partial\,x^\beta}-\theta_\beta\left(x,u\right)\frac{\partial\ln\psi}{\partial\,x^\alpha}\Big)\Big).
\end{aligned}$$

At this point, the generalized, Eulerian Ricci tensor is given in the form

$$R_{\alpha\beta}(x,u) = R^{\lambda}{}_{\alpha\lambda\beta}(x,u) = Z_{\alpha\beta}(\Delta(x,u), K(x,u)) +$$
$$+ N_{\alpha\beta}(Q(x,u)) + X_{\alpha\beta}(K(x,u), Q(x,u)),$$
$$Z_{\alpha\beta}(\Delta(x,u), K(x,u)) = B^{\lambda}{}_{\alpha\lambda\beta}(x,u) + M^{\lambda}{}_{\alpha\lambda\beta}(x,u),$$
$$N_{\alpha\beta}(Q(x,u)) = N^{\lambda}_{\alpha\lambda\beta}(x,u),$$
$$X_{\alpha\beta}(K(x,u), Q(x,u)) = U^{\lambda}{}_{\alpha\lambda\beta}(x,u),$$

which admits the peculiar anti-symmetric part

$$R_{[\alpha\beta]}(x,u) = \frac{1}{2}\left(\frac{\partial}{\partial x^{\alpha}} K^{\lambda}_{\beta\lambda}(x,u) - \frac{\partial}{\partial x^{\beta}} K^{\lambda}_{\alpha\lambda}(x,u)\right) +$$
$$+ \frac{1}{2}\left(\frac{\partial}{\partial x^{\alpha}} Q_{\beta}(x,u) - \frac{\partial}{\partial x^{\beta}} Q_{\alpha}(x,u)\right) +$$
$$+ \breve{\nabla}_{\lambda}\Gamma^{\lambda}_{[\alpha\beta]}(x,u) +$$
$$+ \Gamma^{\lambda}_{[\alpha\beta]}(x,u) K^{\sigma}_{\lambda\sigma}(x,u) + \Gamma^{\lambda}_{[\alpha\beta]}(x,u) Q_{\lambda}(x,u) +$$
$$+ \Gamma^{\lambda}_{[\beta\sigma]}(x,u) Q^{\sigma}_{\alpha\lambda}(x,u) - \Gamma^{\lambda}_{[\alpha\sigma]}(x,u) Q^{\sigma}_{\beta\lambda}(x,u) +$$
$$+ \frac{1}{2}\left(K^{\lambda}_{\alpha\sigma}(x,u) K^{\sigma}_{\lambda\beta}(x,u) - K^{\lambda}_{\beta\sigma}(x,u) K^{\sigma}_{\lambda\alpha}(x,u)\right),$$

where we have made use of the fact that $K^{\lambda}_{[\alpha\beta]}(x,u) = \Gamma^{\lambda}_{[\alpha\beta]}(x,u)$. Let us also keep in mind that the explicit physical structure of the connection form forming our various curvature expressions, as it relates to gravity, electromagnetism, material spin, and the nuclear interaction, is given in Section 3 of this work, naturally following [4].

We can now obtain the complete Eulerian generalization of the first Bianchi identity as follows:

$$R_{\alpha\beta\rho\sigma}(x,u) + R_{\alpha\rho\sigma\beta}(x,u) + R_{\alpha\sigma\beta\rho}(x,u) =$$
$$= -2\, g_{\alpha\lambda}(x,u)\left(\frac{\partial}{\partial x^{\sigma}}\Gamma^{\lambda}_{[\beta\rho]}(x,u) + \frac{\partial}{\partial x^{\beta}}\Gamma^{\lambda}_{[\rho\sigma]}(x,u) +\right.$$
$$\left. + \frac{\partial}{\partial x^{\rho}}\Gamma^{\lambda}_{[\sigma\beta]}(x,u)\right) -$$
$$- 2\, g_{\alpha\lambda}(x,u)\left(\Gamma^{\lambda}_{\gamma\beta}(x,u)\Gamma^{\gamma}_{[\rho\sigma]}(x,u) +\right.$$
$$\left. + \Gamma^{\lambda}_{\gamma\rho}(x,u)\Gamma^{\gamma}_{[\sigma\beta]}(x,u) + \Gamma^{\lambda}_{\gamma\sigma}(x,u)\Gamma^{\gamma}_{[\beta\rho]}(x,u)\right) +$$
$$+ 2\,\Phi_{\alpha\lambda\gamma}\left(\Gamma^{\lambda}_{[\rho\sigma]}(x,u)\nabla_{\beta}u^{\gamma} + \Gamma^{\lambda}_{[\sigma\beta]}(x,u)\nabla_{\rho}u^{\gamma} +\right.$$
$$\left. + \Gamma^{\lambda}_{[\beta\rho]}(x,u)\nabla_{\sigma}u^{\gamma}\right).$$

Similarly, after a somewhat lengthy calculation, we obtain, for the generalization of the second Bianchi identity,

$$\nabla_{\lambda} R_{\alpha\beta\rho\sigma}(x,u) + \nabla_{\rho} R_{\alpha\beta\sigma\lambda}(x,u) + \nabla_{\sigma} R_{\alpha\beta\lambda\rho}(x,u) =$$
$$= 2\left(\Gamma^{\gamma}_{[\rho\sigma]}(x,u) R_{\alpha\beta\gamma\lambda}(x,u) + \Gamma^{\gamma}_{[\sigma\lambda]}(x,u) R_{\alpha\beta\gamma\rho}(x,u) +\right.$$
$$\left. + \Gamma^{\gamma}_{[\lambda\rho]}(x,u) R_{\alpha\beta\gamma\sigma}(x,u)\right) +$$
$$+ \Gamma^{\gamma}_{\beta\rho}(x,u)\left((\nabla_{\lambda}\Phi_{\alpha\gamma\eta})\nabla_{\sigma}u^{\eta} - (\nabla_{\sigma}\Phi_{\alpha\gamma\eta})\nabla_{\lambda}u^{\eta}\right) +$$
$$+ \Gamma^{\gamma}_{\beta\sigma}(x,u)\left((\nabla_{\rho}\Phi_{\alpha\gamma\eta})\nabla_{\lambda}u^{\eta} - (\nabla_{\lambda}\Phi_{\alpha\gamma\eta})\nabla_{\rho}u^{\eta}\right) +$$
$$+ \Gamma^{\gamma}_{\beta\lambda}(x,u)\left((\nabla_{\sigma}\Phi_{\alpha\gamma\eta})\nabla_{\rho}u^{\eta} - (\nabla_{\rho}\Phi_{\alpha\gamma\eta})\nabla_{\sigma}u^{\eta}\right) -$$
$$- \Gamma^{\gamma}_{\beta\rho}(x,u)\Phi_{\alpha\gamma\eta}\left(R^{\eta}{}_{\mu\sigma\lambda}(x,u)u^{\mu} + 2\Gamma^{\mu}_{[\sigma\lambda]}(x,u)\nabla_{\mu}u^{\eta}\right) -$$
$$- \Gamma^{\gamma}_{\beta\sigma}(x,u)\Phi_{\alpha\gamma\eta}\left(R^{\eta}{}_{\mu\lambda\rho}(x,u)u^{\mu} + 2\Gamma^{\mu}_{[\lambda\rho]}(x,u)\nabla_{\mu}u^{\eta}\right) -$$
$$- \Gamma^{\gamma}_{\beta\lambda}(x,u)\Phi_{\alpha\gamma\eta}\left(R^{\eta}{}_{\mu\rho\sigma}(x,u)u^{\mu} + 2\Gamma^{\mu}_{[\rho\sigma]}(x,u)\nabla_{\mu}u^{\eta}\right) +$$
$$+ \Phi_{\alpha\gamma\eta}(\nabla_{\rho}u^{\eta})\left(\nabla_{\sigma}\Gamma^{\gamma}_{\beta\lambda}(x,u) - \nabla_{\lambda}\Gamma^{\gamma}_{\beta\sigma}(x,u)\right) +$$
$$+ \Phi_{\alpha\gamma\eta}(\nabla_{\sigma}u^{\eta})\left(\nabla_{\lambda}\Gamma^{\gamma}_{\beta\rho}(x,u) - \nabla_{\rho}\Gamma^{\gamma}_{\beta\lambda}(x,u)\right) +$$
$$+ \Phi_{\alpha\gamma\eta}(\nabla_{\lambda}u^{\eta})\left(\nabla_{\rho}\Gamma^{\gamma}_{\beta\sigma}(x,u) - \nabla_{\sigma}\Gamma^{\gamma}_{\beta\rho}(x,u)\right),$$

where

$$\nabla_{\sigma}\Gamma^{\lambda}_{\alpha\beta}(x,u) - \nabla_{\beta}\Gamma^{\lambda}_{\alpha\sigma}(x,u) = -R^{\lambda}{}_{\alpha\beta\sigma}(x,u) +$$
$$+ \Gamma^{\rho}_{\alpha\beta}(x,u)\Gamma^{\lambda}_{\rho\sigma}(x,u) - \Gamma^{\rho}_{\alpha\sigma}(x,u)\Gamma^{\lambda}_{\rho\beta}(x,u) -$$
$$- 2\,\Gamma^{\rho}_{[\beta\sigma]}(x,u)\Gamma^{\lambda}_{\alpha\rho}(x,u).$$

By contraction, we may extract a physical density field as follows:

$$J_{\alpha}(x,u) =$$
$$= -\nabla_{\beta}\left(\frac{1}{2}\left(R^{\beta}{}_{\alpha}(x,u) + {}^{*}R^{\beta}{}_{\alpha}(x,u)\right) - \frac{1}{2}\delta^{\beta}_{\alpha} R(x,u)\right),$$

where ${}^{*}R^{\alpha}{}_{\beta}(x,u) = R^{\alpha\lambda}_{\beta\lambda}(x,u)$ are the components of the generalized Ricci tensor of the second kind and $R(x,u) = R^{\lambda}{}_{\lambda}(x,u) = {}^{*}R^{\lambda}{}_{\lambda}(x,u)$ is the generalized Ricci scalar. As we know, the Ricci tensor of the first kind and the Ricci tensor of the second kind coincide only when the connection form is metric-compatible. The asymmetric, generally non-conservative world-entity given by

$$G^{\alpha}{}_{\beta}(x,u) = \frac{1}{2}\left(R^{\alpha}{}_{\beta}(x,u) + {}^{*}R^{\alpha}{}_{\beta}(x,u)\right) - \frac{1}{2}\delta^{\alpha}_{\beta} R(x,u)$$

will therefore represent the generalized Einstein tensor, such that we may have a corresponding geometric object given by

$$C^{\alpha}(x,u) \equiv -g^{\alpha\beta}(x,u) J_{\beta}(x,u) =$$
$$= \nabla_{\beta} G^{\beta\alpha}(x,u) - G^{\beta}{}_{\lambda}(x,u)\nabla_{\beta} g^{\lambda\alpha}(x,u).$$

6 Quantum gravity from the physical vacuum of $\mathbf{U_4}$

We are now in a position to derive a quantum mechanical wave equation from the underlying structure of our present theory. So far, our field equations appear too complicated to handle for this particular purpose. It is quite enough that

we know the structural content of the connection form, which encompasses the geometrization of the known classical fields. However, if we deal with a particular case, namely, that of physical vacuum, we shall immediately be able to speak of one type of emergent quantum gravity.

Assuming now that the world-geometry U_4 is devoid of "ultimate physical substance" (that is, intrinsic material confinement on the most fundamental scale) other than, perhaps, primordial radiation, the field equation shall be given by

$$R_{\alpha\beta}(x,u) = 0$$

for which, in general, $R^{\alpha}_{\beta\mu\nu}(x,u) = W^{\alpha}_{\beta\mu\nu}(x,u) \neq 0$, where $W(x,u)$ is the generalized Weyl conformal tensor. In this way, all physical fields, including matter, are mere appearances in our geometric world-structure. Consequently, from $R_{(\alpha\beta)}(x,u) = 0$, the emergent picture of gravity is readily given by the symmetric Eulerian Ricci tensor for the composite structure of gravity, that is, explicitly,

$$B_{\alpha\beta}(\Delta(x,u)) = -\Big(M_{\alpha\beta}\big(K(x,u)\big) + N_{\alpha\beta}\big(Q(\psi)\big) + U_{\alpha\beta}\big(K(x,u), Q(\psi)\big)\Big),$$

where we have written $Q(x,u) = Q(\psi)$, such that, in this special consideration, gravity can essentially be thought of as exterior electromagnetism as well as arising from the quantum fuzziness of the background non-metricity of the world-geometry. In addition, from $R_{[\alpha\beta]}(x,u) = 0$, we also have the following anti-symmetric counterpart:

$$R_{[\alpha\beta]}(\Delta(x,u), K(x,u)) = \frac{\partial}{\partial x^{\beta}} Q_{\alpha}(\psi) - \frac{\partial}{\partial x^{\alpha}} Q_{\beta}(\psi) - \Gamma^{\lambda}_{[\alpha\beta]}(x,u) Q_{\lambda}(\psi) + \Gamma^{\lambda}_{[\alpha\sigma]}(x,u) Q^{\sigma}_{\beta\lambda}(\psi) - \Gamma^{\lambda}_{[\beta\sigma]}(x,u) Q^{\sigma}_{\alpha\lambda}(\psi),$$

$$Q_{\alpha}(\psi) = \frac{1}{2}\psi^2 \psi_{\beta} \nabla_{\alpha} u^{\beta}.$$

Correspondingly, we shall set, for the "quantum potential",

$$Q_{\alpha}(\psi) = \frac{\partial}{\partial x^{\alpha}} \ln \bar{\psi}$$

such that the free, geodesic motion of a particle along the fuzzy world-path $s(x,u) = \tau\left(\psi\left(\bar{\psi}\right)\right)$ in the empty U_4 can simultaneously be described by the pair of dynamical equations

$$\frac{Du^{\alpha}}{Ds} = 0,$$
$$\frac{D\bar{\psi}}{Ds} = 0,$$

since, as we have previously seen, $Q_{\alpha}\left(\psi\left(\bar{\psi}\right)\right) u^{\alpha} = 0$.

Immediately, we obtain the geometrically non-linear wave equation

$$\frac{1}{\sqrt{\det(g(x,u))}} \frac{\partial}{\partial x^{\alpha}} \left(g^{\alpha\beta}(x,u) \sqrt{\det(g(x,u))} \frac{\partial \bar{\psi}}{\partial x^{\beta}} \right) = \left(R(\Delta(x,u), K(x,u)) + \Lambda(Q(\psi))\right) \bar{\psi}$$

that is,

$$\left(\Delta^2_B - \widehat{R}(x,u)\right) \bar{\psi} = 0,$$

where

$$\Delta^2_B = \frac{1}{\sqrt{\det(g(x,u))}} \frac{\partial}{\partial x^{\alpha}} \left(g^{\alpha\beta}(x,u) \sqrt{\det(g(x,u))} \frac{\partial}{\partial x^{\beta}} \right)$$

is the covariant four-dimensional Beltrami wave operator and, with the explicit dependence of ψ on $\bar{\psi}$,

$$\widehat{R}(x,u) = R(\Delta(x,u), K(x,u)) + \Lambda\left(Q\left(\psi\left(\bar{\psi}\right)\right)\right)$$

is the emergent curvature scalar of our quantum field, for which

$$\Lambda(Q(\psi)) = \widehat{N}\left(Q\left(\psi\left(\bar{\psi}\right)\right)\right) - \frac{1}{\bar{\psi}^2} g^{\alpha\beta}(x,u) \frac{\partial \bar{\psi}}{\partial x^{\alpha}} \frac{\partial \bar{\psi}}{\partial x^{\beta}},$$

$$\widehat{N}\left(Q\left(\psi\left(\bar{\psi}\right)\right)\right) = N\left(Q\left(\psi\left(\bar{\psi}\right)\right)\right) + U\left(K(x,u), Q\left(\psi\left(\bar{\psi}\right)\right)\right) - g^{\alpha\beta}(x,u) \breve{\nabla}_{\beta} Q_{\alpha}\left(\psi\left(\bar{\psi}\right)\right).$$

In terms of the Eulerian Ricci scalar, which is now quantized by the wave equation, we have a quantum gravitational wave equation with two quantized intrinsic sources, namely, the torsional source $M(x,u)$, which combines the electromagnetic and material sources, and the quantum mechanical source $\Lambda\left(Q\left(\psi\left(\bar{\psi}\right)\right)\right) = \Lambda(Q(x,u))$,

$$\left(\Delta^2_B - B(x,u)\right) \bar{\psi} = M(x,u) \bar{\psi} + \Lambda\left(Q\left(\psi\left(\bar{\psi}\right)\right)\right) \bar{\psi}$$

thereby completing the quantum gravitational picture at an elementary stage.

7 Special analytic form of geodesic paths

Here we are interested in the derivation of the generalized geodesic equation of motion such that our geodesic paths correspond to the formal solution of the quantum gravitational wave equation in the preceding section. Indeed, owing to the wave function $\bar{\psi} = \bar{\psi}(x,u)$, these geodesic paths shall be conformal ones.

For our purpose, let $\Psi(x) = const.$ represent a family of hypersurfaces in U_4 such that with respect to a mobile hypersurface Σ, for $\frac{\partial}{\partial x^{\alpha}}(\Psi(x)) \delta x^{\alpha} = 0$, there exists a genuine unit normal velocity vector, given by $n^{\alpha} = \frac{dx^{\alpha}}{d\tau}$, at some point whose extended path can be parametrized by $\tau = \tau(s)$, that is

$$n_{\alpha} = \zeta\left(x, \frac{\partial}{\partial x}\Psi(x)\right) \frac{\partial}{\partial x^{\alpha}} \Psi(x)$$

$$g_{\alpha\beta}(x,u)\, n^{\alpha} \delta n^{\beta} = 0.$$

The essential partial differential equation representing any quantum gravitational hypersurface Σ_{ψ} can then

simply be represented by the arbitrary parametric form $\zeta\left(x, \frac{\partial}{\partial x}\,\Psi(x)\right) = \zeta\left(\bar{\psi}\right) = const$ such that

$$\int_a^b \left(\phi(x,u) - \zeta\left(\bar{\psi}\right)\frac{d}{d\tau}\,\Psi(x)\right) d\tau \geqslant 0$$

where a and b are two points in Σ_ψ.

Keeping in mind once again that $\psi_\alpha\, u^\alpha = 0$ and that

$$u_\alpha = \frac{1}{2}\frac{\partial}{\partial u^\alpha}\,\phi^2(x,u)$$

$$\frac{\partial}{\partial x^\lambda}\,g_{\alpha\beta}(x,u) =$$

$$= \Gamma_{\alpha\beta\lambda}(x,u) + \Gamma_{\beta\alpha\lambda}(x,u) + \psi_\alpha\,\psi_\beta\,\psi_\sigma\,\nabla_\lambda u^\sigma$$

the generalized Euler-Lagrange equation corresponding to our situation shall then be given by

$$\frac{d}{ds}\left(\frac{\partial}{\partial u^\alpha}\,\phi^2(x,u)\right) - \frac{\partial}{\partial x^\alpha}\,\phi^2(x,u) +$$

$$+ \frac{\partial}{\partial u^\beta}\left(\phi^2(x,u)\right)\frac{\partial u^\beta}{\partial x^\alpha} + b_\alpha(x,u) = 0\,,$$

where the "external" term is given by

$$b_\alpha(x,u) = 4\,\Gamma^\lambda_{[\alpha\beta]}(x,u)\,u_\lambda\,u^\beta.$$

As a matter of straightforward verification, we have

$$\frac{du_\alpha}{ds} - \Gamma_{\beta\alpha\lambda}(x,u)\,u^\beta\,u^\lambda = 0$$

A unique general solution to the above equation corresponding to the quantum displacement field $\psi = \psi\left(\bar{\psi}\right)$, which, in our theory, generates the non-metric nature of the world-manifold U_4, can now be obtained as

$$s(x,u) = s\left(\psi\left(\bar{\psi}\right)\right) = C_1 + C_2\int \exp\left(\int H\left(\psi\left(\bar{\psi}\right)ds\right)\right)ds$$

where C_1 and C_2 are integration constants. This is such that, at arbitrary world-points a and b, we have the conformal relation (for $C = C_2$)

$$ds_b = \exp\left(C\int H\left(\psi\left(\bar{\psi}\right)\right)ds\right)\,ds_a\,,$$

which sublimely corresponds to the case of our previous quantum theory of gravity [3].

8 Geometric structure of the electromagnetic potential

As another special consideration, let us now attempt to extensively describe the geometric structure of the electromagnetic potential in our theory.

Due to the degree of complicatedness of the detailed general coordinate transformations in U_4, let us, for the sake of tangibility, refer a smoothly extensive coordinate patch $P(x)$ to the four-dimensional tangent hyperplane $M_4(y)$, whose metric tensor η is Minkowskian, such that an ensemble of Minkowskian tangent hyperplanes, that is,

$$\sum\nolimits_{a\,=\,1,2,\ldots,N} M_4^{(a)}(y)$$

cannot globally cover the curved manifold U_4 without breaking analytic continuity (smoothness), at least up to the third order. Denoting the "invariant derivative" by $\nabla_A = E^\alpha_A(x,u)\,\frac{\partial}{\partial x^\alpha}$, this situation can then basically be described by

$$g_{\alpha\beta}(x,u) = E^A_\alpha(x,u)\,E^B_\beta(x,u)\,\eta_{AB}\,,$$

$$E^A_\alpha(x,u) = \frac{\partial y^A}{\partial x^\alpha},\; E^\alpha_A(x,u) = \left(E^A_\alpha(x,u)\right)^{-1}\,,$$

$$y^A = y^A(x,u)\,,\; x^\alpha = x^\alpha(y)\,,$$

$$E^A_\alpha(x,u)\,E^\beta_A(x,u) = \delta^\beta_\alpha,\; E^\alpha_A(x,u)\,E^B_\alpha(x,u) = \delta^B_A\,,$$

$$\Gamma^\lambda_{\alpha\beta}(x,u) = E^\lambda_A(x,u)\,\frac{\partial}{\partial x^\beta}E^A_\alpha(x,u) =$$

$$= E^\lambda_A(x,u)\,E^B_\beta(x,u)\,\nabla_B E^A_\alpha(x,u)\,.$$

Of fundamental importance in our unified field theory are, of course, the torsion tensor given by

$$\Gamma^\lambda_{[\alpha\beta]}(x,u) = \frac{1}{2}\,E^\lambda_A(x,u)\left(\frac{\partial}{\partial x^\beta}\,E^A_\alpha(x,u) - \frac{\partial}{\partial x^\alpha}\,E^A_\beta(x,u)\right)$$

and the curvature tensor given by

$$R^\lambda{}_{\sigma\alpha\beta}(x,u) =$$

$$= -\,E^\lambda_A(x,u)\left(\left(\frac{\partial}{\partial x^\beta}\frac{\partial}{\partial x^\alpha} - \frac{\partial}{\partial x^\alpha}\frac{\partial}{\partial x^\beta}\right)E^A_\sigma(x,u)\right) =$$

$$= E^A_\sigma(x,u)\left(\left(\frac{\partial}{\partial x^\beta}\frac{\partial}{\partial x^\alpha} - \frac{\partial}{\partial x^\alpha}\frac{\partial}{\partial x^\beta}\right)E^\lambda_A(x,u)\right)\,.$$

Additionally, we can also see that

$$R_{\rho\sigma\alpha\beta}(x,u) =$$

$$= E^A_\sigma(x,u)\left(\left(\frac{\partial}{\partial x^\beta}\frac{\partial}{\partial x^\alpha} - \frac{\partial}{\partial x^\alpha}\frac{\partial}{\partial x^\beta}\right)E_{A\rho}(x,u)\right) +$$

$$+ \left(\frac{\partial}{\partial x^\beta}\frac{\partial}{\partial x^\alpha} - \frac{\partial}{\partial x^\alpha}\frac{\partial}{\partial x^\beta}\right)g_{\rho\sigma}(x,u)\,.$$

Immediately, we obtain

$$R^\lambda{}_{\sigma\alpha\beta}(x,u) = E^\lambda_A(x,u)\,E^B_\alpha(x,u)\,E^C_\beta(x,u)\,\times$$

$$\times\left(\left(\nabla_B\nabla_C - \nabla_C\nabla_B\right)E^A_\sigma(x,u)\right) - 2\,\Gamma^\lambda_{\sigma\rho}(x,u)\,\Gamma^\rho_{[\alpha\beta]}(x,u)\,.$$

Introducing a corresponding internal ("isotopic") curvature form through

$$\bar{R}^\alpha{}_{\beta AB}(x,u) = E^\alpha_C(x,u)\left(\left(\nabla_A\nabla_B - \nabla_B\nabla_A\right)E^C_\beta(x,u)\right),$$

we can write

$$R^{\lambda}{}_{\sigma\alpha\beta}(x,u) = E^{A}_{\alpha}(x,u)\, E^{B}_{\beta}(x,u)\, \bar{R}^{\lambda}{}_{\sigma AB}(x,u) -$$
$$- 2\,\Gamma^{\lambda}_{\sigma\rho}(x,u)\,\Gamma^{\rho}_{[\alpha\beta]}(x,u)\ .$$

In physical terms, we therefore see that

$$R^{\lambda}{}_{\sigma\alpha\beta}(x,u) = E^{A}_{\alpha}(x,u)\, E^{B}_{\beta}(x,u)\, \bar{R}^{\lambda}{}_{\sigma AB}(x,u) -$$
$$- 2\,\Gamma^{\lambda}_{\sigma\rho}(x,u)\, S^{\rho}_{\alpha\beta} - \frac{e}{mc^2}\,\phi^2(x,u)\,\Gamma^{\lambda}_{\sigma\rho}(x,u)\, F_{\alpha\beta}\, u^{\rho}\ ,$$

where the electromagnetic field tensor can now be expressed by the extended form (given in Section 3)

$$\tilde{F}_{\alpha\beta}(x,u) = 2\,\frac{mc^2}{e}\,\phi^2(x,u)\ \Gamma^{\lambda}_{[\alpha\beta]}(x,u)\, u_{\lambda}\ ,$$

that is,

$$\tilde{F}_{\alpha\beta}(x,u) = \frac{mc^2}{e}\,\phi^2(x,u)\left(\frac{\partial\, u_{\alpha}}{\partial\, x^{\beta}} - \frac{\partial\, u_{\beta}}{\partial\, x^{\alpha}} -\right.$$
$$\left. -\ E^{A}_{\alpha}(x,u)\, E^{B}_{\beta}(x,u)\,(\nabla_B\, u_A - \nabla_B\, u_A)\right).$$

An essential feature of the electromagnetic field in our unified field theory therefore manifests as a field of vorticity, somewhat reminiscent of the case of fluid dynamics, that is,

$$\tilde{F}_{\alpha\beta}(x,u) =$$
$$= 2\,\frac{mc^2}{e}\,\phi^2(x,u)\left(\omega_{\alpha\beta} - E^{A}_{\alpha}(x,u)\, E^{B}_{\beta}(x,u)\,\Theta_{AB}\right),$$

where the vorticity field is given in two referential forms by

$$\omega_{\alpha\beta} = \frac{1}{2}\left(\frac{\partial\, u_{\alpha}}{\partial\, x^{\beta}} - \frac{\partial\, u_{\beta}}{\partial\, x^{\alpha}}\right),$$

$$\Theta_{AB} = \frac{1}{2}\,(\nabla_B\, u_A - \nabla_A\, u_B)\ .$$

For our regular Eulerian electromagnetic field, we simply have

$$F_{\alpha\beta} = F_{\alpha\beta}(x,u) = 2\,\frac{mc^2}{e}\left(\omega_{\alpha\beta} - E^{A}_{\alpha}(x,u)\, E^{B}_{\beta}(x,u)\,\Theta_{AB}\right).$$

After some algebraic (structural) factorization, a profound physical solution to our most general Eulerian expression for the electromagnetic field can be obtained in integral form as

$$\varphi_{\alpha}(x,u) = \frac{mc^2}{e}\oint_{C}\phi^2(x,u)\left(\frac{\partial}{\partial\, x^{\beta}}\, E^{A}_{\alpha}(x,u)\right) u_A\, dx^{\beta}$$

such that $\tilde{F}_{\alpha\beta}(x,u) = \frac{\partial}{\partial\, x^{\beta}}\,\varphi_{\alpha}(x,u) - \frac{\partial}{\partial\, x^{\alpha}}\,\varphi_{\beta}(x,u)$, that is, in order to preserve the customary gauge invariance, our electromagnetic field shall manifestly be a "pure curl". This structural form is, of course, given in the domain of a vortical path C covered by a quasi-regular surface spanned in two directions and essentially given by the form $d\,\sigma^{AB} = d_1\, y^{A}(x,u)\, d_2\, y^{B}(x,u) \ - \ d_1\, y^{B}(x,u)\, d_2\, y^{A}(x,u)$. Upon using Gauss theorem, we therefore see that.

$$\varphi_{\alpha}(x,u) = \frac{1}{2}\,\frac{mc^2}{e}\,\times$$
$$\times\iint_{\sigma}\phi^2(x,u)\left((\nabla_B\,\nabla_A - \nabla_A\,\nabla_B)\, E^{C}_{\alpha}(x,u)\right) u_C\, d\,\sigma^{AB}.$$

In other words, we have

$$\varphi_{\alpha}(x,u) = -\frac{1}{2}\,\frac{mc^2}{e}\int\int_{\sigma}\phi^2(x,u)\,\bar{R}^{\lambda}{}_{\alpha AB}(x,u)\, u_{\lambda}\, d\,\sigma^{AB}$$

or, with $d\,\sigma^{\alpha\beta} = E^{\alpha}_{A}(x,u)\, E^{\beta}_{B}(x,u)\, d\,\sigma^{AB}$,

$$\varphi_{\alpha}(x,u) = -\frac{1}{2}\,\frac{mc^2}{e}\int\int_{\sigma}\phi^2(x,u)\,\times$$
$$\times\left(R^{\lambda}{}_{\alpha\beta\sigma}(x,u) + 2\,\Gamma^{\lambda}_{\alpha\rho}(x,u)\,\Gamma^{\rho}_{[\beta\sigma]}(x,u)\right) u_{\lambda}\, d\,\sigma^{\beta\sigma},$$

which means that

$$\varphi_{\alpha}(x,u) = -\frac{1}{2}\,\frac{mc^2}{e}\int\int_{\sigma}\phi^2(x,u)\,\times$$
$$\times\left(R^{\lambda}{}_{\alpha\beta\sigma}(x,u) + 2\,\Gamma^{\lambda}_{\alpha\rho}(x,u)\, S^{\rho}_{\beta\sigma}(x,u)\right) u_{\lambda}\, d\,\sigma^{\beta\sigma} -$$
$$-\ \frac{1}{2}\int\int_{\sigma}\Gamma^{\lambda}_{\alpha\rho}(x,u)\, F_{\beta\sigma}(x,u)\, u^{\rho}\, u_{\lambda}\, d\,\sigma^{\beta\sigma}.$$

Combining the above expression with the geodesic equation of motion given by $\frac{du_{\alpha}}{ds} = \Gamma^{\lambda}_{\alpha\beta}(x,u)\, u_{\lambda}\, u^{\beta}$, we finally obtain the integral equation of motion

$$\varphi_{\alpha}(x,u) = -\frac{1}{2}\,\frac{mc^2}{e}\int\int_{\sigma}\phi^2(x,u)\,\times$$
$$\times\left(R^{\lambda}{}_{\alpha\beta\sigma}(x,u) + 2\,\Gamma^{\lambda}_{\alpha\rho}(x,u)\, S^{\rho}_{\beta\sigma}(x,u)\right) u_{\lambda}\, d\,\sigma^{\beta\sigma} -$$
$$-\ \frac{1}{2}\int\int_{\sigma}\left(\frac{du_{\alpha}}{ds}\right) F_{\beta\sigma}(x,u)\, d\,\sigma^{\beta\sigma},$$

which shows, for the first time, the explicit dependence of the electromagnetic potential on world-velocity (as well as local acceleration), global curvature, and the material spin field.

9 Closing remarks

In the foregoing presentation, we have created a new kind of Finsler space, from which we have built the foundation of a unified field theory endowed with propagating torsion and curvature. Previously [1, 5], we have done it without the "luxury" of killing the metricity condition of Riemannian geometry; at present, the asymmetric connection form of our world-geometry, in addition to the metric and curvature, is a function of both position and world-velocity. Therefore,

looking back on our previous works, we may conclude that, in particular, the theories outlined in [3,4], as a whole, appear to be a natural bridge between generalized Riemannian and Finslerian structures.

A very general presentation of my own version of the theory of non-linear connection has also been given in [3], where, in immediate relation to [4], the enveloping evolutive world-structure can be seen as some kind of conformal Finsler space with torsion. The union between [3] and [4] has indeed already given us the essence of a fully geometric quantum theory of gravity, with electromagnetism and the Yang-Mills gauge field included. The present work mainly serves to complement and enrich this purely geometric union.

Submitted on June 27, 2009 / Accepted on August 06, 2009

References

1. Suhendro I. A four-dimensional continuum theory of space-time and the classical physical fields. *Progress in Physics*, 2007, v. 4, 34–46.
2. Suhendro I. A new semi-symmetric unified field theory of the classical fields of gravity and electromagnetism. *Progress in Physics*, 2007, v. 4, 47–62.
3. Suhendro I. A new conformal theory of semi-classical quantum general relativity. *Progress in Physics*, 2007, v. 4, 96–103.
4. Suhendro I. A unified field theory of gravity, electromagnetism, and the Yang-Mills gauge field. *Progress in Physics*, 2008, v. 1, 31–37.
5. Suhendro I. Spin-curvature and the unification of fields in a twisted space. Svenska fysikarkivet, Stockholm, 2008.
6. Borissova L. and Rabounski D. Fields, vacuum, and the mirror Universe. 2nd edition, Svenska fysikarkivet, Stockholm, 2009, p. 26–29.

Physical Consequences of Mathematical Principles

Eliahu Comay

Characteell Ltd., PO Box 39019, Tel-Aviv, 61390, Israel

E-mail: elicomay@post.tau.ac.il

Physical consequences are derived from the following mathematical structures: the variational principle, Wigner's classifications of the irreducible representations of the Poincaré group and the duality invariance of the homogeneous Maxwell equations. The analysis is carried out within the validity domain of special relativity. Hierarchical relations between physical theories are used. Some new results are pointed out together with their comparison with experimental data. It is also predicted that a genuine Higgs particle will not be detected.

1 Introduction

Physics aims to describe processes which are observed in the real world. For this purpose, mathematical formulations of physical theories are constructed. Mathematical elements of a physical theory can be divided into three sets: elements that play a relative fundamental role and are regarded as cornerstones of the theory's structure, elements used as a derivation tool and final formulas that describe the behavior of a given system. This kind of classification is used here for the convenience of the presentation. In particular, what is regarded here as a fundamental element may, in principle, be derived from more profound mathematical elements.

This work regards the following mathematical structures as cornerstones of the discussion. The variational principle and its relevant Lagrangian density; Wigner's analysis of the irreducible representations of the Poincaré group; the duality invariance of the homogeneous Maxwell equations. Some well known results of these elements are pointed out alongside others that are not very well known. Boldface numbers are used for marking the latter kind of results. It is shown that some of these results fit experimental data whereas others are used as a prediction of yet unknown experimental data.

The discussion is carried out within a framework that is based on the following theoretical elements. First, Special Relativity is regarded as a covering theory and all expressions must be consistent with relativistic covariance. The De Broglie relation between the particle's wave properties and its energy-momentum is used. Another issue is related to the hierarchical relations between physical theories. (A good discussion of this issue can be found in [1], pp. 1–6.) The following lines explain this issue in brief.

Every physical theory applies to a limited set of processes. For example, let us take the problem of moving bodies. It is well known that physical theories yield very good predictions for the motion of planets around the sun. On the other hand, nobody expects that a physical theory be able to predict the specific motion of an eagle flying in the sky. This simple example proves that the validity of a physical theory should be evaluated only with respect to a limited set of experiments. The set of experiments which can be explained by a physical theory is called its domain of validity. The relations between domains of validity define hierarchical relations between the corresponding theories. For example, given theories A, B and A's domain of validity is a subset of B's domain of validity then B's rank is higher than that of A.

An examination of Newtonian mechanics and relativistic mechanics illustrates the notion of hierarchical relations between theories. Newtonian mechanics is good for low velocity experiments (because its predictions are consistent with the error range of measurements). On the other hand, relativistic mechanics is good even for velocities that approach the speed of light. Two conclusions can be derived from these properties of the theories: First, relativistic mechanics has a more profound basis because it is valid for all experiments where Newtonian mechanics holds *and* for many other experiments where Newtonian mechanics fails. Another aspect of the relations between Newtonian mechanics and relativistic mechanics is that Newtonian mechanics imposes constraints on the form of the low velocity limit of relativistic mechanics. Indeed, the low velocity limit of relativistic mechanics is (and must be) consistent with Newtonian formulas. Below, this kind of constraint is called *constraint imposed by a lower rank theory*. Some of the theoretical derivations included below rely on this principle.

The Lorentz metric used is diagonal and its entries are $(1,-1,-1,-1)$. Greek indices run from 0 to 3. Expressions are written in units where $\hbar = c = 1$. In this system of units there is just one dimension. Here it is taken to be that of length. Therefore, the dimension of a physical quantity is a power of length and is denoted by $[L^n]$. In particular, energy and momentum take the dimension $[L^{-1}]$. The symbol $Q_{,\mu}$ denotes the partial derivative of the quantity Q with respect to x^μ. An upper dot denotes a differentiation with respect to time.

The second section discusses quantum mechanical consequences of the variational principle. The Dirac equation is examined in the third section. The fourth section shows incon-

sistencies of the Klein-Gordon (KG) and the Higgs equations. The fifth section examines results obtained from Wigner's classification of the irreducible representations of the Poincare group. Consequences of the duality invariance of the homogeneous Maxwell equations together a regular charge-monopole theory are discussed in the sixth section. The seventh section contains concluding remarks.

2 The Variational Principle

This section is dedicated to the form of a quantum theory of a *massive particle*. Let us examine the pattern obtained in a two slit interference experiment. Here one finds bright and dark strips. A completely dark interference point indicates that a full anti-phase destruction takes place there. Obviously, this property should be obtained in every Lorentz frame of reference. It follows that the phase must depend on a Lorentz scalar.

The quantity which is suitable for this purpose is the action of the system. Thus, let us examine a Lagrangian density of the system and its action

$$S = \int \mathcal{L}(\psi, \psi_{,\mu})\, d^4x^\mu . \tag{1}$$

Now, if the Lagrangian density is a Lorentz scalar then also the action is a Lorentz scalar. Therefore, it is concluded that

1. A relativistically consistent quantum theory may be derived from a Lagrangian density which is a Lorentz scalar.

Another issue is related to the dimension of the quantities. The phase is an argument of an exponent. Therefore, it must be dimensionless. Thus, in the system of units used here the action is dimensionless and satisfies this requirement. It follows that

2. An acceptable Lagrangian density must have the dimension $[L^{-4}]$.

This conclusion means that the wave function ψ acquires a well defined dimension.

Remark:

The foregoing arguments indicate that if one wishes to take an alternative way for constructing a relativistically self-consistent quantum theory, then one must find another physically meaningful quantity that is a dimensionless Lorentz scalar and is suitable for taking the role of the particle's phase. Apparently, such a quantity does not exist. If this claim is correct then the variational principle is also a necessary condition for constructing a self-consistent relativistic quantum theory.

Another point is related to the independent variables x^μ of the wave function

$$\psi(x^\mu) \tag{2}$$

which is a *single set* of four space-time coordinates. Therefore (2) cannot describe a composite particle, because such a particle requires, besides a description of the space-time location of its center of energy, additional coordinates for describing its internal structure. Therefore,

3. The wave function $\psi(x^\mu)$ describes an elementary structureless pointlike particle.

This result is consistent with the nature of an elementary classical particle (see [2], pp. 46, 47). Below it is applied as a useful criterion for evaluating experimental data.

The Lagrangian density is used here as the cornerstone of the theory. Hence, the particle's equations of motion are the corresponding Euler-Lagrange equations (see [3], p. 14; [4], p. 16)

$$\frac{\partial}{\partial x^\mu}\frac{\partial \mathcal{L}}{\partial \frac{\partial \psi}{\partial x^\mu}} - \frac{\partial \mathcal{L}}{\partial \psi} = 0 . \tag{3}$$

On this basis it is concluded that

4. The particle's equations of motion are the Euler-Lagrange equations derived from the Lagrangian density.

Obviously, different kinds of Lagrangian density yield different equations of motion. This point is discussed later.

Another issue is the consistency of a quantum theory of a massive particle with the classical theory, where the latter provides an example of constraints imposed by a lower rank theory. The classical limit of quantum mechanics is discussed in the literature (see [5], pp. 19–21 and elsewhere; [6], pp. 25–27, 137–138).

In order to do that, the quantum theory should provide expressions for the energy and the momentum of the particle. As a matter of fact, having an appropriate expression for the energy at the system's rest frame is enough. Indeed, a Lorentz boost guarantees that the theory provides appropriate expressions for the energy and momentum in any reference frame. Therefore, the following lines examine the construction of an expression for the energy of a massive quantum mechanical particle *in its rest frame*. For this end, let us take the Lagrangian density and construct the following second rank tensor (see [4], p. 19)

$$\mathcal{T}_{\mu\nu} = \frac{\partial \mathcal{L}}{\partial \frac{\partial \psi}{\partial x_\mu}}\frac{\partial \psi}{\partial x^\nu} - \mathcal{L} g_{\mu\nu} . \tag{4}$$

Now, density is a 0-component of a 4-vector and the same is true for energy. Hence, energy density is a (0,0) component of a second rank tensor. Moreover, like the dimension of the Lagrangian density, the dimension of $\mathcal{T}_{\mu\nu}$ of (4) is $[L^{-4}]$. This is also the dimension of energy density. Now, in quantum mechanics, the Hamiltonian is regarded as the energy operator. Thus, the entry $\mathcal{T}_{00}$ of (4) is regarded as an expression for the Hamiltonian density

$$\mathcal{H} = \dot{\psi}\frac{\partial \mathcal{L}}{\partial \dot{\psi}} - \mathcal{L} . \tag{5}$$

It is explained below why an expression for density is required. Here, density properties can be readily taken from electrodynamics (see [2], pp. 73–75). Density must have the dimension $[L^{-3}]$ and be a 0-component of a 4-vector satisfying the continuity equation

$$j^{\mu}_{,\mu} = 0\,. \tag{6}$$

At this point, one may take either of the following alternatives:

A. Use the Hamiltonian density $\mathcal{H}$ together with the density expression and extract the Hamiltonian differential operator H, operating on ψ. The energy is an eigenvalue of this operator:

$$H\psi = E\psi\,, \tag{7}$$

Now the De Broglie relation

$$i\,\frac{\partial\psi}{\partial t} = E\psi\,, \tag{8}$$

yields the differential equation

$$i\,\frac{\partial\psi}{\partial t} = H\psi\,. \tag{9}$$

At this point one can construct a Hilbert space that includes all eigenfunctions of the Hamiltonian H.

B. Use the expression for density as an inner product for ψ and construct an orthonormal basis for the corresponding Hilbert space. Next construct the Hamiltonian matrix. For the i, j functions of the Hilbert space basis, the Hamiltonian matrix element is

$$H_{ij} = \int \mathcal{H}(\psi_i, \psi_{i,\mu}, \psi_j, \psi_{j,\nu})\, d^3x\,. \tag{10}$$

At this point, the Hamiltonian matrix is diagonalized and its energy eigenfunctions and eigenvalues are obtained.

Obviously, the mathematical structures of A and B are relevant to the same data. Therefore, both methods construct one and the same Hilbert space.

Equation (9) makes the following problem. As stated above, the Euler-Lagrange equation (3) is the system's equation of motion. On the other hand, (9) is *another* differential equation. Hence, the following requirement should be satisfied.

5. Requirement 1: The first order differential equation (9) should be consistent with the Euler-Lagrange equation of the theory (3).

The next two sections are devoted to two specific kinds of Lagrangian density of massive particles.

3 The Dirac field

It is shown here that the Dirac field satisfies the requirements derived above and that experimental data support the theory. The formulas are written in the standard notation [3,7].

The Dirac Lagrangian density is

$$\mathcal{L} = \bar{\psi}\left[\gamma^{\mu}(i\partial_{\mu} - eA_{\mu}) - m\right]\psi\,. \tag{11}$$

A variation with respect to $\bar{\psi}$ yields the corresponding Euler-Lagrange equation

$$\gamma^{\mu}(i\partial_{\mu} - eA_{\mu})\psi = m\psi\,. \tag{12}$$

As stated in section 2, the dimension of a Lagrangian density is $[L^{-4}]$. Therefore, the dimension of ψ is $[L^{-3/2}]$ and the Dirac 4-current

$$j^{\mu} = \bar{\psi}\gamma^{\mu}\psi \tag{13}$$

satisfies the required dimension and the continuity equation (6) (see [7], p. 9). Thus, the density is the 0-component of (13)

$$\rho_{Dirac} = \psi^{\dagger}\psi\,. \tag{14}$$

Substituting the Dirac Lagrangian density (11) into the general formula (5), one obtains the Dirac Hamiltonian density

$$\mathcal{H} = \psi^{\dagger}\left[\boldsymbol{\alpha}\cdot(-i\nabla - e\mathbf{A}) + \beta m + eV\right]\psi\,. \tag{15}$$

The density $\psi^{\dagger}\psi$ can be factored out from (15) and the expression enclosed within the square brackets is the Dirac Hamiltonian written as a differential operator. Its substitution into (9) yields the well known Dirac quantum mechanical equation

$$i\,\frac{\partial\psi}{\partial t} = \left[\boldsymbol{\alpha}\cdot(-i\nabla - e\mathbf{A}) + \beta m + eV\right]\psi\,. \tag{16}$$

It is also interesting to note that due to the linearity of the Dirac Lagrangian density (11) with respect to $\dot{\psi}$, the Dirac Hamiltonian density (15) as well as the Dirac Hamiltonian *do not contain a derivative of ψ with respect to time.* Hence, (16) is an explicit first order differential equation. It is easily seen that (16) agrees completely with the Euler-Lagrange equation (12) of the Dirac field. It follows that Requirement 1 which is written near the end of section 2 is satisfied.

A Hilbert space can be constructed from the eigenfunctions obtained as solutions of the Dirac equation (16). Here the inner product of the Hilbert space is based on the density of the Dirac function (14). The eigenfunctions of the Hamiltonian are used for building an orthonormal basis

$$\delta_{ij} = \int \psi_i^{\dagger}\psi_j\, d^3x\,. \tag{17}$$

Now, the form of an energy eigenfunction is

$$\psi(\mathbf{x}, t) = e^{-iEt}\chi(\mathbf{x}). \tag{18}$$

This form enables a construction of a Hilbert space based on $e^{-iEt}\chi(\mathbf{x})$ (the Schrödinger picture) *or* on $\chi(\mathbf{x})$ (the Heisenberg picture). Here, in the Heisenberg picture, wave functions of the Hilbert space are time independent.

As is well known, the non-relativistic limit of the Dirac equation agrees with the Pauli equation of a spinning electron (see [7], pp. 10–13). Hence, in accordance with the discussion presented in the first section, the Dirac relativistic quantum mechanical equation is consistent with the constraint imposed by the lower rank theory of the non-relativistic quantum mechanical equations. A related aspect of this constraint is the density represented by the Dirac wave function (14). Indeed, in the non-relativistic limit of Dirac's density, (14) reduces to the product of the "large" components of Dirac's ψ (see [7], pp. 10–13). Hence, (14) agrees with the density of the Pauli-Schrödinger equations $\Psi^{\dagger}\Psi$. This agreement also proves the compatibility of the Hilbert space of the Pauli-Schrödinger equations with that of the non-relativistic limit of the Dirac equation.

Beside the satisfactory status of Dirac's theory, his equation has an extraordinary success in describing experimental results of electrons and muons in general and in atomic spectroscopy in particular. Moreover, experiments of very high energy prove that quarks are spin-1/2 particles. In particular, high energy experimental data are consistent with the *point-like* nature of electrons, muons and quarks (see [8], pp. 271, 272; [9], p. 149). Hence, the Dirac equation satisfies item 3 of section 2.

4 Lagrangian density of second order equations

This section discusses second order quantum equations of motion (denoted here by SOE) which are derived from a Lagrangian density. The presentation is analogous to that of the previous section where the Dirac equation is discussed. The analysis concentrates on terms containing the highest order derivatives. Thus, the specific form of terms containing lower order derivatives is not written explicitly and all kinds of these terms are denoted by the acronym for Low Order Terms LOT. Second order quantum differential equations are derived from Lagrangian densities of the following form:

$$\mathcal{L} = \phi^{*}_{,\mu}\phi_{,\nu}g^{\mu\nu} + LOT. \tag{19}$$

This form of the Lagrangian density is used for the KG (see [3], p. 38) and the Higgs (see [4], p. 715) fields.

Applying the Euler-Lagrange variational principle to the Lagrangian density (19) one obtains a second order differential equation that takes the following form

$$g^{\mu\nu}\partial_{\mu}\partial_{\nu}\phi = LOT. \tag{20}$$

Here, unlike the case of the Dirac field, the dimension of ϕ is L^{-1}. Hence, in order to satisfy dimensional requirements, the expression for density must contain a derivative with respect to a coordinate. Thus, the 4-current takes the following form (see [3], p. 40; [10], p. 199)

$$j_{\mu} = i\left(\phi^{*}\phi_{,\mu} - \phi^{*}_{,\mu}\phi\right) + LOT \tag{21}$$

and the density is

$$\rho = i\left(\phi^{*}\dot{\phi} - \dot{\phi}^{*}\phi\right) + LOT. \tag{22}$$

The left hand side of (21) is a 4-vector. Therefore, ϕ of SOE is a Lorentz scalar.

Using the standard method (5), one finds that the Hamiltonian density takes the following form (see [3], p. 38; [10], p. 198)

$$\mathcal{H} = \dot{\phi}^{*}\dot{\phi} + (\nabla\phi^{*})\cdot(\nabla\phi) + LOT. \tag{23}$$

An analysis of these expressions shows that, unlike the case of the Dirac equation, SOE theories encounter problems. Some of these problems are listed below.

a. One cannot obtain a differential operator representing the Hamiltonian. Indeed, the highest order time derivative of the SOE density (22) is *anti-symmetric* with respect to $\dot{\phi}^{*}, \dot{\phi}$ whereas the corresponding term of the Hamiltonian density (23) is *symmetric* with respect to these functions (see [11], section 3, which discusses the KG equation). Hence, in the case of SOE theories, one cannot use method A of section 2 for constructing a Hilbert space for the system.

b. The density associated with the wave function ϕ is an indispensable element of the Hilbert space. The dependence of the SOE density (22) on time-derivatives proves that a SOE Hilbert space *is built on functions of the four space-time coordinates* x^{μ}. Hence, SOE cannot use the Heisenberg picture where the functions of the Hilbert space are time independent $\psi_H = \psi_S(t_0)$ (see [3], p. 7).

c. In the Schrödinger theory $\Psi^{*}\Psi$ represents density. It follows that like the case of the Dirac field, the dimension of this Ψ is $[L^{-3/2}]$. On the other hand, the dimension of the SOE function ϕ is $[L^{-1}]$. Therefore, the nonrelativistic limit of SOE theories is inconsistent with the Schrödinger theoretical structure.

d. Unlike the Dirac Hamiltonian, which is independent of time-derivatives of ψ, the SOE Hamiltonian density has a term containing the *bilinear product* $\dot{\phi}^{*}\dot{\phi}$. Hence, it is not clear how a SOE analogue of the fundamental quantum mechanical equation (9) can be created. Moreover, it should be proved that this *first order implicit nonlinear differential equation* is consistent with the corresponding *second order explicit differential equation* (20) of SOE, as stated by requirement 1 which is formulated near the end of section 2. Without substantiating the validity of the Hamiltonian, SOE

theories violate a constraint imposed by a lower rank theory which is explained in the lines that precede (4).

e. Some SOE theories apply to *real* fields (see [3], p. 26; [4], p. 19 etc.). New problems arise for these kinds of physical objects. Indeed, density cannot be defined for these particles (see [12], pp. 41–43). Moreover, a massive particle may be at rest. In this case its amplitude should be independent of time. But a *real* wave function has no phase. Therefore, in the case of a motionless real particle, *the time-derivative of its wave function vanishes identically*. For this reason, its physical behavior cannot be described by a differential equation with respect to time. Thus, a real SOE particle *cannot* be described by the SOE equation of motion (20) and it cannot have a Hamiltonian.

f. Another problem arises for a charged SOE particle. As stated in item *a* above, this particle cannot have a differential operator representing the Hamiltonian. Hence, method *A*, discussed near (7)-(9), cannot be used for a Hilbert space construction. Moreover, the inner product of a time-dependent Hilbert space is destroyed in the case of an external charge that approaches a charged SOE particle (see [13], pp. 59–61). Hence, method *B* does not hold either. It follows that a charged SOE particle has no Hamiltonian. Therefore, a charged SOE particle does not satisfy a constraint imposed by a lower rank theory.

This discussion points out theoretical difficulties of SOE fields. The experimental side responds accordingly. Point 3 of section 2 is useful for evaluating the data. Thus, a field $\psi(x^\mu)$ used in a Lagrangian density describes *an elementary point-like particle*. It turns out that as of today, no scalar pointlike particle has been detected.

In the history of physics, the three π-mesons have been regarded as KG particles and the electrically neutral π^0 member of this triplet was regarded as a Yukawa particle, namely, a real (pseudo) scalar KG particle. However, it has already been established that π-mesons are not elementary pointlike particles but composite particles made of $q\bar{q}$ and they occupy a nonvanishing spatial volume. Thus, as of today, there is no experimental support for an SOE particle. The theoretical and experimental SOE problems mentioned above are regarded seriously here. On the basis of the foregoing analysis, it is predicted here that no genuine elementary SOE particle will be detected. A special case is the following statement: a genuine Higgs particle will not be detected.

5 Irreducible representations of the Poincaré group

The profound significance of Wigner's analysis of the irreducible representations of the Poincaré group (see [14]; [15], pp. 44–53; [16], pp. 143–150) is described by the following words: "It is difficult to overestimate the importance of this paper, which will certainly stand as one of the great intellectual achievements of our century" (see [16], p. 149). Wigner's work shows that there are two physically relevant classes of irreducible representations of the Poincaré group. One class is characterized by a mass $m > 0$ and a spin s. The second class consists of cases where the self mass $m = 0$, the energy $E > 0$ and two values of helicity. (Helicity is the projection of the particle's spin in the direction of its momentum.) Two values of helicity $\pm s$ correspond to a spin s. Thus, each massive particle makes a basis for a specific irreducible representation that is characterized by the pair of values (m, s). A massless particle (like the photon) has a zero self mass, a finite energy and two values of helicity (for a photon, the helicity is ± 1).

A result of this analysis is that a system that is stable for a long enough period of time is a basis for an irreducible representation of the Poincaré group (see [15], pp. 48–50). Let us take a photon. Cosmic photons are detected by measuring devices on earth after traveling in space for a very very long time, compared to the duration of an electromagnetic interaction. Therefore, photons must belong to a unique irreducible representation of the Poincaré group. This conclusion is inconsistent with the idea of Vector Meson Dominance (VMD). VMD regards the photon as a linear combination of a massless real photon *and* a massive vector meson. (For a presentation of VMD see [9], pp. 296–303; [17].)

The VMD idea has been suggested in order to explain experimental results of scattering of energetic photons on nucleons. The main points of the data are:

i. The overall charge of a proton is $+e$ whereas the overall charge of a neutron vanishes. Therefore, charge constituents of a proton and a neutron are different.

ii. In spite of the data of the previous item, interaction of a hard photon with a proton is nearly the same as its interaction with a neutron.

The theoretical analysis of Wigner's work shows that VMD is unacceptable. Other inconsistencies of VMD with experimental data have also been published [18]. This state of affairs means that the currently accepted Standard Model has no theoretical explanation for the photon-nucleon interaction. This point is implicitly recognized by the PACS category of VMD which does not belong to a theoretical PACS class. Thus, on July 2009, VMD is included in the class of "Other models for strong interactions". Hence, the Standard Model does not provide a theoretical explanation for the scattering data of hard photons on nucleons.

6 Duality transformations of electromagnetic fields

Electromagnetic fields travel in vacuum at the speed of light. Therefore, the associated particle, namely — the photon, is massless. For this reason, it cannot be examined in a frame where it is motionless. This result means that the argument of

point e of section 4 does not hold for electromagnetic fields. It follows that, unlike the wave function of a massive particle, electromagnetic fields can be described by a Lagrangian density that depends on *real functions*. This well known fact is another aspect of the inherent difference between massive and massless particles, which has been obtained by Wigner and discussed in the previous section.

Thus, the system consists of electromagnetic fields whose equations of motion (Maxwell equations) are derived from a Lagrangian density and charge carrying massive particles whose equation of motion (the Lorentz force) is derived from a classical Lagrangian. Below, this theory is called ordinary electrodynamics. All quantities are described by real functions. The action of the system is (see [2], p. 75)

$$S = -\int m\sqrt{1-v^2}\,dt - \int A_\mu j^\mu_{(e)}\,d^4x - \\ - \frac{1}{16\pi}\int F_{\mu\nu}F^{\mu\nu}d^4x\,, \qquad (24)$$

where the subscript $_{(e)}$ indicates that j^μ is a current of electric charges, A_μ denotes the 4-potential of the electromagnetic fields, and $F^{\mu\nu}$ is the corresponding fields tensor

$$F_{\mu\nu} = A_{\nu,\mu} - A_{\mu,\nu}\,. \qquad (25)$$

The explicit form of this tensor is

$$F^{\mu\nu} = \begin{pmatrix} 0 & -E_x & -E_y & -E_z \\ E_x & 0 & -B_z & B_y \\ E_y & B_z & 0 & -B_x \\ E_z & -B_y & B_x & 0 \end{pmatrix}. \qquad (26)$$

These expressions enable one to derive Maxwell equations (see [2], pp. 78, 79 and 70, 71)

$$F^{\mu\nu}_{\ \ ,\nu} = -4\pi j^\mu_{(e)};\quad F^{*\mu\nu}_{\ \ ,\nu} = 0\,. \qquad (27)$$

Here $F^{*\mu\nu}$ is the dual tensor of $F^{\mu\nu}$

$$F^{*\mu\nu} = \begin{pmatrix} 0 & -B_x & -B_y & -B_z \\ B_x & 0 & E_z & -E_y \\ B_y & -E_z & 0 & E_x \\ B_z & E_y & -E_x & 0 \end{pmatrix}. \qquad (28)$$

These tensors satisfy the following relation

$$F^{*\mu\nu} = \frac{1}{2}\,\varepsilon^{\mu\nu\alpha\beta}F_{\alpha\beta}\,, \qquad (29)$$

where $\varepsilon^{\mu\nu\alpha\beta}$ is the completely antisymmetric unit tensor of the fourth rank.

The Lorentz force, which describes the motion of a charged particle, is obtained from a variation of the particle's coordinates (see [2], pp. 49–51)

$$ma^\mu_{(e)} = eF^{\mu\nu}v_\nu\,. \qquad (30)$$

The foregoing expressions describe the well established theoretical structure of ordinary electrodynamics. Let us see the results of introducing duality transformations. Duality transformations (also called duality rotations by $\pi/2$) of electromagnetic fields take the following form (see [19], pp. 252, 551; [20], p. 1363)

$$\mathbf{E} \to \mathbf{B},\quad \mathbf{B} \to -\mathbf{E}\,. \qquad (31)$$

These transformations can be put into the following tensorial form

$$F^{\mu\nu} \to F^{*\mu\nu};\quad F^{*\mu\nu} \to -F^{\mu\nu}. \qquad (32)$$

An examination of the *homogeneous* Maxwell equations

$$F^{\mu\nu}_{\ \ ,\nu} = 0;\quad F^{*\mu\nu}_{\ \ ,\nu} = 0, \qquad (33)$$

proves that they are invariant under the duality transformations (32). On the other hand, an inequality is obtained for the inhomogeneous Maxwell equation

$$F^{*\mu\nu}_{\ \ ,\nu} \neq -4\pi j^\mu_{(e)}. \qquad (34)$$

This problem can be settled by the introduction of the notion of magnetic monopoles (called briefly monopoles). Thus, duality transformations of the electromagnetic fields (32) are augmented by the following transformation that relates charges and monopoles

$$e \to g;\quad g \to -e\,, \qquad (35)$$

where g denotes the monopole strength.

Two things are established at this point:

1. The theoretical foundation of ordinary electrodynamics (24), and its equations of motion (27) and (30).
2. The mathematical form of duality transformations (32) and (35).

Now, a theory for a system of monopoles and electromagnetic fields (called below monopole electrodynamics) is obtained from the application of duality transformations to ordinary electrodynamics. The action principle of this system is

$$S = -\int m\sqrt{1-v^2}\,dt - \int A_{(m)\mu}j^\mu_{(m)}\,d^4x - \\ - \frac{1}{16\pi}\int F^*_{(m)\mu\nu}F^{*\mu\nu}_{(m)}\,d^4x\,, \qquad (36)$$

where the subscript (m) denotes that the quantities pertain to monopole electrodynamics. Here the fields are derived from a 4-potential

$$F^*_{(m)\mu\nu} = A_{(m)\nu,\mu} - A_{(m)\mu,\nu}\,, \qquad (37)$$

which is analogous to (25). Maxwell equations of monopole electrodynamics are

$$F^*_{(m)}{}^{\mu\nu}_{\ \ ,\nu} = -4\pi j^\mu_{(m)};\quad F_{(m)}{}^{\mu\nu}_{\ \ ,\nu} = 0 \qquad (38)$$

and the Lorentz force is

$$ma^{\mu}_{(m)} = g F^{*\mu\nu}_{(m)} v_{\nu} \,. \tag{39}$$

Thus, we have two theories for two distinct systems: ordinary electrodynamics for a system of charges and fields and monopole electrodynamics for a system of monopoles and fields. The first system does not contain monopoles and the second system does not contain charges. The problem is to find the form of a unified theory that describes the motion of charges, monopoles and fields. Below, such a theory is called a charge-monopoly theory. The charge-monopole theory is a higher rank theory whose domain of validity includes those of ordinary electrodynamics and of monopole electrodynamics as well. On undertaking this assignment, one may examine two postulates:

1. Electromagnetic fields of ordinary electrodynamics are identical to electromagnetic fields of monopole electrodynamics.
2. The limit of the charge-monopole theory for a system that does not contain monopoles agrees with ordinary electrodynamics and limit of the charge-monopole theory for a system that does not contain charges agrees with monopole electrodynamics.

It turns out that these postulates are mutually contradictory.

A charge-monopole theory that relies (implicitly) on the first postulate has been published by Dirac many years ago [21, 22]. (Ramifications of Dirac monopole theory can be found in the literature [20].) This theory shows the need to define physically unfavorable irregularities along strings. Moreover, the form of its limit that applies to a system of monopoles without charges is inconsistent with the theory of monopole electrodynamics, which is derived above from the duality transformations. Therefore, it does not satisfy the constraint imposed by a lower rank theory. The present experimental situation is that in spite of a long search, there is still no confirmation of the existence of a Dirac monopole (see [23], p. 1209).

The second postulate was used for constructing a different charge-monopole electrodynamics [24, 25]. This postulate guarantees that the constraints imposed by the two lower rank theories are satisfied. Moreover, this theory does not introduce new irregularities into electrodynamics. Thus, it is called below regular charge-monopole theory. The following statements describe important results of the regular charge-monopole theory: The theory can be derived from an action principle, whose limits take the form of (24) and (36), respectively. Charges do not interact with bound fields of monopoles; monopoles do not interact with bound fields of charges; radiation fields (namely, photons) of the systems are identical and charges as well as monopoles interact with them. Another result of this theory is that the size of an elementary monopole g is a free parameter. Hence, the theory is relieved from the huge and unphysical Dirac's monopole size $g^2 = 34.25$.

The regular charge-monopole theory is constructed on the basis of the second postulate. This point means that it is not guided by new experimental data. However, it turns out that it explains the important property of hard photon-nucleon interaction which is mentioned in the previous section. Indeed, just assume that quarks carry a monopole and postulate that the elementary monopole unit g is much larger then the electric charge e (probably $|g| \simeq 1$). This property means that photon-quark interaction depends mainly on monopoles and that the photon interaction with the quarks' electric charge is a small perturbation. Therefore, the very similar results of photon-proton and photon-neutron scattering are explained. (Note also that all baryons have a core which carries three units of magnetic charge that attracts the three valence quarks. The overall magnetic charge of a hadron vanishes.) Other kinds of experimental support for the regular charge-monopole theory have been published elsewhere [26].

7 Concluding remarks

This work is based on the main assumption of theoretical physics which states that results derived from physically relevant mathematical structures are expected to fit experimental data [27]. Three well known mathematical structures are used here: the variational principle, Wigner's analysis of the irreducible representations of the Poincaré group and duality transformations of electromagnetic fields.

The paper explains and uses three points which are either new or at least lack an adequate discussion in textbooks.

1. Constraints are imposed by a lower rank theory on properties of the corresponding limit of a higher rank theory (see a discussion in the Introduction).
2. The need to prove consistency between the Euler-Lagrange equation obtained from a Lagrangian density and the quantum mechanical equation $i\,\partial\psi/\partial t = H\psi$ which holds for the corresponding Hamiltonian.
3. The field function $\psi(x^{\mu})$ describes an elementary pointlike particle (see the discussion near (2)).

Points 1 and 2 are useful for a theoretical evaluation of the acceptability of specific physical ideas. Point 3 is useful for finding an experimental support for these ideas.

The main results of the analysis presented in this work are as follows: Dirac equation is theoretically consistent and has an enormous experimental support. Second order quantum mechanical equations (like the Klein-Gordon and the Higgs equations) suffer from many theoretical problems and have no experimental support. (π-mesons are not pointlike, therefore, they are not genuine Klein-Gordon particles.) Real fields cannot be used for a description of massive particles. The idea of Vector Meson Dominance is inconsistent with Wigner's analysis of the irreducible representations of the Poincaré group.

Therefore, VMD is unacceptable and the Standard Model has no theoretical explanation for the data of a scattering process of an energetic photon on nucleon. Monopole theories that introduce irregularities along strings are inconsistent with point 1 of this section and have no experimental support. The regular charge monopole theory [24–26] is consistent with point 1 and has experimental support.

Submitted on August 02, 2009 / Accepted on August 06, 2009

References

1. Rohrlich F. Classical charged particles. Addison-Wesley, Reading (Mass), 1965.
2. Landau L. D., Lifshitz E. M. The classical theory of fields. Elsevier, Amsterdam, 2005.
3. Bjorken J. D., Drell S. D. Relativistic quantum fields. McGraw-Hill, New York, 1965.
4. Peskin M. E., Schröder D. V. An introduction to quantum field theory. Addison-Wesley, Reading (Mass), 1995.
5. Landau L. D., Lifshitz E. M. Quantum Mechanics. Pergamon, London, 1959.
6. Schiff L. I. Quantum Mechanics. McGraw-Hill, New York, 1955.
7. Bjorken J. D., Drell S. D. Relativistic Quantum Mechanics. McGraw-Hill, New York, 1964.
8. Perkins D. H. Introduction to high energy physics. Addison-Wesley, Menlo Park (CA), 1987.
9. Frauenfelder H., Henley E. M. Subatomic physics. Prentice Hall, Englewood Cliffs, 1991.
10. Pauli W., Weisskopf V. The quantization of the scalar relativistic wave equation. *Helv. Phys. Acta*, 1934, v. 7, 709–731. English translation: Miller A. I. Early Quantum Electrodynamics. University Press, Cambridge, 1994. pp. 188–205. (In the text, page references apply to the English translation.)
11. Comay E. Further diffculties with the Klein-Gordon equation. *Apeiron*, 2005, v. 12, 26–46.
12. Berestetskii V. B., Lifshitz E. M., Pitaevskii L. P., Quantum Electrodynamics. Pergamon, Oxford, 1982.
13. Comay E. The significance of density in the structure of quantum theories. *Apeiron* 2007, v. 14, 50–64.
14. Wigner E. On unitary representations of the inhomogeneous Lorentz group. *Ann. Math.* 1939, v. 40, 149–204.
15. Schweber S. S. An introduction to relativistic quantum field theory. Harper & Row, New York, 1964.
16. Sternberg S. Group theory and physics. Cambridge University Press, Cambridge, 1994.
17. Bauer T. H., Spital R. D., Yennie D. R., Pipkin F. M. The hadronic properties of the photon in high-energy interactions. *Rev. Mod. Phys.* 1978, v. 50, 261–436.
18. Comay E. Remarks on photon-hadron interactions. *Apeiron* 2003, v. 10, 87–103.
19. Jackson J. D. Classical Electrodynamics. John Wiley, New York, 1975.
20. Goddard P., Olive D. I. Magnetic monopoles in gauge field theories. *Rep. Prog. Phys.*, 1978, v. 41, 1357–1437.
21. Dirac P. A. M. Quantized singularities in the electromagnetic field. *Proc. Royal Soc. A*, 1931, v. 133, 60–72.
22. Dirac P. A. M. The theory of magnetic poles. *Phys. Rev.*, 1948, v. 74, 817–830.
23. Amsler C. et al. Review of particle physics. *Phys. Lett. B*, 2008, v. 667, 1–1340.
24. Comay E. Axiomatic deduction of equations of motion in classical electrodynamics. *Nuovo Cimento B*, 1984, v. 80, 159–168.
25. Comay E. Charges, monopoles and duality relations. *Nuovo Cimento B*, 1995, v. 110, 1347–1356.
26. Comay E. A regular theory of magnetic monopoles and its implications. Published in *Has the Last Word Been Said on Classical Electrodynamics?* Editors: A. Chubykalo, V. Onoochin, A. Espinoza, and R. Smirnov-Rueda. Rinton Press, Paramus (NJ), 2004.
27. Wigner E. P. The unreasonable effectiveness of mathematics in the natural sciences. *Comm. in Pure and Appl. Math.*, 1960, v. 13, 1–14.

Progress in Physics **is an American scientific journal on advanced studies in physics, registered with the Library of Congress (DC, USA): ISSN 1555-5534 (print version) and ISSN 1555-5615 (online version). The journal is peer reviewed and listed in the abstracting and indexing coverage of: Mathematical Reviews of the AMS (USA), DOAJ of Lund University (Sweden), Zentralblatt MATH (Germany), Scientific Commons of the University of St. Gallen (Switzerland), Open-J-Gate (India), Referential Journal of VINITI (Russia), etc.** ***Progress in Physics*** **is an open-access journal published and distributed in accordance with the Budapest Open Initiative: this means that the electronic copies of both full-size version of the journal and the individual papers published therein will always be acessed for reading, download, and copying for any user free of charge. The journal is issued quarterly (four volumes per year).**

Electronic version of this journal:
http://www.ptep-online.com

Postal address for correspondence:

Department of Mathematics and Science
University of New Mexico
200 College Road, Gallup, NM 87301, USA

Printed in the United States of America